Projectile Fragmentation Reactions and Production of Nuclei near the Neutron Drip-line

Doctoral Dissertation

by

Masahiro Notani

Department of Physics, School of Science
University of Tokyo

2000

Abstract

The production mechanism of projectile-like fragments at intermediate energies has been investigated to understand the mechanism itself and to make precise prediction of the secondary beam intensity for designing experiments. We focus the target dependence of momentum distributions and production cross sections of fragments. Measurement of longitudinal momentum distributions of projectile-like fragments ranging $3 \leq Z \leq 18$ in the neutron-rich side has been performed with a 90-94A MeV ^{40}Ar beam using ^{9}Be and ^{181}Ta targets at RIKEN-RIPS. The momentum distribution was fitted with an asymmetric function where free parameters are momentum shift, momentum widths for high and low momentum side, and the cross section. Based on a splitting picture for fragmentation process, one can understand the momentum shift of fragment. The fact that the momentum width of high momentum side corresponds to Goldhaber formula proves that high energy reaction mechanism still governs in this energy region. On the other hand, a reaction channel of nucleon transfer is competitive to a fragmentation channel. The momentum spectra are asymmetric with a low momentum tail indicative of a large energy damping. The production of elements heavier or more neutron-rich than the projectile indicates that the interaction time is still sufficient to permit the exchange of nucleons between projectile and target. The target dependence on production cross sections of the projectile-like fragments has been investigated. We clearly show the breakdown of factorization hypothesis for neutron-rich nuclei far from stability. For quantitative discussion, the production cross sections are compared with the semi-empirical parametrization (EPAX). The breakdown of factorization is represented by the target dependence of the U parameter. The U parameter, which was known to be a constant for neutron-rich side, looks to have fragment-mass dependence and target dependence for ^{9}Be and ^{181}Ta. The U parameter is very sensitive to the production of neutron-rich nuclei. The present result has strong effect on improving the accuracy of cross-section estimation for the production of nuclei near the neutron drip-line.

Contents

List of Figures

List of Tables

Chapter 1

Introduction

Unstable nuclear physics has recently become one of the most interesting fields of nuclear physics. The study of nuclei lying far from β-stability has been performed with radioactive isotope beams. For long time, nuclear physics experiments were carried out with the reactions between beams and targets of stable isotopes that can be found in nature. With the recent development of heavy-ion accelerators as well as the technique of radioactive isotope beam production, the investigation of nuclear reactions with the radioactive isotope beams has revealed the new phenomena observed for unstable nuclei. Radioactive isotope beams brought the discovery of new forms of nuclei such as the neutron halo [1], and the neutron skin [2] [3]. The properties of nuclei with extremely high neutron-to-proton ratio is different from that of stable nuclei. For instance, the neutron-rich N~20 region (i.e.^{31}Na-^{32}Mg) is referred as the island of inversion where the neutron closed shell structure disappears. The N=20 nucleus ^{32}Mg has been proven to be well deformed as confirmed by the large $B(E2; 0_1^+ \rightarrow 2_1^+)$ value observed [4]. The result of experiments that the magicity of N=20 is lost in the neutron-rich region surprised us since the deformation could not have been predicted from the knowledge of nuclei lying closer to β-stability.

Concerning the production and separation techniques of radioactive isotopes, an in-flight method with a magnetic spectrometer is very useful. The in-flight method has some advantages for production of radioactive beams. A wide range of radioactive nuclei are produced as projectile fragments or fission fragments and emitted in a narrow forward cone nearly at the primary-beam velocity. Without a post acceleration, the secondary beam can be selected from the fragments by a magnetic spectrometer efficiently. The pioneering work in the 1980s was performed with the radioactive beam line at LBL [5]. The separation technique had been developed at

the LISE spectrometer at GANIL [6]. The accumulative techniques have led to the development of next generation facilities such as A1200 at MSU [7], FRS at GSI [8], and RIPS at RIKEN [9].

Recently, facilities of heavy-ion beams have been upgraded in order to obtain the strong secondary beams for experiments of the isospin frontier of unstable nuclear physics. The aims of the upgrade are higher intensities of primary beams and higher energies up to several hundred A MeV. The several A GeV beams at the Schwerionen Synchrotron accelerator (SIS) in Darmstadt has achieved one of the aims. The high energy beams afford a thick production target. On the other hand, the cyclotrons in other facilities provide one hundred A MeV heavy-ion beams. Yet a cyclotron has an advantage in the beam intensity, which is about two orders of magnitude higher than that of synchrotrons. Thus, the high-intensity heavy-ion beams at intermediate energies are very useful to produce unstable nuclei from light to medium masses, including the drip-line nuclei, via fragmentation reactions. Furthermore, the projectile fragmentation at energies of 20-100A MeV still retain an important advantage for stopping process of unstable nuclei. In some experiments, unstable nuclei should be stopped so that their β-decay can be characterized by the detection of emitted particles (β, γ and neutron). At intermediate energies, only a few percent of the nuclei are lost by nuclear reactions before they stop. On the other hand, at relativistic energies, about 80% exotic fragments could be lost due to the nuclear reactions. Thus, intermediate-energy primary beams would be also one of the most valuable sources of unstable nuclei.

The radioactive beam lines are now available for experiments to study unstable nuclear physics. The design of experiments is performed seeking for efficient production of radioactive isotopes to be studied. What should we choose as projectile and target nuclei? And how about the beam energy? To optimize the condition for experiments, understanding of the reaction mechanisms is very important. The reaction mechanisms of projectile fragmentation have been investigated with the fragmentation data in many combinations of projectile and target, and in a wide energy range. However, the data were acquired only for fragments close to the β-stability line. The problems about the optimization of beam parameters still remain especially for the production of very neutron-rich nuclei. To clarify the problems, we first review the reaction mechanisms of projectile fragmentation. Secondly, practical problems for production of very neutron-rich nuclei are discussed. Finally, we present objectives

in this thesis.

1.1 Projectile-Fragmentation Reaction

The discovery of projectile fragmentation reaction at LBL [10, 11] brought a new field of nuclear research in 1970s. A considerable number of experimental and theoretical works have been performed to understand the reaction mechanism. Figure 1.1 shows a schematic view of the projectile fragmentation process on an abrasion-ablation scheme. The abrasion process is described as the geometrical picture of fireball model [12]. The projectile and target make clean cylindrical cuts through each other [13], then a spectator piece of projectile nucleus is leaving. The spectator is named as a "prefragment". Through the ablation process, the prefragment emits light particles and γ-rays to become a "fragment" observed in experiments.

The production cross sections of fragments are independent of projectile energy in the range 1-2A GeV and vary only slowly with target mass [14]. These observations suggest the applicability of the concepts of "limiting fragmentation" and "factorization", respectively. Assumed the validity of factorization, a target dependence of the cross sections is limited only by taking account of the nuclear-size effect [15]. These ideas were developed initially to account for similar phenomena in peripheral reactions between elementary particles [16, 17].

The assumption of factorization has confirmed as a basic law of the projectile fragmentation reaction for a wide range of projectile energy and target nuclei for long time. D.L.Olson et al. [18] have investigated the factorization of fragment-production cross sections in relativistic heavy-ion collisions. The analysis of cross sections has been performed for projectiles of ^{12}C, ^{16}O, ^{18}O and ^{56}Fe in the 1 to 2 A GeV energy region for targets ranging from Be to U. The projectile-like fragments were observed within a range of $\Delta Z \cong 2$ from the β-stability line. It was found that there is no target dependence of fragmentation at relativistic energies so far.

In the following sections, we discuss momentum distributions and production cross sections of projectile-like fragments for a wide range of the incident beam energies.
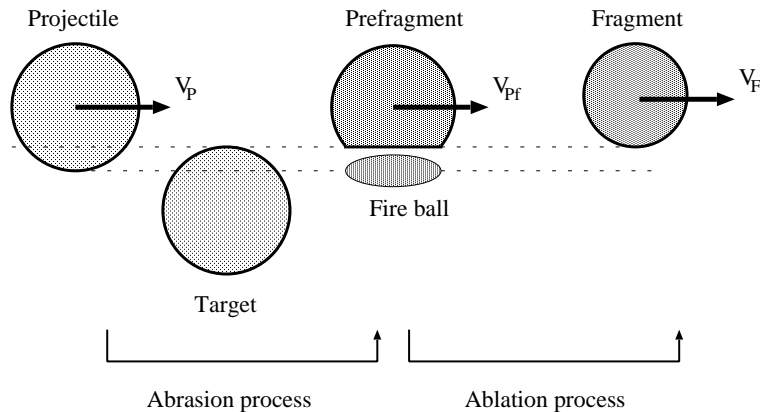
Figure 1.1: Schematic view of the projectile fragmentation.

1.1.1   Momentum Distribution

The momentum distributions of projectile-like fragments provide valuable information about the reaction mechanism leading to their formation. The early results of experiments with relativistic heavy ions ($\sim 1A$ GeV) irradiated on various targets were reported, and the momentum distributions of fragments were intensively discussed. In the rest frame of projectile, momentum distributions of fragments were found to have Gaussian-function $exp(-P^2/2\sigma^2)$ by Heckman et al [19]. Furthermore, the fragments were found to be slowed down during a fragmentation reaction [20, 21]. This slow-down is often called as momentum shift.

Abul-Magd et al. [22] viewed the momentum shift of fragments as a friction phenomenon. In order to remove nucleons from projectile nuclear bonds have to be broken. They tend to pull on the projectile and slow it down. Obviously, this simplified picture is related to the concept of reaction Q-value used for pre-fragment production, where several nucleons are removed out from the projectile [23]. Although a large number of studies have been made on the momentum shift, there is little agreement as to the excitation energy of prefragment. For the study of the initial stage of nuclear fragmentation reaction, the momentum shift should be investigated more carefully.

Goldhaber made an attempt to understand the momentum width of fragments with a statistical model [24]. The Goldhaber model assumes two simple conditions. First, nucleons in a projectile are described as a Fermi gas system which consists

of free fermions in a volume. Secondly, the fragmentation process can be described as sudden removal of nucleons from the projectile, Since the total momentum of projectile nucleons is zero in the projectile rest frame, the fragment momentum can be calculated as the sum of each nucleon remained in the projectile residue. Thus, the Gaussian momentum width σ is given by the expression:

$$\sigma^2 = \sigma_0^2 \frac{A_f(A_p - A_f)}{A_p - 1} \quad (1.1)$$

where $A_{p,f}$ are the mass number of the projectile and fragment, respectively. The square width σ^2 depends parabolically on the fragment mass. Several models can also account for this behavior [25, 26]. Since the σ in Eq.(1.1) corresponds to one cartesian component of the three momentum, the reduced width σ_0 can be described as:

$$\sigma_0^2 = \frac{<p^2>}{3} \quad (1.2)$$

where $<p^2>$ is the mean square momentum of A_f nucleons in projectile. Feshbash and Huang [27] quote that the mean square momentum can be expressed in terms of the Fermi momentum (p_F) as:

$$<p^2> = \frac{3p_F^2}{5}. \quad (1.3)$$

By the quasi-elastic electron scattering [28], the Fermi momentum has been measured as $p_F \simeq 230$ MeV/c for ^{16}O, leading to a reduced width of $\sigma_0 \simeq 100$ MeV/c. This yields above 10% the experimental data of nuclear fragmentation. The discrepancy has been investigated as mentions later, however, the result is in reasonable agreement with the experimental data.

At intermediate energies, the energy dependence of reduced width σ_0 is observed. For instance, the systematics of reduced width σ_0 in Goldhaber formula (1.1) was investigated in $27.6A$ MeV ^{40}Ar+^{68}Zn reaction [29, 30]. Two groups of σ_0 values were observed in the experiment, suggesting the presence of two reaction mechanisms. The average value of the σ_0 measured for the nucleides with $A{<}36$ is 84 MeV/c, while the average value for $^{36-38}$S and ^{37,38}Cl is 49 MeV/c. The first value agrees with values measured at projectile energies as high as $213A$ MeV [31] and $2.1A$ GeV [21], in which a typical high-energy fragmentation processes is observed. The second value σ_0=49 MeV/c is also in agreement with the systematics in the 24-40A MeV region,

in which the fragmentation process may compete with a low-energy process, direct nucleon transfer [32].

W.A.Friedman suggested that it is important to incorporate the effect of Coulomb distortion at low energies (10-20A MeV) [33]. It follows that :

$$\sigma_0(E_0) \;\; = \;\; \sigma_0(1 - \frac{E_{CO}}{E_0})^{1/2} \tag{1.4}$$

where E_{CO} is the Coulomb barrier, E_0 the beam energy. This correction is not large enough to reproduce the observed energy dependence. Another suspicion is that Pauli corrections [34] and phase-space constraints [35] which are not included in the Goldhaber model, would decrease the value of σ_0 at low energies [36]. These corrections lead to agreement with the energy dependence of σ_0.

Another feature at intermediate energies, which is different from at relativistic energies, is the shape of momentum distributions of fragments at forward angles. At relativistic energies, momentum distributions have a symmetric shape like a Gaussian function. At intermediate energies, on the other hand, the distributions have an asymmetric shape with a tail at low momentum side. Figure 1.2 shows the comparison of momentum distribution with the calculation. The energy spectra of ^{34}S and ^{25}Mg were obtained at $4°$ in ^{40}Ar + ^{58}Ni reaction at $26.5A$ MeV (histograms). The spectra show asymmetric distributions clearly. A theoretical attempt have been made to reproduce the asymmetric shape, by taking into account nucleon flows between projectile and target in the collision time [37]. In this model, stochastic transfers using a Monte Carlo method and sequential evaporation were taken into account. This model can reproduce the low-momentum-side tails (dots in Fig. 1.2). However, due to a large "friction" force, the whole of predicted distributions are shifted toward the low momentum side. A recent AMD calculation also gives the similar trend [38]. Experimental works performed so far at intermediate energies have not focused on the asymmetric shape of momentum distributions, maybe partly due to such complicated features of reaction mechanisms. The lack of systematic data on the shape leads to no further discussions for the reaction mechanism at intermediate energies.
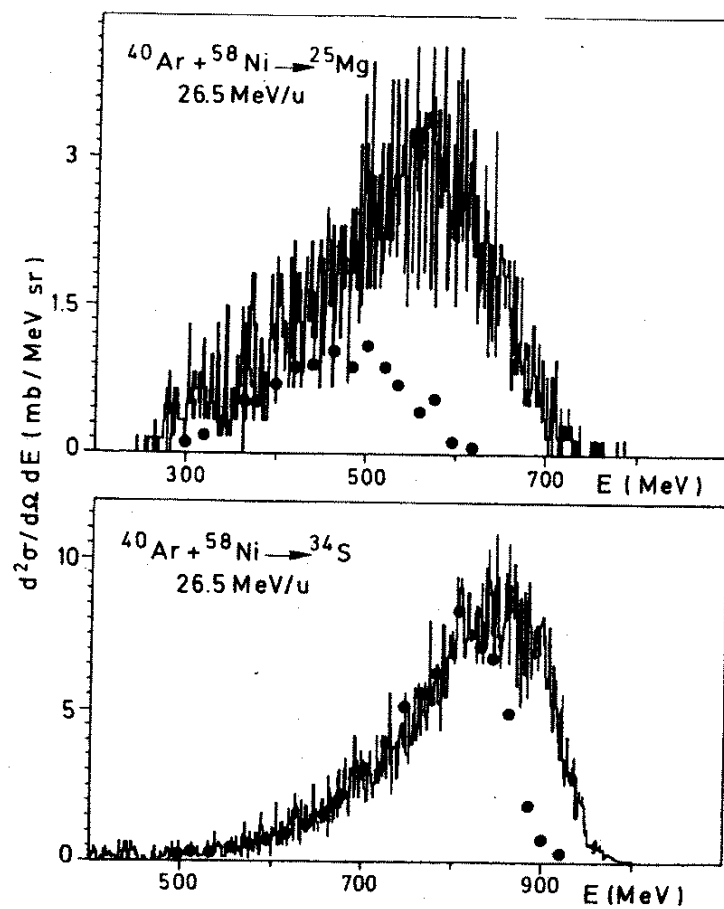
Figure 1.2: Energy spectra of ^{34}S and ^{25}Mg detected in the reaction at 26.5A MeV, in taken from Ref. [37]. The histograms are energy spectrum obtained experimentally. The dots are the simulation results of stochastic transfer model with no normalization.

1.1.2   Production Cross Section

To understand the production cross sections of fragments, several fragmentation-reaction models have been proposed at high energies ($\geq 0.2A$ GeV) [39, 40, 41]. Many of these models are based on the abrasion-ablation scheme [42], which was introduced by Bowman, Swiatecki, and Tsang [43]. As shown in Fig. 1.1, the abrasion process of projectile determines the production cross sections of prefragments geometrically. Then in next ablation process, the formation of fragments is described as a 'cool-down' process through particle or γ-ray emission from the prefragments. Each model is characterized by the treatment of the abrasion process; how to calculate the Z and N distributions of the prefragments [44] and how to calculate excitation energies of prefragments [45].

The prediction of production cross sections with fragmentation models based on the abrasion-ablation scheme (AA model [46]) shows good agreement to the experimental data for unstable nuclei near the β-stability line. However, the predictive power of models is not good enough for very neutron-rich nuclei far from the stability. Figure 1.3 shows a typical comparison of predictions by the AA model [47] with experimental data for production cross sections of oxygen isotopes. This model overestimates the production cross section of ^{23}O (The heaviest oxygen isotope is so far ^{24}O experimentally). Among several models for excitation energy estimation, the best one was tried to be found to reproduce production cross section. However, all of the models can not reproduce the ^{23}O cross section. For better prediction for intensities of radioactive isotope beams, the development of the AA models is needed. In addition, the measurement of production cross sections of very neutron-rich nuclei has become important.

Below $20A$ MeV, as systematics of production cross sections, the Q_{gg} rules have been found in the cross sections of isotopes produced in low-energy nucleus-nucleus collisions [48, 49]. The cross sections for the nucleon stripping and nucleon exchange reactions depend exponentially on the Q-values, calculated for the ground state masses of the reaction products. The applicability of this rule stems from a fact that reactions are generally treated within the framework of two-body transfer processes. For better agreement with experimental data, we apply corrections and modifications in the choice of Q_{gg} [50]. The cross sections are determined by the relation [51] :

$$\sigma_f \quad = \quad \exp\left\{[Q_{gg} + \Delta E_c - \delta]/T\right\} \qquad (1.5)$$

where Q_{gg} is the energy necessary for rearrangement of the nuclei in the input channel into the nuclei in the exit channel, ΔE_c is the change in the Coulomb energy of the system due to the redistribution of protons between the nuclei and to the deformation of the system, δ is the nucleon pairing correction, and T is the temperature of the nuclear system.

Since the energy of $20A$ MeV is close to the average Fermi energy of a nucleon in projectile nucleons, this energy is expected to define a transition between the phenomena characteristic of low- and high-energy heavy-ion reactions [52]. This energy also defines the threshold of the supersonic region, where particle velocities exceed the velocity of sound in nuclear matter [53][54]. Gelbke et al. [55] discussed the transition with the data acquired by using ^{16}O ions of 8.8, $19.7A$ MeV and $2.1A$ GeV beam energy on heavy targets (A_T>90). The similarity of cross sections at $19.7A$ MeV and $2.1A$ GeV shows that the hypothesis of limiting fragmentation applies. From the target dependence of the cross sections, the concept of factorization also applies over the range of target nuclei. The results indicated that the isotope production cross sections at $19.7A$ MeV are significantly different from those at $8.8A$ MeV but rather similar as $2.1A$ GeV. The smooth transition from deeply-inelastic to fragmentation phenomena begins at $20A$ MeV. At $19.7A$ MeV, the Q_{gg} systematics is not defined very well. The breakdown of the Q_{gg} systematics at $2.1A$ GeV is quite obvious. The breakdown is not easily interpreted, but one may conclude that at higher energies the reaction mechanism is different from the binary mechanism (transfer), and contributions of other processes become important [32].

In 1980s and '90s, the development of new generation facilities drove experimental and theoretical studies on nuclear reaction mechanisms at intermediate-energy region 20-$100A$ MeV. The reaction mechanism at intermediate energies is more complicated than at higher energies [56] [57]. The production of projectile-like fragments at intermediate energies seems not to be "pure fragmentation", but to have other contributions of reaction mechanisms [58].

One of the most interesting aspects at intermediate energies is the target dependence of production cross sections for neutron-rich nuclei. D.Guerreau et al. [59] reported the isotopic yields of projectile-like fragments produced in Ar+Ni, Ar+Au reactions at $44A$ MeV. The curves of isotopic yields show that the most probable A/Z for fragments is much closer to that of the projectile. This observation is different from that of projectile+target compound system, which is expected to be formed in

deep inelastic process at a low energy ($6A$ MeV). The measured A/Z indicates that the projectile fragmentation is dominant process at intermediate energies [56, 60].

If the reaction mechanism at intermediate energies is just only the projectile fragmentation, we cannot find any target dependence except the nuclear-size effect for total cross sections. Namely, we can apply the factorization hypothesis. As written in Ref. [59], the production rates of projectile-like fragments depend on target nuclei. Especially for very neutron-rich fragments, the production yields are larger in heavier target nuclei beyond the target size dependence of cross sections. The work of Ref. [59] suggested that the reason might be due to the transfer process involved. However, no quantitative discussions have not been done.

This target dependence of production yields may imply a breaking of the factorization. Since Ref. [59] were presented, no experimental efforts have been made so far to measure production cross sections, instead of yield rates, and to deduce the target dependence systematically. It is very important to confirm the target dependence of production cross sections.
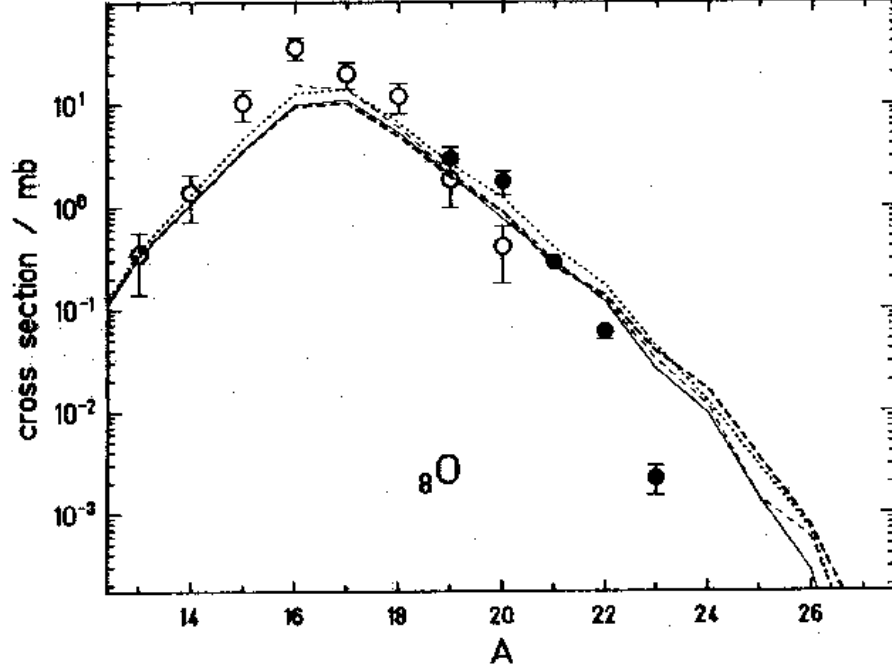
Figure 1.3: Cross sections for the production of O isotopes in different projectile-fragmentation reactions, in taken from Ref. [47]. Open points : experimental data of the reaction ^{40}Ar + ^{12}C at $213A$ MeV [31]. Full points : experimental data of the reaction ^{48}Ca + ^{9}Be at $212A$ MeV [61]. The curves are the results of model calculations for the two systems by use of the modified macroscopic evaporation model. The charge distribution of the prefragments is given by the hypergeometrical model. Different options for the excitation energy of the prefragments are used: Full line (^{40}Ar + ^{12}C) and thin dashed line (^{48}Ca + ^{9}Be) : surface energy [13]. Dotted line (^{40}Ar + ^{12}C) and thick dashed line (^{48}Ca + ^{9}Be): surface energy plus friction [45].

1.2   Production of Neutron-rich Nuclei toward the Dripline

For designing experiments using a radioactive isotope beam, where fragment-yield estimation is very important, analytical descriptions of fragmentation cross sections are convenient tools. Actually, such descriptions are used in simulation programs for projectile-fragment separators (like e.g. INTENSITY [62] and MOCADI [63]). Analytical formulae have the possibility to obtain fragmentation cross sections calculated by computers in a short time beyond Monte-Carlo calculations based on AA models. As shown in Section 1.1.2, the predictive power of the AA models is quite poor for the very neutron-rich nuclei. In order to predict the production cross sections, analytical formulae of fragmentation cross sections are more useful than the AA models.

An analytical formula for fragmentation cross sections was first suggested by Rudstam [64, 65, 66]. This formula is expressed as

$$\sigma(A, Z) \;\; = \;\; \sigma_0 \exp(PA - R|Z - SA + TA^2|^U), \tag{1.6}$$

where A is the fragment mass number. The factor of $\exp(-R|Z - SA + TA^2|^U)$ describes the distribution of isotopic cross sections of an element of atomic number Z. Two values for U are used, $U=3/2$ or 2 with nearly equal success. The equation has been developed by many authors, notably by Silberberg and Tsao [67, 68].

An attempt to derive a universal Empirical PArametrization of fragmentation CROSS sections ("EPAX") was reported in Ref. [69]. The parameters of EPAX were adjusted with the experimental data based on multi-GeV proton-induced spallation cross sections, since scarce heavy-ion induced experimental data were available at that time. Meanwhile, more data from relativistic heavy-ion-induced fragmentation reactions allow to obtain the parameters of the modified formula. The data show that the isotopic distributions of production cross sections can be well described by Gaussian-like analytical functions with parameters that vary smoothly as a function of Z and A of fragments like as,

$$\sigma(A, Z) \;\; = \;\; Y(A)\, W(A, Z) \tag{1.7}$$
$$= \;\; Y(A)\, n\, exp(-R|Z_{prob} - Z|^U). \tag{1.8}$$

The first term $Y(A)$ represents the mass yield, i.e., the sum of the isobaric cross sections with a mass A. The second term $W(A, Z)$ describes the charge distribution

of isobaric cross sections, where the distribution has the maximum magnitude at $Z = Z_{prob}$. The factor n is a normalization factor of the charge distributions. Features that were not in the previous formulae by Rudsam and Silberberg and Tsao are the "memory effect" Δm, i.e., the influence of the projectile N/Z ratio on the fragment N/Z ratio [70, 71]; and the proton-excess Δ [72, 73]. The EPAX formula includes both of the effects to evaluate the value of Z_{prob} with $Z_p = Z_\beta + \Delta + \Delta_m$, where Z_β is the β-stable charge for a fragment with a mass number A [74]. The EPAX formula is very often used for the experiments with the radioactive isotope beams.

The EPAX formula has been also used for the intermediate-energy experiments, since the formula can reproduce reasonably well even at intermediate energies the production cross sections of stable and unstable nuclei near the β-stability line. However, the recent experiments show that the production yields of nuclei far from stability line are quite different from the EPAX formula, and strongly dependent on the N/Z ratio of the target [75]. Figure 1.4 shows the cross sections; experimental ones with a $80A$ MeV ^{50}Ti beam and predicted ones by the EPAX formula. Details of the experiment are described elsewhere [76].

For the new isotope search experiment near the neutron drip-line, the accuracy to predict the production cross section is very important. We can confirm that an isotope is particle bound by the observation. However, the non-observation of an isotope does not prove its unbound character. For example, the stability of ^{28}O has been investigated for a long time since the isotope is a doubly magic nucleus in a sense of the nuclear shell structure near the stability line. A result of ^{28}O search is shown in Fig. 1.5. The experimental yields of the N=20 nuclei were measured for the extrapolation of the systematic trend. The upper limit of one event for ^{28}O is described with the point and arrow. For the extrapolation method, the accuracy to predict the production cross section of ^{28}O is important. By the recent experiment, the particle instability of ^{28}O was found more clearly. The result is already published [77]. Figure 1.6 shows the isotopic production for nuclei with the neutron number $N = 2Z + 4$. The squares of ^{19}B, ^{22}C and ^{31}F are the number of observed events. The first observation of ^{31}F gives a strong evidence of the particle stability of ^{31}F as well as instability of ^{25}N and ^{28}O. As seen as the arrows in Fig. 1.6, the yields of ^{25}N and ^{28}O between ^{22}C and ^{31}F can be estimated with fair reliability by the interpolation method.

In general case of new isotope search experiments, we cannot expect to find the

"^{31}F" for the interpolation method to estimate the yield of an isotope which has not found yet. Therefore, to enhance predictive powers for production cross sections, deeply understanding reaction mechanism as well as observing systematic behaviours of production cross sections are necessary.

As we mentioned above, the EPAX formula is a very useful tool to obtain the fragmentation cross sections. However, the recent experiments show that the production yields of nuclei far from stability line are quite different from the EPAX formula, and strongly dependent on the N/Z ratio of the target. To enhance the predictive power of the EPAX formula for the cross sections of very neutron-rich nuclei, the EPAX modification was often performed by using the measured cross sections of very neutron-rich nuclei. For instance, the U parameter was used to change the value ranging from 1.5 to 1.7 case by case. The reason is that we have insufficient knowledge of the momentum distributions and the production cross sections for projectile-like fragments at intermediate energies. The measurements of very neutron-rich nuclei have been performed using very thick targets to earn the yields. As distortions of momentum distributions due to target thickness, the momentum distributions of fragments cannot be obtained from these data clearly.
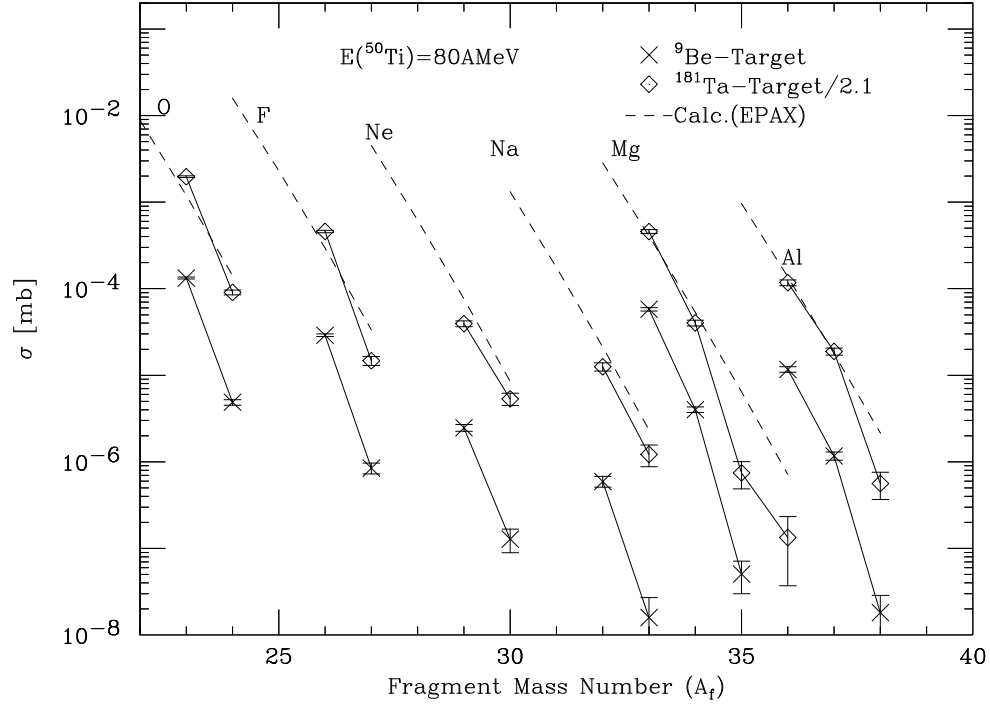
Figure 1.4: Production cross sections of projectile-like fragments with a $80A$ MeV ^{50}Ti beam for ^{9}Be and ^{181}Ta targets [76], compared with the cross sections calculated by the INTENSITY code using the EPAX formula. The cross sections for ^{181}Ta targets are divided by a factor of 2.1; thus one prediction curve for each isotope presents the cross sections for two targets at once.
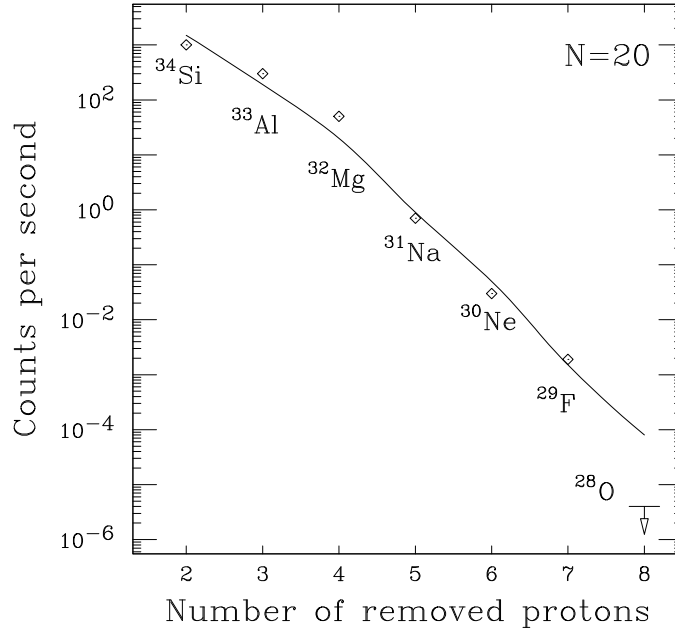
Figure 1.5: Experimental yields of the N=20 nuclei with a $75A$MeV ^{36}S beam, in taken from Ref. [78]
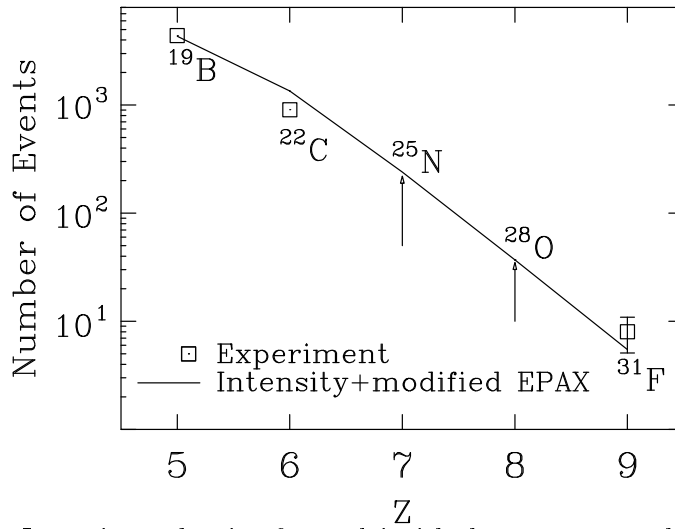
Figure 1.6: Isotopic production for nuclei with the neutron number $N = 2Z+4$ in taken from Ref. [77]

1.3 Thesis Objectives

The nuclear fragmentation reactions are very useful to experimentally study unstable nuclei. However, the reaction mechanisms have not been well known and any pictures for the mechanisms have not been established, as described in the previous sections. Even in such situations, radioactive isotope beams produced via projectile fragmentation reactions are being used, based on empirical results; isospin-dependence or target-dependence of production cross sections. As pointed out previously, how to enhance the predictive power of the cross sections is very important to determine particle-stability, for instance. This enhancement should rely on understanding the reaction mechanisms. Many experimental works have provided data in many combinations of projectile and target, and in the wide energy range. However, the data were acquired only for fragments close to the β-stability line.

In this thesis, we focus the target dependence of momentum distribution of projectile-like fragment (PLF) produced by nuclear fragmentation reactions at an intermediate energy around 90-94A MeV. To investigate the target dependence of the production cross sections systematically, we use two production targets of Be and Ta. To avoid distortions of momentum distributions due to the target thickness, we prepare thin targets. We perform the experiment with the RIKEN-RIPS to eliminate the primary beam and to collect the projectile-like fragments. Compared with the previous experiments performed so far, the data of this experiment have the following features; (1) a wide range for fragment mass including very neutron-rich side ($N/Z_f \approx 3$) toward the neutron drip-line and light mass ($A_f \geq 3$), and (2) a good statistics for momentum-distribution tails.

From the experimental data, the target dependence of charge distributions for production cross sections is confirmed. The reaction mechanism is investigated with the momentum distributions of fragments for both of the targets.

The experimental setup and the run conditions are described in Chapter 2. The calibration of primary beam intensity monitor and analysis of the data are presented in Chapter 3. In Chapter 4, the momentum distribution of fragments are shown. Then, the fitting method and the procedure to obtain the cross sections are described. In Chapter 5, we discuss the reaction mechanisms of projectile fragmentation at intermediate energies. Finally, we summarize the conclusions of thesis in Chapter 6.

Chapter 2

Experimental Setup

The projectile fragmentation experiment using a ^{40}Ar beam was performed at the RIKEN Accelerator Research Facility (RARF), shown in Fig 2.1. The measurement of momentum distributions of projectile-like fragments was carried out at the E6 room with the RIKEN Projectile-fragment Separator (RIPS) which consists of two dipole magnets, twelve quadrupole magnets and four sextupole magnets. The schematic layout of RIPS and the experimental setup are shown in Fig 2.2.

The primary beam accelerated by the ring cyclotron (K=540) with an energy up to 90-94A MeV irradiated production targets of Be and Ta. The primary beam intensity necessary for normalization was monitored by using a plastic counter telescope located close to the target position (F0). Heavy-ion fragments were produced and collected at RIPS. The fragments were transported to the doubly achromatic focal plane (F2), where a plastic counter and a silicon telescope were placed for particle-identification as well as fragment counting. Momentum distribution was obtained by changing $B\rho$ values of RIPS. At each $B\rho$ setting, the primary beam intensity was tuned to avoid the pileup at the detectors. Here, we describe the experimental setup in details.
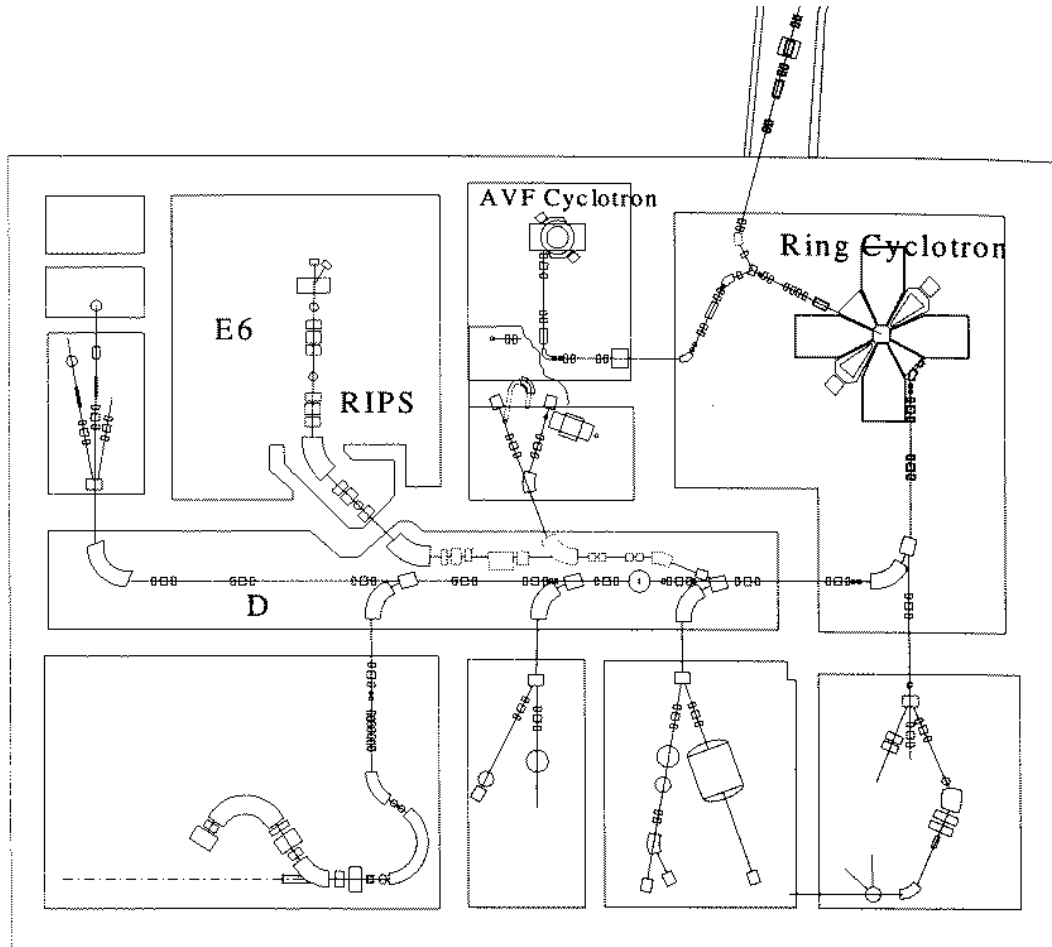
Figure 2.1: Configuration of RIKEN Accelerator Research Facility (RARF)
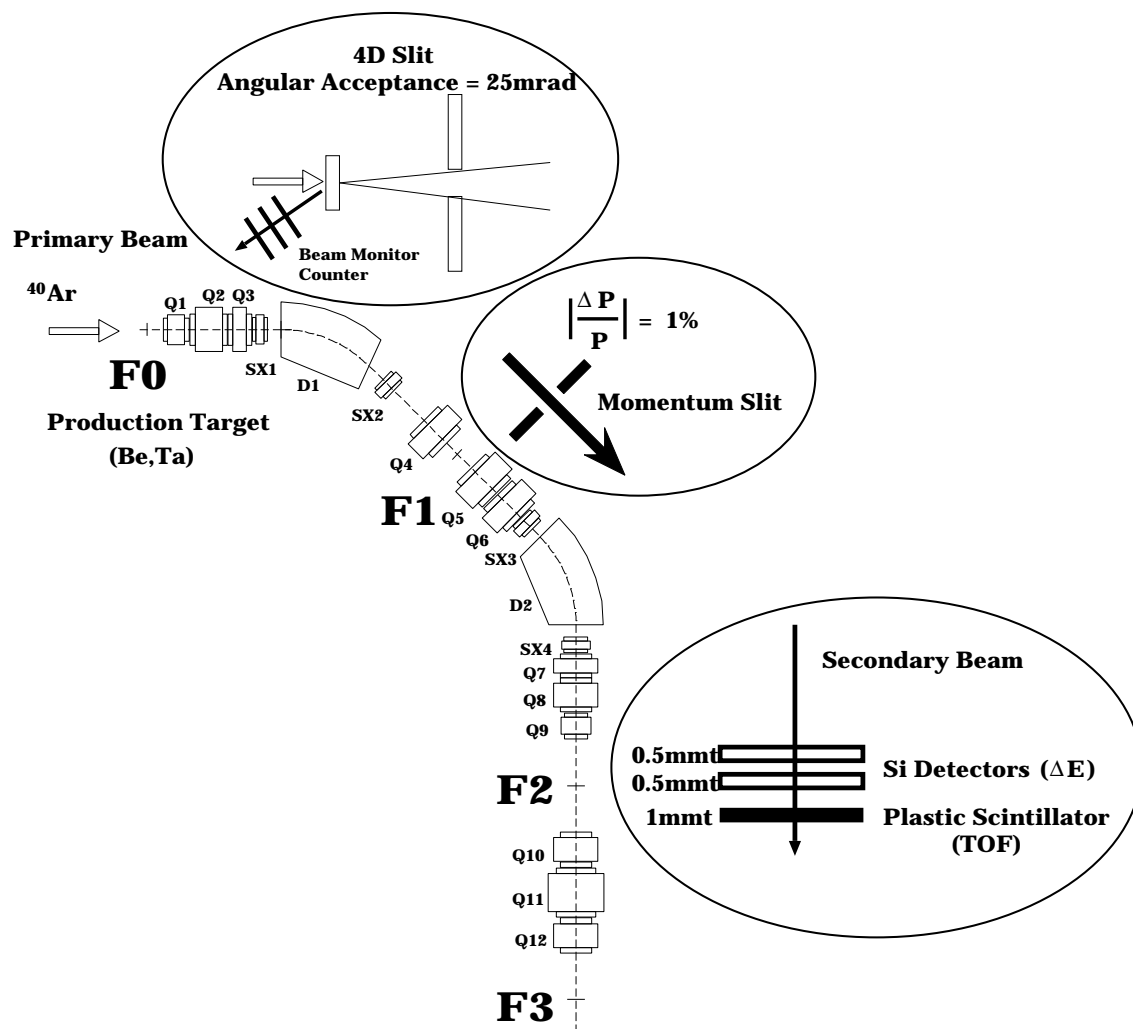
Figure 2.2: Projectile-fragment separator RIPS and layout of detector system

2.1 Beam

^{40}Ar^{17+} ions were accelerated in the ring cyclotron to an energy of 90-94A MeV. The acceleration condition of the primary beam is tabulated in Table 2.1. The beam energy was measured by using RIPS for both Be and Ta experiments. A direct measurement of magnetic rigidity for the primary beam was performed with a NMR method presented in Section 2.4.3. The maximum beam intensity used for this experiment was about 17 particle nano-ampere (pnA), which corresponds to approximately 1.1×10^{11} particles per second(pps). The beam intensity was controlled down to 1/10000 by a beam attenuator which is a series of meshes ($\sim$1/2 and $\sim$1/5) at the exit of the ECR ion-source. The beam spot size on the target was about 1mm ϕ.

2.2 Target

We used a 94.6mg/cm^2 thick ^{9}Be target and 17.0mg/cm^2 thick ^{181}Ta target as shown in Table 2.1. The target thickness was measured by using RIPS for both of the targets. The target thickness was obtained from an energy loss of the primary beam in the targets. The beam energy was measured with the targets installed at F0 by using the NMR method.

The target thickness was determined with the condition to optimize yields of isotopes far from the stability as well as distortions of momentum distributions due to target thickness.

The maximum target thickness is set to measure the 'raw' momentum distribu-

Target		Primary Beam (^{40}Ar)		
	Thickness [mg/cm^2]	Energy [A MeV]	Charge State	RF Frequency [MHz]
^{9}Be	94.6±0.1	90.04±0.05	17+	27.6
^{nat}Ta	17.0±0.1	94.02±0.05	17+	28.1

Table 2.1: Experimental conditions of primary beam and production targets.

tion without large distortions originating from target thickness. Assuming only a projectile fragmentation mechanism, the fragment momentum distributions are described by Gaussian functions, of which widths are obtained from the formalism of Goldhaber (σ_{GH}). Dufour et al. [6] have pointed out that the width of the momentum distribution becomes wide owing to the different energy loss of the projectile and the fragment in the target material. The energy-loss uncertainty caused by the uncertainty of reaction points inside the target (σ_{TG}) can be described as the form,

$$\sigma_{TG} \quad = \quad C_{TG}(\frac{Z_p^2}{A_p} - \frac{Z_f^2}{A_f}) \tag{2.1}$$

where C_{TG} is a constant value determined from species and thickness of target, and $Z_{p,f}$ and $A_{p,f}$ are the proton number and the mass number for the projectile and the fragment, respectively. According to this formula, the σ_{TG} of target-effect is large for light and neutron-rich isotopes. Here, the ratio of σ_{TG}/σ_{GH} should be smaller than 1.0 for good measurement of momentum distributions. When a 100mg/cm^2 thick ^{9}Be target is used, the ratio is 21% for ^{28}Ne as an example of the worst case in the measurement.

Overall, the ratio for isotopes in $2 \leq A/Z \leq 3$ are approximately between 10 and 20% for the target thickness. Thus, the fraction of σ_{TG} contributions to the measured σ can be estimated to be 0.5~2% by the following equation,

$$\sqrt{\sigma_{TG}^2 + \sigma_{GH}^2} \quad = \quad \sigma_{GH}\sqrt{1 + (\frac{\sigma_{TG}}{\sigma_{GH}})^2} \tag{2.2}$$

$$\cong \quad \sigma_{GH}(1 + \frac{1}{2}(\frac{\sigma_{TG}}{\sigma_{GH}})^2). \tag{2.3}$$

For the effective production of very neutron-rich isotopes, the target should be thick. When the target thickness is quite thiner than the range of the Ar beam (2.4g/cm^2), e.g., less than 100mg/cm^2, the yield rate is proportional to a thickness of the target. For a 100mg/cm^2 thick target, the maximum value of luminosity is 2.8×10^{32} [cm^{-2}sec^{-1}] and corresponds to 1cps for a cross section of 3.6×10^{-5} mb. In the neon isotopes, where $^{17-32}$Ne are found to be particle stable experimentally [80], ^{22}Ne is the most probable production and the cross section is known to be about 10mb in a ^{40}Ar fragmentation reaction [81]. Assuming that the cross section decreases on the average by one order of magnitude with increasing neutron number, ^{28}Ne has 1×10^{-5} mb. Compared with the isotope range measured so far $^{19-25}$Ne, the target thickness

leads to wider isotope range for momentum distribution measurement. Therefore, the target-thickness of ^{9}Be was determined about $\sim$100mg/cm^2.

The thickness of tantalum target was much thiner than the range of the Ar beam (1.8g/cm^2) to confirm the correction of the target-thickness effect by comparison between two targets.

2.3 Primary Beam Intensity Monitor

The primary beam intensity was monitored for normalization of fragment yields to obtain the momentum distribution. A direct measurement using a Faraday cup was performed at the behind of the production target. The absolute beam intensity was determined by this method. However, we cannot use the direct method for all the time to measure the momentum distribution. The fragments produced by nuclear reactions are also trapped by the Faraday cup. Therefore, the primary beam intensity was monitored with an indirect method of plastic counters calibrated by a Faraday cup.

In order to monitor the primary beam intensity, a plastic telescope consisted of three plastic counters were placed at a backward angle of 135°, closed to the target position, as shown in Fig. 2.3. The plastic detectors counted yield rates of light particles produced with nuclear reactions at the production target. The three photomultiplier tubes (PMTs) were mounted on the plastic scintillators one-by-one. The counting rate of triple coincidence was used to measure the primary beam intensity.

Using the primary beam, the primary beam monitor was calibrated with a Faraday cup. A galvanometer was used to measure an electric current from the Faraday cup. Figure 2.3 shows schematic views of experimental conditions for the beam intensity monitor in (a) momentum distribution measurement and (b) calibration runs. By changing the primary-beam intensity over the range 10^{-4} to 1.0 of the full beam intensity, the calibration data were taken. Then a relation between the triple coincidence at the monitor and the primary-beam intensity measured by the Faraday cup was obtained.

In the calibration runs, the backgrounds from the materials of the Faraday cup and other materials around the target (e.g., beam pipes) were also measured. When the Faraday cup was installed without a production target, the background rate of triple coincidence was proportional to the intensity of primary beam. In the case of

neither Faraday cup nor production target on the beam line, the background rate was negligibly small. Procedures of background subtraction and results of calibration data are presented in Section 3.1, where the triple coincidence rate with the background subtraction was confirmed to be proportional to the primary beam intensity.
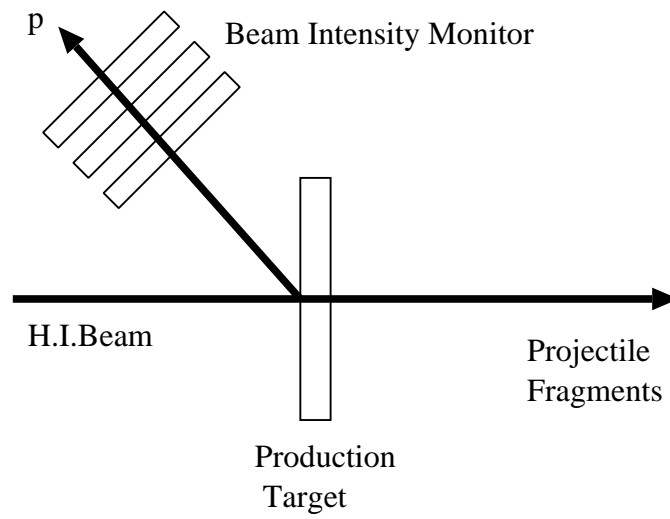
(a) Primary beam monitor in momentum distribution measurement
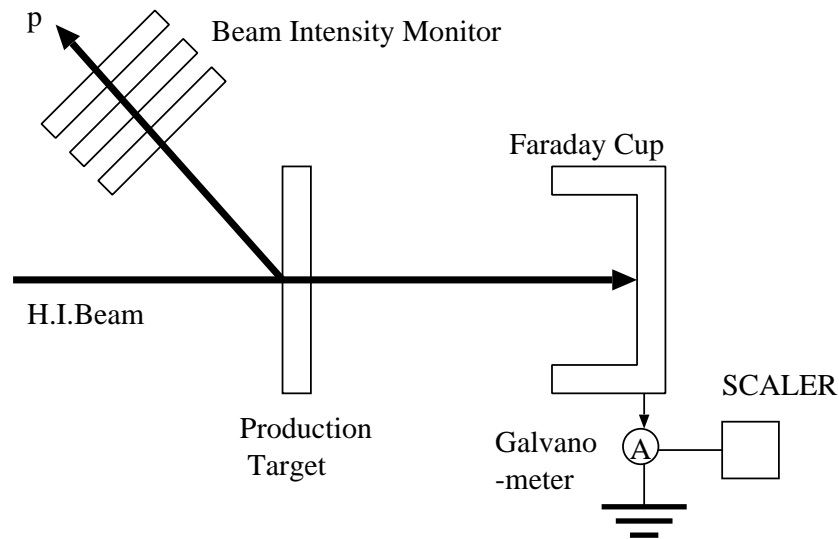
(b) Calibration of beam monitor

Figure 2.3: Schematic view of the primary beam monitor

2.4   RIPS

The RIPS was used as a doubly achromatic spectrometer. Projectile fragments pro-
duced at the production target and emitted at 0° were collected and transported to a
double achromatic focal plane (F2). At this experiment, the sextupole magnets were
tuned off. We evaluate the effect that the tilted focal plane causes a transmission
loss in Section 3.3.1. Here, the RIPS setting of momentum and angular acceptances
are described. The method of magnetic fields measurement is also shown.

2.4.1   Momentum Acceptance

The momentum acceptance was set to be $\Delta p/p$=1% at a momentum dispersive focal
plane (F1) where left and right slits formed the rectangle window of momentum
acceptance. Here we discuss the validity of the momentum window. First, according
to the 1st order optics conditions of RIPS, F1 has a dispersion of 2.4cm/%. The
slits' positions were well controlled with an accuracy of 0.02mm. This uncertainty is
negligibly small.

For all fragments, the momentum acceptance is narrow compared to the longitudi-
nal momentum distribution of fragments. The ratio of the widths of Goldhaber (σ_{GH})
and the most probable momentum (P_0) of fragments are 1.2% for the heavy fragment
^{34}P, and 7.0% for the light fragment ^{6}Li.

2.4.2   Solid Angle Acceptance

The angular acceptance was set with a square window formed by four slits (upper,
lower, left and right), which were placed at the behind of the production target. The
θ and ϕ angular acceptances were ±12.5mrad, which is narrower than the width of
angular distribution of fragments. The angular distribution is described as a Gaussian
function. For produced fragments, the narrowest angular distribution is expected to
be 17mrad(r.m.s.) for the ^{36}P isotopes [82]. Even if we assumed that the sliced
area of the Gaussian distribution is a rectangle, the difference of area for the sliced
Gaussian and rectangle is taken to be 9% at most. Thus, the angular distribution of
fragments in the square window can be regarded as a constant. We use the constant
value of 6.25×10^{-1}msr as the solid angle of $\Delta\Omega$.

2.4.3 $B\rho$ Setting and B Measurement

Momentum distributions of fragments were measured at 23 settings of magnetic rigidity ($B\rho$) over a range of $2.520-4.068$Tm using ^{9}Be target. In the case of ^{181}Ta target, the measurement of momentum distribution for each fragment was performed at 31 magnet settings as same as Be case. The detail of the magnetic settings is discussed in Section 2.7. The measurement of magnetic fields of two dipoles (D1, D2) was performed with a multiplexed NMR system. The $B\rho$ values of fragments were determined using the radius of orbit of ρ=3.6m in RIPS. When the magnetic field was changed for each run, the F2 image of secondary beam was measured by means of a PPAC to confirm transmission, and the x-position of the beam at F2 was corrected to center precisely by tuning the D2 field. The beam position was monitored with an accuracy of 1mm. The systematic error of magnetic rigidity was about 3×10^{-4} from the ratio of 1mm to 3.6m. The difference between D1 and D2 magnetic fields was less than 0.05%.

2.5   Detectors for Particle Identification

The identification of fragments was carried out event-by-event by means of measurement of time of flight (TOF) and energy deposit (ΔE) for each fixed $B\rho$ run with the 1% momentum slit. According to an estimation of charge state distribution [83], all fragments in flight are fully striped ($Q{\cong}Z$). At the Be-target experiment, the charge state distribution of the primary beam passed through the target was measured, and a ratio of ^{40}Ar^{17+}/^{40}Ar^{18+} was found to be $(6.0\pm0.6)\times10^{-4}$. Therefore, we indeed concluded that we can assume that all fragments are fully stripped, namely Z=Q.

Under this assumption, the particle identification can be performed on the basis of the relations:

$$B\rho \quad \propto \quad \frac{A}{Z}\beta \tag{2.4}$$

$$\Delta E \quad \propto \quad (\frac{Z}{\beta})^2 \tag{2.5}$$

$$\frac{\beta}{c} \quad \propto \quad \frac{1}{TOF}, \tag{2.6}$$

where A and Z are mass number and atomic number, respectively.

When the small $B\rho$ acceptance of 1% is realized for a given $B\rho$ value for all of fragments, the energy loss is proportional to square of mass number of nuclei

($\Delta E \propto A^2$). As the TOF is inversely proportional to the fragment velocity, the TOF
is proportional to the A/Z after all.

The detectors of two 0.5mm thick surface-barrier-type silicon counters (SSD1,SSD2)
and a 0.5mm thick plastic scintillation counter(PL) were installed for the ΔE and
TOF measurement at the double-achromatic focal plane (F2). To use two silicon
detectors allowed us to deduce Z number independently, and to take correlations
between them to achieve good S/N ratio.

Both SSD1 and SSD2 have 48mm×48mm sensitive area which is wide enough to
accept all particles reaching to F2 where FWHM of the beam profile is 6 mm. Two
photomultiplier tubes (PMTs) were mounted on both sides of the plastic scintillation
counter (Left and Right).

The TOF of each fragment over 21.3m flight path between the production target
and the F2 was determined from the difference of timing signals between RF signal
of the cyclotron and the PL timing. The TOF resolution was measured with a faint
beam to be 0.27ns (r.m.s.), which included the timing jitter of RF signal ($\sim$0.09ns).
Thus, the intrinsic resolution for PMT was estimated to be 0.18ns.

2.6   Data Aquisition System

Figure 2.4 shows a schematic diagram of the circuit for this experiment. The event
trigger was produced by the PL signals. The timing and analogue signals from the
PL and SSD1-2 were recorded by standard-CAMAC TDC's, and QDC's or ADC's, re-
spectively. The primary beam was accelerated with a frequency of 27.6MHz (36.2nsec)
and 28.1MHz (35.6 nsec) for the energy of $90A$ MeV and $95A$ MeV, respectively.
Therefore, the full TDC range was set to 100nsec.

The shaping time of main amplifiers (S-Amps) for the SSD1-2 was 1μsec. In order
to reduce ΔE-pile-up events, the event trigger rate at each $B\rho$ setting was kept about
1kcps by changing the attenuation of primary beam intensity at the exit of the ECR
source.

The data was collected using the standard data-aquisition system at RIKEN,
which consists of J11 CPU (starburst 2180 ACC) and Micro VAX II [84]. All data
were written on 120m DAT tapes.
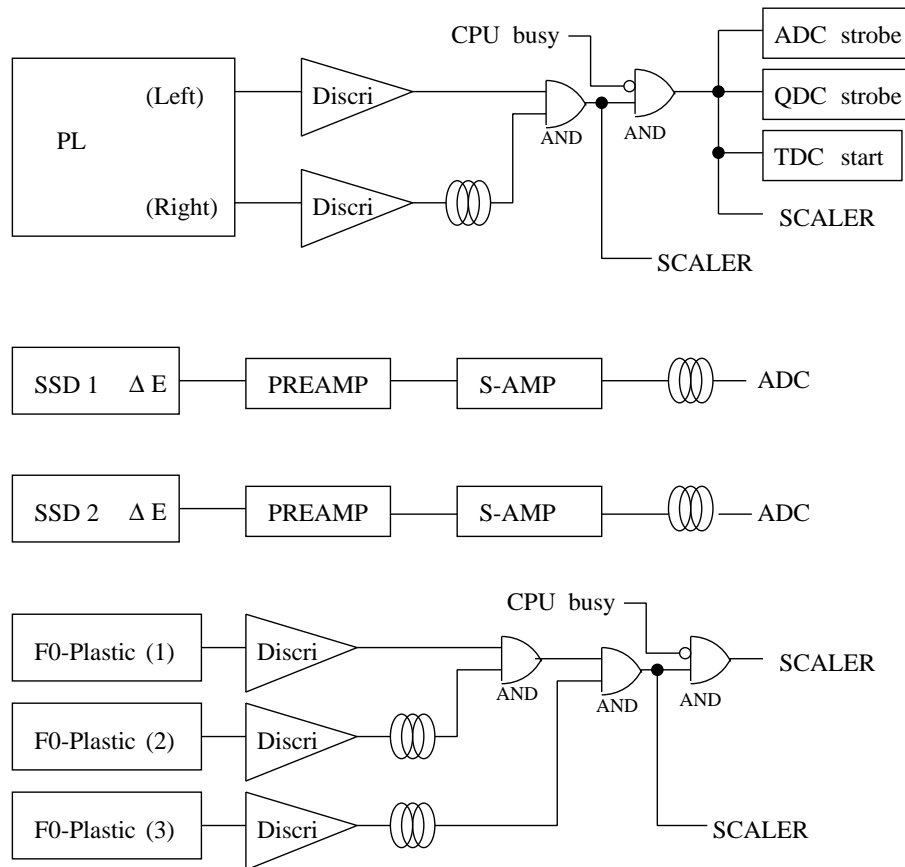
Figure 2.4: A diagram of the circuit.

2.7   Magnet Rigidity Setting

The measurement of fragment momentum distributions was carried out by sweeping magnetic fields of RIPS to observe fragments in a wide dynamic-range of A/Z ($2 \leq$ A/Z ≤ 3).

Figure 2.5 shows all magnet settings of data in this experiment for a) ^{9}Be and b) ^{181}Ta target. The data were acquired in the 23 and 34 samplings of $B\rho$ with the production targets of Be and Ta, respectively. The step size was 0.072Tm which corresponds to 2% at a $B\rho$ of 3.6Tm. To avoid the primary beams of fully strip ($Q=Z$) and hydrogen-like state ($Q=Z-1$) to come to the detectors at F2, the data at the relevant $B\rho$ settings were not taken, as shown in Fig. 2.5.
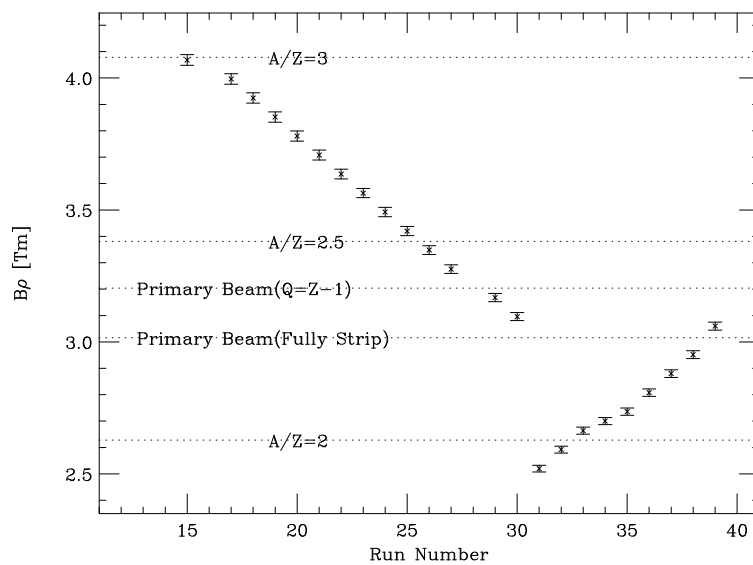
a) ^{9}Be$(^{40}$Ar,X$)$ reaction
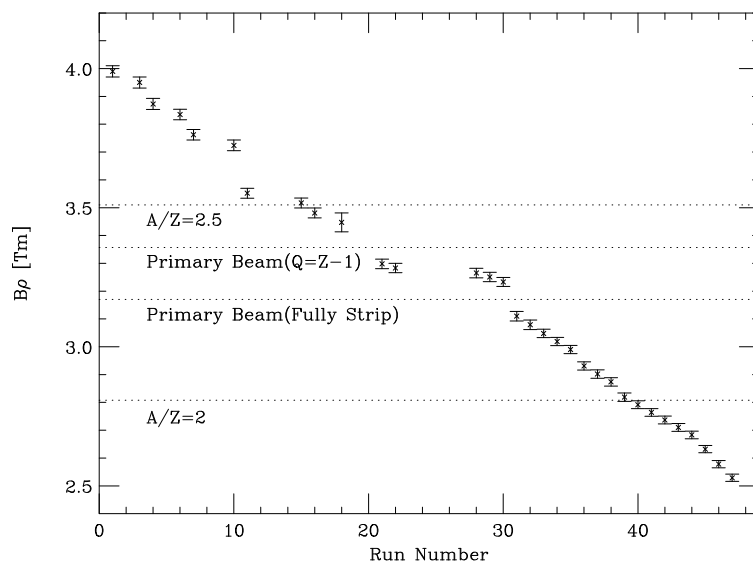
b) ^{181}Ta$(^{40}$Ar,X$)$ reaction

Figure 2.5: Magnetic Rigidity for each run.

Chapter 3

Data Analysis

This chapter gives analysis procedures for the calibration of beam intensity monitor counter, particle identification, and evaluation of differential cross sections. Systematic errors for the cross section evaluation are summarized at the last section.

3.1   Calibration of Beam Intensity Monitor

In this section, the result of calibration of beam intensity monitor as noted in Section 2.3 is presented, and the linearity and error of the beam monitor are discussed. The schematic view of beam monitor system was shown in Fig. 2.3. First, the contribution of materials except the production target was investigated. Next, the measurement of calibration data was carried out for both Be and Ta targets.

The background rate at the beam intensity monitor was found to come from the Faraday cup and other materials around the target (e.g. beam pipes). When the target was removed and the primary beam was on, the beam monitor had some counts from both the Faraday cup and other materials. Next, when both the target and Faraday cup were removed, very small counting rates were observed, which show the contribution of the other materials. From these measurements for the background, the fractions of background to the total counting rates were found 1~2 % and 2×10^{-2} %, from the Faraday cup and the other materials, respectively. The former fraction was independent of primary-beam intensities used, and the latter was small enough to be ignored.

As shown in Fig. 2.3, a galvanometer was used to measure the electric current from the Faraday cup. Even if the primary beam was off, the galvanometer had a dark current due to an induction of other electric circuits in the acceleration facility.

Therefore, a background subtraction was also performed for the Faraday-cup current. The dark current was measured for each calibration run when the primary beam was off.

The calibration data were measured for both Be and Ta targets. The triple coincidence rates and the electric current from the Faraday cup were measured for various beam intensities. The primary beam intensity was controlled down over the range 10^{-4} to 1.0 of the full beam intensity.

With all background subtractions, the triple coincidence rates were fitted to a linear function. The fitting procedure was performed in a range of the actual beam intensity for momentum distribution measurement. The fitting results for both targets of (a) Be and (b) Ta are shown in Fig. 3.1. The dashed curves are raw data of the triple coincidence rates as a function of the electric currents from the Faraday cup. The circles in this figure indicate the corrected data with the background subtractions. The fitting results of the corrected data were obtained as the solid line. Even in the case of the high intensity beam ($10^2 enA \simeq 6pnA$), where accidental coincidence rate is expected to be the largest, a non-linear part was less than 2~4%.

At several $B\rho$ settings, the total numbers of counts of the beam intensity monitor were small. Even at these settings, the statistical errors of the total counts are at most 4%. Therefore, the total systematic error of the beam normalization is estimated to be 5~7%.
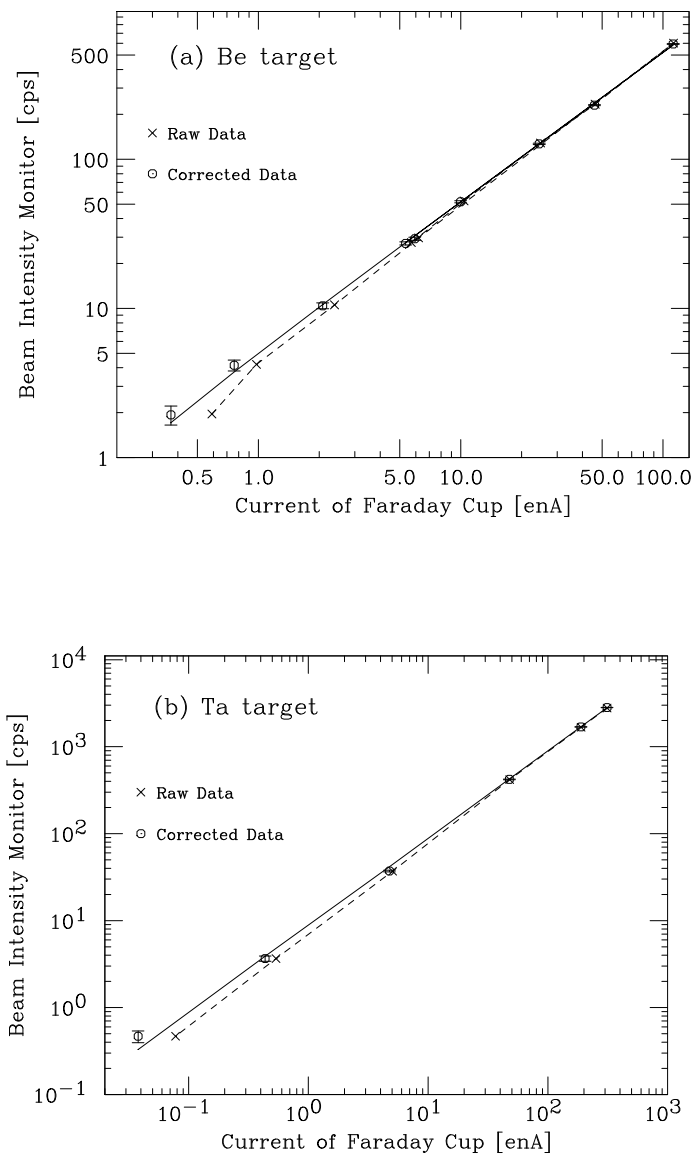
Figure 3.1: Calibration of Beam Intensity Monitor.

3.2   Particle Identification

The particle identification was performed by the TOF-ΔE method as described in Section 2.5. By the analysis of the TOF-ΔE, we determine the mass-to-charge ratio A/Z and the atomic number Z of fragments. To obtain the fragment yields from scattering plots, the A/Z-Z plane is more suitable than the TOF-ΔE. The ΔE of an isotope in SSD depends on the velocity of each fragment, while the atomic number of a fragment obtained from the TOF and ΔE is independent of the fragment velocity. Thus, the fragments can be identified with good separation by using the A/Z-Z plane.

Figure 3.2 shows a two-dimensional plot of TOF between F0 and F2 versus ΔE in SSD1 for one $B\rho$ setting using the Be target. The TOF was determined from the difference of timing signals between RF signal of the cyclotron and the PL timing. The ΔE was obtained from SSD1. A good identification was achieved for the isotopes ranging from F to Si.

All channels of TDC for the RF signal and the PL timing were calibrated by using a time calibrator module. The absolute value of TOF was determined by the velocity of a primary beam.

The energy calibration of the silicon detector was carried out with the particle identification at A/Z=2 isotopes. First, the ADC channel for SSD signal was calibrated by the primary beam energy with subtraction of ADC pedestal. Secondly, we confirmed the energy calibration with the Z-spectrum of an 'A/Z=2' data obtained by using the Be target at the $B\rho$ setting of 2.523Tm. As we found a systematic shift of energy loss slightly, the re-calibration was performed to reproduce the atomic number Z of isotopes. The non-existence of a particle unstable nuclei ^{8}Be was a clue of the particle identification for this experiment.

Figure 3.3(a) shows typical particle-identification spectra of nuclear charge (Z) versus mass-charge ratio (A/Z) of fragments. Background events can be seen in the valley among isotope islands. The background events were originating from the primary beam scattered at F1 into the beam pipes and the nuclear reaction of fragments in the silicon detector.

The rejection of the background events was carried out to achieve a good separation between the atomic number Z. A correlation gate with ΔE signals from two silicon detectors at F2 was applied to reduce the background events. Figure 3.4 shows a ΔE correlation between SSD1 and SSD2 at F2. The kinetic energy of all

projectile-like fragments was large enough to penetrate through the silicon telescope. These fragments are presented as a main component around a fitting line in the ΔE plane. On the other hand, background events were found far from the fitting line. The background events were caused by heavy-ion beams scattered at the beam pipes and fragments penetrating the edge of SSDs. By using the fitting result, a distance from the fitting line to a point of each event was obtained with the energy loss of SSDs. From the distance, the correlation gate was obtained. The gate width corresponded to $\pm 3\sigma$ for Z=4. Figure 3.3(b) shows the particle identification obtained by the background subtraction of the SSDs' gate. By use of the SSDs' correlation gate, we achieved the particle identification of fragments with low background events.

Fragment yields (Y) were obtained by counting the isotopes from the particle identification. The counting gate of isotopes was a rectangle region with ± 3-σ of the resolution σ(r.m.s.) for Z and A/Z. Figure 3.5 shows the Z- and A/Z-projection of the particle identification at $B\rho$ =2.523Tm setting using the Be target. In Fig. 3.5(a), the Z spectrum was obtained with a gate on A/Z=2$\pm$0.3. The A/Z spectrum was obtained with a gate on Z=13$\pm$0.5, as shown in Fig. 3.5(b). The peak position and the width of isotopes were obtained from these spectra.

The Z-resolution was defined as the 1-σ width (r.m.s.) of the Z-distribution of the isotopes. Figure 3.6(a) shows the Z-resolution of 'A/Z=2' fragments. To apply the ± 3-σ gate for fragment counting, the resolution should be less than $1/6 \cong 17\%$. The A/Z=2 isotopes is the most severe case in the separation since we cannot distinguish the isotopes by using the A/Z.

The A/Z-resolution was defined as $\sigma(A/Z)/\Delta(A/Z)$, where σ is the 1-σ width (r.m.s.) of the A/Z-distribution of an isotope, and $\Delta(A/Z)$ is the distance between the isotopes with the same Z. Figure 3.6(b) shows the A/Z-resolution of Al isotopes. The σ for each isotope was $7-9\times10^{-3}$ and the $\Delta(A/Z)$ was $1/13 \cong 0.077$. The A/Z-resolution for Al isotopes was $9-12\%$. Since the resolution is less than 17%, we can apply the ± 3-σ gate for fragment counting. The worst resolution of A/Z was 16% for Ar isotopes. We applied the counting gate for all the isotopes.

From the data using Be target, the analyzed isotopes were $^{6-9}$Li, $^{7-12}$Be, $^{10-15}$B, $^{11-18}$C, $^{13-21}$N, $^{15-24}$O, $^{17-27}$F, $^{19-29}$Ne, $^{21-32}$Na, $^{23-34}$Mg, $^{25-36}$Al, $^{27-38}$Si, $^{29-39}$P, $^{33-38}$S, $^{36-39}$Cl, and ^{39}Ar, as shown in Fig. 3.7. Most of these isotopes are neutron-rich ones. It should be noted that the ^{36}Al,^{37,38}Si, and ^{38,39}P isotopes analysed have $N \geq 23$, which are produced through neutron pick-up process.

We analyzed from the Ta-target data for $^{6-8}$Li, $^{9-11}$Be, $^{10-14}$B, $^{11-17}$C, $^{13-19}$N, $^{15-21}$O, $^{17-24}$F, $^{19-27}$Ne, $^{21-29}$Na, $^{23-31}$Mg, $^{24-34}$Al, $^{26-34}$Si, $^{29-36}$P, $^{30-37}$S, $^{33-37}$Cl, and $^{35-39}$Ar $^{37-40}$K. The potassium isotopes should be produced by the reaction with proton pick-up process. In the nuclear chart shown in Fig. 3.8, the boxes drawn in solid lines are observed isotopes in this experiment.
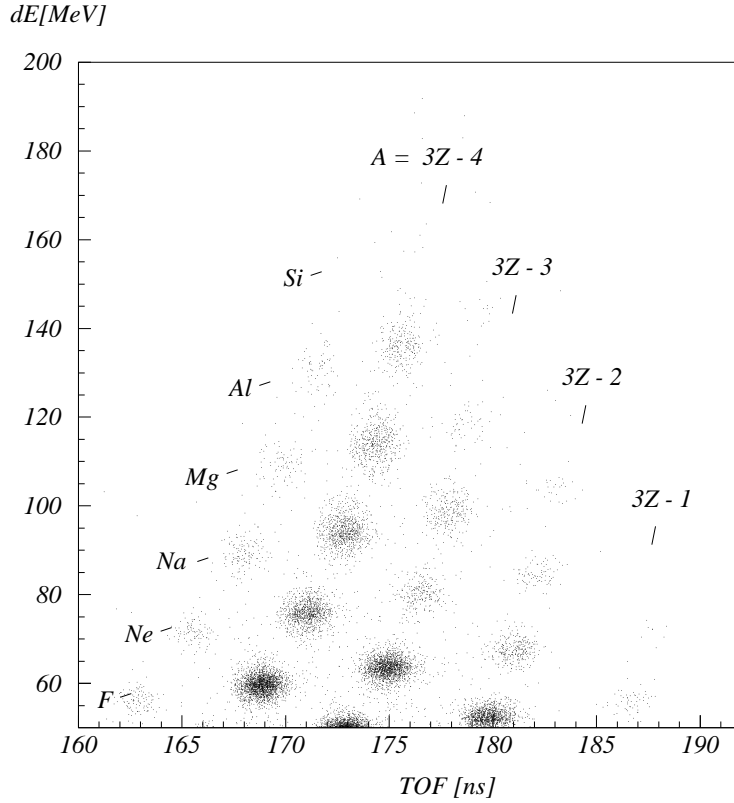
Figure 3.2: Particle identification in the dE-TOF plane at $B\rho = 3.708$Tm (Be target)
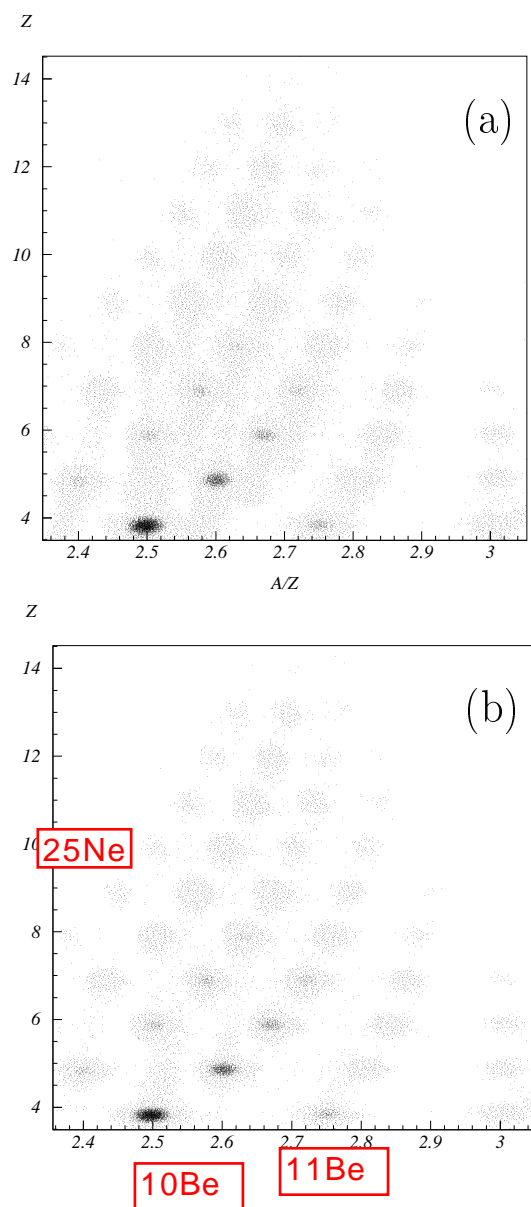
Figure 3.3: Particle identification in the Z and A/Z plane using the Be target at $B\rho = 3.708$Tm (a)without and (b)with the correlation gate of SSD1-2.
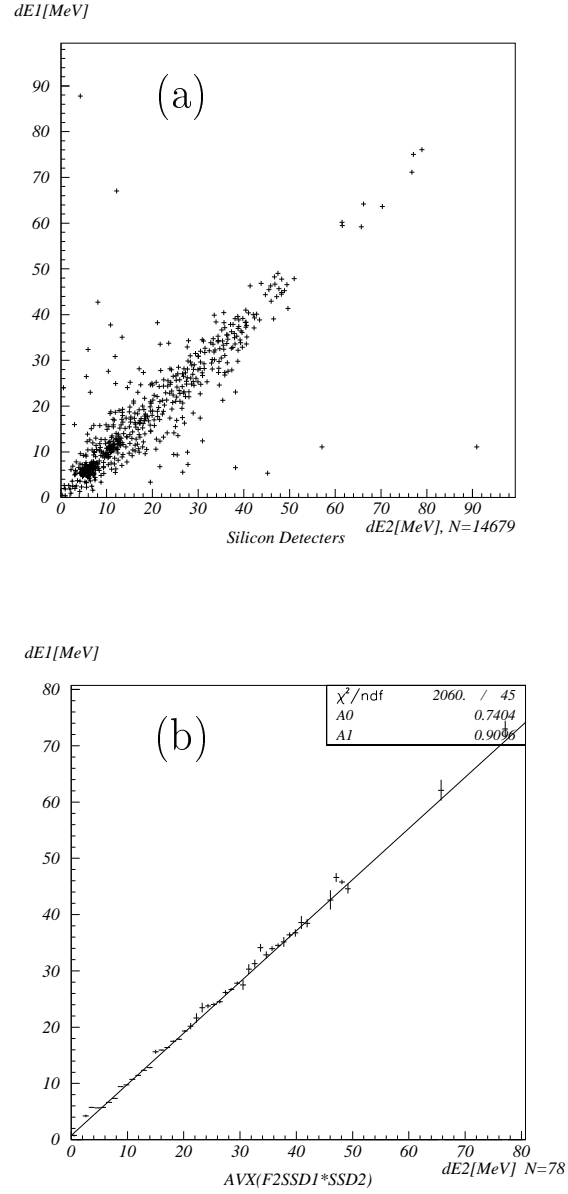
Figure 3.4: Correlation gate of SSD1-2. (a) Scattering plots of ΔE signals from SSD1-2 using the Be target at $B\rho$=3.708Tm. (b) Fitting result of the scattering plots with the average of each x-bin.
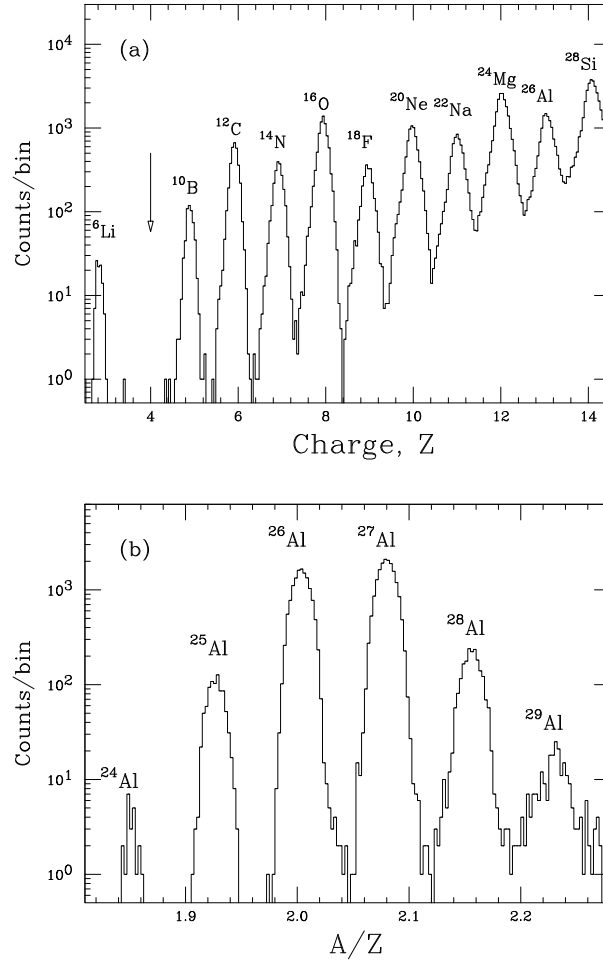
Figure 3.5: (a) *Z*-projection spectrum for *A/Z*=2±0.3 and (b) *A/Z*-projection spectrum for *Z*=13.0±0.5 at *Bρ*=2.523Tm (Be target). The arrow in (a) indicates the lack of ^{8}Be, which is particle unbound.
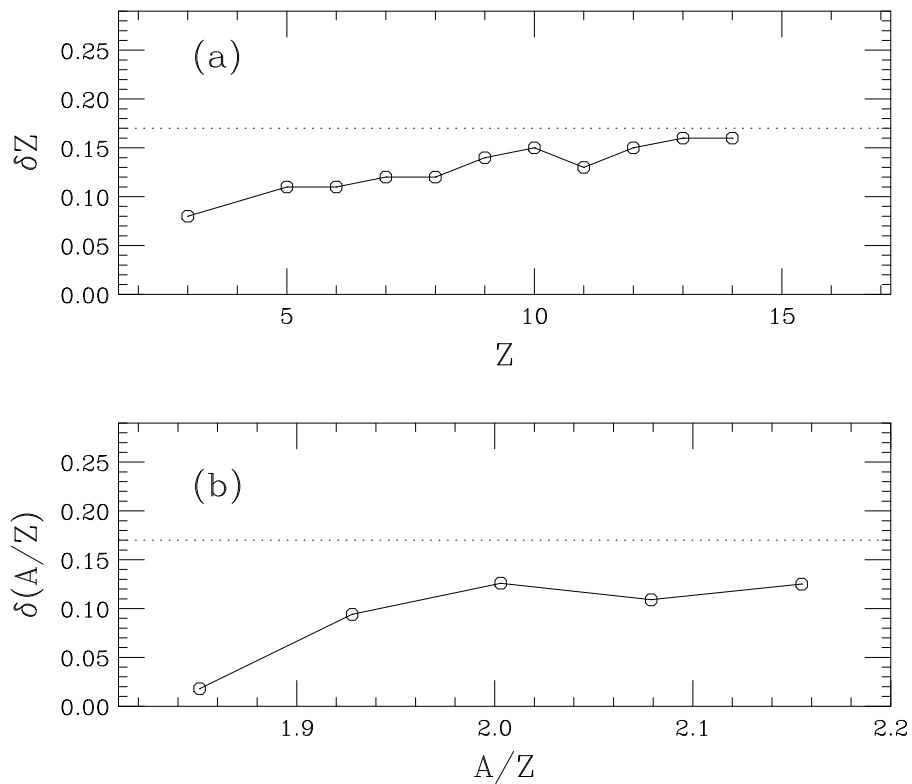
Figure 3.6: (a) *Z*-resolution and (b) *A/Z*-resolution obtained from the spectra as shown in Fig. 3.5. The dotted line is a limit of 17%, which we can apply the 3-σ gate. Solid lines are to guide the eye.
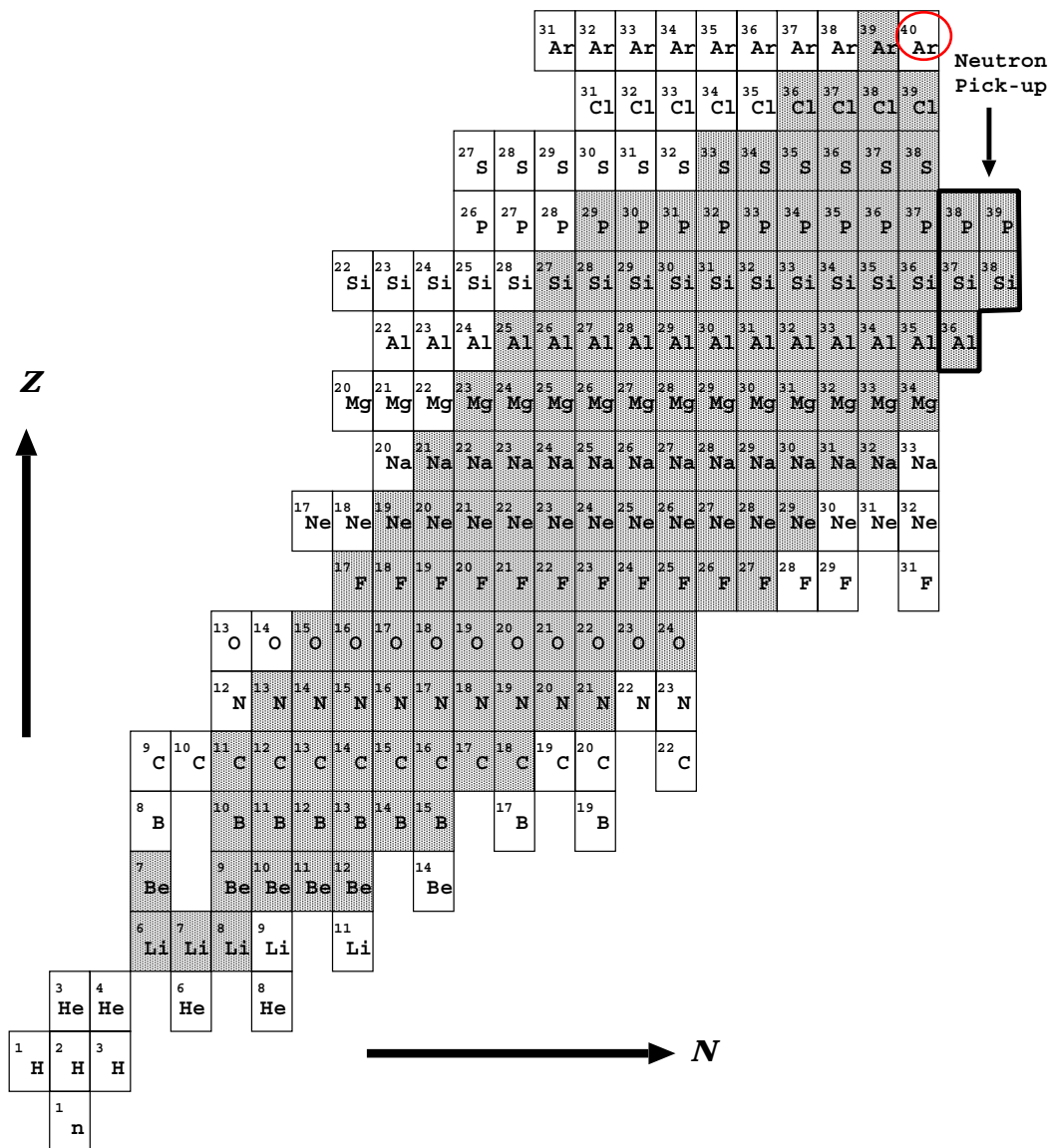
Figure 3.7: Analysed isotopes for the experiment using the Be target. Hatched boxes are the observed isotopes in this experiment. Neutron pickup fragments ^{36}Al,^{37,38}Si, and ^{38,39}P were also observed.
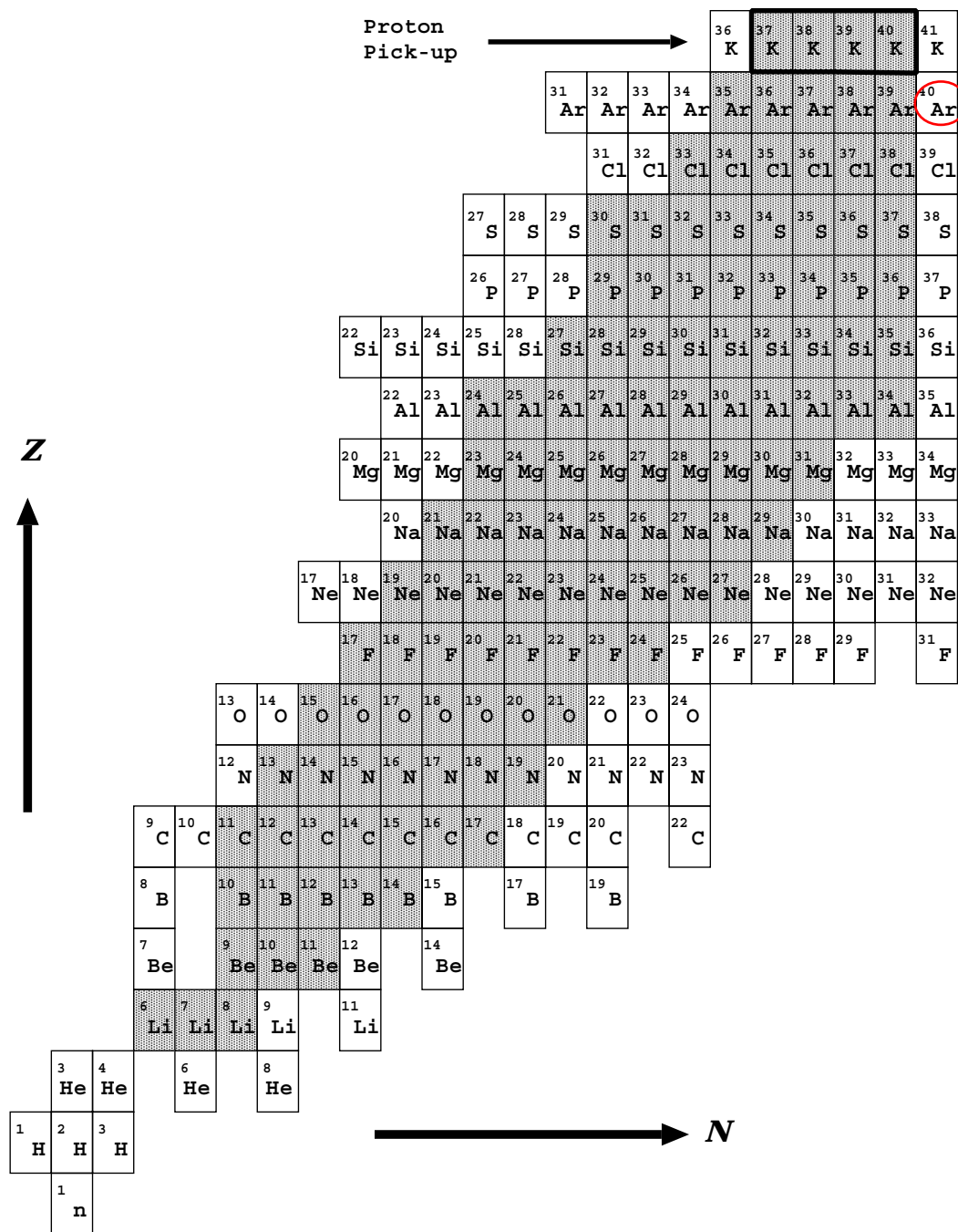
Figure 3.8: Analysed isotopes for the experiment using the Ta target. Hatched boxes are the observed isotopes in this experiment. Proton pickup fragments $^{37-40}$K were also observed.

3.3   Evaluation of Differential Cross Sections

To obtain longitudinal momentum distributions, the doubly-differential cross sections were evaluated from fragment yields, as the following,

$$
\frac{d^2\sigma}{dPd\Omega}[mb/(MeV/c)/sr] = Y\frac{A_t}{N_b N_A d_t}\frac{1}{\Delta P\Delta\Omega},
\tag{3.1}
$$

where

Y	:	Fragment yield
N_b	:	Primary beam intensity
N_A	:	Avogadro number 6.022×10^{23} mol^{-1}
A_t	:	Atomic number of target: Be 9.012 g/mol, Ta 180.95 g/mol
d_t	:	Target thickness: Be 9.46×10^{-2} g/cm^2, Ta 16.99×10^{-3} g/cm^2
ΔP	:	Momentum acceptance: 1%
$\Delta\Omega$	:	Angular acceptance: 6.25×10^{-1}msr.

First, the transmission loss, energy loss correction at the targets, and reaction loss at the detectors are estimated. Next, we evaluate the systematic errors of the differential cross sections.

3.3.1   Transmission

As mentioned in Section 2.4, we evaluated the effect that the tilted focal plane causes a transmission loss in this section. To deduce the transmission between F0 and F2, a Monte Carlo simulation by MOCADI [63] was performed. The MOCADI code has been used for studying the beam transport system where heavy ions are penetrating through layers of matter in an ion-optical system. By ray trace of particles, our experiment was simulated by using the optical conditions of RIPS, including the 3rd order matrices.

A reference beam of ^{40}Ar was generated at F0. The beam distribution was assumed to be homogeneous in the momentum-angular space. Figure 3.9 shows the transmission in the momentum-angular space at F0 for the particles which reach F2, as (a) a scattering plot in the θ and $B\rho$ coordinates, (b) $B\rho$-projection and (c) θ-projection. The edge of the reference beam in the momentum-angular space corresponds to the geometrical cut by the slits. The transmission was evaluated from the ratio of particle numbers between F0 and F2.
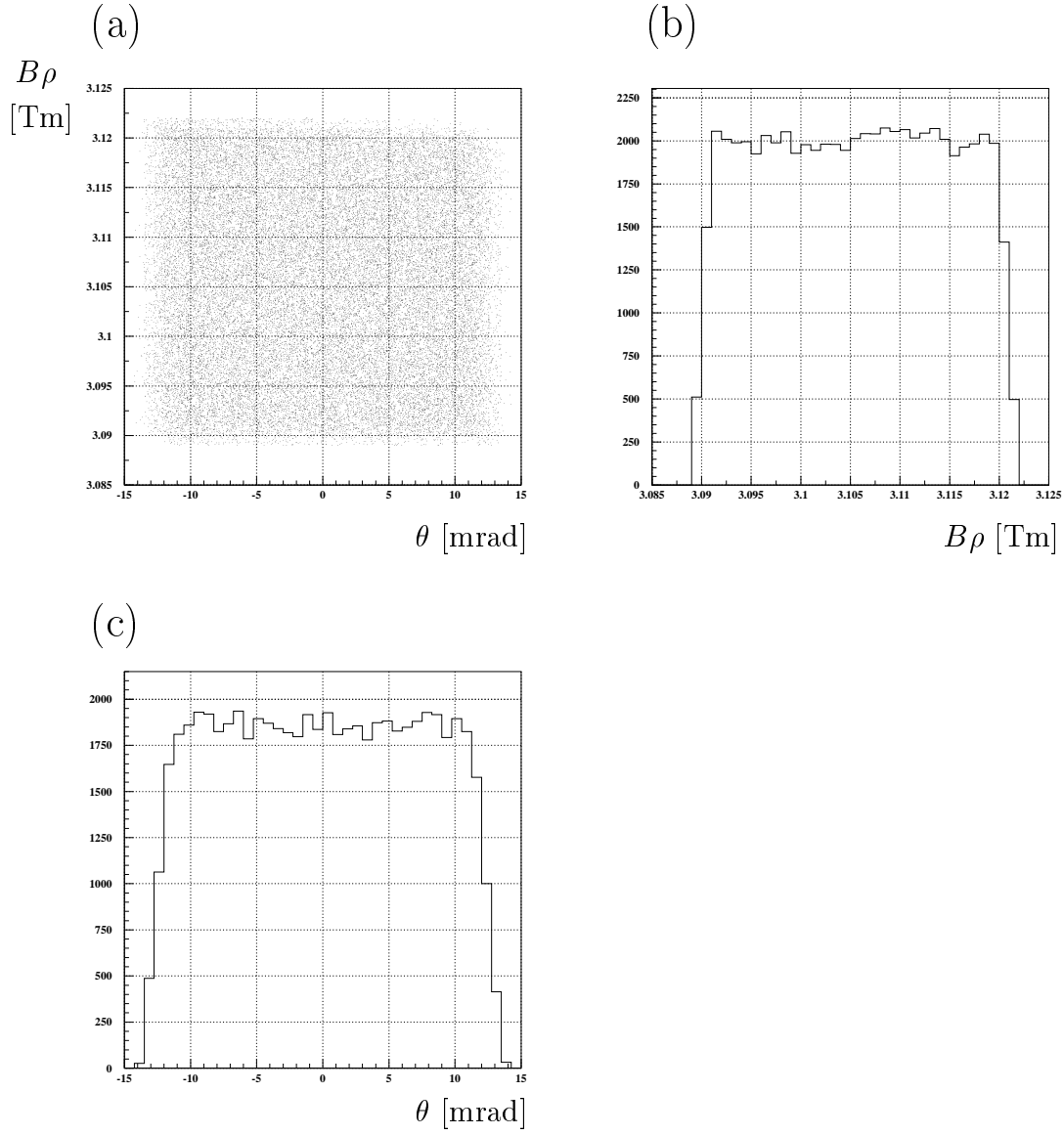
Figure 3.9: Momentum and angular dependence of F0-F2 transmission was simulated with the MOCADI code. Reference particles of ^{40}Ar were emitted homogeneously for the solid angle without a target. The transmission in the momentum-angular space at F0 for the particles reaching F2 as (a) a scattering plot, (b) $B\rho$-projection and (c) θ-projection.

The value of transmission was found to be 95.3±0.3%. The homogeneous distribution in momentum-angular space for the reference beam is a rather specific situation. The transmission of an isotope is better than the result, because the angular distributions of fragments have a forward peak.

All the corrections concerned for the F1 slits were small amounts, hence were not applied for the cross section evaluation. We used the values of momentum and angular acceptance determined by the slits in the differential cross sections.

3.3.2   Correction for Energy Loss at Target

The energy losses of the primary beam and fragments caused distortions of momentum distributions of the fragments. Here we present how to correct the effects. If we assume that the fragmentation reactions occur at the half depth of the target, the energy loss of ^{40}Ar beam is $2.5A$ MeV and $2.7 \times 10^{-1}A$ MeV for the Be- and Ta-targets, respectively. The energy loss of fragments in the rest part of the target depends on Z and β of fragments. In order to minimize the isotope dependence of the momentum distributions, fragment momenta defined with $B\rho$ values of RIPS were corrected by taking into account the energy loss at the half depth of the target.

Figure 3.10 shows a typical energy-loss correction. The momentum distributions for ^{27}Mg are drawn with and without the correction of energy loss in the Be target.
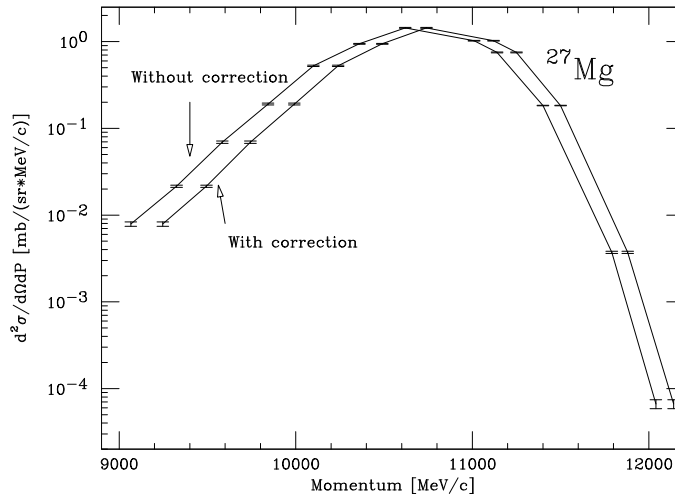
Figure 3.10:   Correction for energy loss

3.3.3 Reaction Loss at Detectors

The nuclear reaction loss of fragment in two silicon detectors was evaluated. We assumed that the reaction loss was proportional to the total reaction cross section for passing through the silicon detectors. The reaction cross section was estimated by means of the following equations:

$$\sigma_R = \pi R_{int}^2 \tag{3.2}$$
$$R_{int} = r_0(A_p^{1/3} + A_t^{1/3}) \tag{3.3}$$

where σ_R is the total reaction cross section, r_0 is a constant value of 1.1 fm, and $A_{p,t}$ is the mass number of projectile and silicons, respectively. According to rough estimation for the ^{40}Ar projectile, the reaction loss for ^{40}Ar is 0.8%. All fragments have smaller mass number than ^{40}Ar and the fragment reaction loss is less than 0.8%.

As the nuclear reaction loss is negligible for every fragment, no correction was applied for the cross section evaluation.

3.3.4 Systematic Error

Table 3.3.4 shows all of the correction factors and associated systematic errors. The measurement of target thickness was described in Section 2.2. After all, the systematic error was about $\pm 9\%$ for evaluation of the fragment cross sections.

Type of correction	Typical correction value	Systematic error
Primary beam intensity	0	$\pm$ 5-7%
Target thickness	0	$\pm 0.6\%$
Transmission	(5%)	5%
Background rejection (SSD1-SSD2)	0	$\sim 1\%$
Reaction loss	0	$\sim 1\%$
Total		$\approx 9\%$

Table 3.1: List of correction factors and associated systematic errors. The correction value was smaller than the systematic error and not applied for the evaluation.

Chapter 4

Results

This chapter gives results of momentum distributions and production cross sections of fragments produced in the fragmentation of ^{40}Ar using the Be and Ta targets. In the first section, typical momentum distributions are shown. Many of them have one component described as a Gaussian-like function which includes an asymmetric part in the low momentum side. Only in the case of the Be-target data, two components are found in the momentum distributions for light fragments. Procedures to deduce parameters which represent the distributions are presented. In the second section, the deduced parameters of momentum distributions are shown. The momentum widths for high and low momentum side are compared with the Goldhaber model. The momentum distributions for transfer-like fragments are shown. In the third section, procedures to evaluate production cross sections are described. The systematic errors of cross sections are shown as a function of fragment mass. Verification of the factorization is examined with the measured cross sections for Be and Ta targets. In the final section, the results of this experiment are summarized.

4.1   Fitting Procedure for Momentum Distributions

Momentum distributions of fragments have information for understanding reaction mechanisms. At relativistic energies, the projectile fragments have symmetric momentum distributions fitted to a Gaussian form, of which width has been discussed with respect to the Fermi motion of nucleons or temperatures of pre-fragments [24].

The results obtained in this work are different from at relativistic energies. Figure 4.1 shows a typical momentum distribution of this experiment. By comparison of the momentum distribution with a Gaussian function, asymmetric feature of the

distribution is observed. <mark>The momentum distribution of projectile-like fragments produced at intermediate energies are generally asymmetric with a tail on the low momentum side</mark> [85].

   To deduce the most probable momentum and width from such asymmetric shapes, the momentum distributions have been fitted so far with several kinds of trial functions. The fitting functions to reproduce the momentum distribution of fragments are summarized as follows (1)-(3).

(1) R. Pfaff et al. [85] have measured momentum distributions of fragments produced in 70 AMeV ^{86}Kr + Al reaction. Although the momentum distributions were asymmetric, the momentum width and the mean momentum of fragments were obtained by fitting of a single Gaussian function. Because of the Gaussian function, the fitting results depend on momentum region in which the experimental data were measured. To minimize the effect of low momentum tail on fitting results, the fitting was carried out with the data in a momentum range which corresponds to a full width at half maximum. No information on the low momentum tail was obtained from this method.

(2) D. Bazin et al. [86] have chosen an analytic function $F(p)$ of a polynomial exponential function as follows,

$$F(p) \;=\; \exp \sum_{i=0}^{5} \alpha_i (p/K)^i, \tag{4.1}$$

where K is a normalization factor. They show fitting results of this function. However, physical meaning of the parameters is not clear.

(3) Ch.O.Bacri et al. [87] used a Gaussian function for high momentum side and an exponential tail function for low momentum side. This procedure is useful to know the behavior of low momentum tail, though another artificial Gaussian function with the same maximum but a different width is necessary to link the exponential function to the high-momentum Gaussian function.

Since physical models have not been established for the low momentum tail, what kind of functions to be used is not unique.

   There is another kind of complexity. We found two components in the momentum distributions of light fragments only for the Be-target data. Figure 4.2 shows the momentum distributions of the ^{10}Be and ^{30}Mg isotopes from the Be-target data. The
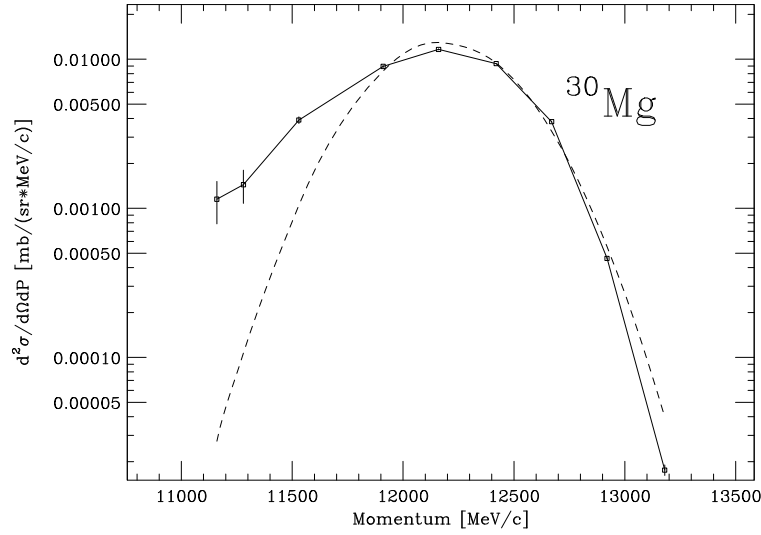
Figure 4.1: Typical fragment momentum distribution (solid lines) fitted by a Gaussian function (dashed curve). It shows clearly asymmetric distribution.

both distributions are also scaled as a function of velocity (β). Two arrows in the figure indicate the velocities of projectile (β_{proj}) and center-of-mass system (β_{cm}), respectively. In the distribution of ^{30}Mg (Fig. 4.2(b)), a single component is observed near the projectile velocity (β_{proj}). On the other hand, the ^{10}Be distribution (Fig. 4.2(a)) shows two components at β_{proj} and β_{cm}. Here, the component around β_{proj} is defined as a high-energy side of peak (HE), and that of β_{cm} is as a low-energy side of peak (LE). With increasing the fragment mass number, the LE-component decreases. At last, no significant LE-component has been observed for heavy fragments like the ^{30}Mg data (See Appendix.D). In our data, we have found clearly the LE-component for the fragments with A of 9~12. The LE-component has been observed for light fragments in Ar+Be reaction, while, the LE-component has not been found in the momentum distributions of Ar+Ta reaction data in the momentum region where the experimental data were taken.
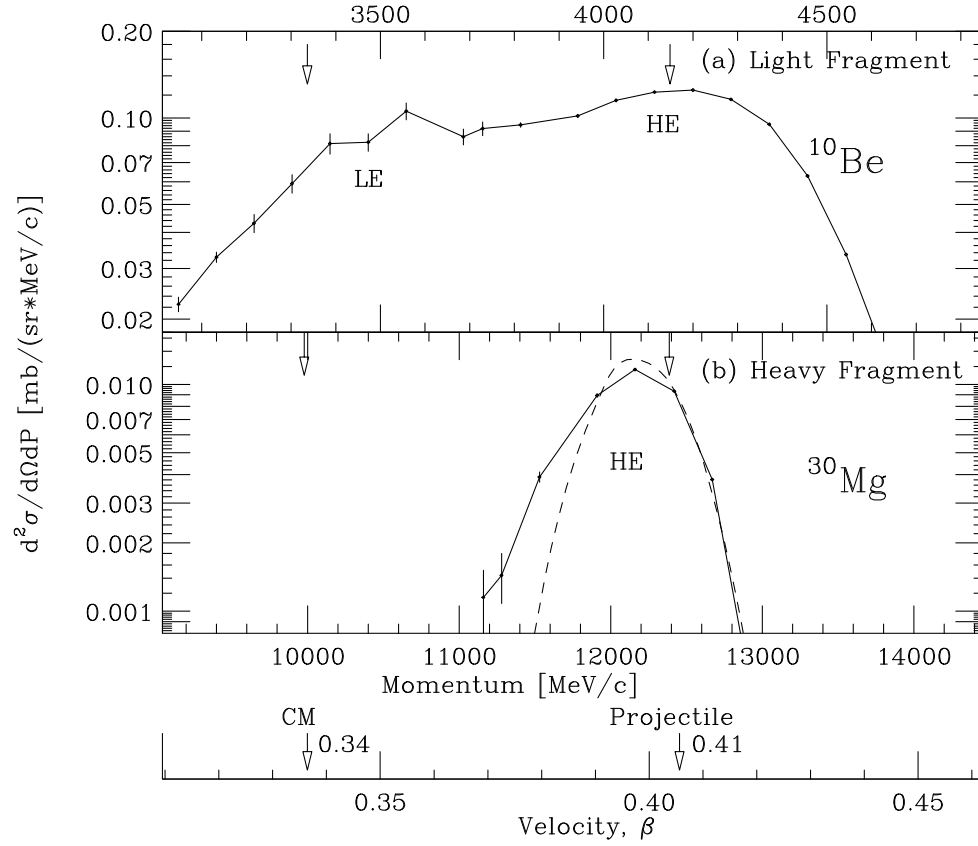
Figure 4.2: Typical fragment momentum distributions for (a) ^{10}Be and (b) ^{30}Mg produced in Ar+Be reaction. The ^{10}Be distribution has two components on momentum distribution, while the ^{30}Mg distribution has one component.

What is the origin of the HE- and LE-components? For all fragments from both Ar+Be and Ar+Ta reactions, we observed the HE-component. The HE-component has a peak close to the projectile velocity (β_{proj}). The two facts show that the HE-component can be associated with the projectile-fragmentation reaction. On the other hand, the LE-component may be explained as another reaction process related to central collisions.

To clarify further this hypothesis, we made a plot of the cross sections for LE-component as a function of fragment mass number. The figure is shown in the Appendix D.2. With increasing mass number, the cross sections of LE-component decreases. The mass dependence of cross sections may show that the LE-component is proper in the production reaction of very light fragments. The fact that the LE-component has been observed for light fragments in the Ar+Be reaction shows the LE-component is related to a reaction mechanism with a small impact parameter. When a light fragment like ^{10}B is produced in the Ar+Be reaction, the Ar projectile collides the Be target nucleus with a small impact parameter. Due to the deep impact, the reaction makes a compound nuclear system running at a velocity near the center-of-mass system of Ar+Be (β_{cm}). The compound nucleus is heated up to a very hot nuclear system due to an energy conversion from a kinetic energy of projectile to an internal energy of the compound system. The highly excited state from the mass asymmetric system of projectile and target is discussed in Ref. [88]. When a light fragment like ^{10}B is produced in the Ar+Ta reaction, the impact parameter is much larger than in the case of the Ar+Be reaction. Thus, we found the LE-component only for the Ar+Be system. Since we focus the projectile fragmentation reaction, we discuss mainly the HE-component in this thesis.

We have identified the component originating from the projectile fragmentation reaction in the momentum distribution. The HE-component is asymmetric distribution as shown in Fig. 4.1. As written in (1), a fitting to a Gaussian form was carried out by excluding the low-momentum data, reported by Pfaff et al. The fit to a Gaussian form gives three free parameters, amplitude (A), peak position (P_0) and width (σ) (type I);

$$\frac{d^2\sigma}{dPd\Omega}(\theta = 0^\circ)[\frac{mb}{(sr \cdot MeV/c)}] \quad = \quad A \cdot \exp(-\frac{(P - P_0)^2}{2\sigma^2}). \qquad (4.2)$$

[Type I : Gaussian Function]

Obviously, the simple Gaussian form includes no information of the low-momentum side.

To argue a systematics of low-momentum tail in next chapter, the following asymmetric function with four free parameters (type II) is applied for the data fitting,

$$
\frac{d^2\sigma}{dPd\Omega}(\theta = 0^\circ)[\frac{mb}{(sr \cdot MeV/c)}] \;=\; \begin{cases} A \cdot \exp(-\dfrac{(P - P_0)^2}{2\sigma_L^2}) & (P \leq P_0) \\ A \cdot \exp(-\dfrac{(P - P_0)^2}{2\sigma_H^2}) & (P \geq P_0), \end{cases}
\tag{4.3}
$$

[Type II : Asymmetric Gaussian-like Function]

where P_0 is the most probable peak value of momentum in the distribution, σ_L and σ_H are momentum width in low and high energy side, respectively.

To check if the asymmetric Gaussian-like function is appropriate for fitting the present data, the fitting result of ^{30}Mg is shown in Fig. 4.3 compared with the fitting to the type I function. In this fitting procedure, the maximum likelihood method was used to treat the small statistics at the tail parts of distribution. The solid lines are the results of fitting with the functions. The type II function gives a better fit for the low momentum side as well as the high momentum side.

In the case of light fragments, the fitting function should be taken to a sum of two functions for the HE- and LE-components. The type I function was used to fit the LE part. The $B\rho$ settings of the experiment do not cover the whole region of a LE-component. In addition, the data for the LE-component have small statistics in many cases. The type I + type II functions were applied for three isotopes, ^{10,11}Be, and ^{14}C. To decrease the number of fitting parameters, the type I + type I functions were used for 23 light fragments data with low statistics.

The typical result is shown in Fig. 4.4. The light isotope of ^{10}Be was fit to the sum (solid line) of HE- and LE-component (dashed lines). On the other hand, the heavy isotope of ^{30}Mg was fitted to a single type II function (solid line). In both results, the symmetric part of HE-component is shown with a dotted line. The HE-component has been analysed mainly in this thesis for the origin of projectile-fragmentation reaction. For all fragments, the results of fitting parameters are tabulated in Appendix A. In the following section, we show the results of fitting parameters for HE-component with figures.
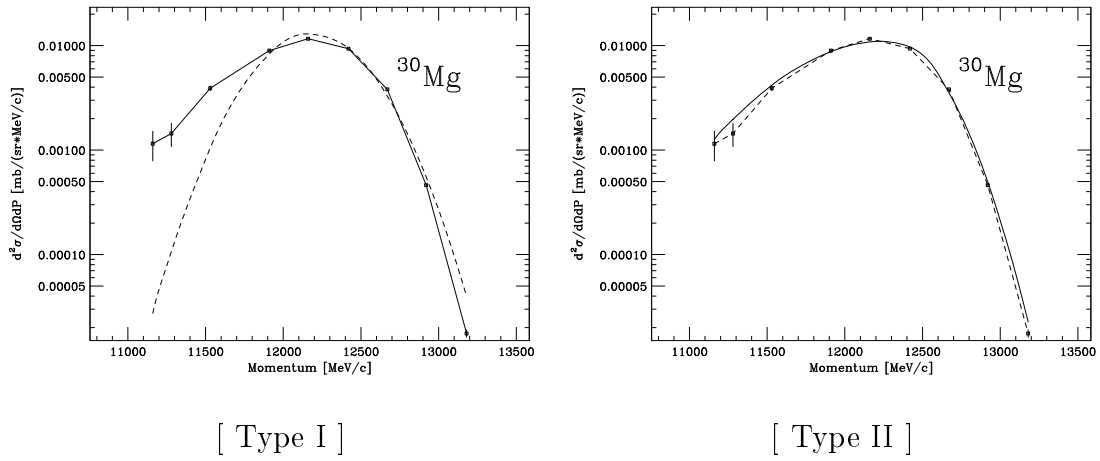
[Type I] [Type II]

Figure 4.3: Fitting for momentum distribution of ^{30}Mg data in Ar+Be reaction. The dashed curves indicate fitting results with two types of functions; the left figure is obtained form type I, and the right is form type II. See text for further details.
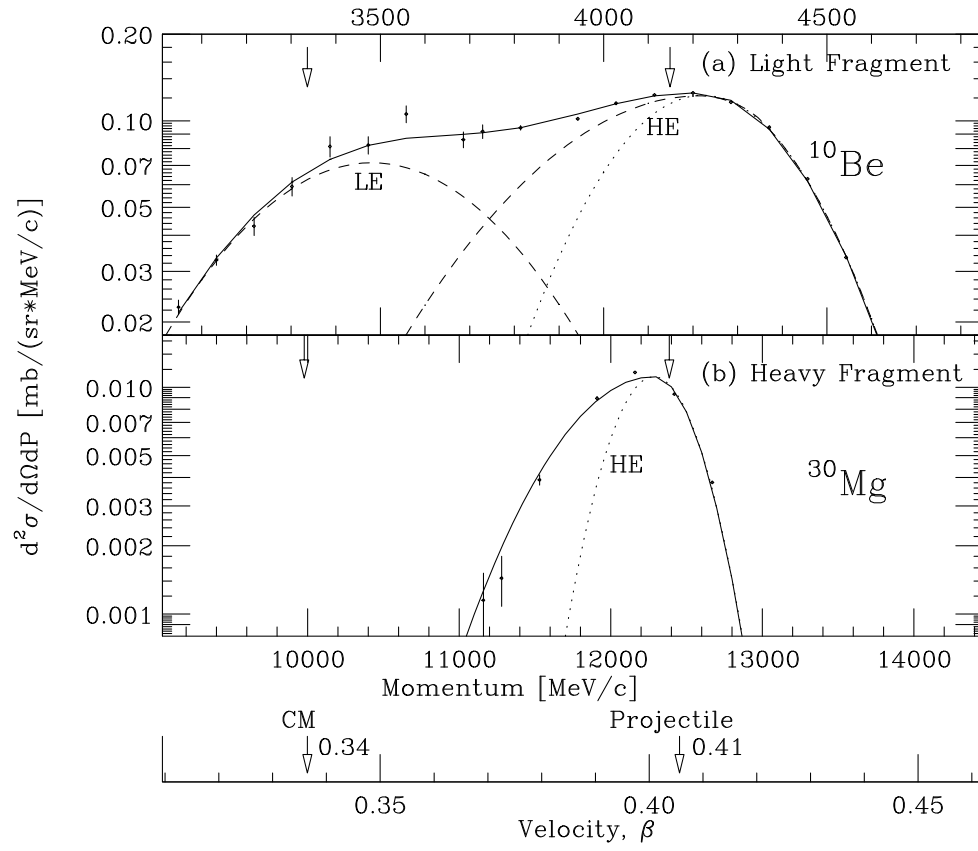
Figure 4.4: Fitting results of Fig. 4.2 are shown with solid lines. Light fragment has two peaks (dashes lines) of HE- and LE-components. HE-component for both isotopes have a low momentum tail and the symmetric parts are shown with dotted lines.

4.2   Fitting Results

The fitting results with the asymmetric Gaussian function are presented in this section. From the most probable value of momentum distribution of fragments, the momentum shift is obtained. The momentum widths for high and low momentum side are compared with the Goldhaber model. We show that transfer-like fragments have rather large momentum shift.

4.2.1   Momentum Peak Shift

In the nuclear fragmentation process, a part of the kinetic energy of projectile is converted into excitation energies of fragments, and the projectile velocity is decreased. This energy loss in projectile fragmentation reaction is called as 'momentum peak shift'. The momentum peak shift is obtained from the difference of the projectile velocity and the most probable velocities of fragments. We present the result of momentum peak shift in a unit of energy per nucleon, which is proportional to square of velocity. This unit is convenient to discuss the kinetic energy consumption in the nuclear reaction.

Figure 4.5 shows the momentum peak shift of fragments produced in Ar+Be and Ar+Ta reactions. Each value of peak shift is plotted with a statistical error. The solid line for each isotope is drawn to guide the eye. The primary beam energies were shown with the correction of the mean energy loss in the production target. The values of the most probable energies of fragments were also corrected with energy losses in the targets (see Section 3.3.2). The negative shift of data from the solid line of the primary beam energy indicates the energy loss by nuclear fragmentation process.

The systematic error of momentum shift was estimated to be 0.9% in the unit of energy per nucleon. This value was evaluated from artificial changes of the momentum distribution within the systematic errors of 9%. We increased or decreased the measured cross sections artificially within the systematic errors to maximize the effect on the fitted values of the momentum peak shift. We made a new fit to the modified data. The fitting results have changed from the original fits. From the difference of both fits, we obtained typical values of systematic errors of fitting parameters.

The deviation for a given element chain in the Be target is comparable to the systematic error. As seen in Fig. 4.5, the measured momentum shifts for the Be

target (a), compared with the case of the Ta target (b), vary widely. One could understand the deviation as an effect of the target thickness in atomic energy-loss process [6], because the target thickness of Be is six times thicker than that of Ta.

The bounce of momentum peak shift as a function of fragment mass was observed in the results of both targets. The momentum peak shift increases when the number of removed nucleons $\Delta A = A_p - A_f$ is increased up to a half of projectile mass ($A_f \geq 20$). On the other hand, the momentum shift decreases when the mass loss ΔA is increased beyond 20 ($A_f < 20$). In short, we observed the maximum of momentum peak shift around $A_f = 20$.

A phenomenon of fragment acceleration was observed in the Be-target data. In Fig. 4.5(a), the solid line of $87.5A$ MeV corresponds to the primary beam energy. Velocities of the fragments ^{6,7}Li, $^{9-11}$Be, and $^{10-13}$B are larger than the projectile velocity. The very light fragments are accelerated in the reaction process. On the other hand, no acceleration phenomenon for all fragments $A_f \geq 8$ was observed in the Ta-target data.

No significant difference between both targets was observed in the momentum peak shift for the projectile-like fragments $A_f \geq 20$. I shall have more to say about the transfer-like fragments of ^{36}Al,^{37,38}Si,^{38,39}P, and $^{37-40}$K. These results are taken up in Section 4.2.4.

We found two features in the momentum peak shift. First, the maximum of momentum peak shift is observed for the fragments around $A_f = 20$ in Fig. 4.5 for both targets. This behavior is called hereafter 'parabolic mass dependence of momentum shift'. Secondly, the acceleration phenomenon was observed in light fragments only for the Be target. Namely, the most probable velocities of light fragments are beyond the projectile velocity. We discuss the details in the next chapter.

4.2.2 High Momentum Side Width

The momentum distribution widths of the individual fragments were obtained from the data fit with the asymmetric Gaussian-like functions. The asymmetric function has two width parameters, σ_H and σ_L for high and low momentum side, respectively.

The high momentum side widths σ_H as a function of fragment mass are shown in Fig. 4.6(a) and Fig. 4.7(a), for the Be and Ta targets, respectively. The high momentum side widths of all the observed fragments are compared to the formulation

by Goldhaber as follows,

$$\sigma_{\parallel} \quad = \quad \sigma_0 \sqrt{\frac{A_f(A_p - A_f)}{A_p - 1}} \tag{4.4}$$

where $A_{p,f}$ is the mass number of the projectile and fragment, respectively. The solid curves are drawn with the reduced width σ_0=90 MeV/c from experimental results at relativistic energies [24]. The deduced values of σ_0 for the fragments in the mass range 9 to 36 are shown in Fig. 4.6(b) and Fig. 4.7(b). The dashed lines denote the mean value of σ_0 =93.5±2.6$_{stat}$±7.5$_{sys}$ for the Be target, and 97.4±1.8$_{stat}$±7.8$_{sys}$ MeV/c for the Ta target, respectively. The systematic error of σ_0 for each target was estimated from comparison of the fitting results of the measured momentum distribution with those of the artificially modified one, as described in Section 4.2.1. No significant difference between both targets was observed in the high momentum side widths. The light fragments A_f<13 produced by using the Be target show slightly a deviation from the Goldhaber model. The deviation is originating from the LE-component and the fitting function to be used. To avoid a digression from the main purpose, we do not follow up the deviation further. These results are in good agreement with high-energy experiments [24].

At relativistic energies, the reduced width σ_0 is independent of the primary beam energy. At lower energies, the reduction of σ_0 has been observed [89]. The reduction mechanism has been argued by several theoretical works, where the reason is for example due to the Pauli blocking. Due to the effect, the σ_0 has the energy dependence at 30-40A MeV [56, 57], and becomes constant up to 90A MeV. The fact that the measured σ_0 is the same as high-energy one is consistent with this picture.

4.2.3   Low Momentum Side Width

The results of momentum width at low momentum side are shown in Fig. 4.8. The widths of low momentum side σ_L are plotted as a function of fragment mass with the statistical errors. We compared the results with the high momentum side width σ_H. Instead of showing individual data of σ_H, the dashed curve calculated with the Goldhaber model is presented. The systematic error of σ_L is estimated 8%, which is not shown in the figure. The procedure of the estimation was described as Section 4.2.1.

In the Be-target data, each isotope chain has a mountain-style structure (solid curves). On the other hand, the low momentum widths σ_L of the Ta data may have

no such a structure. One can understand the deviation as the target thickness effect. Another reason for the mountain-style structure should be noted. The momentum distribution of light fragments has the LE-component at the low momentum side only for the ^{9}Be target data. In the fitting procedure by use of the asymmetric Gaussian-like function, the LE-component may also affect the results. Therefore, the mountain-style structure of σ_L for fragment mass should be ignored as a systematic error.

As seen in Fig. 4.8, the measured widths of σ_L are twice wider than σ_H approximately. Obviously, the large width cannot be explained by the Goldhaber model. The σ_L may have a linear dependence as a function of mass loss $\Delta A = A_p - A_f$, which is very different from the parabolic feature of σ_H. No target dependence of σ_L between the Be and Ta targets was found in our data. As any models for the low momentum tail have not been established, it is difficult to discuss the low momentum tail only from the systematics of σ_L. Yet we should comment that the low momentum tail may not depend on the target.

In addition, another interesting point was found in the result. At the limit $\Delta A \rightarrow 0$, the σ_L may not converge on 0, but 300$\sim$400MeV/c. This feature is different from the Goldhaber formula. Even if the fragmentation reaction is the dominant process for production of fragments, these new observations may lead to an additional reaction process necessary for intermediate energy reactions.

4.2.4 Momentum Distribution for Transfer-like Fragmentation

The transfer-like fragments of ^{36}Al,^{37,38}Si,^{38,39}P, and $^{37-40}$K were observed at this experiment. These fragments have more neutrons or protons than the projectile nucleus. The fragments cannot be produced with projectile fragmentation reactions. Neutron and proton pick-up processes are needed for the production of the fragments.

Figure 4.9 shows the momentum distribution of ^{36}Al by using the Be target. This isotope production needs at least one neutron pick-up process from target nucleus. We made an attempt to fit the momentum distribution with the Type II function. Due to the limit of data at low-momentum tail, we assumed that the fitting parameters of momentum widths were fixed. The σ_H was given from the Goldhaber formula with σ_0=90MeV/c. The σ_L was assumed to be $(400 \pm 60_{sys})$MeV/c. This value was obtained from the systematics as shown in Fig. 4.8.

The fitting result is shown as a dotted curve in Fig. 4.9. The peak of the momentum distribution corresponds to $83.9A$ MeV. As the primary beam energy was measured as $87.5A$ MeV, the momentum peak shift was obtained as $(3.6\pm1.2)A$ MeV. The systematic error was estimated by taking into account the systematic error of measured momentum distribution as well as σ_L.

The measured momentum peak shows clearly a larger shift toward low momentum side, compared with that of the same mass number, $\sim0.9A$ MeV. The large momentum shift of transfer-like fragments was also observed in the fragments of $^{37-40}$K requiring to proton pick-up process in production.
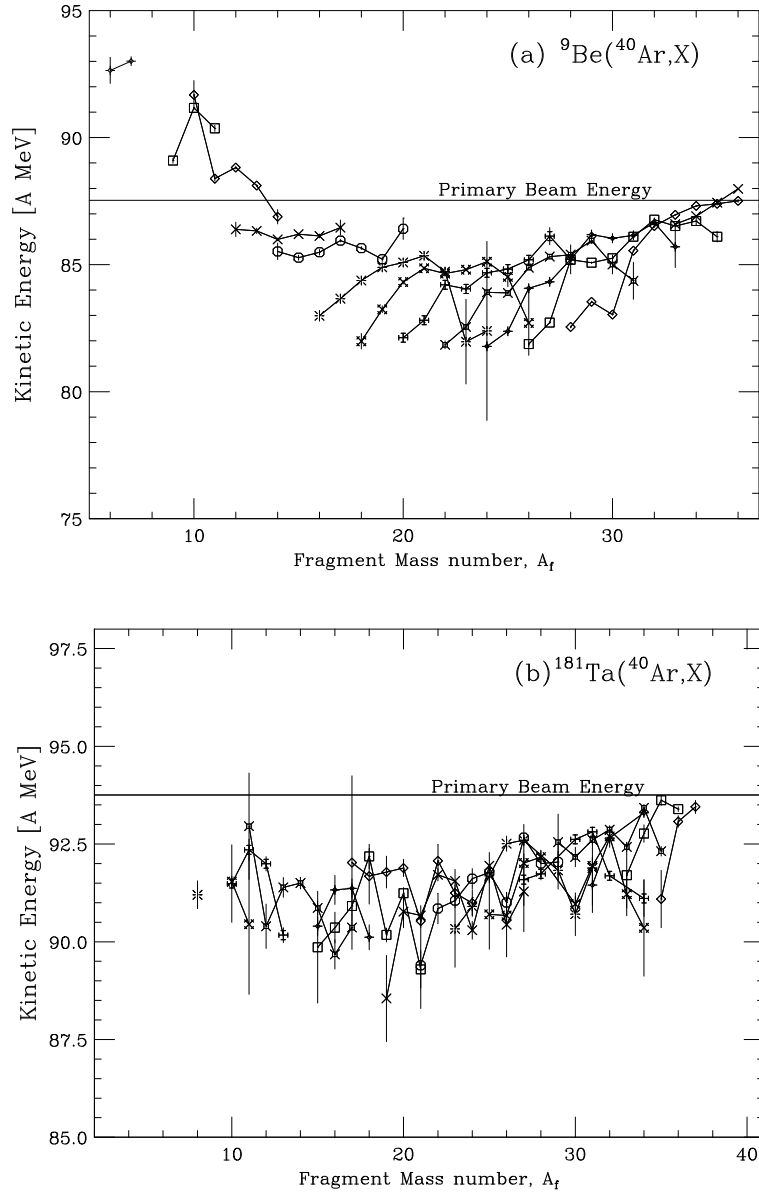
Figure 4.5: Momentum peak shift of fragments produced in (a) Ar+Be and (b) Ar+Ta.
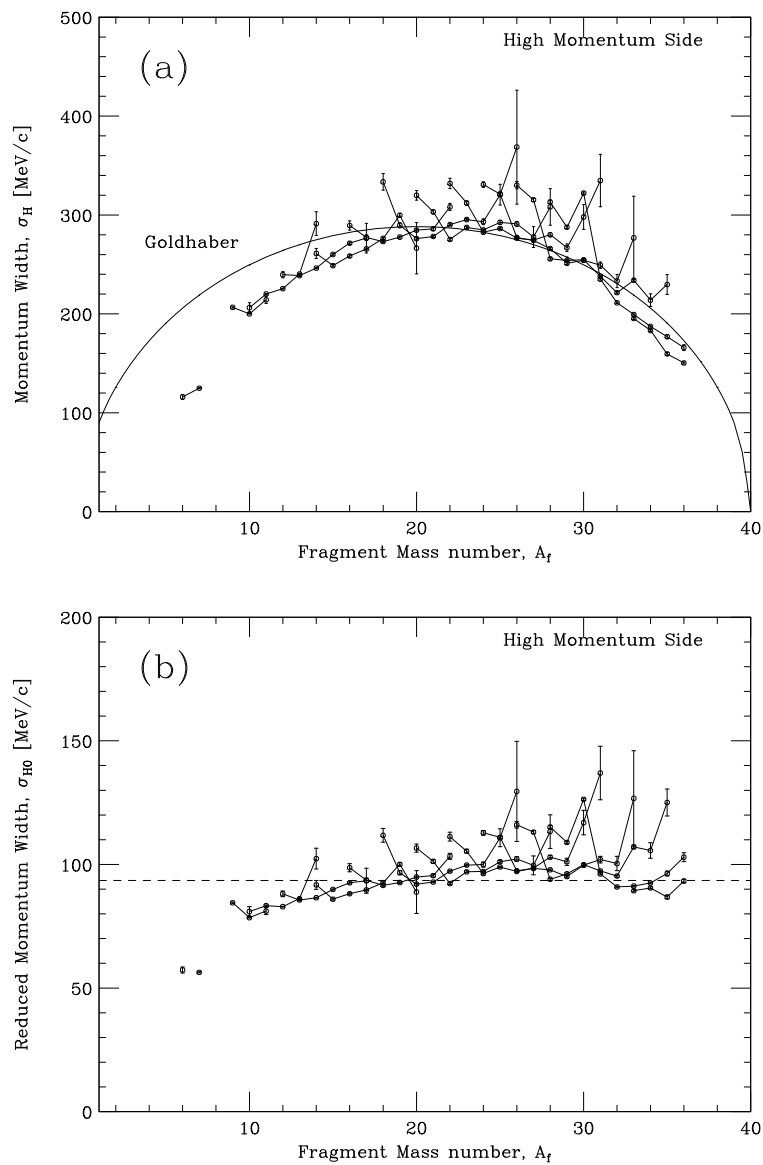
Figure 4.6: Momentum widths at high momentum side (Be target); (a) for σ_H and (b) for reduced widths according to the Goldhaber model.
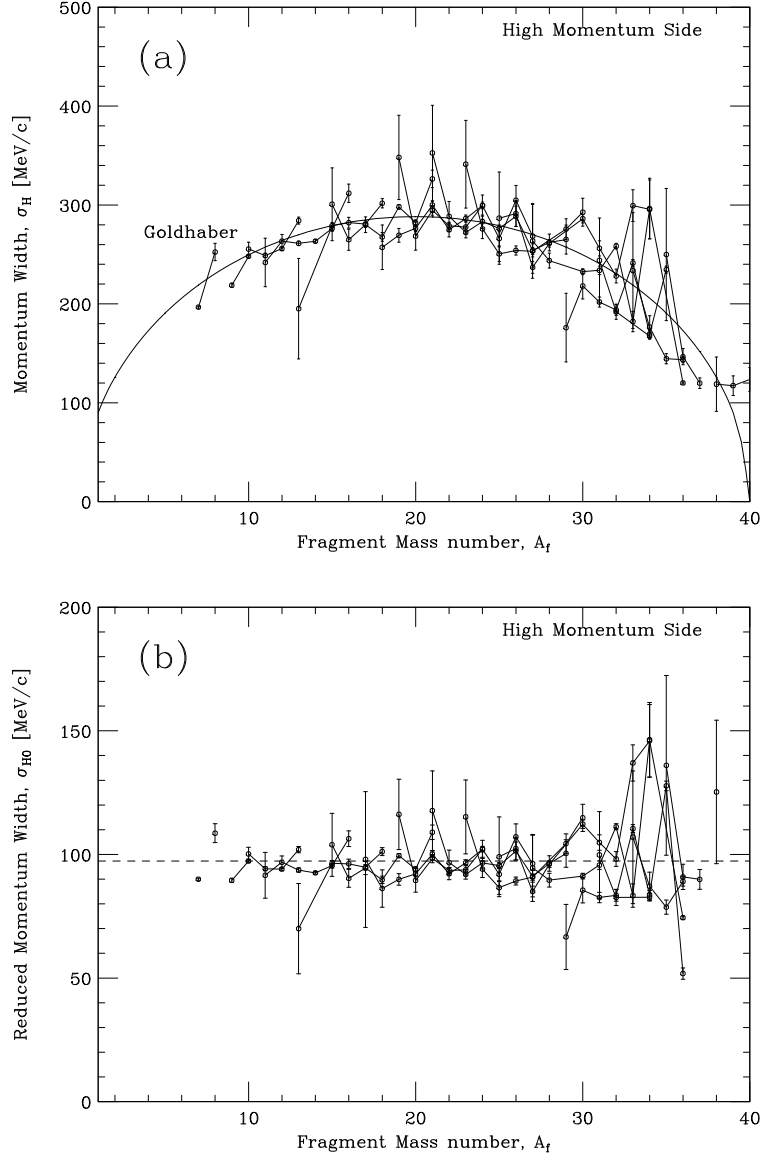
Figure 4.7: Momentum widths at high momentum side (Ta target); (a) for σ_H and (b) for reduced widths according to the Goldhaber model.
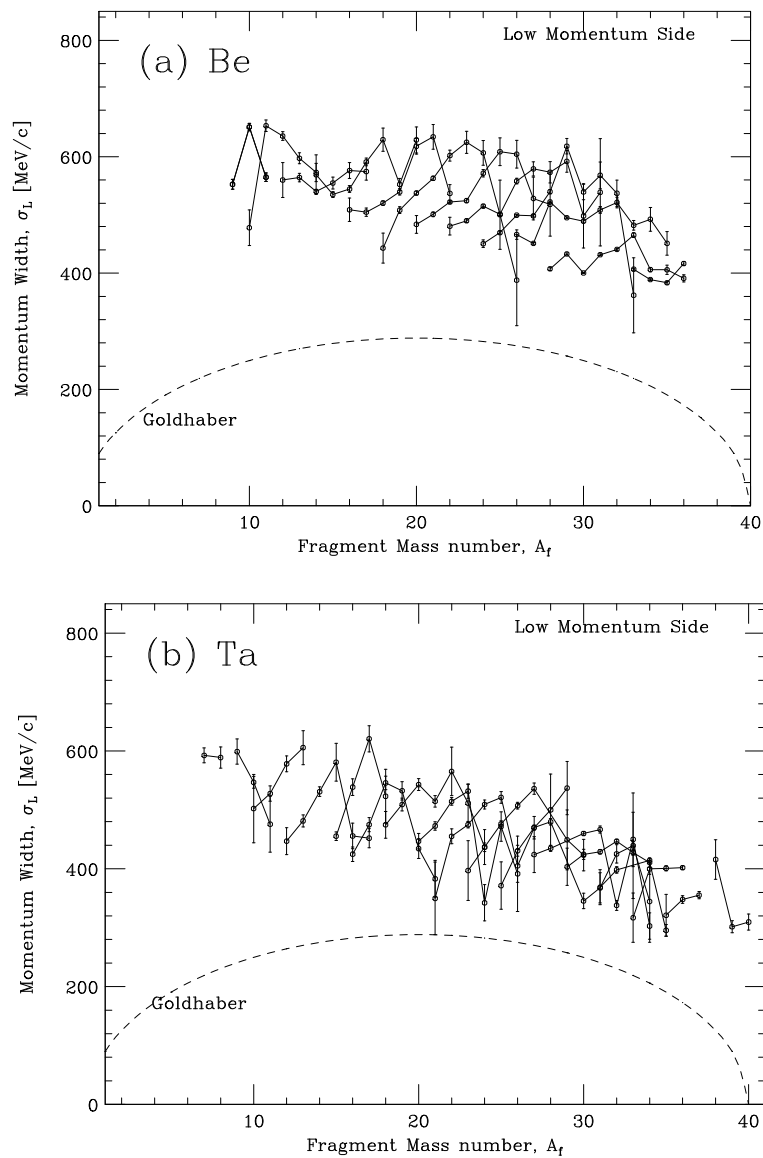
Figure 4.8: Momentum widths at low momentum side by using (a) the Be target and (b) the Ta target.
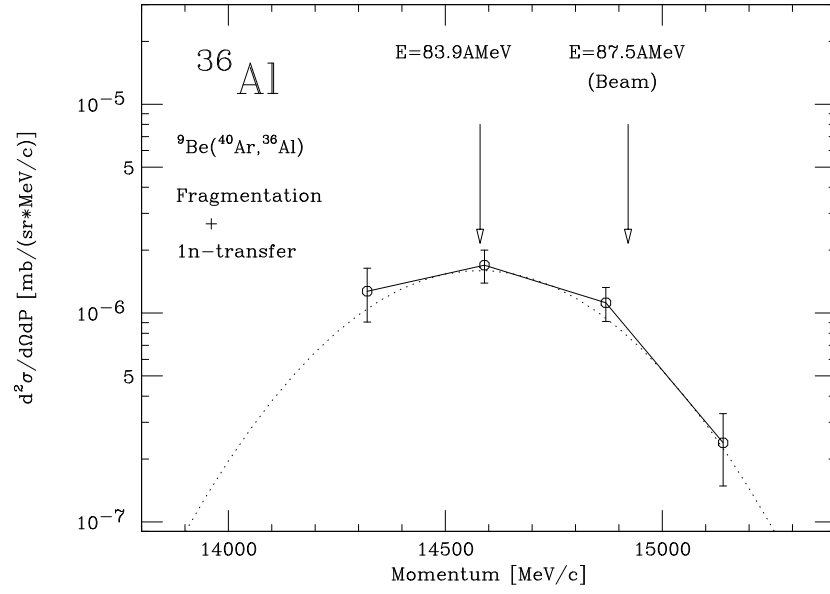
Figure 4.9: Momentum distribution for ^{36}Al. This isotope cannot be produced with only the nuclear fragmentation process. One neutron should be picked up from target. The measured peak momentum corresponds to $83.9A$ MeV. The measured momentum peak shows a larger shift toward low momentum side, compared with that of the same mass number, $\sim 0.9A$ MeV.

4.3   Cross Sections

The production cross sections of fragments were evaluated from the longitudinal momentum distributions with the fitting results. The ambiguity of transverse momentum distributions was taken into account as the systematic error of the cross sections. From the production cross sections, we investigated the validity of factorization assumption for both stable and unstable isotopes. The target dependence of cross sections except the nuclear-size effect was confirmed at neutron-rich nuclei far from stability.

4.3.1   Evaluation of Production Cross Sections

To obtain the production cross sections for the projectile fragmentation, the transverse momentum distributions are needed. Here, the transverse momentum distributions are assumed to be a Gaussian function with a width of $\sigma_\perp$,

$$\sigma_\perp^2 \;=\; \sigma_H^2 + \frac{A_f(A_f - 1)}{A_p(A_p - 1)}\sigma_D^2, \tag{4.5}$$

where σ_D is a parameter of the deflection effect, and $A_{p,f}$ are mass numbers of a projectile and a fragment, respectively.

In Ref. [82], Van. Bibber et al. have shown the deflection parameters for two targets of ^{27}Al and ^{197}Au with 92.5 and 117.5A MeV ^{16}O beams. The results from their measurement were σ_D=190$-$220MeV/c, as tabulated in Table 4.1. It should be noted that no significant target dependence of σ_D was observed.

According to Ref. [90], the value of σ_D shows an energy dependence in the intermediate energy region. According to the energy dependence, we used σ_D of 195MeV/c around 90A MeV for the present experiment. We discuss the systematic error from this assumption later.

Then, the function of doubly-differential cross section for the production of an isotope may be written as,

$$\frac{d^2\sigma}{dPd\Omega}[\frac{mb}{(sr \cdot MeV/c)}] \;=\; \exp(-\frac{P_\perp^2}{2\sigma_\perp^2}) \times \begin{cases} A \cdot \exp(-\dfrac{(P_\parallel - P_0)^2}{2\sigma_L^2}) & (P_\parallel \leq P_0) \\[2ex] A \cdot \exp(-\dfrac{(P_\parallel - P_0)^2}{2\sigma_H^2}) & (P_\parallel \geq P_0) \end{cases} \tag{4.6}$$

Since the fragments are emitted in a narrow forward cone in the laboratory system,

the following approximation can be applied,

$$P_\parallel = P cos\theta \simeq P \qquad (4.7)$$
$$P_\perp = P sin\theta \simeq P\theta. \qquad (4.8)$$

Based on these approximations, the production cross sections are calculated with the following equation:

$$\sigma = \int_0^{2\pi} d\phi \int_0^\pi \theta d\theta \int_0^\infty dP \frac{d^2\sigma}{dPd\Omega} \qquad (4.9)$$
$$\simeq \pi A \left\{ \int_0^{P_0} dP(\frac{2\sigma_\perp^2}{P^2}) \exp(-\frac{(P-P_0)^2}{2\sigma_L^2}) + \int_{P_0}^\infty dP(\frac{2\sigma_\perp^2}{P^2}) \exp(-\frac{(P-P_0)^2}{2\sigma_H^2}) \right\} . \quad (4.10)$$

The cross section table is presented in Appendix C. The isotopic distributions of the production cross sections are shown in Fig. C.1.

The systematic error of cross sections originated from the ambiguity of the transverse momentum distribution assumed in this analysis has been estimated. To investigate the target dependence of deflection parameter (σ_D), we have compared the deflection parameter reduced with the grazing angle in Table 4.1. Within the small-angle approximation, the grazing angle in the laboratory frame of projectile (p) and target (t) is described as [87],

$$\theta_{gr} = \frac{1.44 Z_p Z_t}{R\, E\, A_p}, \qquad (4.11)$$

where Z is atomic charge, A is mass number and EA_p is the total incident kinetic energy. The grazing angle θ_{gr} and the deflection parameter σ_D are tabulated with ^{16}O beams of $92.5A$ MeV and $117.5A$ MeV for the production targets of aluminum ($Z_t = 13$) and gold ($Z_t = 79$). The grazing angle for Au is 4 times larger than for Al. However, the measured value of σ_D shows the difference for targets is at most 11%. Asumming that the deflection parameter is 195±30 MeV/c for both the $90A$ MeV Ar+Be collision and the $94A$ MeV Ar+Ta collision, we obtained the systematic error of production cross sections, as shown in Fig. 4.10. A typical value of systematic error is 20% for a fragment mass of 32.

The systematic error from the fitting procedure of the momentum distribution is 9%. Hence, overall systematic error for cross sections increases when fragment mass number is increased. The overall systematic error for the production cross sections is shown in Fig. 4.11.

System	Energy	θ_{gr} [mrad]	σ_D [MeV/c]
$^{16}O + ^{27}Al$	$92.5A$ MeV	16.6	223.5±3.5 [82]
$^{16}O + ^{197}Au$	$92.5A$ MeV	67.0	199.5±5.8 [82]
$^{16}O + ^{27}Al$	$117.5A$ MeV	13.1	192.5±4.4 [82]
$^{16}O + ^{197}Au$	$117.5A$ MeV	52.7	187.8±6.7 [82]
$^{40}Ar + ^{9}Be$	$87.5A$ MeV	4.9	195±20 [91]
$^{40}Ar + ^{181}Ta$	$87.5A$ MeV	50.4	

Table 4.1: Experimental data of deflection parameter σ_D, compared with the grazing angle θ_{gr}.
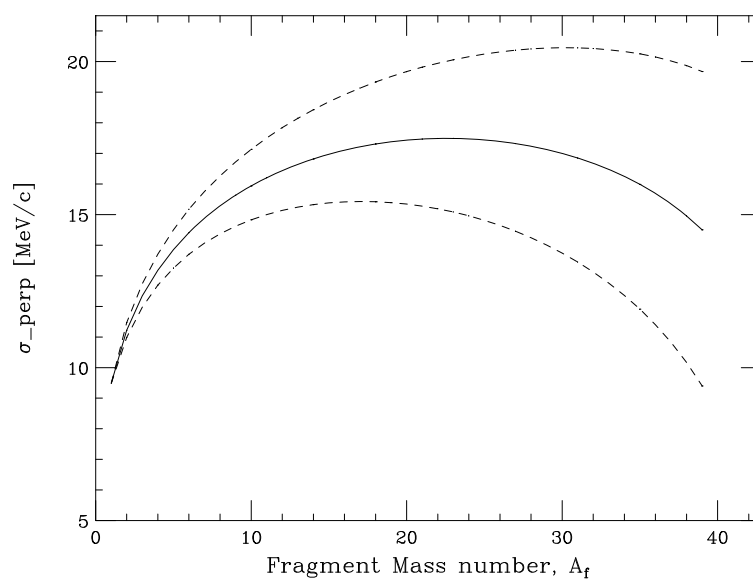
Figure 4.10: Fragment mass dependence of $\sigma_\perp$ when the deflection parameter σ_D is assumed to be $195\pm30\mathrm{MeV/c}$.
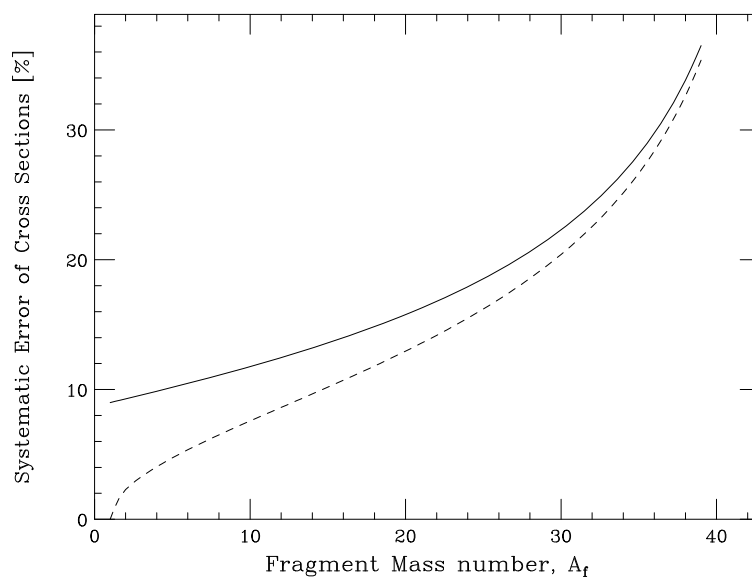
Figure 4.11: Overall systematic error for the production cross sections (solid line). The dashed line shows error originated from ambiguity of $\sigma_\perp$.

4.3.2 Target Dependence of Cross Sections

The target dependence of cross sections was investigated with the results of our experiments. We have obtained the cross sections in wide range of fragment charge for each fragment mass with small statistical and systematic errors, and for the same projectile (^{40}Ar) with two sets of targets (^{9}Be and ^{181}Ta). So we can investigate the validity of factorization for fragmentation reactions at intermediate energies.

Figure 4.12 shows the ratios of cross sections for a fragment in Ar+Ta reactions to those in Ar+Be reactions. The cross sections are normalized with the experimental mass yield $Y(A_f)$ to eliminate the target size effect. The mass yields were obtained from the sum of fragment cross sections with the same mass number. The ratio is shown as a function of charge difference between the most stable charge $Z_\beta(A_f)$ and the fragment charge Z_f. Thus, the target dependence of projectile fragmentation cross sections except the target size effect is represented for the wide range of isotopes near and far from the stability line. If the factorization is valid for production of an isotope, the ratio has no $Z_\beta - Z_f$ dependence.

In Fig. 4.12, the ratios near the β-stability line are constant. It corresponds that the factorization is valid for the production of the nuclei. According to the previous work [18], the factorization is valid for the isotopes in $Z_\beta - Z_f \leq 2$. On the other hand, the ratios increases when $Z_\beta - Z_f$ is increased. This deviation shows that the factorization hypothesis is clearly broken down for neutron-rich nuclei with $(Z_\beta - Z_f) \geq 2$.
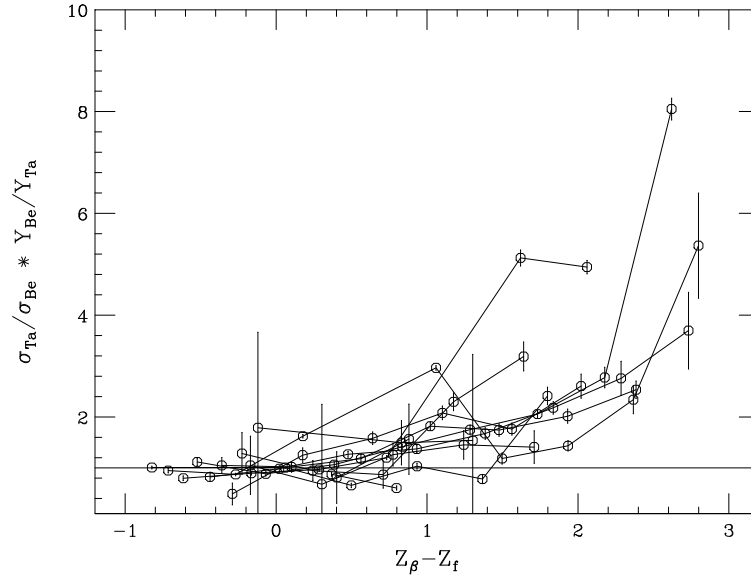
Figure 4.12: Ratio of the production cross sections for each fragment produced with Be and Ta targets. The solid lines are drawn for the same mass number of nuclei, i.e. isobars. The Z_β is the β-stable charge for each isobar. The cross-section ratio of $\sigma_{Ta}(A,Z)/\sigma_{Be}(A,Z)$ is normalized with the mass-yield ratio of $Y_{Ta}(A)/Y_{Be}(A)$ observed.

4.4 Summary

Our projectile fragmentation experiment was performed to obtain the data in a wide range for fragment mass and isospin toward the neutron drip-line. Our experimental results described in this chapter are summerized as follows.

1. We found two features in the momentum peak shift. First, the maximum of momentum peak shift was observed for the fragments around $A_f = 20$. This behavior is called hereafter 'parabolic mass dependence of momentum shift'. Secondly, the acceleration phenomenon was observed in light fragments only for the Be target. For the projectile-like fragments $A_f \geq 20$, no significant difference between both targets was observed in the momentum peak shift.

2. The high momentum side widths σ_H of all the observed fragments were compared with the formulation by Goldhaber. The reduced width σ_0=90 MeV/c is consistent with high-energy experiments. No significant difference between both targets was observed in the high momentum side widths.

3. The low momentum side widths σ_L were found to be twice wider than σ_H approximately. The σ_L may have a linear dependence as a function of mass loss $\Delta A = A_p - A_f$, which is quite different from the parabolic feature of σ_H. Furthermore, another feature of the results should be noted. At the limit $\Delta A \to 0$, the σ_L may not converge on 0, but 300$\sim$400MeV/c. These observations of σ_L cannot be explained by the Goldhaber model. No significant target dependence of σ_L between the Be and Ta targets was found in our data.

4. The transfer-like fragments were observed at this experiment. These fragments have more neutrons or protons than the projectile nuclei. The measured momentum peak shows clearly a large shift toward low momentum side.

5. For the fragments $A_f > 20$, no significant target dependence of the momentum distributions was found in our data.

6. We investigated the validity of factorization assumption for both stable and unstable isotopes. For this purpose, the ratios of cross sections for a fragment in Ar+Ta reactions to that in Ar+Be reactions were obtained as a function of charge difference between the most stable charge and the fragment charge. The cross sections were normalized with experimental mass yield to eliminate the target size effect. The breakdown of factorization (BOF) was confirmed at very neutron-rich nuclei.

We have investigated the target dependence of the momentum distributions and the cross sections in our data. The acceleration phenomenon and the LE-component of light fragments $A_f \leq 13$ were observed only in the Be data, while the fitting results of momentum distributions have shown no significant difference between the Be and Ta targets for the fragments $A_f > 20$. On the other hand, the target dependence of cross sections except the nuclear-size effect was observed in the production of very neutron-rich nuclei. In short, the breakdown of factorization was observed for unstable nuclei far from stability. With the results of our experiment, we discuss the mechanism of projectile fragmentation reaction in the next chapter.

Chapter 5

Discussion

In this chapter, we try to understand the results of our experiments. The target dependence of the momentum distributions and the cross sections has been investigated in our data. The results of momentum distributions have shown no significant difference between both targets for the fragments $A_f > 20$. On the other hand, we found the breakdown of factorization (BOF) for the cross sections in the production of very neutron-rich nuclei. To understand these results, the reaction mechanism of nuclear fragmentation at intermediate energies is discussed. First of all, the fitting results of momentum distributions are compared with several formulae taken from reaction models. We have shown the fragment momentum distributions with the fitting results in Chapter 4. The result of high momentum side width can be understood by the Goldhaber model. However, we need the further discussion of the momentum peak shift and low momentum side width. Next, we discuss the systematics of isotope production cross sections. The charge distribution of the cross sections for a fragment mass is obtained from our data. The most probable charge Z_{prob} and the slope parameter U are discussed. We show that the BOF is represented as a target dependence of the U-parameter. Finally, we discuss the prefragment production mechanism in projectile fragmentation reactions to search for the origin of BOF.

5.1   Characterization of Momentum Distribution

Nuclear fragmentation is generally described as a two-step process [92] (typically the abrasion-ablation process [13][42]). At the first process, nucleons are removed from the projectile by nucleus-nucleus collision. Then, an excited prefragment comes out. Secondly, the prefragment deexcites by the emission of light particles and γ rays in

a cascade process to become the fragment observed by experiment.

Momentum distributions of fragments provide valuable information about the reaction mechanism. The fragment velocity is one of the most interesting, observable values. From the point of view of Swiatecki's participant-spectator model [93], all nucleons in both colliding partners are participants in a central collision. By contrast, all nucleons out of the overlap zone are spectators of which the momentum and energy transfer are relatively small. Thus, the prefragment velocity is nearly equal to the projectile one. The particle emission from the prefragment should be described by an isotropic evaporation. As total momentum of the evaporated particles is nearly zero in the projectile rest frame, although we cannot ignore the effect for very light fragments comparatively. In short, a fragment produced by the projectile fragmentation has a peak momentum which is close to the velocity of projectile. The difference of the velocities between projectile and fragment is generally called as 'momentum peak shift'. The measured values are related to deacceleration of prefragment in the abrasion process.

The parallel momentum width is related to the distribution of nucleon momenta in the projectile before collision (see Section 1.2). At relativistic energies, a Gaussian function is used as a fitting function for the momentum distribution of projectile fragments. From the viewpoint of fitting function for momentum distribution, the Gaussian function has a peak position (P_0), width (σ) and height (A). At intermediate energies, the momentum distribution of projectile-like fragment (PLF) is asymmetric. The asymmetric distribution of fragment momentum at an intermediate energy has been already reported by Gregoire et al [58]. Such an asymmetric distribution comes from the enhancement of the low momentum side of the distribution. The asymmetric part is called as a 'low momentum tail' here. In the previous work, the asymmetric distribution of PLF has been fitted with the Gaussian function in a limiting momentum region using a cut-off parameter. We made an attempt to extract information of the low momentum tail. Among some trial functions, an asymmetric Gaussian-like function (see Chapter 4) is chosen to describe the shape of the low momentum tail. The empirical function has one more parameter of the low momentum width than the Gaussian function. By use of the asymmetric Gaussian-like function, we obtained the fitting result of momentum peak (P_0), both high and low momentum side widths ($\sigma_{H,L}$).

As shown in Chapter 4, the high momentum side width can be understood with

the Goldhaber model. On the other hand, the low momentum side width is much larger than the prediction of Goldhaber model and different from the parabolic mass dependence. Even if nuclear fragmentation reaction is the main process for production of fragments, these features of σ_L may lead to an additional reaction process. Thus, we try to understand the origin of low momentum tail.

We discuss P_0 and σ_L in the following subsections.

5.1.1 Momentum Peak Shift

We discuss the fitting result of momentum peak (P_0). When the momentum distributions are scaled as a function of velocity, the momentum peak (P_0) is located around the velocity of projectile (β_{proj}). At relativistic energies, the near equality of the beam and projectile-fragment velocities has been found in early studies of the projectile fragmentation process [19].

Momentum peak shift is defined as the difference between the velocities of projectile and fragment. It was reported that the velocity of the fragment is measured to be smaller than projectile by high-energy experiments like as LBL [20]. Quantitatively, the momentum peak shift was reported by Greiner et al. [21] for the first time.

The high energy data suggested that the average momentum is slightly lower than the projectile. Abul-Magd et al. [22] viewed the peak shift with a simple picture where the slow-down of the projectile nucleus during the fragmentation reaction is described as a friction phenomenon. When nucleons from the projectile are removed, nuclear bonds have to be broken. They tend to pull on the projectile and slow it down. The number of removed nucleons are related with the momentum peak shift.

After that, many measurements were performed for both high and intermediate energies [85, 94]. In comparison with them, we present a new aspect of the momentum peak shift.

The experimental results for the peak values P_0 of fragment-momentum distributions for Ta and Be targets are shown in Fig 5.1. The results are shown as a function of fragment mass. The primary beam energies are drawn with dotted lines at 94.0 and $90.0A$ MeV, and the kinetic energies at the half point of target thickness are the solid lines at 93.5 and $87.5A$ MeV. The peak values of fragment-momentum distribution were also corrected to energy loss in target (see Section 3.3.2). Each symbol means the same isotope. The isotopes are connected with solid lines. This figure is the same as Fig. 4.5.

As discussed in Section 4.2.2, we found two interesting features; (1) parabolic mass dependence of peak shift, and (2) acceleration phenomenon for light fragments. P_0 increases when A_f decreases down to mass 20, i.e., the half of projectile mass. When A_f decreases down to lower mass, P_0 decreases. At very light mass region, below mass of 13, the fragment velocities are beyond the beam velocity. The rebound of fragment velocity at the half mass was found in Ref. [56]. However, the dynamic range of A_f is narrower than that of this work. The parabolic dependence of peak shift as a function of fragment mass suggests the previous models cannot predict the peak shift for light fragments. In the next subsection, a new formula will be deduced from a simple model.

The 'acceleration' phenomenon for light fragments is also discussed later in following subsection.
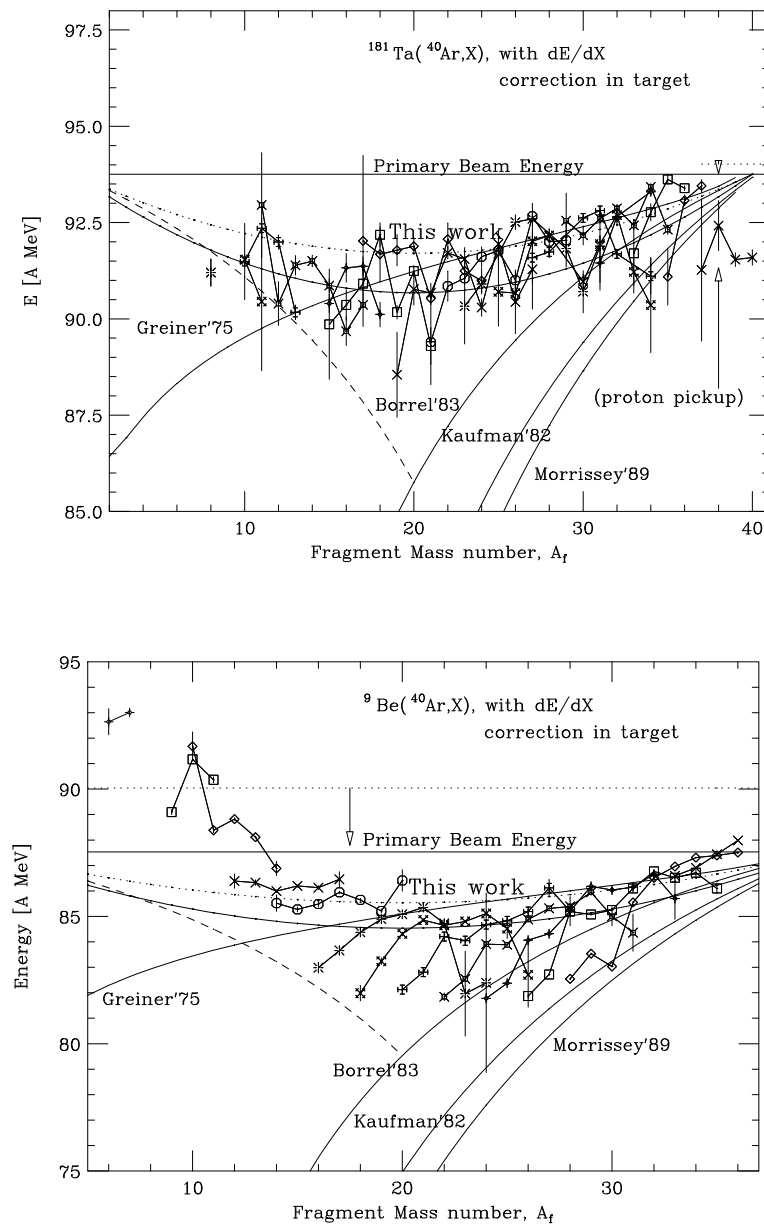
Figure 5.1: Momentum peak of fragments produced in Ar+Ta and Ar+Be reactions. The primary beam energies are drawn with dotted lines, and the kinetic energies at the half point of target thickness are the solid lines. See the text for the labels and curves.

Parabolic mass dependence of peak shift

We discuss the "parabolic" mass dependence of peak shift. The momentum peak shift has been investigated for long time. Many of the reports have shown a linear mass dependence of the peak shift for fragments with $A_f \geq A_p/2$. Several formulae are proposed so far to reproduce the momentum peak shift for the heavy fragments produced in peripheral collisions. We compare our experimental results for the wide fragment mass range with the formulae and try to introduce a new picture to reproduce the parabolic mass dependence.

In Fig 5.1, four formulae are shown with the labels as Greiner75, Kaufman82, Borrel85 and Morrissey89. Greiner et al. [21] reported the projectile-frame parallel-momentum distribution in the fragmentation of ^{12}C projectile at an energy $2.1A$ GeV and found that the average momentum $<P_{//}>$ of fragment is shifted and the fragment velocity is smaller than the beam velocity. The values of $< P_{//} >$ had a linear dependence on $< P_{//} >= - 0.5\ \sigma_{P//} + 30.0\ [MeV/c]$ where $\sigma_{P//}$ is a standard deviation of the momentum distribution. This empirical formula suggested that the small energy transfers to the fragment exclude the possibility of nuclear reactions involving charge exchange.

To describe the dependence of average forward momentum transfer $< p_{//} >$ on the mass loss, another formula was derived, based on a simple picture which treats peripheral reactions as a quasi-two-body process. Cumming et al. [96] [97] proposed a relation of the form

$$p_0 \quad = \quad \frac{E_0}{\beta}[1 + k(1 - \beta^2)^{1/2}] \tag{5.1}$$

where p_0 is the average longitudinal momentum transfer per unit mass loss, E_0 is the energy transferred to the initial target residue, and β is the projectile velocity. The parameter k represents the rate at which $< p_{//} >$ decreases as β increases. The values k differ among the different models. According to Kaufman et al. [98], the analysis of the $0.4-2.1A$ GeV ^{20}Ne $+ ^{197}$Au reaction gave values of E$_0$=13 MeV per unit mass loss and k=0. On the other hand, Morrissey [99] obtained k=1 and E$_0$=8 MeV for $0.4A$ GeV ^{12}C + copper.

At intermediate energies, a simple picture to describe the velocity shift between

projectile and fragment has been given by Borrel et al. [56] [95] as following,

$$\frac{v_f}{v_p} \;=\; \sqrt{1 \;-\; \frac{8\,(A_p - A_f)}{A_f E_p}} \tag{5.2}$$

where E_p is the projectile energy in A MeV. It depends on the projectile mass A_p and fragment one A_f. The function is led when an average energy used to pull out a single nucleon from projectile nucleus is assumed to be 8 MeV. As shown Fig. 5.1, it begins to overestimate the velocity shift below $A_f \sim A_p/2$. To compensate for the deviation, J.A.Winger et al. [62] made a symmetric formula mathematically with respect to $A_p/2$ (dashed line). It should be noted that all of formulae above cannot predict the parabolic mass dependence.

The previous investigations were mainly performed in the region of fragments close to the projectile mass. For whole fragment mass region observed in this work, a parabolic dependence, where the symmetric point is at the half mass of projectile, is observed. As Borrel commented first in Ref. [95], the symmetric behavior of the velocity shift implies another mechanism less costly, compared with the removal of individual nucleons. The mechanism may be splitting or instant crack of projectile into two pieces. We try to make a new formula for P_0 based on the splitting picture.

First, we assumed that the projectile splits in two fragments which are not exited state. The empirical mass formula of Weizsäcker-Bethe is written as follows,

$$M(N, Z) \;=\; N M_n + Z M_p - B(N, Z) \tag{5.3}$$

$$B(N, Z) \;=\; b_{vol} A - b_{surf} A^{2/3} - \frac{1}{2} b_{sym} \frac{(N - Z)^2}{A} - \frac{3}{5} \frac{Z^2 e^2}{R_c} \tag{5.4}$$

where (N,Z) is the neutron and charge number of nuclei [100]. The energy loss in the splitting process is described as $M(N_f, Z_f) + M(N_p - N_f, Z_p - Z_f) - M(N_p, Z_p)$. The change of binding energy shows the parabolic mass dependence of peak shift. However, the energy loss by the splitting process gives only several tens percent of the value measured as momentum peak shift, quantitatively.

Secondly, we try to obtain an empirical formula. The splitting process consumes the kinetic energy of projectile due to the excitation. Here we assume that an energy cost to form a fragment is proportional to the number of pairs of nucleons interacting in long range forces which are broken in the reaction. In this picture, we assume that

1. Nucleons in projectile are bound each other. The paring number of nucleons is, $_{Ap}C_2 = A_p(A_p - 1)/2$.

2. The projectile splits into the spectator (A_f) and the participant $(A_p - A_f)$.

3. Then, the decrease of paring number is $_{Ap}C_2 - (_{Af}C_2 + _{(Ap-Af)}C_2) = A_f(A_p - A_f)$

4. The kinetic-energy loss for one nucleon removal from projectile is ε.

When one nucleon is removed $(A_f = A_p - 1)$, the decrease of pairing number in the splitting process is $A_p - 1$. The energy loss of one nucleon removal can be defined as ε MeV. Thus, the energy loss per nucleon pair is $\varepsilon/(A_p - 1)$ MeV on average. The number of pairing broken in the splitting process is $A_f(A_p - A_f)$ from the item 3. Thus, the kinetic-energy loss in the splitting process can be written as,

$$\Delta E \;\; = \;\; \frac{\varepsilon A_f(A_p - A_f)}{A_p - 1}. \tag{5.5}$$

In the case of non-relativistic beam energy, the energy conservation between projectile and two pieces gives a new formula as follows:

$$\frac{v_f}{v_p} \;\; = \;\; \sqrt{1 \; - \; \frac{\varepsilon \, A_f(A_p - A_f)}{A_p E_p(A_p - 1)}}. \tag{5.6}$$

If we select the energy loss parameter of $\varepsilon = 8$ MeV, this formula corresponds to Borrel's for the case of one-nucleon removal. However, the value of ε may not be 8 MeV. In Fig. 5.1, the P_0 values predicted by the formula (This work) were compared with the present data. The dashed curve is drawn with $\varepsilon = 8$ MeV. On the other hand, the solid curve is $\varepsilon = 12$ MeV. The experimental data may support that $\varepsilon = 12$ MeV is better than 8 MeV.

To study the target dependence of momentum peak shift, the above formula has been compared with the Ta-target data. The result of momentum peak shift for the Ta-target data is shown in Fig. 5.1 (b). The ε of 12 MeV (solid curve) is also applied for the Ta data, better than 8 MeV (dashed curve).

Concerning beam energy dependence of the momentum peak shift, this formula is compared with the data obtained from other experiments at lower and higher energies. The formula based on the splitting picture may be quite independent of the beam energy. The PLF's data of V.Borrel et al. with a $44A$ MeV Ar beam can be well reproduced by this formula.

At relativistic energy of $500A$ MeV, Weber et al. [94] reported the results of fragment-momentum distribution with the reaction of ^{86}Kr + ^{9}Be. Figure 5.2 shows the momentum peak shift in the high-energy experiment and predicted by the formula with $\varepsilon = 12$ MeV (solid curve). The calculation was carried out by use of the ΔE equation (5.5) and relativistic energy conservation. The results may agree with the splitting model with $\varepsilon = 12$ MeV. For very light fragments $10 \leq A_f \leq 30$, the momentum shift is larger than predictions by the splitting model. This system is also inverse kinematics with the light target nucleus of Be, like as the present experiment with Ar + Be. Another reaction mechanism based on central collision may be dominant in the light mass region. The detail is discussed in the next subsection.

The systematics of momentum peak shift measured in the other experiments at lower and higher energies than our experiment are well reproduced by our formula based on the splitting picture.
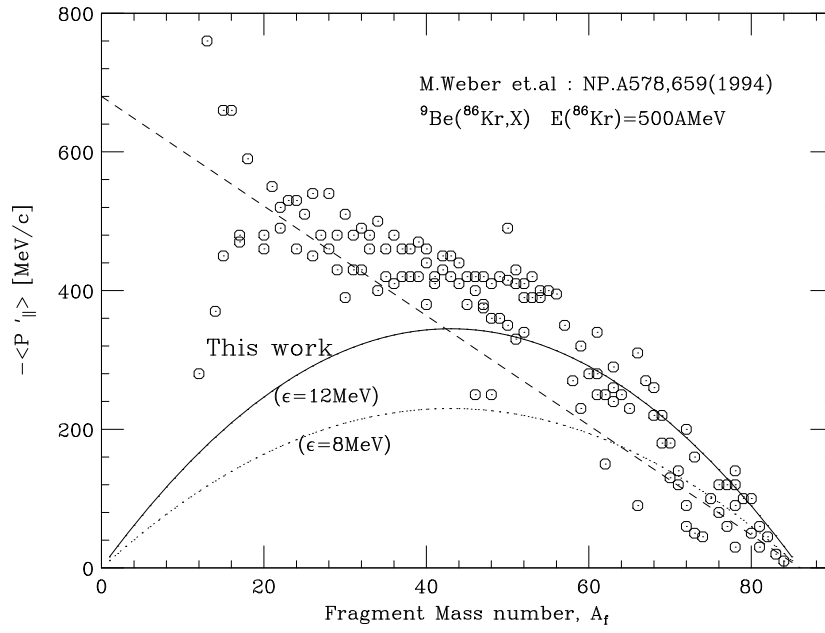
Figure 5.2: Momentum peak shift for high energy experiment [94]. The splitting model (solid line) shows good agreement in $\varepsilon=12$MeV.

Acceleration phenomenon

We discuss the acceleration phenomenon of the data using the Be target. As described in Section 4.2.1, the most probable velocity of very light isotopes ($A_f \lesssim \sim 13$) is larger than the beam velocity. The acceleration effect cannot be explained by a fragmentation model based on the abrasion-ablation picture, in which the projectile always loses the kinetic energy in the laboratory system for abrasion process of nucleons.

The acceleration phenomenon may be peculiar to the ^{9}Be(^{40}Ar, X) reaction, namely inverse kinematics. We have the evidence of the phenomenon observed only in the case of light target nuclei like ^{9}Be. The results of the Be and Ta targets are shown in Fig. 4.5. No acceleration effect was found in the Ta target data.

By comparison between both targets, we found two particular features of momentum distributions for light fragments produced in the Ar+Be reaction. One feature is the acceleration phenomenon. The other feature is the existence of LE-component. In Appendix D, we show the discussion about the LE-component in details. Both phenomena coincide in our data. Therefore, the acceleration phenomenon may be related to the LE-component.

F.Auger et al. [88] suggested that the light fragments in ^{86}Kr+C and ^{86}Kr+Al collisions originate from the splitting of a composite system. As shown in Fig. 5.3, two components of velocity around the CM velocity of the compound system are clearly seen. At the experiment, the beam energy was relatively low, $35A$ MeV. So, the authors suggested that two fission-like-fragments may be produced from a highly excited compound system. In short, it is posibile that the LE-component and the accelerated HE-component comes from one source.

As shown in Fig. 5.4, the velocities of the LE-component observed in this work are not below but just on the CM velocity. In addition, the mean energy of HE- and LE- component is around $80A$ MeV. Thus, the observed phenomenon is different from the work of Ref. [88].

Then, we suggest two source model that the LE-component and the accelerated HE-component come from two sources produced in different reactions, respectively. One source is an excited compound system from projectile and target nuclei running on the CM velocity. The source emits light particles homogeneously in angular space

and becomes a fragment in the LE-component. On the other hand, the other source is a hot projectile. The hot projectile is formed by a strong impact of target nucleus to convert the kinetic energy of projectile nucleus to the internal energy for the excitation of projectile nuclus. The hot projectile decays to two components again, which consists of a faster component and a slower component than the projectile velocity, like the model suggested by F. Auger et al. This two source model predicts a third component in the momentum distribution of light fragments. Such third component was not observed in our data. After all, the origin of the acceleration phenomenon has not been understood so far.

Neither the acceleration effect or the LE-component were found in the Ta target data. The different situation from the Be target comes from the large impact parameter. For a fragment mass, the impact parameter in the Ar+Ta reaction is larger than in the Ar+Be reaction when the fragment is formed by the geometrical cut. The hot compound system is not produced in the peripheral collision with the large impact parameter. Therefore, the exotic phenomena may not be observed in the Ta target data.
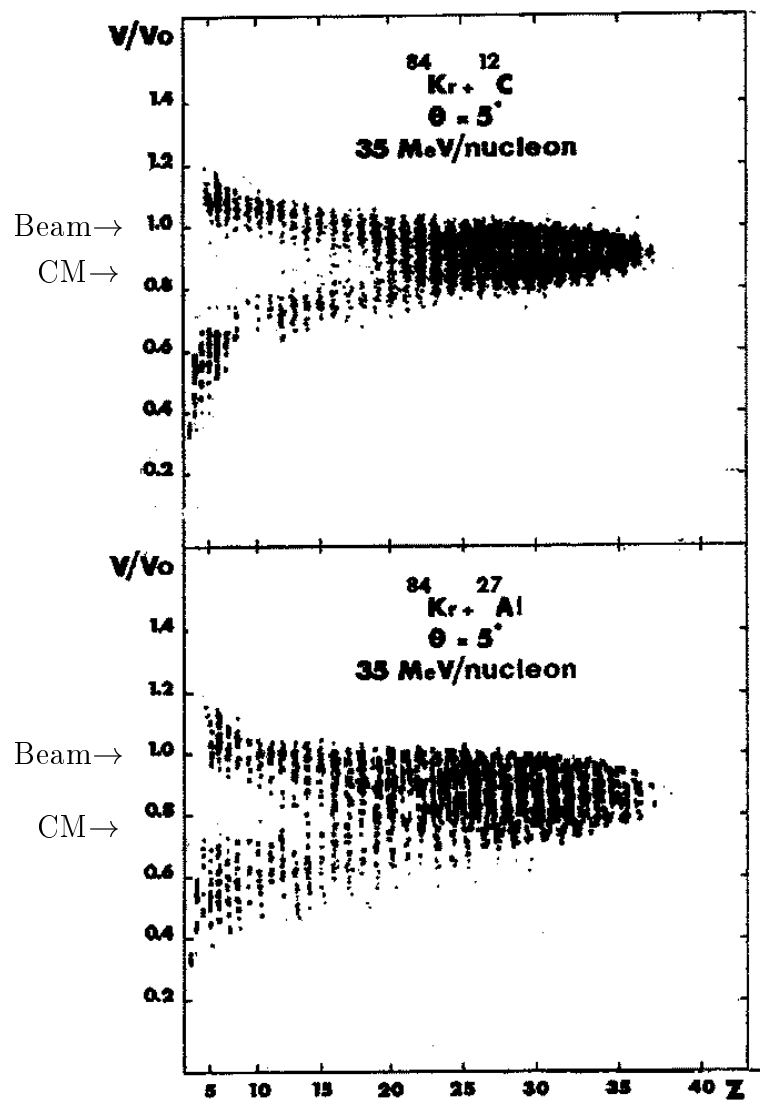
Figure 5.3: Two-dimensional velocity vs atomic number spectra in the ^{84}Kr$+^{12}$C and ^{84}Kr$+^{27}$Al reactions at $35A$ MeV, taken from [88].
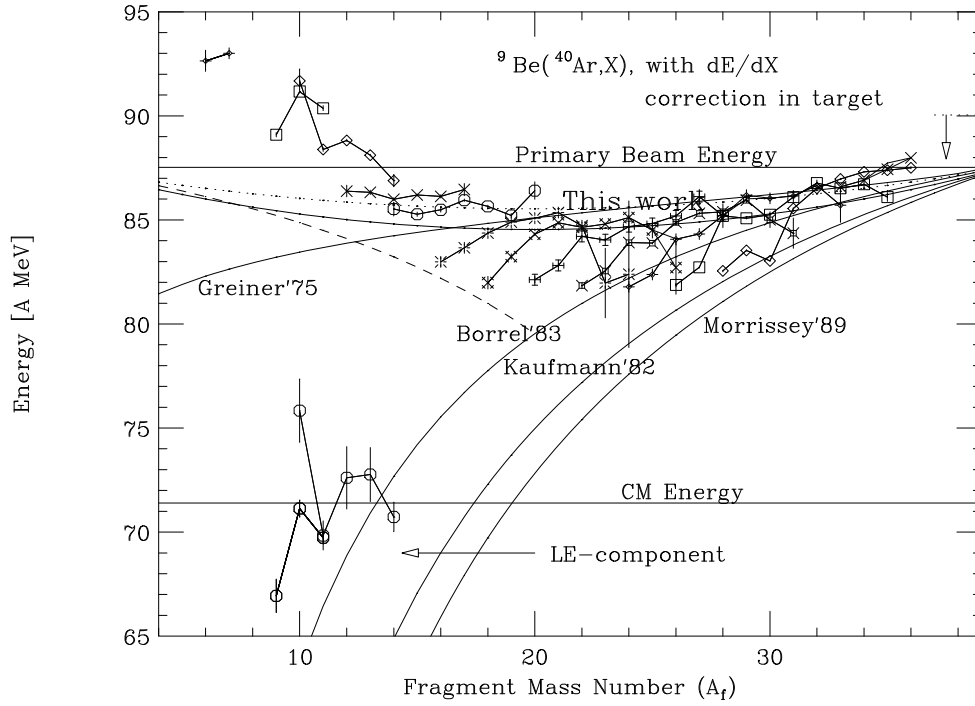
Figure 5.4: Peak value, P_0, of fragment momentum distribution for HE-component and LE-component.

5.1.2   Low Momentum Side Width

The low momentum side widths have been compared with the Goldhaber model. The results are summarized again as,

1. Simple increase of σ_L as a function of mass loss $\Delta A = A_p - A_f$
2. At the point of $\Delta A = 0$, $\sigma_L \neq 0$.

Only a few attempts have been made so far for the low momentum tail at intermediate energies. For analysis of low momentum tail with the $44A$ MeV Ar + Ni data, Ch.O.Bacri et al. have ever used an exponential tail function for the low momentum side [87]. The exponential width parameter show the similar dependence on A_f. The exponential width is parametrized as,

$$W_E(A_f) \;\; = \;\; p_1 \exp(\sqrt{p_2^2(A_f - p_3)^2 + p_4}) \tag{5.7}$$

where p_{1-4} are fitting parameters. The physical significance of the result has never been investigated.

Figure 5.5 shows momentum widths at low momentum side from the data using the (a) Be and (b) Ta targets. Since no LE-component was observed in the Ta data, we tried a linear fitting of the Ta target data. The fitting lines are drawn in both figures. The experimental results (σ_L) and the fitting lines are located far from a prediction of the Goldhaber model.

What is the origin of the large width of low momentum side? The large width is indeed produced by an energy-loss process in the nuclear reaction. The energy-loss process for σ_L may be different from the "pure" fragmentation process, because the width of low momentum side strongly depends on the beam energy. At relativistic energies, the momentum distribution becomes symmetric with $\sigma_L = \sigma_H$. For a low energy beam at $30A$ MeV, the large tail of low momentum side appears obviously [101]. Macroscopic friction process of nuclear dissipation is not the satisfactory mechanism for σ_L because the momentum peak P_0, which has no significant energy dependence, may also be changed at the same time.

The energy-loss process to produce the width of low momentum side may be explained by nucleon exchange reaction between target and projectile [58]. For instance, transfer mechanism adds one nucleon to the projectile or fragment, the energy per nucleon E may be changed as $E_{+1n} = E \cdot A/(A + 1)$, where A is the mass number before transfer reaction. The nucleon transfer may contribute the low momentum

tail. The velocity of projectile is reduced by the nucleon exchange reaction. When the projectile gives a nucleon to the target nuclei, the velocity of the remained nucleons in the projectile does not change significantly. Like the effect of momentum peak shift, the change of potential energy in projectile affects slightly the velocity of projectile nucleus. On the other hand, when the projectile pickups a nucleon from the target nuclei, the projectile velocity should be deduced because nucleons in target nuclei are much slow on average at the laboratory system. Thus, we suppose the nucleon exchange reaction as an origin of the low momentum tail.

Assumed that the probability of nucleon exchange is described as the Poisson distribution and the average of number of transfer nucleons in a reaction is quite small, the transfer process does not contribute the peak shift P_0 of fragment-momentum distribution but the large width of low momentum tail. If the probability of transfer process is small on average, the peak shift of fragment-momentum distribution, which is related to the case of no nucleon transfer, does not suffer from the transfer process to be independent of the beam energy. On the other hand, the low momentum width is sensitive to the transfer probability.

We next discuss the linear dependence of σ_L as a function of ΔA. First, we try to explain this dependence in terms of the surface abraded. If the transfer probability is proportional to area of the surface, the probability may be described as a symmetric function with respect to the half of projectile mass. However, the observed behaviour has a linear dependence. So, the abraded surface may not be directly related to the transfer process.

Secondly, we think about the overlap volume of projectile and target nuclei, i.e., total number of nucleons in the participant region (A-part). A-part has almost linear dependence as a function of A_f. Thus, the linear dependence of σ_L may be connected with A-part. We will discuss this picture later in Section 5.3.
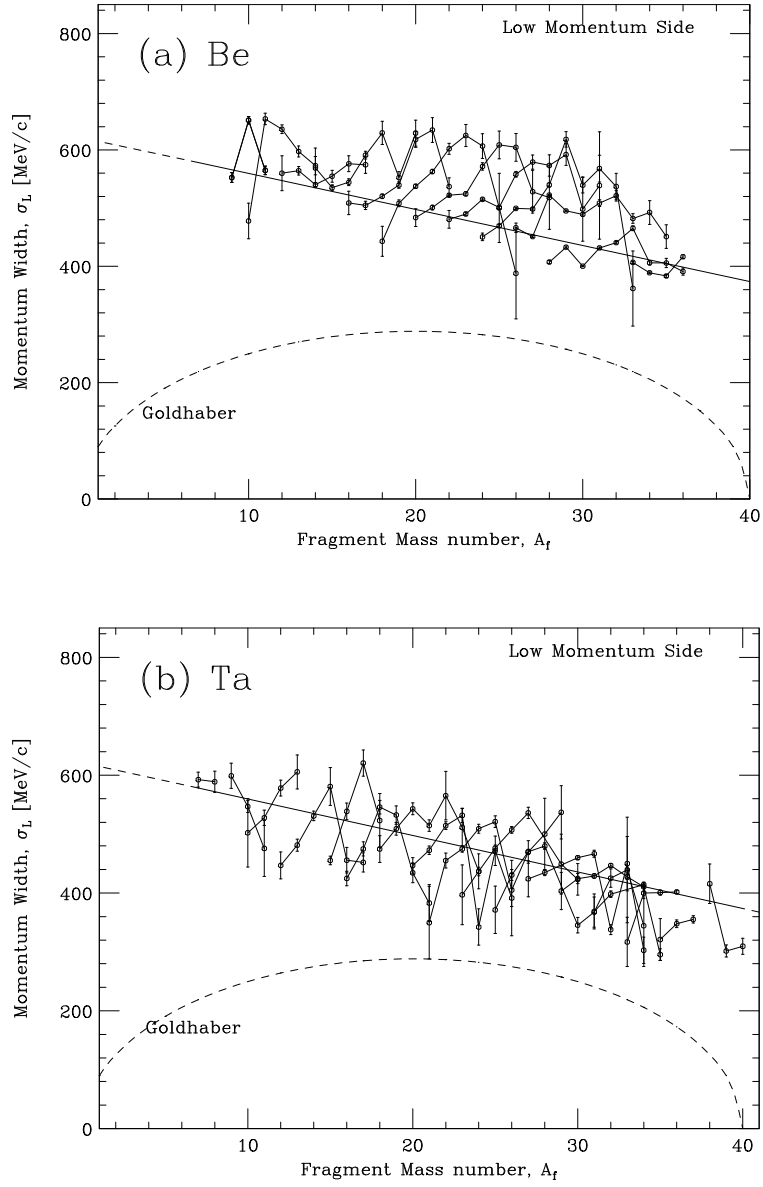
Figure 5.5: Momentum widths at low momentum side from the data using the (a) Be and (b) Ta targets. The solid lines in both figures are the linear fitting of the Ta target data. The experimental results (σ_L) and the fitting lines are located far from a prediction of the Goldhaber model. The isotope chains of experimental data are also drawn as solid lines.

5.2   Cross Sections

We discuss the systematics of isotope production cross sections in this section. In the previous chapter, the production cross sections of fragments were evaluated from the momentum distributions. We have already shown the target dependence of cross sections beyond the nuclear-size effect. The breaking of factorization (BOF) was confirmed in the production of very neutron-rich nuclei. We try to represent the systematics of cross sections by an empirical parametrization. As described in Section 1.1.2, the EPAX formula has been used for designing experiments with radioactive isotope beams for many years. We improve the EPAX formula using the measured cross sections.

First, we describe the framework of the EPAX formula. The EPAX function is represented as the product of mass yield and charge distribution. Secondly, the charge distribution of the cross sections for a fragment mass is obtained from our data. We renew the parametrization for the accurate cross section prediction for both of the targets. The most probable charge Z_{prob} and the slope parameter U in the charge distribution function are discussed. Thirdly, the predictive power of the new parametrization is displayed by using a recent report of ^{24}O experiment. Finally, we summarize the results of investigation for the systematics of isotope production cross sections in this section.

5.2.1   EPAX Formula

We review the EPAX formula briefly. The EPAX was developed by using data of the spallation reactions and heavy-ion induced fragmentation reactions at several A GeV. There are two kinds of versions for EPAX in the present time. In this thesis, we use the revised version EPAX2 [102]. The cross section of a fragment with mass A and proton number Z produced by projectile fragmentation from a beam (A_p, Z_p) impinging on a target (A_t, Z_t) can be written as,

$$\sigma(A, Z) \;=\; Y(A) \cdot W(A, Z) \tag{5.8}$$

$$W(A, Z) \;=\; n \cdot \exp(-R \cdot |Z_{prob} - Z|^{U}) \tag{5.9}$$

where $Y(A)$ represents the mass yield which is the sum of the isobaric cross sections for fragments with mass number A, and $W(A,Z)$ describes the charge distribution

which means the cross-section distribution of a given fragment mass which has a maximum peak at Z_{prob}.

The charge dispersion $W(A, Z)$ is described as R, Z_{prob} and U parameter. The most probable charge, Z_{prob}, is written as,

$$Z_{prob} = Z_\beta + \Delta + \Delta_m, \tag{5.10}$$

where Z_β is the β-stable charge for a fragment of mass number, A [74], Δ is a proton-excess between the stability line and the most probable line of fragmentation reaction, and Δ_m is the so-called "memory effect", i.e., the influence of the projectile N/Z ratio on the fragment N/Z ratio. The R is a function of fragment mass number, A, which shows a fragment mass dependence of a steepness controlling cross sections of isotopes from the stability line to the drip lines. The mass dependence has been confirmed from many combinations of projectiles and targets. The U parameter is a constant for all neutron-rich isotopes so far.

The EPAX formula has been also used for intermediate-energy experiments so far. The accuracy of the formula is good for many stable and unstable nuclei near the β-stability line. The assumptions of limiting fragmentation and factorization are valid for the production of such nuclei at intermediate energies.

The EPAX formula is valid for the "limiting fragmentation" regime, where the fragmentation process is no longer energy dependent. The energy dependence of fragmentation cross sections has been investigated by Silberberg and Tsao [67, 68]. We can see the similar energy dependence in the total reaction cross section. The total reaction cross section has been studied both theoretically and experimentally for more than 50 years. A detailed list of reference is found in Ref. [103]. Figure 5.6 shows the energy dependence of ^{12}C+^{12}C reaction cross sections. Compare the cross section at $90A$ MeV with $900A$ MeV, the difference of cross sections is about 30%. The difference of cross sections is nearly equal to the systematic error of measured cross sections in this work. Thus, we can assume that the limiting fragmentation hypothesis is valid in this work.

The EPAX formula follows the factorization hypothesis. The mass yield has a target dependence, however it is limited to the target nuclear-size effect. The charge dispersion $W(A, Z)$ is independent of the target nucleus. These relations imply that the EPAX formula follows weak factorization.

In this work, however, the BOF has been found in the production of very neutron-rich nuclei. An investigation of the charge distribution is necessary to find appropriate
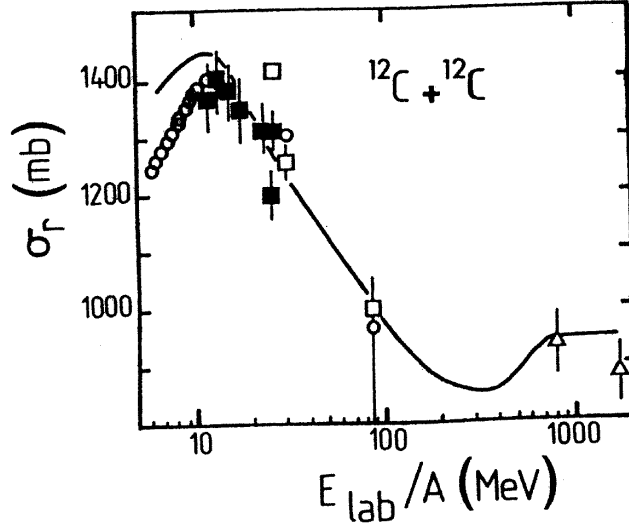
Figure 5.6: Reaction cross section for the ^{12}C+^{12}C system as a function of the incident energy per nucleon. The curve is a calculation in the eikonal approximation. From Ref. [104].

description for cross sections from our data. In the charge distribution of EPAX, the U parameter is a constant of 1.65 for neutron-rich side, and has no target dependence. The value of U parameter is very sensitive to the production cross sections of the isotopes far from the β-stability line. In the following section, we reduce the U parameter for each fragment mass with both targets from our data. At the same time, we investigate the target dependence of Z_{prob} since Z_{prob} is also sensitive to the cross sections of isotopes far from the β-stability line.

5.2.2   Charge Distribution

We make an attempt to fit the data with the EPAX function. The function is represented as the product of $Y(A)$ and $W(A, Z)$. The charge distribution $W(A, Z)$ is characterized with the most probable charge Z_{prob}, the slope constant U and the width parameter R. The R parameter has slightly fragment-mass dependence and an effect to the slope of charge distribution. We have two kinds of U parameters of U_p for proton-rich side and U_n for neutron-rich side. In the fitting procedure, the values of the U_p and the R parameters are fixed, originally given by the EPAX formula. The fitting procedure was performed with the experimental data of each fragment mass.

First, we obtain the maxima of the charge distribution $Z_{prob}(\text{EXP})$ as a function of fragment mass number from the experimental data with both targets. The values are compared with the EPAX ones, the β-stability line, and N/Z ratio of projectile nuclei. Next, the U parameters are deduced from the data when we assume the same parametrization of Z_{prob} for both of the targets.

Most Probable Charge Z_{prob}

We have investigated the target dependence of Z_{prob}. The measured cross sections for each fragment mass were fitted with $Y(A) \times W(A, Z)$. The mass yield Y is a constant for a fragment mass. Fitting parameters were U parameter in neutron-rich side, Z_{prob}, and the mass yield. Figure 5.7 shows the charge distribution of fragment mass 29, produced in Ar+Ta reaction. The Z_{prob} is obtained as $13.47\pm0.01(stat)\pm0.04(sys)$. Similarly, the Z_{prob} value for each fragment mass is deduced from our experimental data.

The experimental Z_{prob} is compared with the value from the EPAX formula. Figure 5.8 shows the deviation of $Z_{prob}(\text{EXP})$ from $Z_{prob}(\text{EPAX})$ for Ar+Be and Ar+Ta data. Solid lines are drawn to guide the eye. The EPAX reproduces the Z_{prob} very well, especially for the mass number between 20 to 35. The deviation of Z_{prob} is less than 0.2. Due to the lack of proton-rich side data, we obtained only three values of Z_{prob} for the Ar+Be data in A_f=18, 22 and 26. To compare both data of Be and Ta targets shows no significant target dependence of Z_{prob}.

Figure 5.9 shows the most probable charge in N/Z unit as a function of fragment mass for the Be and Ta targets. The most probable charge Z_{prob} from the EPAX is close to the β-stable charge Z_β. The ratio N_p/Z_p of the projectile is 1.22. For the composite system of projectile and target, the ratio is represented as $(N_p + N_t)/(Z_p + Z_t)$, of which values are 1.23 and 1.43 for Ar+Be and Ar+Ta, respectively. The $Z_{prob}(\text{EXP})$ is well described as the $Z_{prob}(\text{EPAX})$ as well as Z_β. The difference of $Z_{prob}(\text{EPAX})$ and Z_β is mainly the memory effect Δ_m. The memory effect is not clearly seen in our data.

No significant difference of $Z_{prob}(\text{EXP})$ between the Be and Ta targets has been observed, however the BOF has been found in the very neutron-rich nuclei. What does it mean? It should be noted that the BOF had never been found in the projectile fragmentation at other experiments. This fact is consistent with our observation of $Z_{prob}(\text{EXP})$ for the Be and Ta targets. To understand the charge distribution, we

show the Z_{prob} of projectile-like fragments produced by the reactions at low and intermediate energies.

At low energies, the most probable charge shows the existence of two different reaction mechanisms. A typical contour plot of isotope yields in the fragment mass and energy plane is shown in Fig. 5.10. The Cl isotopes are produced in $7A$ MeV ^{40}Ar$+^{50}$Ni reaction. We clearly see two areas, one corresponding to quasi elastic reactions centered at a high energy and a mass of 39. The second one is centered around a mass of 36 and a small kinetic energy. The most probable charge obtained from the mass number is near the N/Z of both projectile and composite system which corresponds to the quasi elastic and deep inelastic reactions, respectively [105]. An intermediate composite system has been shown as the result of a complete damping of the relative motion between the projectile and target nuclei. The projectile-like fragments are produced via binary nuclear system that collective effects dominate. On the other hand, at high energies, the process is dominated by individual nucleonic collisions that described as participant-spectator models. The values of most probable charge distinguish the reaction mechanisms to produce the projectile-like fragments.

At intermediate energies, D.Guerreau et al. [59] reported the observation of the systematic shift of isotope distributions between two targets. The isotope distributions of fragment yield were measured in ^{40}Ar+Ni and ^{40}Ar+Au reactions at $44A$ MeV. The systematic shift of the isotope distributions for a given element of Si in ^{40}Ar+Au reaction was observed about 0.3 mass unit towards the neutron rich side. However, their result is different from our data. The fitting results of our charge distributions have shown no significant difference of Z_{prob}(EXP) between the Be and Ta targets.

Figure 5.11 shows the target dependence and energy dependence for the isotope production yields of silicon isotopes from the ^{40}Ar fragmentation. The fragment yields are normalized as the sum of them is 100%. At less than $10A$ MeV, the most probable Z shifts close to the A/Z for the composite system of projectile and target nuclei. The production cross sections by $213A$ MeV Ar + C reaction show typically characteristic peak of projectile fragmentation at Z_{prob}. The results of $44A$ MeV and $90A$ MeV reactions resemble the high energy ones in the mass number of the most probable peak. The fact indicates that the projectile fragmentation reaction is dominant in the intermediate energies. The Z_{prob} is independent of target nuclei and beam energy, in the region of more than $44A$ MeV. We have already found that the

factorization assumption is invalid for production of neutron-rich nuclei. In Fig. 5.11, our data show the difference of cross sections of neutron-rich isotopes between Be and Ta targets. The difference of cross sections are larger and wider towards the more neutron-rich side ($^{31-34}$Si). The $44A$ MeV Ar data also show the same behaviour for both the Ni and Au targets. In the two energies of $44A$ MeV and $90A$ MeV, the target dependence of cross sections is represented with the change of steepness in the charge distribution. Thus, we would seek for the origin of target dependence in the slope constant U. Due to the breakdown of factorization, the U may change from a simple constant to a complex parameter which depends on target nuclei.

Slope Parameter U

As the target dependence of Z_{prob} has not been found, we assume now that the Z_{prob} can be described as the EPAX formula for both of the targets. We make an attempt to fit the data with the function of charge distribution. Fitting parameters were U in neutron-rich side and mass yield Y, and fragment mass dependence of U is tried to be obtained. The fitting procedure is performed for the data of each fragment-mass group, where every 4 mass units are combined to avoid poor statistics.

Figure 5.12 shows the U parameters as a function of fragment mass for both targets. We plot the values with the systematic errors. The slope parameter U of EPAX is a constant of 1.65 (dashed lines). The average of U is 1.62 for the Ta target. The smaller U gives larger values of production cross sections for neutron-rich nuclei. On the other hand, the U parameter of Be target is larger than 1.65 and shows fragment mass dependence. As shown in Section 5.2.1, the cross sections factorize for production of β-stable nuclei. Our data demonstrate the breakdown of factorization for very neutron-rich nuclei as the target dependence of U parameter.
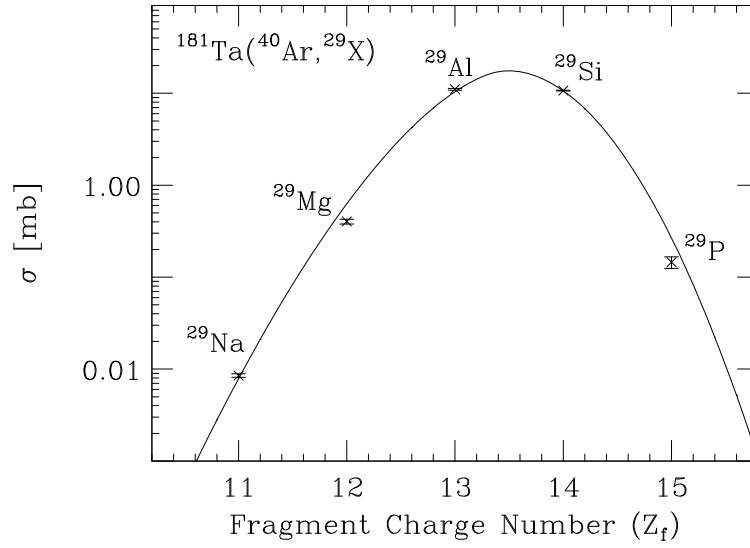
Figure 5.7: Charge distribution for $A_f=29$.
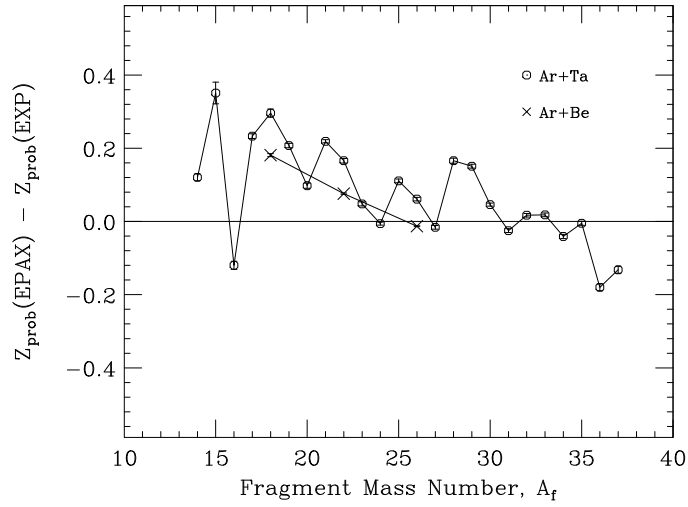
Figure 5.8: Deviation of the most probable charge from the EPAX parametrization to experimental data for the production targets of Be and Ta.
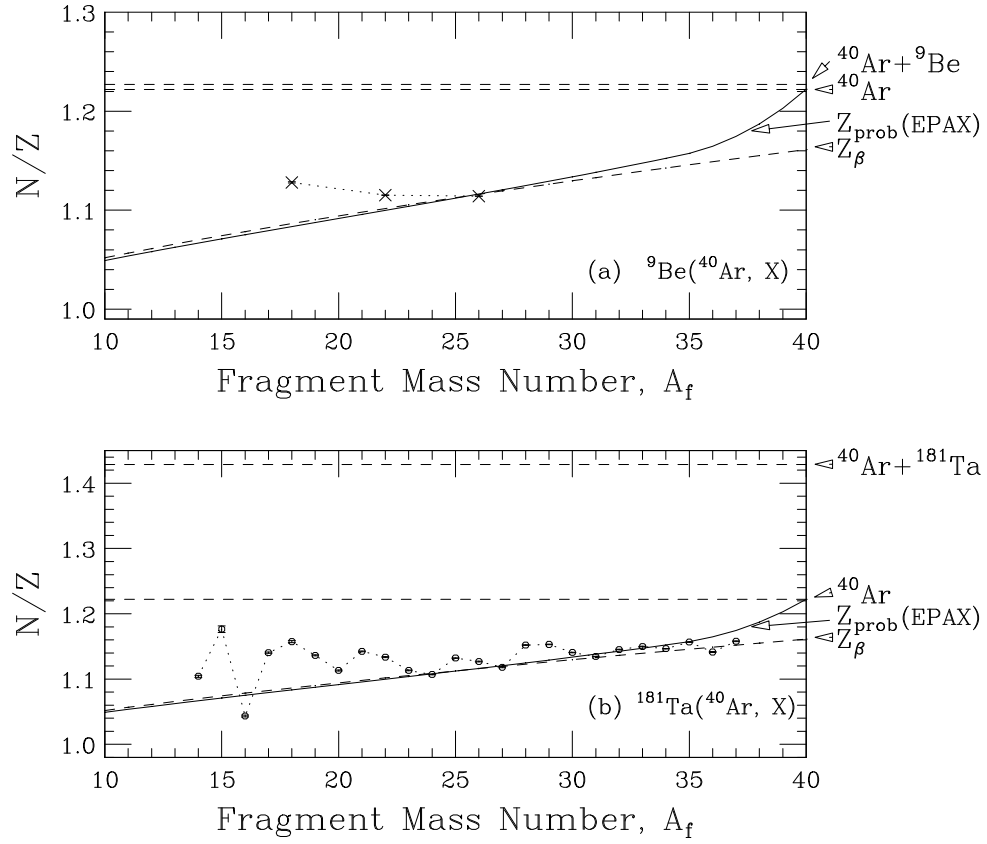
Figure 5.9: Peak of charge distributions as a function of fragment mass for the production targets of (a) Be and (b) Ta. The solid curves are the most probable charge Z_{prob} of EPAX. The dashed curves are the β-stable charge Z_β. The dashed lines are the N/Z ratio of ^{40}Ar projectile and compounds of ^{40}Ar+^{9}Be and ^{40}Ar+^{181}Ta, respectively.
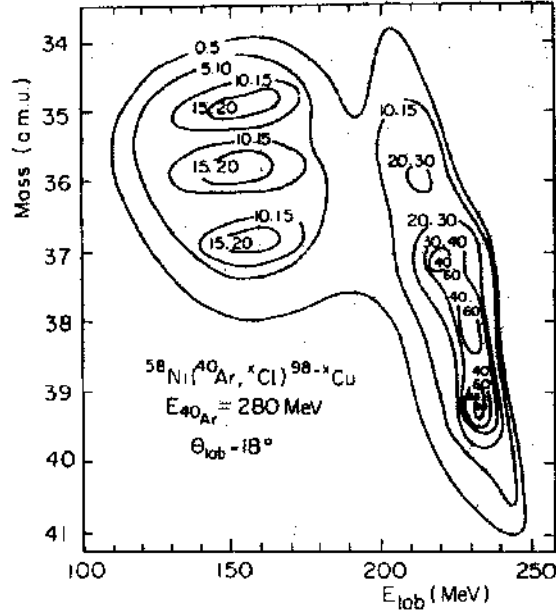
Figure 5.10: Contour plot of the Cl isotope yields ($a.u.$) in the M, E plane in the reaction ^{40}Ar (7.0A MeV) + ^{50}Ni (from [106])
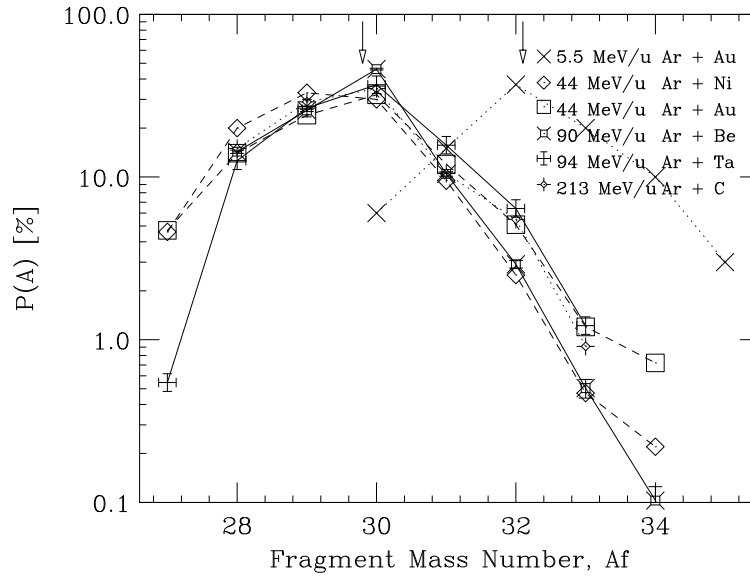
Figure 5.11: Comparison of silicon production from 5.5A MeV Ar+Au (Ref. [107]), 44A MeV Ar+Ni and Ar+Au (Ref. [59]), and 90A MeV Ar+Be and 94A MeV Ar+Ta (this work), and 213A MeV Ar+C (Ref. [31]).
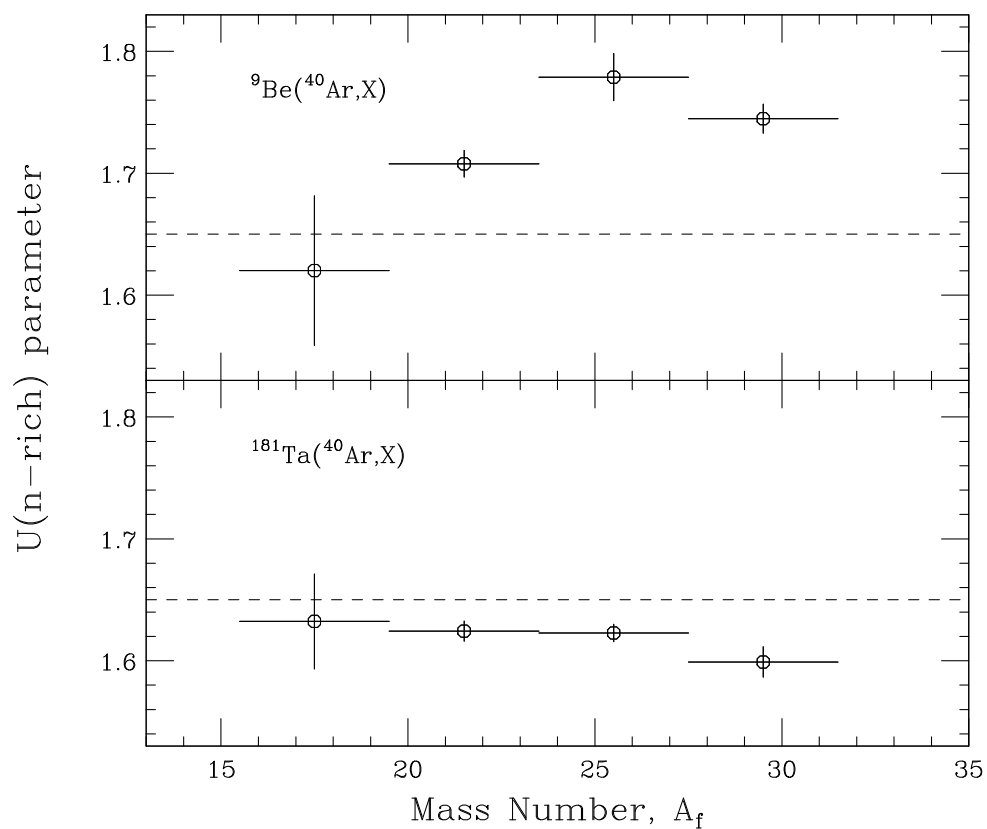
Figure 5.12: *U* parameters as a function of fragment mass for the production targets of Be and Ta. On the assumption that the value of *U* is same for. every group of four sets of A_f data, the fitting results are shown with the systematic error. The dashed lines are the values of *U*=1.65 from the EPAX.

5.2.3   Predictive Power of the New Parametrization

We have obtained the modified EPAX formula for the nuclear fragmentation at an intermediate energy for both Be and Ta targets.

To confirm the validity of our parametrization, we show an example of the production cross section predicted for extremely neutron-rich nuclei. Figure 5.13 shows the predictive power of the new parameterization. The dashed and solid curves are the charge distribution for mass-24 isotopes produced in ^{40}Ar+^{9}Be and ^{40}Ar+^{181}Ta reactions, respectively. The solid box is the cross section of fragmentation channel for ^{181}Ta(^{40}Ar,^{24}O). The data was not measured in this experiment. The experimental data agrees with our new parametrization clearly.
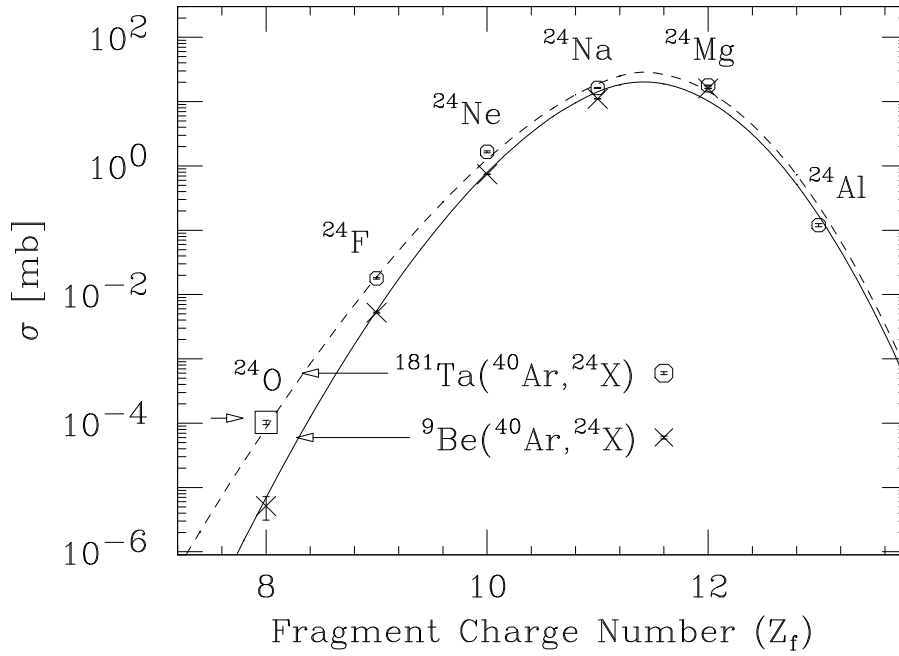
Figure 5.13: Predictive power of cross sections of the new parametrization. The solid box is the data of ^{24}O with a tantalum target taken from Ref. [108].

5.2.4   Summary

The target dependence of cross sections has been investigated systematically and the EPAX parametrization has been modified to reproduce the BOF for very neutron-rich nuclei. We summarize the results of investigation for the systematics of isotope production cross sections as follows,

1. The cross sections obtained in this work show the violation of factorization in the production of very neutron-rich nuclei using the Be and Ta targets. Since the EPAX formula follows factorization exactly, we cannot apply the original formula to predict the production cross sections of very neutron-rich nuclei.

2. To investigate the BOF quantitatively, we examined the EPAX parametrization, especially the charge distribution $W(A, Z)$. We focus the most probable charge Z_{prob}, and the slope parameter U which is constant so far in the EPAX formula. As a result of data fitting to $W(A, Z)$, no significant difference of Z_{prob} between the Be and Ta targets has been observed. It is inconsistent to the report of D. Guerreau et al. We found that the Z_{prob} is not shifted towards the neutron rich side even in the case of neutron-rich target (^{181}Ta).

3. To obtain the U parameters as a function of fragment mass, the data were fitted to the charge distribution $W(A, Z)$ by assuming the Z_{prob} given by the EPAX. We found that the slope parameter U depends on the target nuclei, and may have fragment mass dependence for the Be target. The results of our experiment show that the U parameter is dependent on target nuclei at least.

On the basis of the results, we discuss the mechanism of prefragment production by projectile fragmentation reactions at intermediate energies in Section 5.3.

5.3   Mechanism of Prefragment Production

We have investigated the nuclear fragmentation reaction in nucleus-nucleus collisions
at intermediate energies. The momentum distributions of projectile-like fragments
have been measured for a wide range of fragment mass including very neutron-rich
nuclei. The charge distributions of fragment cross sections from the Be and Ta targets
have revealed the breakdown of factorization (BOF) for very neutron-rich nuclei. In
order to explain the origin of BOF, we discuss the mechanism of prefragment pro-
duction in terms of the abrasion-ablation scheme (AA model). In the AA model, the
production cross section of a final fragment is determined by the charge distribution
and the excitation energy of prefragments.

First, we discuss the charge distribution of prefragments on the basis of AA model.
The abrasion model is a macroscopic description which gives a picture of a clean cut
of the projectile nucleus by the target nucleus [39]. The concept of geometrical
separation in an overlap or participant zone does not specify its proton-to-neutron
ratio. A few different methods to calculate the charge distribution of the prefragments
are proposed so far. First, Ref. [61] suggested that the proton-to-neutron ratio of the
prefragment is exactly that of the initial projectile nucleus, which corresponds to
a situation where the removed nucleons are completely correlated. Secondly, the
opposite opinion was suggested that every nucleon removed has a statistical chance
to be a neutron or a proton as determined by the proton-to-neutron ratio of the initial
projectile. Assumed that both protons and neutrons are uniformly distributed over
the initial projectile, the probability factor may be describes as

$$P(a) \;=\; \frac{\dbinom{Z_p}{z}\dbinom{N_p}{n}}{\dbinom{A_p}{a}}, \tag{5.11}$$

where the mark of $\dbinom{Z_p}{z}$ is the combinatorial which gives the number of ways of
choosing z out of Z_p, where Z_p, N_p, and A_p are the numbers of protons, neutrons,
and nucleons in the initial projectile, respectively, while z, n and a are the numbers
of the corresponding particles removed from the projectile. This hypergeometrical
model corresponds to the extreme situation of no correlation among the nucleons
during the abrasion process [33]. Thirdly, Morrissey et al. [44] proposed that the
charge distribution of the prefragment is given by the fluctuation of the proton-

to-neutron ratio of the giant dipole resonance (GDR). This model corresponds to an intermediate situation between the two preceding cases. After all, the charge distribution of prefragments from these methods depends on the projectile nuclei but has no target dependence.

Next, we discuss the excitation energy of prefragments. In an old model [13], the average excitation energy of a prefragment after abrasion was estimated from the additional surface energy due to the excess surface area. Several studies have been made on the source of the excitation energy [70, 45, 47]. According to the researches, the surface energy is not the main source of the excitation energy, but, one of the energy sources for prefragment excitation. At least, the target dependence of the excitation energy can be seen in the surface energy. Figure 5.14 shows a schematic view of prefragment production. The prefragments of the same mass number A_f' are produced by the projectile fragmentation reaction with target nuclei of different nuclear radius. If a target nucleus has a large size, the impact parameter is also large to produce the prefragment (case A). On the other hand, the small size of a target nucleus caused the violent collision to form the prefragment with the same mass number (case B). In the geometrical model, we calculate the surface energy of prefragments in Ar+Be and Ar+Ta reactions. Figure 5.15 shows the additional surface energy (E_s) of prefragments as a function of the mass number for the Be and Ta targets. Large difference of E_s is presented for both of the targets. As for the prefragments of $\Delta A = 20$, the values of E_s are approximately 90 MeV and 10 MeV for the Be and Ta targets, respectively. The target dependence of prefragment excitation energies stems from the additional surface energies in the AA model.

We tried to find the target dependence of excitation energies of prefragments in our experiment. Assumed that nucleons are emitted homogeneously from the hot prefragment in the ablation process, the velocity of a prefragment does not change on average when it becomes the final fragment. The results of momentum peak shift show that the energy losses in the fragmentation process for the fragment of $\Delta A = 20$ were 60~80 MeV for both of the targets (see Section 4.2.1). The energy losses are not correlated to the additional surface energies on the calculation. Furthermore, no significant target dependence of momentum peak shift was found in the data for the projectile-like fragments of $A_f \geq 20$. Thus, we cannot say easily that the BOF for very neutron-rich nuclei originates from the target dependence of surface energies of prefragments.

As shown in Section 1.1.2, the difference of prefragment excitation energies in the models gives quite a small change of the charge distribution of final fragments. We discuss the reason to keep the charge distribution so stiff. The charge distributions of our data were fitted with Eq.(5.9). The results exhibit the bell-shaped form which has a peak at Z_{prob} located near the β-stability line. Hüfner suggested that the key to understand the data is the following universality: charge distribution curves do not depend on the reaction dynamics, nor on the target, projectile or beam energy. Campi et al. [41] take an extreme thermodynamic point of view: independent of the earlier steps of the reaction, one always forms some intermediate excited prefragments, which decay into the particle stable observed fragments via evaporation. The basic assumption in evaporation is that all transition matrix elements are the same and each level is populated with the same probability. This assumption also holds for the last step of the evaporation chain. Thus, all particle stable levels of the observed fragment are populated with the same probability. This is why the cross section to find a particular fragment N, Z is proportional to the number of its bound levels as follows,

$$\sigma(N, Z) \quad \propto \quad \int_{E_0(N,Z)}^{E_{th}(N,Z)} \Omega(E, N, Z) dE, \tag{5.12}$$

where Ω is the level density and E_0 and E_{th} are the position of the lowest threshold energy for particle emission, respectively. As Ω increases exponentially with E, the integral is dominated by the behaviour at $E \cong E_{th}$ as,

$$\sigma(N, Z) \quad \propto \quad \Omega(E_{th}(N, Z), N, Z) \propto \exp\{S(E_{th}, N, Z)\}, \tag{5.13}$$

where S is the entropy function which is the logarithm of the level density. Although the thermodynamic model is based on an idealized picture, the stiffness of bell-shaped charge distribution is well explained.

As the breakdown of the universality, we have already known two phenomena, i.e. the memory effect and the BOF for very neutron-rich nuclei. The memory effect is observed in the production of heavy fragments close to the projectile mass. This fact implies that the number of removal nucleons are related to the memory effect. The memory effect may come from insufficient excitation energies of prefragments. Due to the small number of removed nucleons, a prefragment close to the mass of a neutron-rich or proton-rich projectile nucleus cannot be heated up to the excited states for particle emission to decay toward the β-stable nuclei [110]. On the other hand, the

BOF has been found for very neutron-rich nuclei in a wide range of fragment mass. Even if the excitation energy of prefragments increases a little, the charge distribution does not change easily, at least near the β-stability line. Actually, by our modified EPAX, the most probable Z_{prob} does not depend on the species of target nuclei. Thus, we cannot deny the possibility that the BOF originates from the target dependence of the charge distributions for prefragments except the excitation energies.

To apply this idea to the BOF problem, we suggest two mechanisms of a fluctuation giving for the charge distributions of prefragments. One is the nucleon exchange process during the fragmentation process, and another is the effect from the difference of nucleon-nucleon total cross sections (σ_{pp},σ_{nn} and σ_{pn}).

We found the nucleon exchange process during the fragmentation process in our data. The fitting results of P_0 and σ_H carry the information at the abrasion stage and supporting that "pure" projectile fragmentation is a dominant process at intermediate energies. As for σ_L, the larger values of σ_L than σ_H may be related to the energy loss due to the transfer process. Unlike the behaviour of σ_H, σ_L has a linear dependence as a function of fragment mass. The linear dependence may be connected from both projectile and target nuclei. So, the source of transferred nucleons can be assumed to be the participant region. Since the Ta target nucleus is more neutron-rich than the Be, the probability of neutron transfer should be large. The nucleon exchange reaction between projectile and target nuclei during the abrasion process may break the factorization of fragment production cross sections.

The difference of the total cross sections between proton-to-proton (σ_{pp}) and proton-to-neutron (σ_{pn}) may bring the fluctuation of prefragment charge distributions. Figure 5.16 shows the energy dependence of the total cross sections in nucleon-nucleon collision. The σ_{np} is larger than the σ_{nn} and σ_{pp} when the nucleon energy is less than 500MeV. In projectile fragmentation process, a neutron-rich target nucleus easily knocks out protons in the projectile nucleus, so that the production of neutron-rich prefragments is promoted.

The discussions so far are qualitative. However, they gives several predictions. First, if the nucleon exchange process is just the reason of BOF, the probability of nucleon exchange reaction becomes large at low energies. The nuclear fragmentation experiments with lower incident beam energies than at our experiment may reveal the large BOF effect for very neutron-rich nuclei. Secondly, if the difference of N-N reaction cross sections causes the BOF, the nuclear fragmentation experiment with

100-800A MeV beams should be carried out to confirm the BOF for very neutron-rich nuclei. Since the cross section curves of σ_{pp} and σ_{pn} cross at $500A$ MeV, the difference of U-parameter between the Be and Ta targets might change to be reversed.

The experiments mentioned above give an answer of the question: what kind of combination in projectile nuclei and target nuclei, and incident beam energy should we choose for the efficient production of a radioactive isotope beam? The quantitative discussions are of course necessary for further investigations.
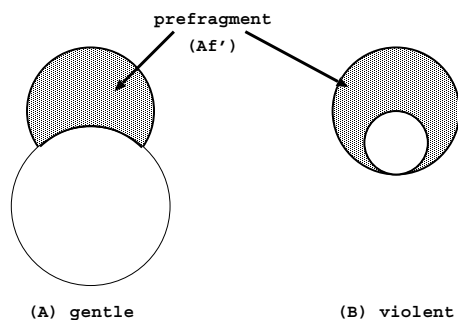
Figure 5.14: A schematic drawing of prefragment production. The prefragments of the same mass number (A_f') are produced by projectile fragmentation reaction with target nuclei of different nuclear radius. For the large target nuclei, the large impact parameter leads to (A) gentle reaction, and (B) violent reaction is expected for the small impact parameter with the small target nuclei.
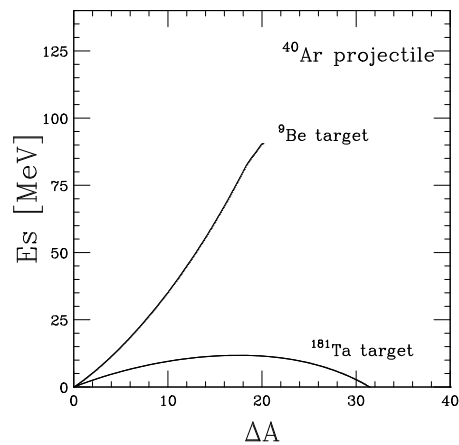
Figure 5.15: Excitation energy to the surface excess (E_s) for removal of ΔA nucleons. Large excitation energy is caused by Be target due to the violent collision.
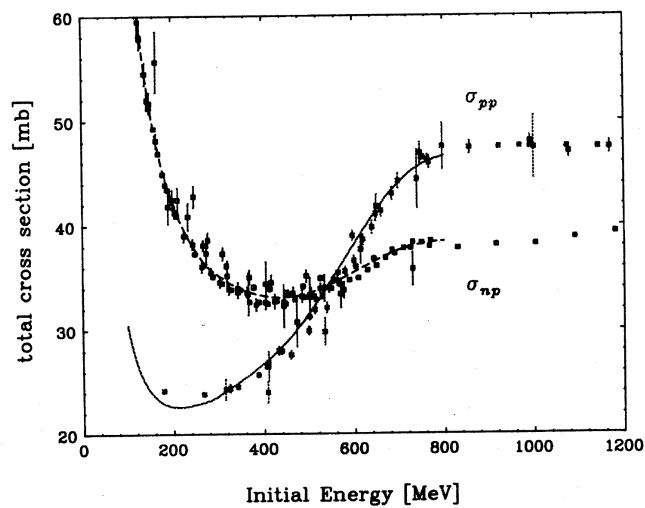
Figure 5.16: The total cross section σ_{pp} (σ_{np}) of the p + p (n + p) reaction as a function of the initial laboratory energy of protons is indicated by solid (dashed) line, taken from Ref. [109].

Chapter 6

Conclusions

Since the discovery of projectile fragmentation reaction, many kinds of radioactive isotope beams have been available for nuclear physics experiments. Radioactive isotope beams brought the discovery of new forms of nuclei such as the neutron halo and the neutron skin. Concerning the production and separation techniques of radioactive isotopes, an in-flight method with a magnetic spectrometer is very useful. A wide range of radioactive nuclei are produced as projectile fragments or fission fragments. The secondary beam can be selected from the fragments by a magnetic spectrometer efficiently. The intense heavy-ion beams from cyclotron accelerators are useful to produce high-isospin nuclei via projectile fragmentation reactions at intermediate energies.

The design of experiments is performed seeking for efficient production of radioactive isotopes to be studied. For this purpose, the production cross sections are estimated by use of the abrasion-ablation model and the semi-empirical formula EPAX. However, the predictive power of these methods is not good enough for very neutron-rich nuclei far from the stability line because the fragmentation data for such nuclei have not been acquired well so far.

To optimize the condition of radioactive isotope beams for experiments, understanding of the reaction mechanisms is very important. However, the reaction mechanisms have not been well known and any pictures for the mechanisms have not been established, especially for the production of very neutron-rich nuclei using the heavy-ion beams at intermediate energies. At relativistic energies, the momentum distribution of projectile fragments was found to have a symmetric shape like a Gaussian function. The production cross sections of fragments are independent of projectile energy in the range 1-2A GeV and vary only slowly with target mass. These

observations suggest that the applicability of the concepts of "limiting fragmentation" and "factorization", respectively. On the other hand, at intermediate energies, the momentum distributions of fragments have an asymmetric shape with a tail at low momentum side. For the very neutron-rich fragments, the production yields are larger in heavier target nuclei beyond the target-size dependence of cross sections. This target dependence of production yields may imply a breaking of the factorization hypothesis. In such situations, further experimental works of projectile fragmentation reactions have been required for many years.

The aim of this thesis is the investigation of reaction mechanisms for projectile fragmentation at intermediate energies. We focused the target dependence of momentum distribution of projectile fragments. The measurement of momentum distributions of projectile fragments was performed for wide range of isotopes even far from stability line. From the experimental data, the target dependence of isotope production cross sections was confirmed.

We performed the projectile fragmentation experiment using a 90-94A MeV ^{40}Ar beam at RIKEN-RIPS. In order to study the systematics of asymmetric shape of momentum distributions at intermediate energies, we measured the momentum distribution of fragments emitted at 0°. To confirm the target dependence of the production cross sections for each isotope systematically, we used two targets of Be and Ta. The target thickness was determined by considering the following points. First, the target thickness was optimized to earn yields of isotopes far from the stability. Secondly, the maximum target thickness is set to measure the "raw" momentum distribution without large distortions originating from target thickness due to the different energy loss between the primary beam and fragments. We prepared the primary beam intensity monitor with less than 10% errors in the wide range of several orders for normalization of fragment yields. The measurement of fragment momentum distributions was carried out by sweeping magnetic fields of RIPS.

The particle identification was performed using the TOF-ΔE method by using silicon detectors and a plastic scintillation counter. By analysis of the TOF-ΔE, we determined the mass-to-charge ratio A/Z and the atomic number Z of fragments. Fragment yields were obtained by counting the isotopes in the scatter plot of the A/Z-Z plane. Momentum distribution of each isotope was obtained from the fragment yields for the various magnet settings of RIPS.

The typical momentum distributions have one component described as a Gaussian-

like function which includes an asymmetric part in the low momentum side although two components were found in the Be data for very light fragments. The momentum distributions of fragments have been fitted with an asymmetric Gaussian-like function to deduce the most probable momentum and the widths for high and low momentum side from the asymmetric shapes. The production cross sections of fragments were evaluated from the momentum distributions with the fitting results. The target dependence of cross sections was investigated with the results of our data. Our experimental results are summarized as follows.

1. We found two features in the momentum peak shift. First, the maximum of momentum peak shift was observed for the fragments around $A_f = 20$. This behavior is called hereafter 'parabolic mass dependence of momentum shift'. Secondly, the acceleration phenomenon was observed in light fragments only for the Be target. For the projectile-like fragments $A_f \geq 20$, no significant difference between both targets was observed in the momentum peak shift.

2. The high momentum side widths σ_H of all the observed fragments were compared with the Goldhaber model. The reduced width σ_0=90 MeV/c is consistent with high-energy experiments. No significant difference between both targets was observed in the high momentum side widths.

3. The low momentum side widths σ_L were found to be twice wider than σ_H approximately. The σ_L may have a linear dependence as a function of mass loss $\Delta A = A_p - A_f$, which is quite different from the parabolic feature of σ_H. Furthermore, another feature of the results should be noted. At the limit $\Delta A \to 0$, the σ_L may not converge on 0, but 300~400MeV/c. These observations of σ_L cannot be explained by the Goldhaber model. No significant target dependence of σ_L between the Be and Ta targets was found in our data.

4. The transfer-like fragments were observed at this experiment. These fragments have more neutrons or protons than the projectile nuclei. The measured momentum peak shows clearly a large shift toward low momentum side.

5. For the fragments $A_f > 20$, no significant target dependence of the momentum distributions was found in our data.

6. We investigated the validity of factorization assumption for both stable and unstable isotopes. For this purpose, the ratios of cross sections for a fragment in Ar+Ta reactions to that in Ar+Be reactions were obtained as a function of charge difference between the most stable charge and the fragment charge. The cross sections were normalized with experimental mass yield to eliminate the target size effect. The breakdown of factorization (BOF) was confirmed at very neutron-rich nuclei.

We tried to understand the results of momentum distributions. The momentum peak shift was compared with several formulae taken from reaction models. However, all of the formulae cannot predict the parabolic mass dependence. As the reaction mechanism, the splitting picture of projectile nucleus into two pieces was supported by the parabolic feature of momentum peak shift. We obtained the empirical formula based on the splitting picture. The acceleration phenomenon in the Ar+Be reaction was discussed in the point of view on the splitting of a composite system merged from the projectile and target nuclei. The low momentum side width was interpreted as a result of nucleon exchange reaction during the projectile fragmentation.

We investigated the systematics of isotope production cross sections and the EPAX parametrization, especially the charge distribution, has been modified to reproduce the BOF for very neutron-rich nuclei. The results of investigation for the systematics of isotope production cross sections as follows.

1. The cross sections obtained in this work show the violation of factorization in the production of very neutron-rich nuclei using the Be and Ta targets. Since the EPAX formula follows factorization exactly, we cannot apply the original formula to predict the production cross sections of very neutron-rich nuclei.

2. To investigate the BOF quantitatively, we examined the EPAX parametrization, especially the charge distribution $W(A, Z)$. We focus the most probable charge Z_{prob}, and the slope parameter U which is a constant so far. As the result of data fitting with $W(A, Z)$, no significant difference of Z_{prob} between the Be and Ta targets. It is inconsistent to the report of D. Guerreau et al. We found that the Z_{prob} is not shifted towards the neutron rich side even in the case of neutron-rich target (^{181}Ta).

3. To obtain the U parameters as a function of fragment mass, the data were fitted with the charge distribution $W(A, Z)$ by assuming the Z_{prob} of the EPAX. We found that the slope parameter U depends on the target nuclei, and may have fragment mass dependence for the Be target. The results of our experiment show that the U parameter is dependent on target nuclei at least.

The predictive power of the EPAX formula for both targets was improved via the re-parametrization. We can estimate the production cross sections even for very neutron-rich nuclei, e.g. ^{24}O.

In order to understand the physics underlying the BOF, we discussed the prefragment production in terms of a microscopic abrasion-ablation model (AA model). In the scenario of AA model, the fragmentation cross sections are determined by both charge distribution and excitation energy of prefragments. In the present models, the charge distribution has no target dependence. The excitation energy is described as an additional surface energy due to the excess surface area, however there are several different models for the excitation energy. We can find that the excitation energy has a target dependence which stems from the additional surface energies.

We tried to find the target dependence of excitation energy in our data. Assumed that nucleons are emitted homogeneously from the hot prefragment in the ablation process, we can observe the target dependence of excitation energy in the momentum peak shift. However, no significant target dependence of momentum peak shift was found in the data for the projectile-like fragments of $A_f \geq 20$. Thus, we cannot say easily that the BOF for very neutron-rich nuclei originates from the target dependence of additional surface energies of prefragments. We cannot deny the possibility that the BOF originates from the target dependence of the charge distributions for prefragments.

To apply this idea to the BOF problem, we suggested two mechanisms of a fluctuation giving for the charge distributions of prefragments. One is the nucleon exchange process during the fragmentation process, and another is the effect from the difference of nucleon-nucleon total cross sections (σ_{pp}, σ_{nn} and σ_{pn}). In order to understand the origin of BOF for very neutron-rich nuclei, we need another experiment of projectile fragmentation at low and high energies.

Acknowledgment

First, I would like to express my sincerely thanks to my supervisor, Prof. Masayasu Ishihara, who suggested me many ideas for physical models of reaction mechanisms in nuclear physics. He has given me continuous support,and encouragement. Special thanks are also due to Prof. Hiroyoshi Sakurai for contributing to every part of the experiment, analysis and for teaching me "everything" as a researcher studing the nuclear physics. I am also grateful to Dr. Sadao Momota from his collaboration for doing the fragmentation experiment and analysis.

I would also like to thank Dr. Z.Liu, Dr. S.M.Lukyanov and Dr. Yu.E.Penionzhkevich for working together. I was very impressed by their strong will to encounter any troubles during experiments.

I would like to acknowledge the many fruitful discussions with Prof. I.Tanihata, Dr. T.Kubo, Prof. T.Nakamura and Dr. K.Yoshida.

I would like to thank Dr. A.Ozawa, K. Kusaka and Dr. A.Yoshida for their helpful advices.

I also thank researchers and students in our office, Dr. M.Hirai, Mr. X.Y.Watanabe, Mr. K.Yoneda, Dr. H.Ogawa, Dr. B.Didier, Mr. H.Iwasaki, Mr. N.Fukuda, Mr. N.Imai, Dr. N.Aoi, Dr. T.Teranishi and Dr. E.Ideguchi for the good environment and nice atomosphere in doing research during my Ph.D study.

I would also like to express thanks to Dr. H.Okuno, Dr. S.Ito, Dr. N.Inabe and Prof. K.Suzuki and many researchers in RIKEN, for their many fruitful discussion.

Appendix A

# Doubly-Differential Cross Sections

The fitting results of the momentum distributions were tabulated for the projectile-like fragments produced in the fragmentation of ^{40}Ar using the Be and Ta targets.
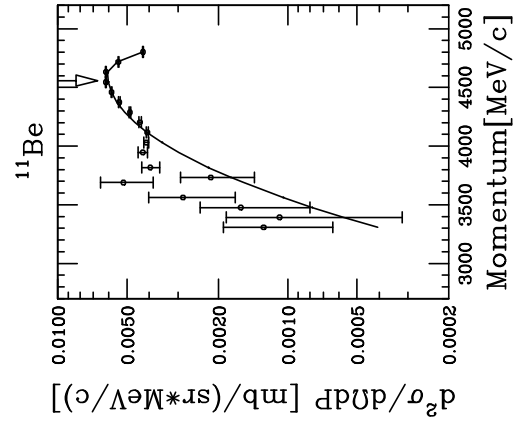
The momentum distributions of fragments were fitted with the asymmetric Gaussian-like functions for the high-energy side of the peak. The fitting procedure are described in Section 4.1. First, the momentum distributions are shown with the fitting results. Secondly, the results of fitting parameters, A, P_0, σ_H and σ_L are tabulated.

A.1   Results of Be Target Data

The momentum distributions of fragments produced in Ar+Be are shown with the fitting results with the Type-II function.

A.1.1   Momentum Distributions of Be Target Data
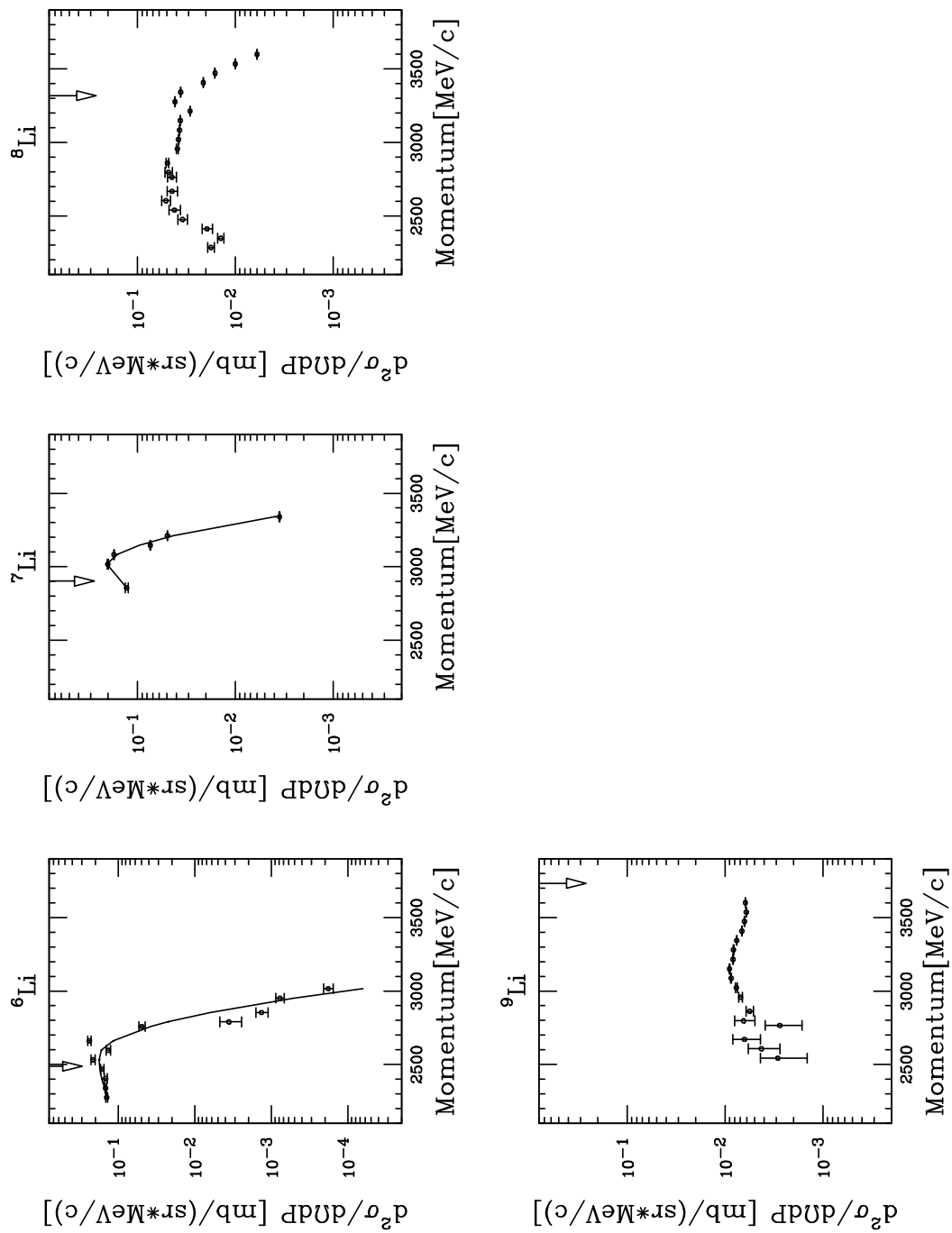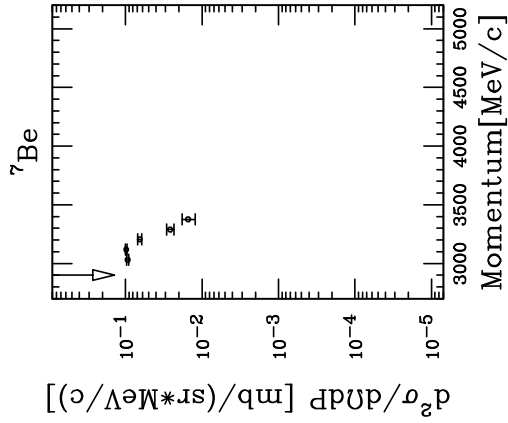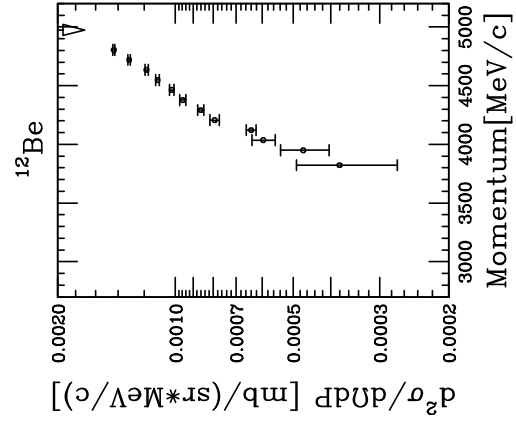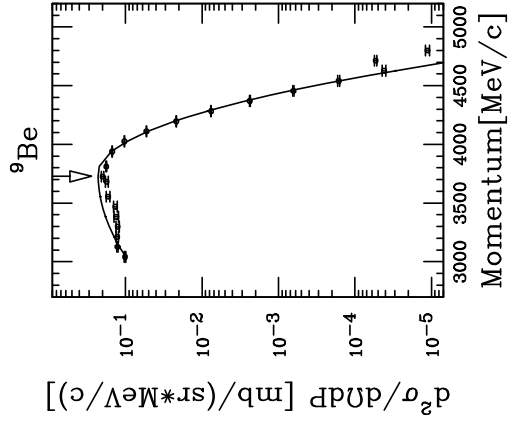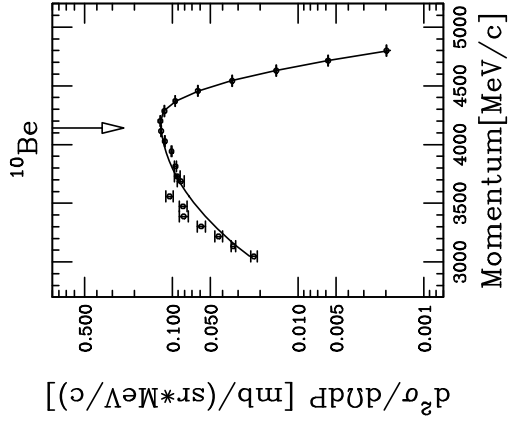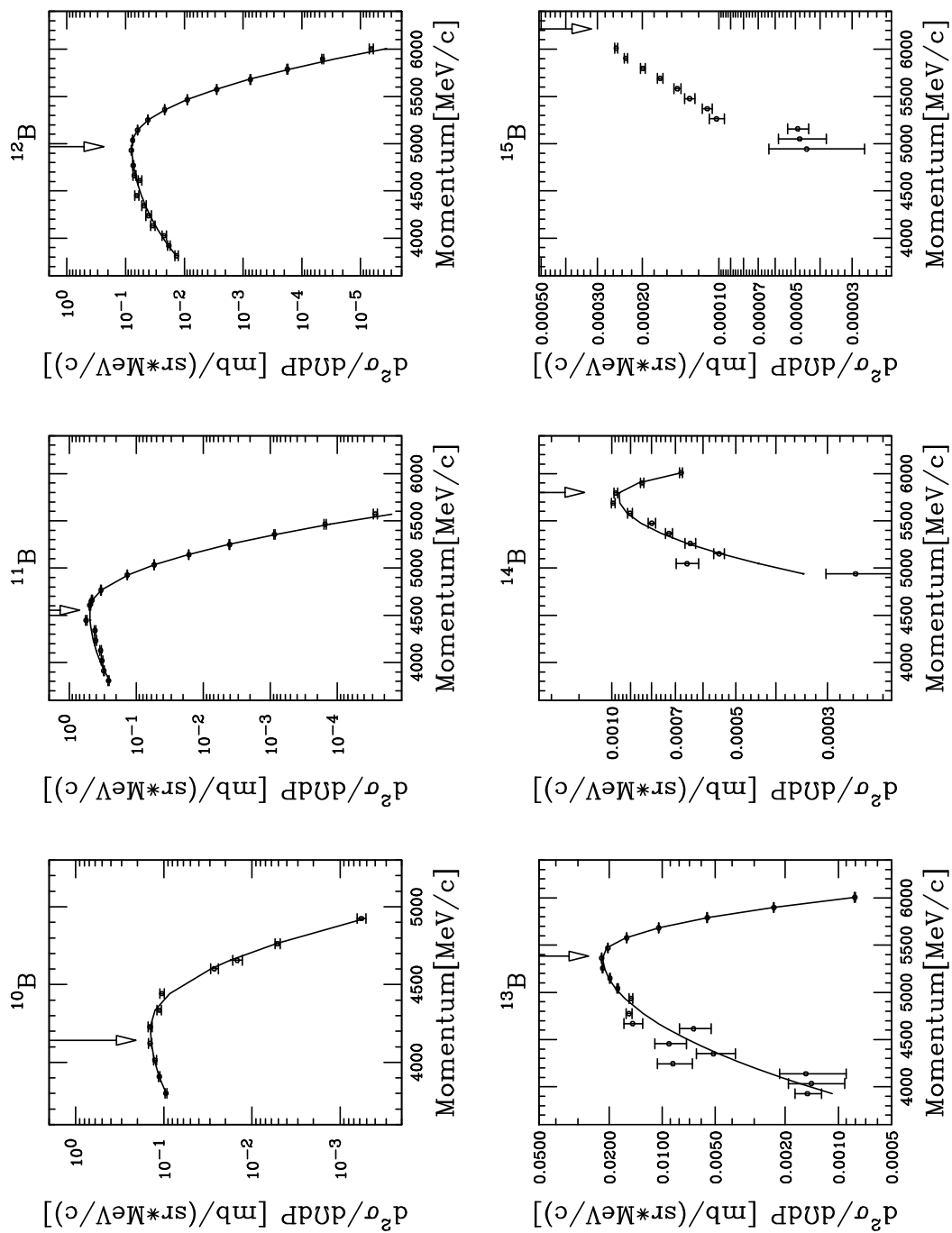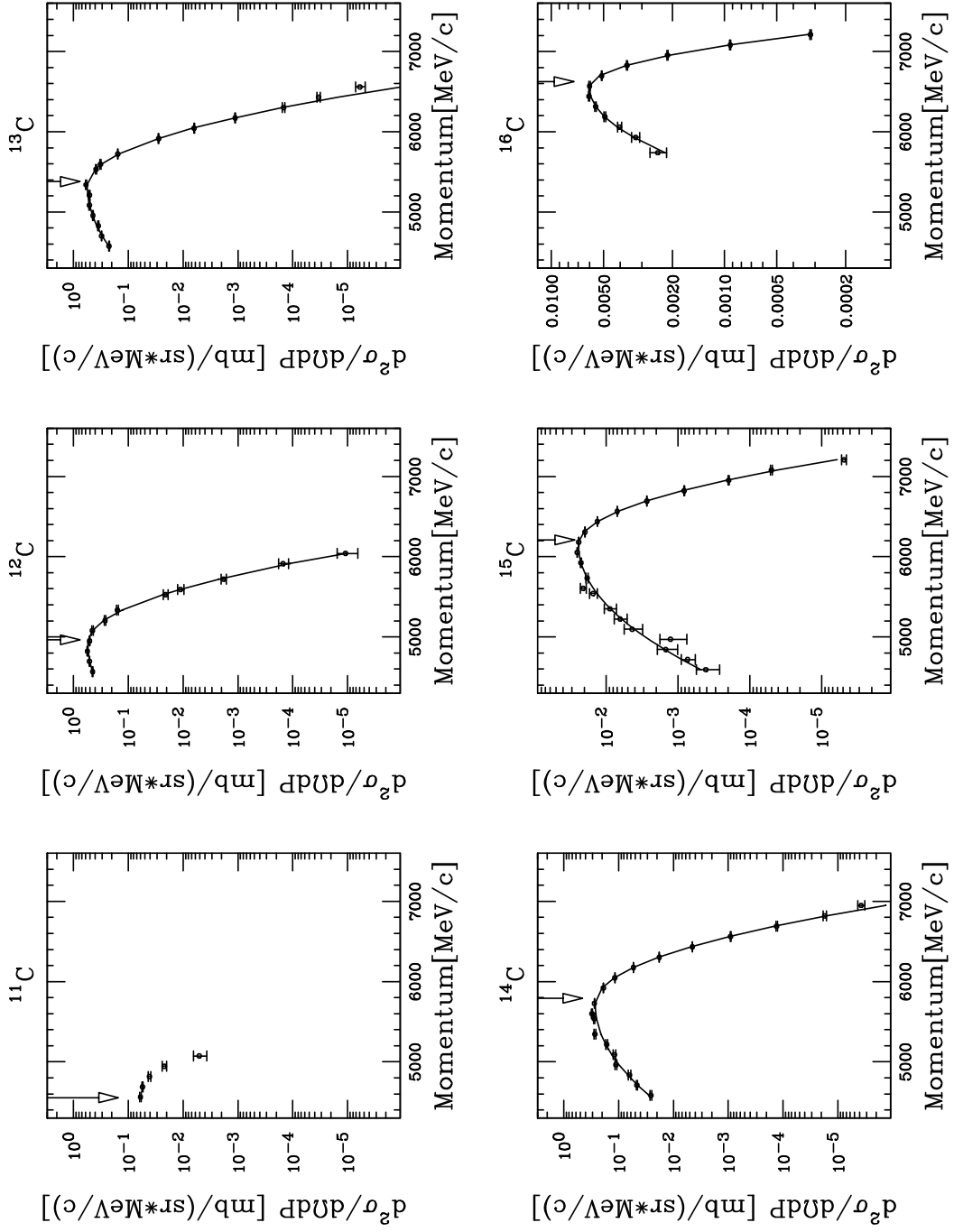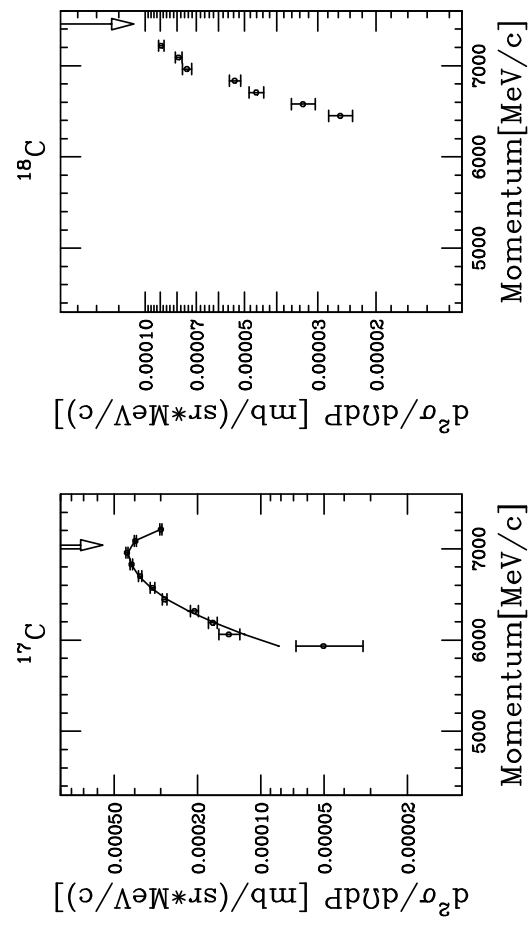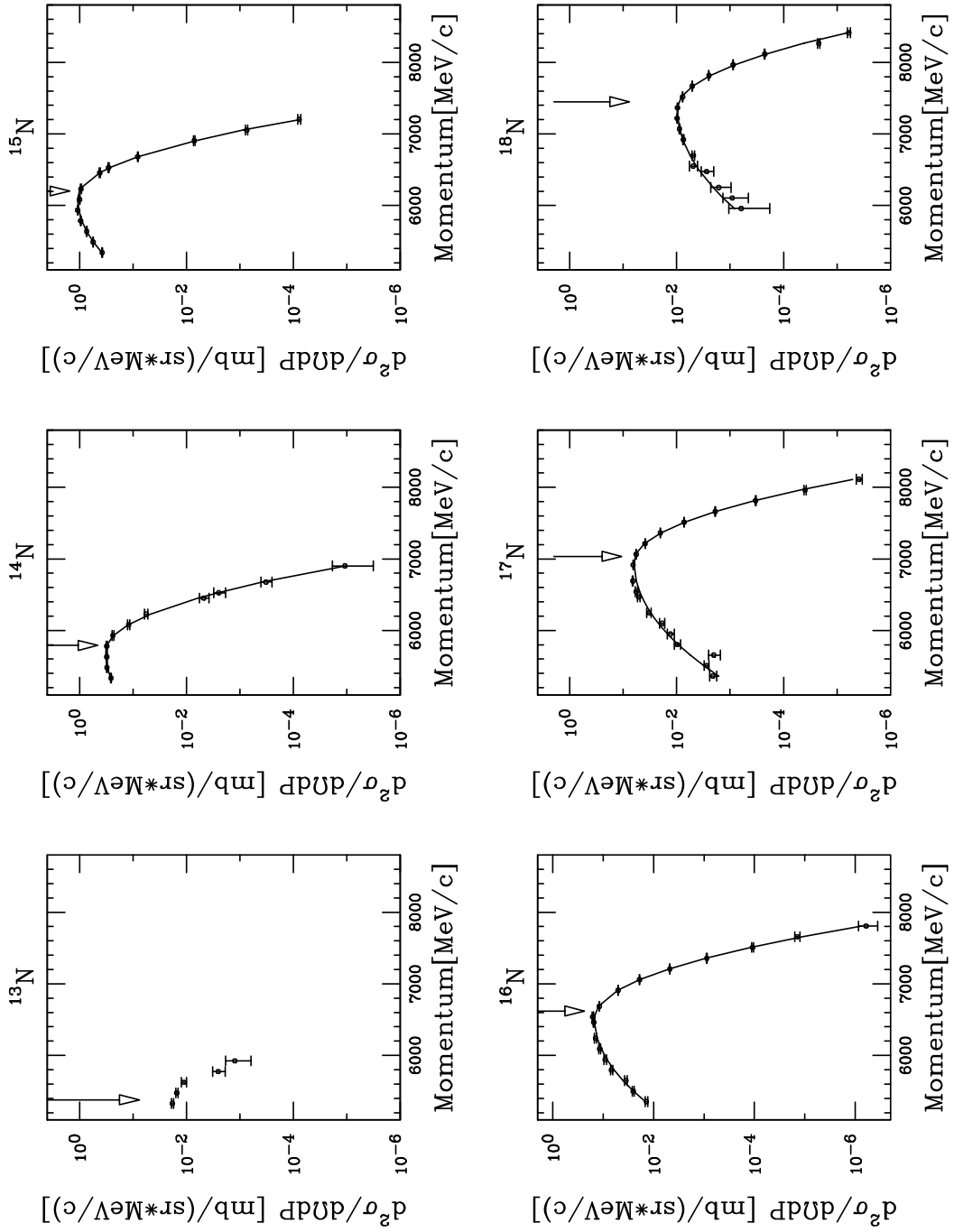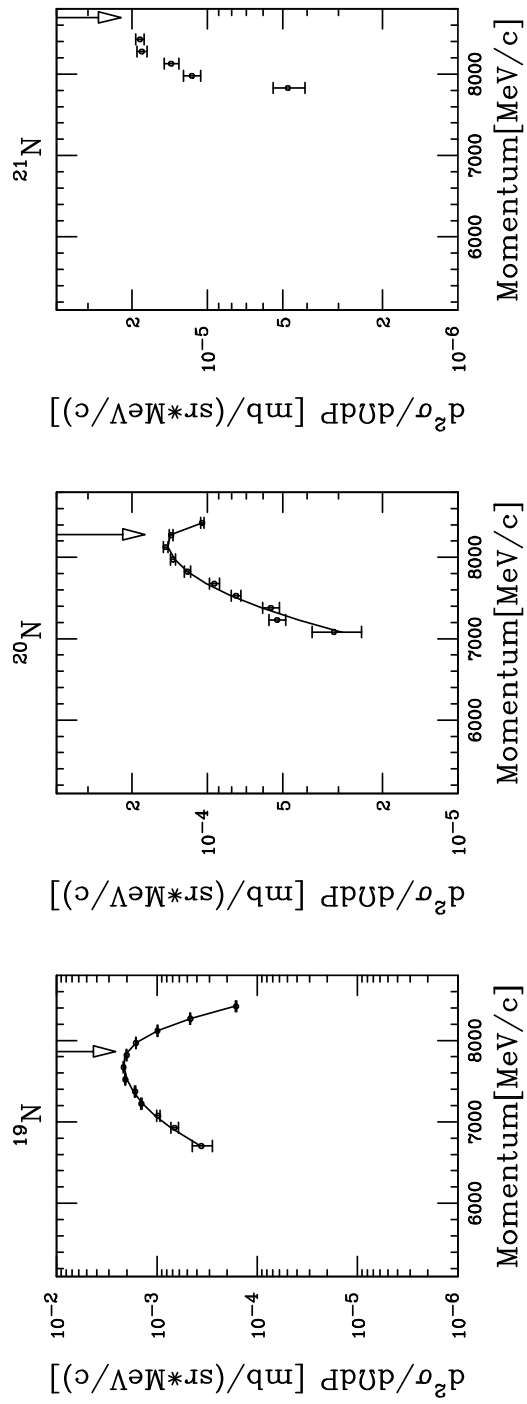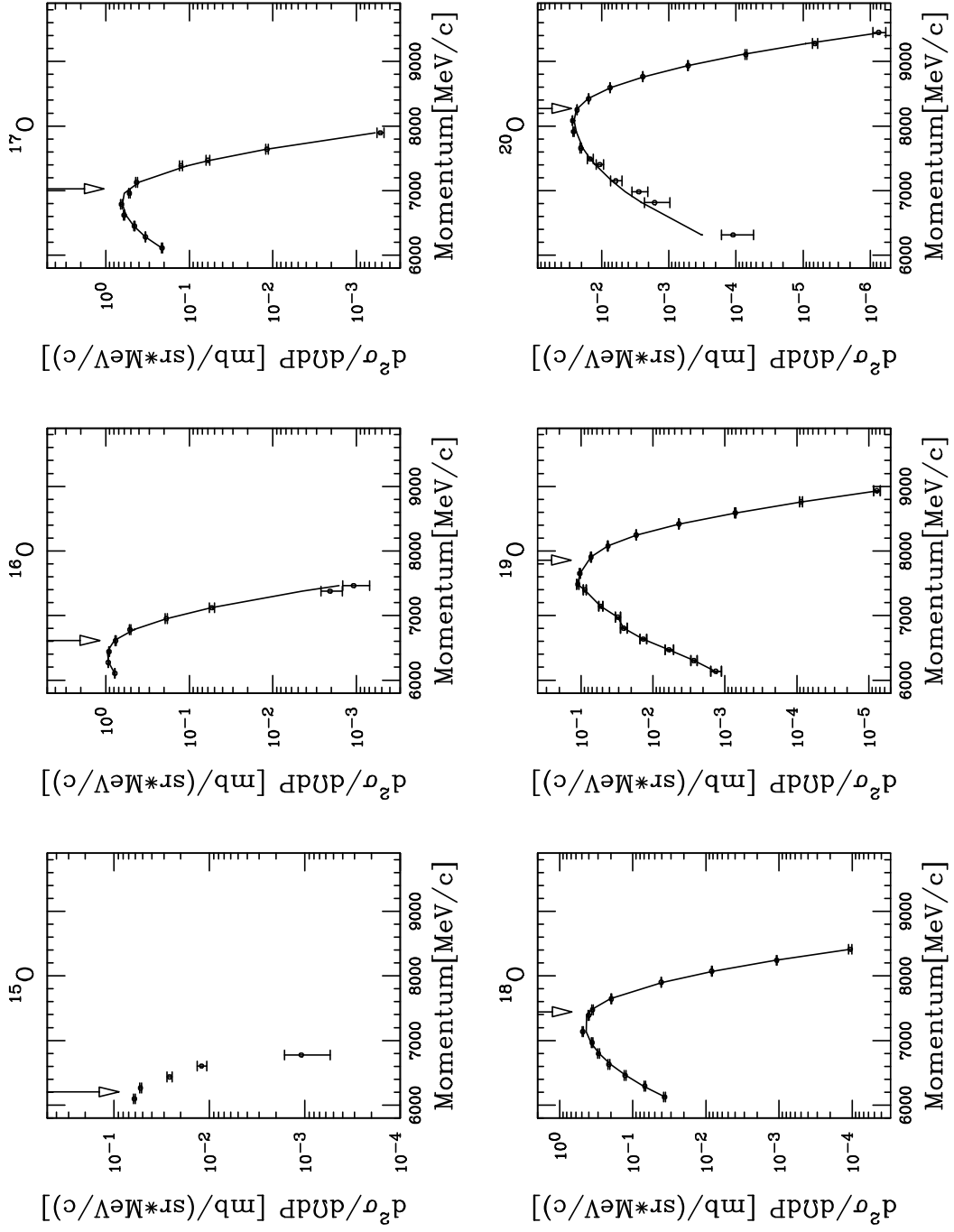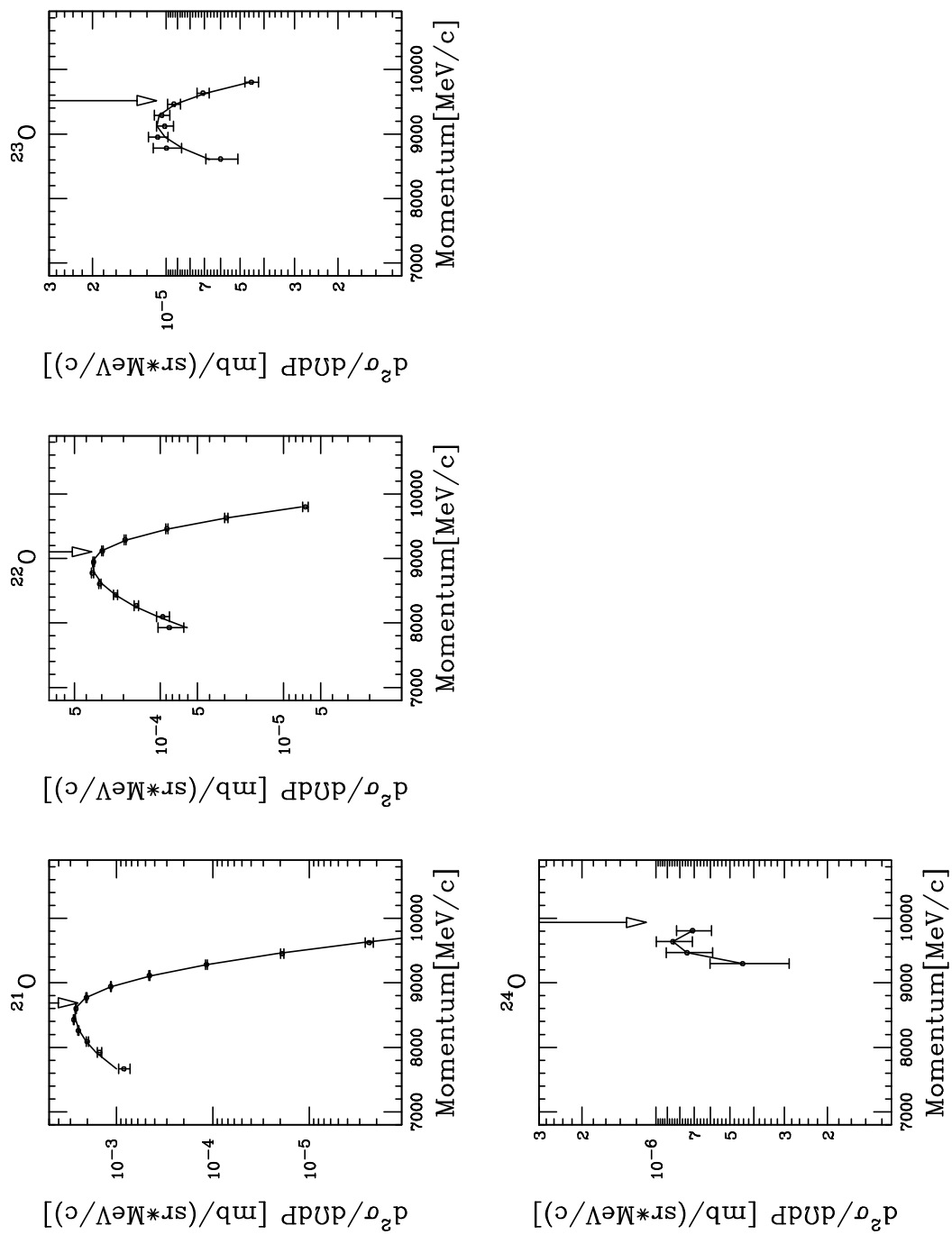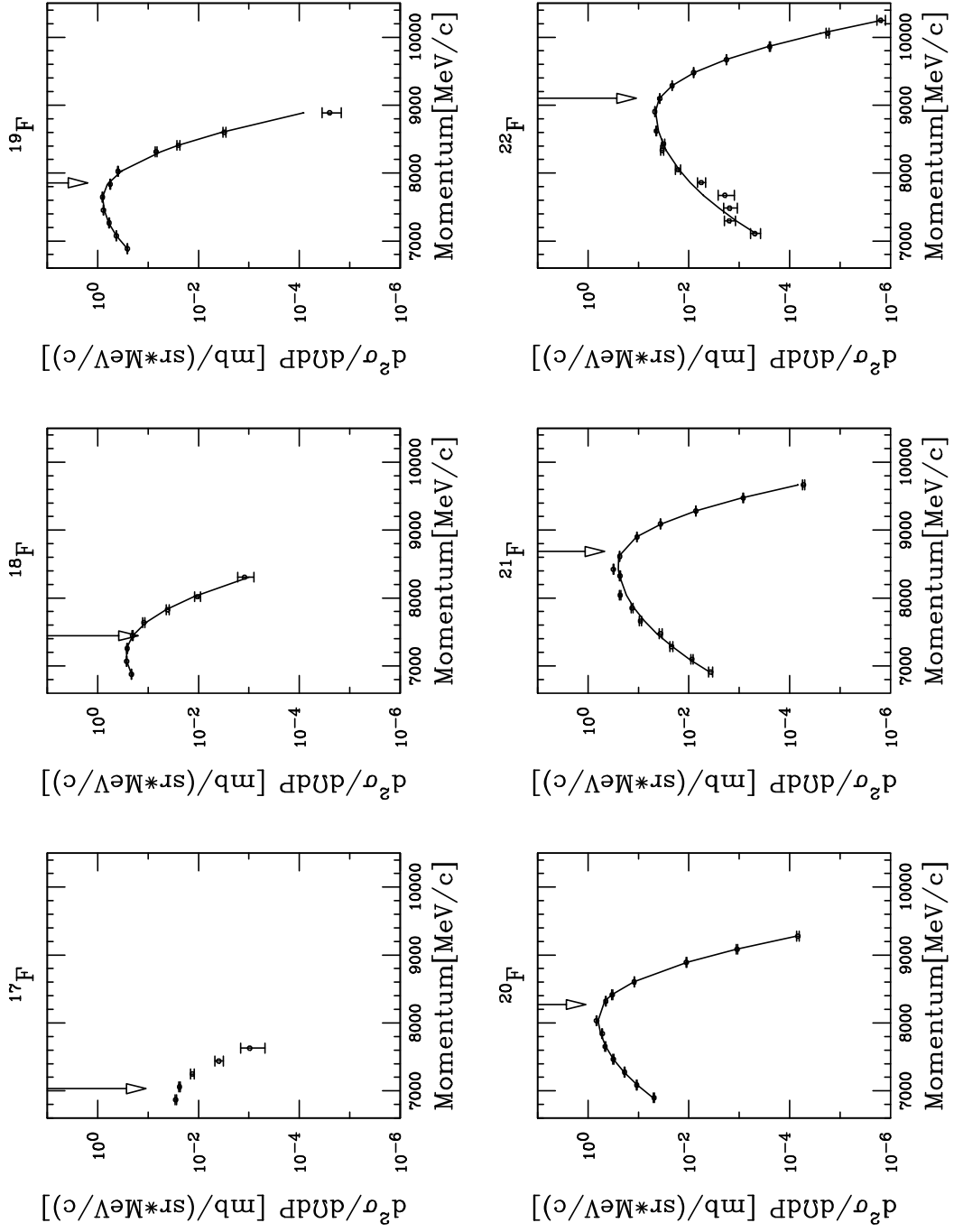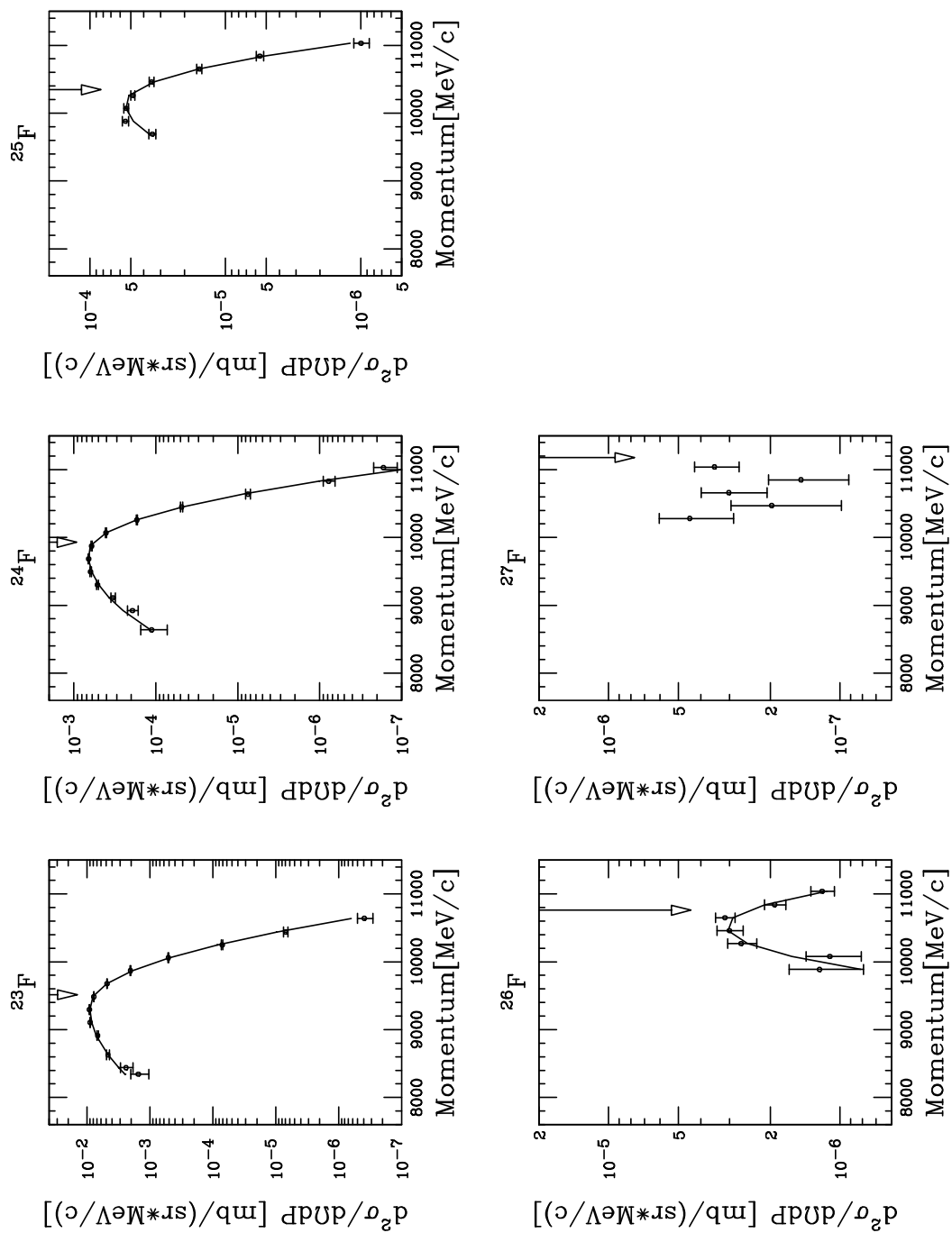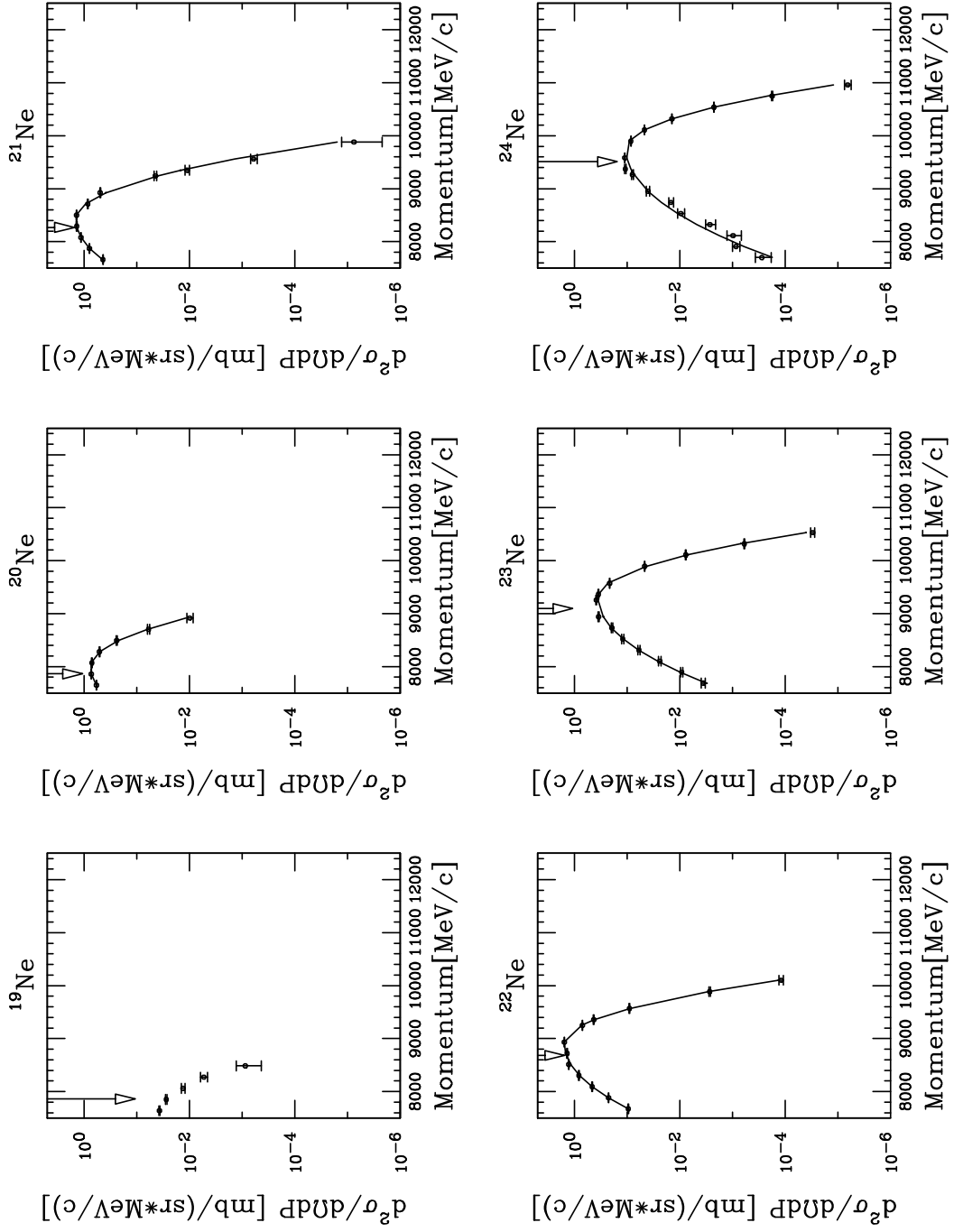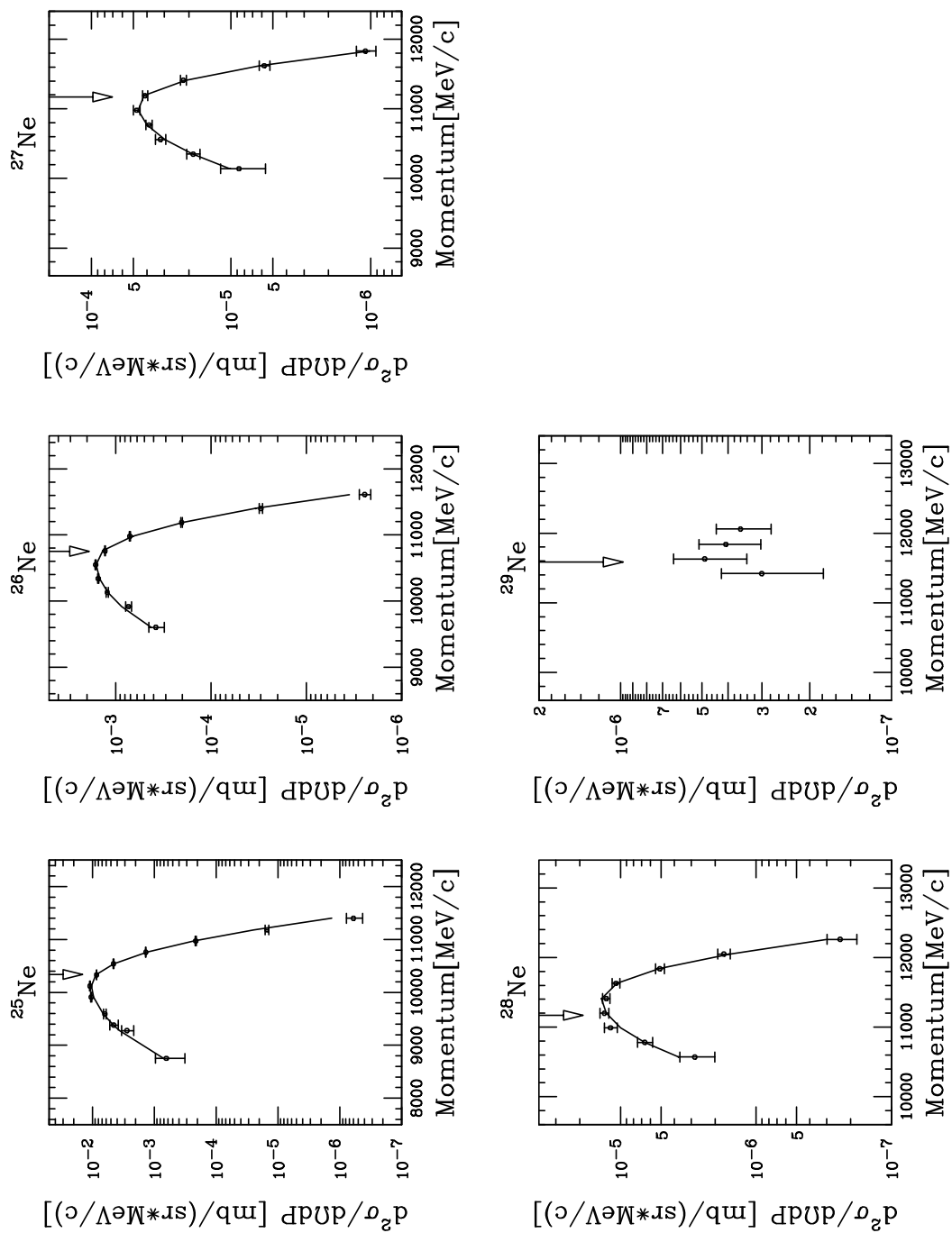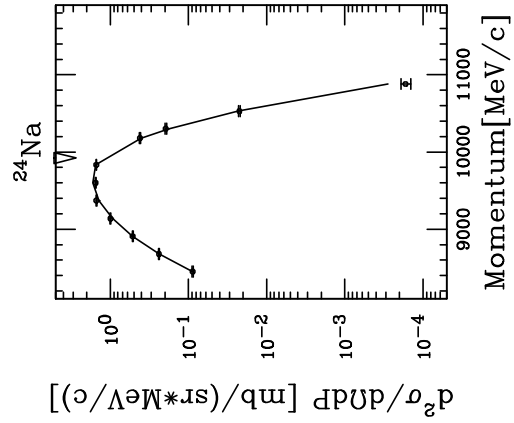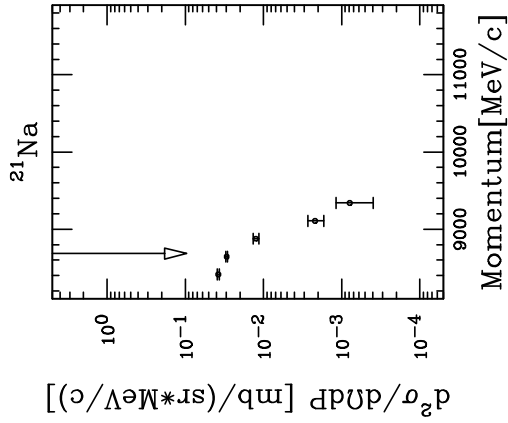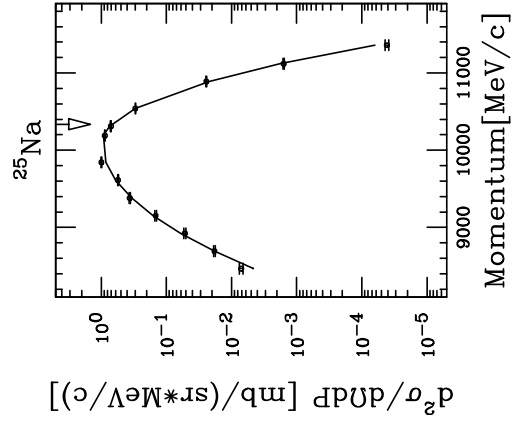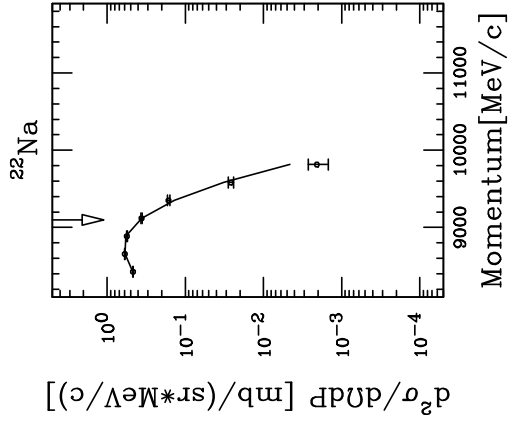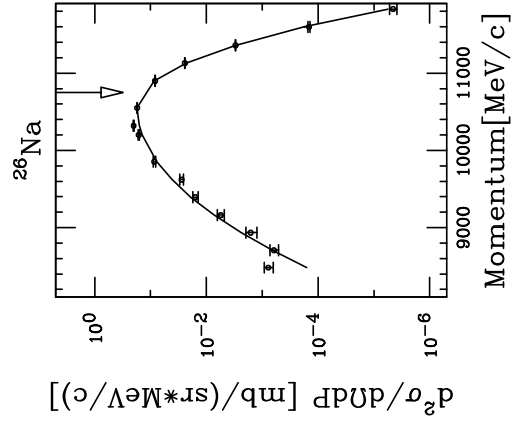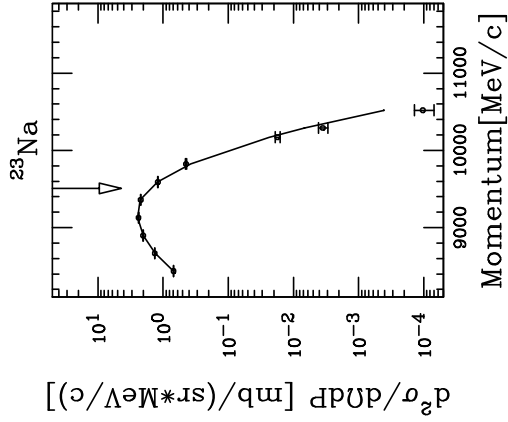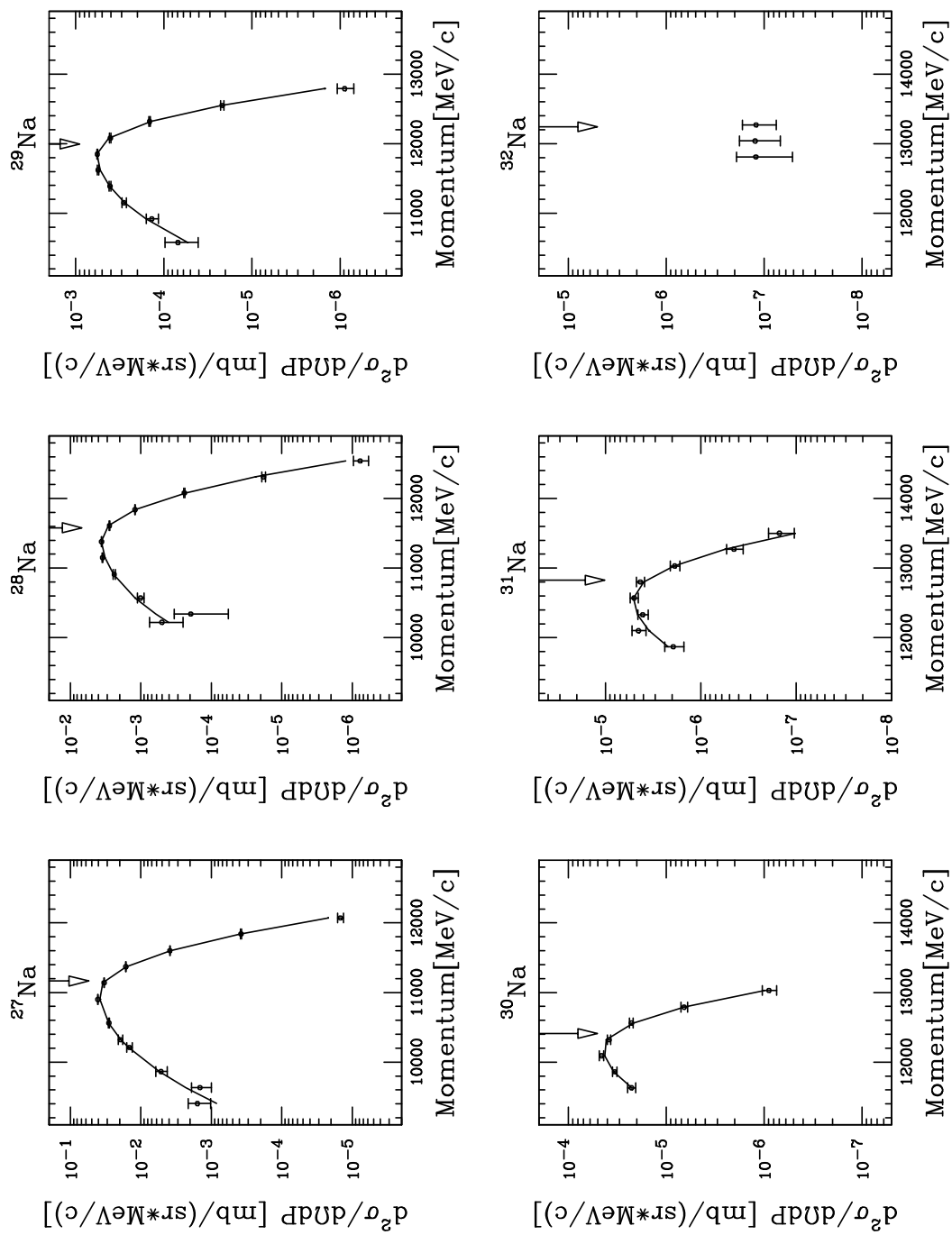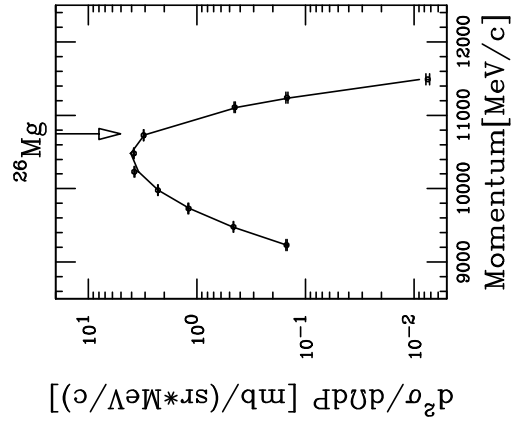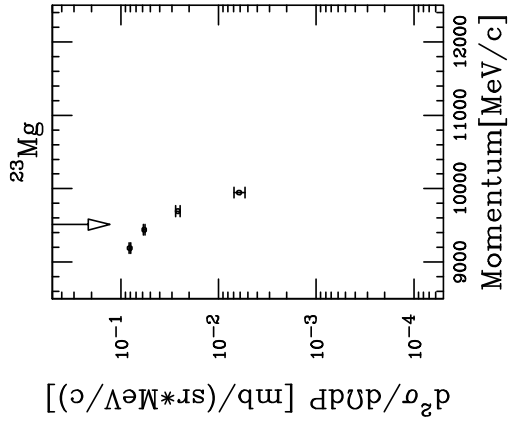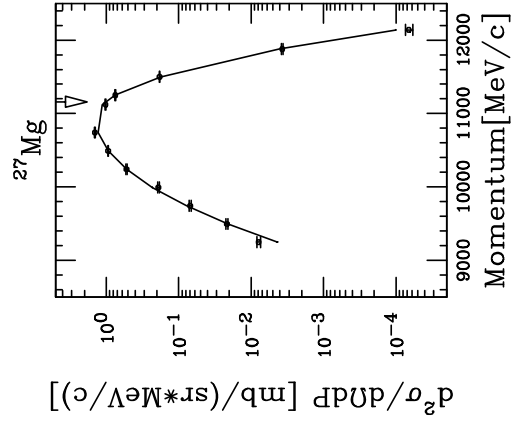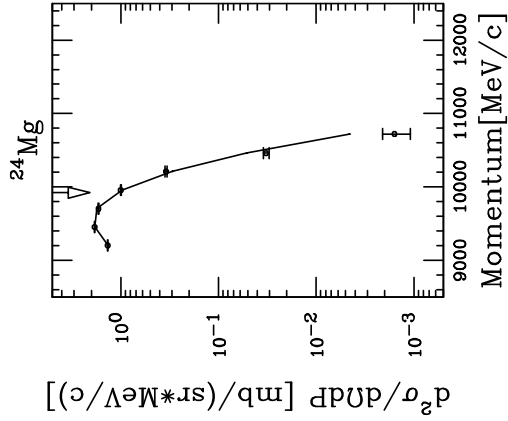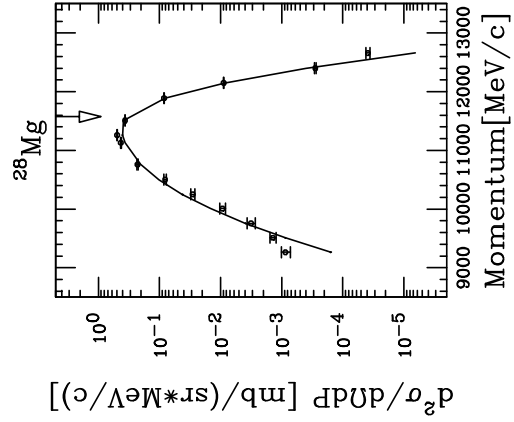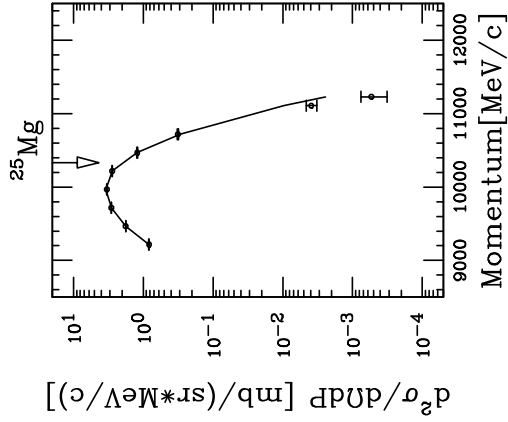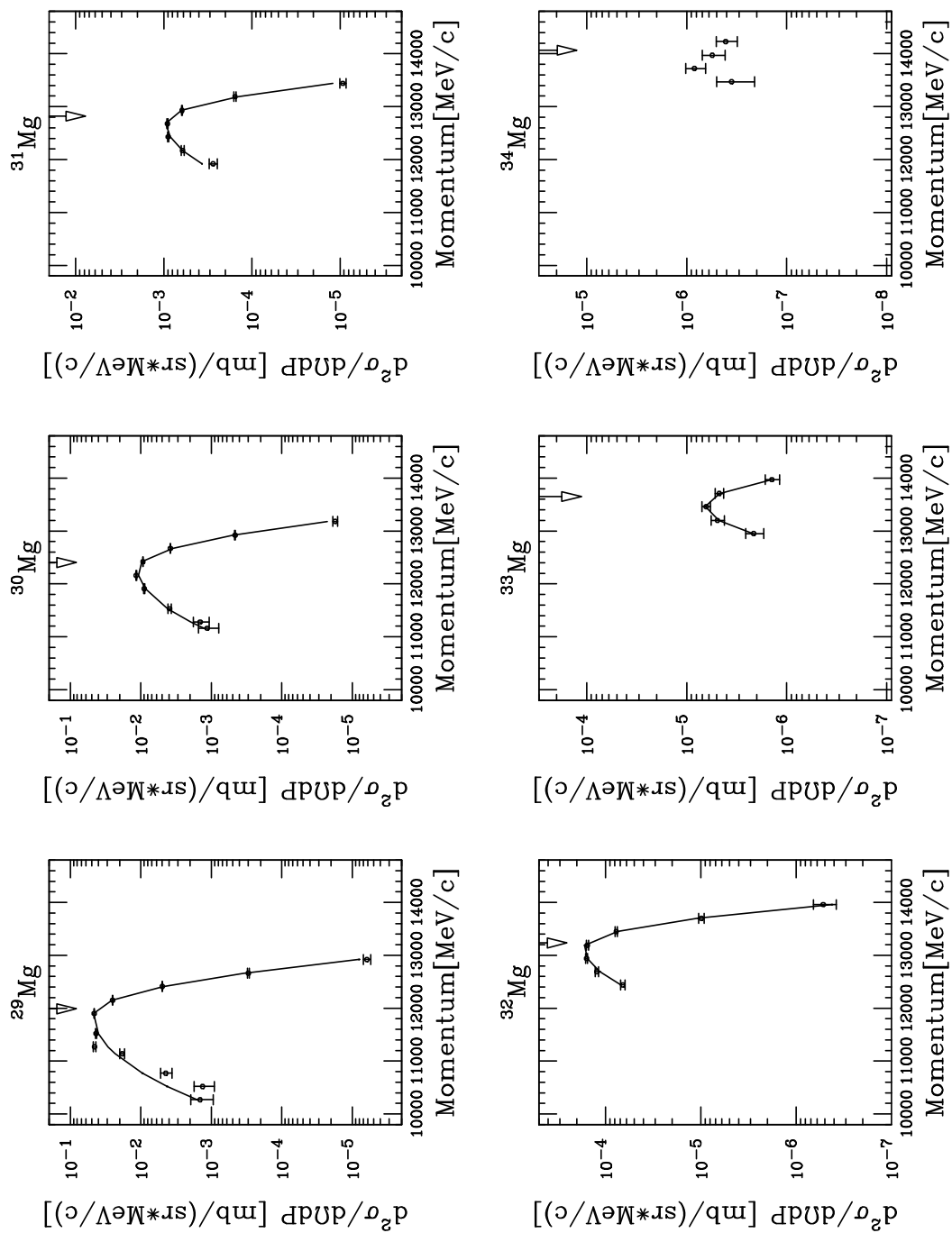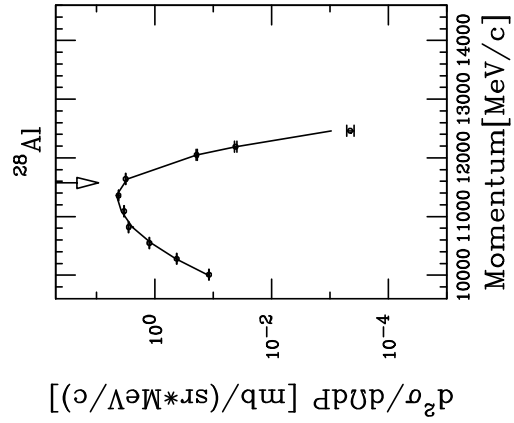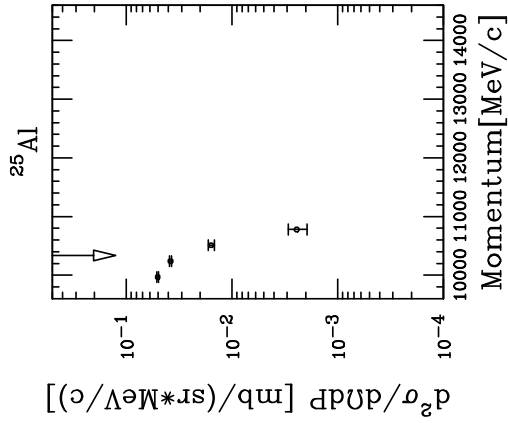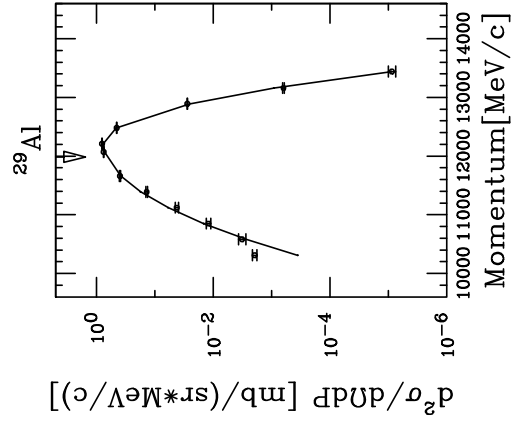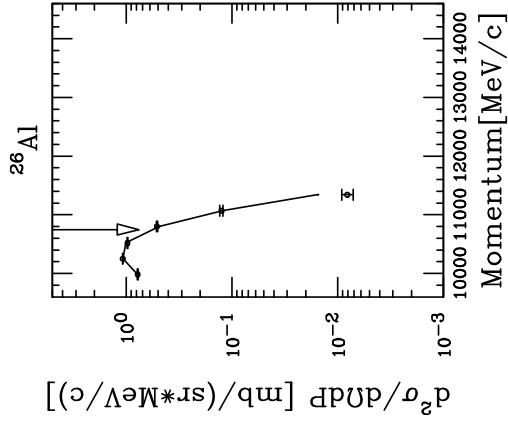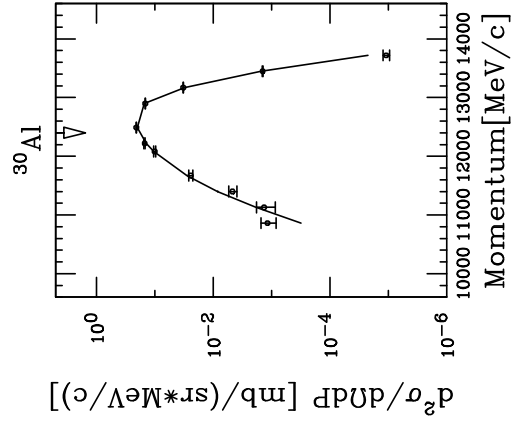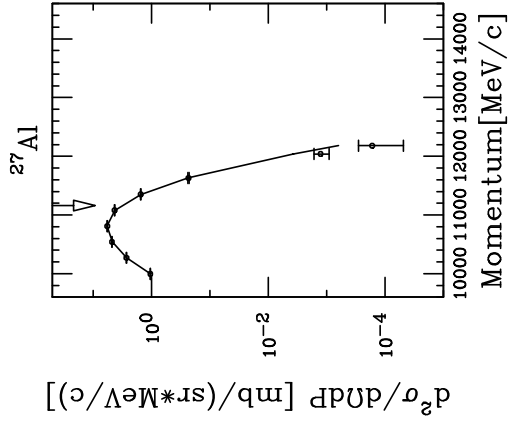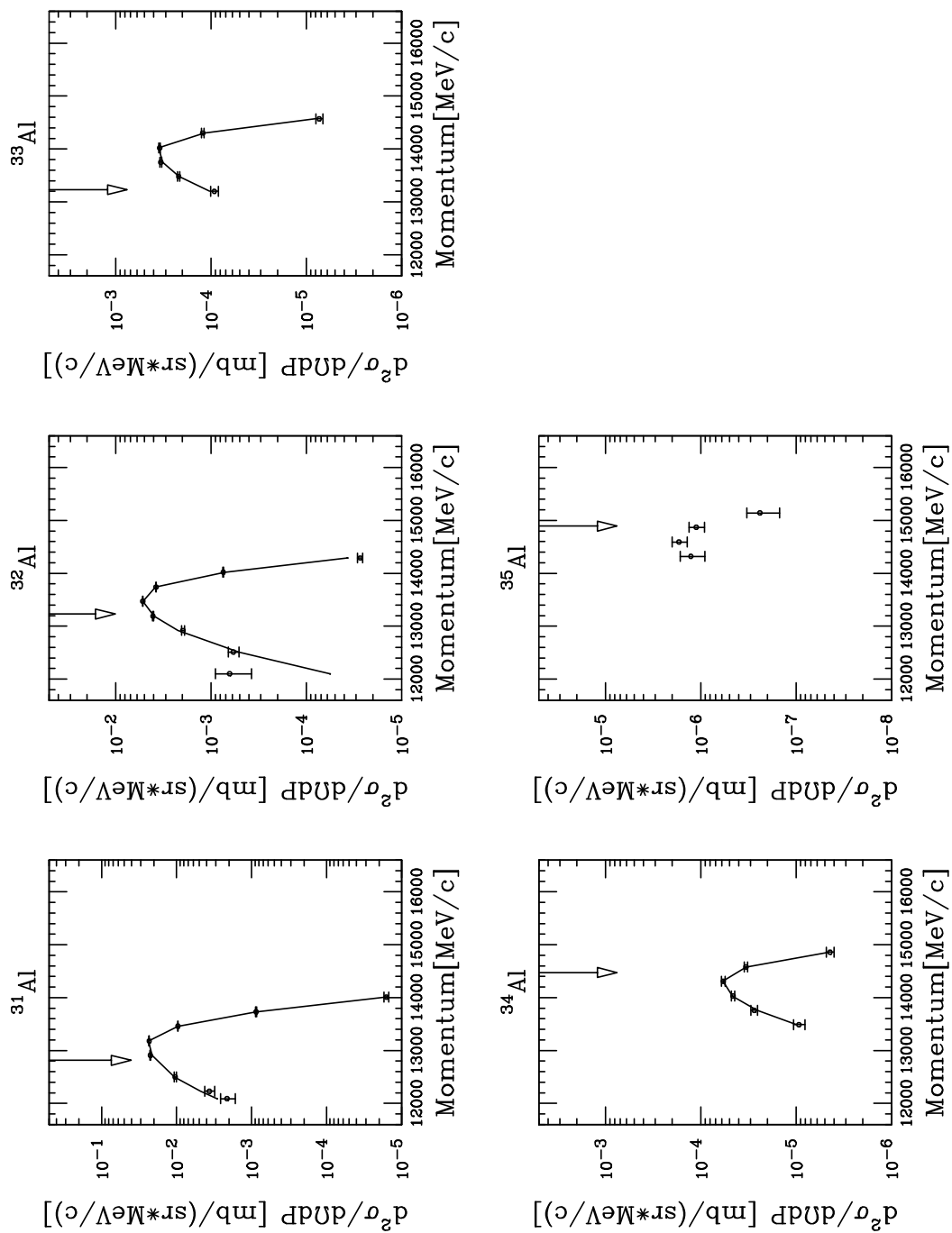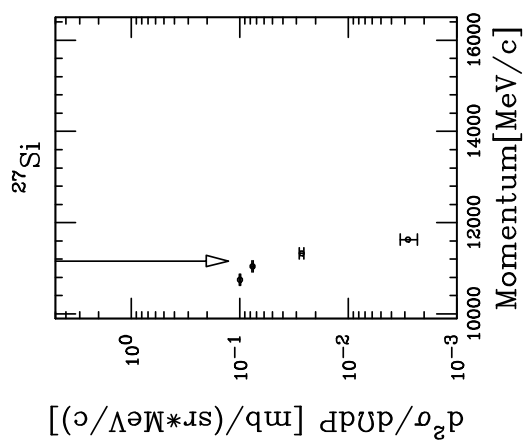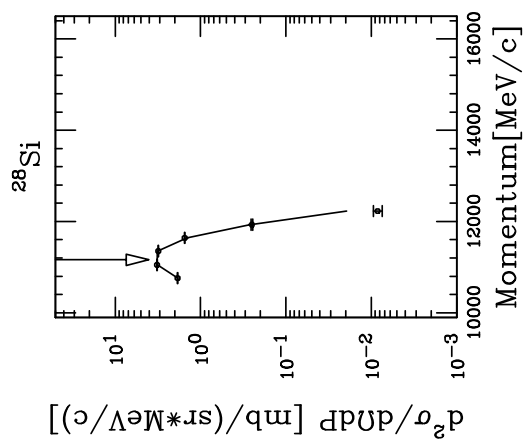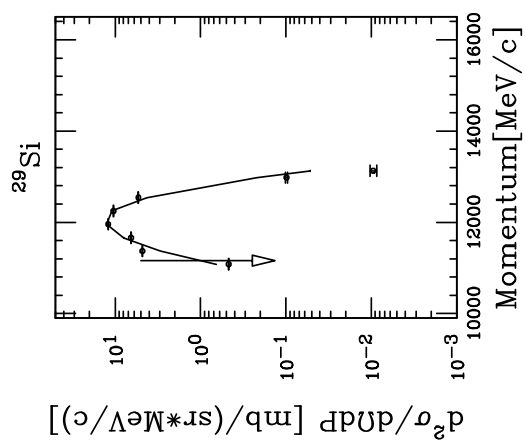
A.1.2 Fitting Results of Be Target Data

In next page, we show the results of fitting parameters, A, P_0, σ_H and σ_L for Be target data. The fitting procedure was performed with type-I function. Two components were found in the momentum distributions of light fragments. For the light fragments, we made an attempt to fit with the function of type-I + type-II as shown with the asterisk marks (*).

| Z_f	A_f	A [$\frac{mb}{(sr \cdot MeV/c)}$]	P_0 [MeV/c]	σ_H [MeV/c]	σ_L [MeV/c]
3	6	1.782e−1 (4.8e−3)	2553.9 (7.1e+0)	116.0 (2.5e+0)	376.3 (3.3e+1)
3	7	2.107e−1 (2.0e−3)	2991.9 (1.7e+0)	123.2 (5.4e−1)	137.5 (5.5e+0)*
4	9	2.276e−1 (2.2e−3)	3753.3 (2.1e+0)	206.6 (5.5e−1)	552.6 (8.5e+0)
4	10	1.238e−1 (1.5e−4)	4220.9 (5.1e−1)	200.0 (2.2e−1)	651.0 (6.2e+0)
4	10	1.228e−1 (1.2e−3)	4221.9 (2.1e+0)	200.0 (5.9e−1)	339.5 (2.6e+1)*
		7.147e−2 (6.1e−3)	3481.1 (2.4e+1)	278.2 (1.2e+1)	
4	11	6.083e−3 (1.5e−5)	4621.5 (3.1e+0)	214.3 (3.8e+0)	564.8 (7.3e+0)
4	11	6.183e−3 (4.9e−5)	4599.0 (5.6e+0)	236.0 (6.0e+0)	365.4 (6.1e+0)*
		3.605e−3 (3.4e−4)	3768.4 (4.0e+1)	265.3 (4.1e+1)	
5	10	1.424e−1 (3.3e−3)	4233.2 (1.3e+1)	206.3 (5.0e+0)	477.9 (3.1e+1)
5	11	5.000e−1 (5.1e−3)	4568.2 (2.5e+0)	220.1 (6.6e−1)	653.3 (9.9e+0)
5	12	7.807e−2 (3.3e−4)	4996.4 (1.5e+0)	225.6 (4.9e−1)	635.5 (7.5e+0)
5	13	2.177e−2 (4.7e−5)	5390.2 (1.2e+0)	240.3 (5.4e−1)	597.4 (9.4e+0)
5	14	9.636e−4 (6.0e−6)	5762.4 (9.4e+0)	291.3 (1.2e+1)	573.0 (1.6e+1)

Z_f	A_f	A [$\frac{mb}{(sr \cdot MeV/c)}$]	P_0 [MeV/c]	σ_H [MeV/c]	σ_L [MeV/c]
6	12	5.523e−1 (5.6e−3)	4924.4 (8.0e+0)	239.7 (3.1e+0)	560.0 (3.0e+1)
6	13	5.624e−1 (6.1e−3)	5332.8 (3.2e+0)	238.7 (9.3e−1)	564.3 (7.3e+0)
6	14	2.701e−1 (1.8e−3)	5731.4 (1.9e+0)	246.2 (5.4e−1)	540.3 (3.6e+0)
6	14	2.003e−1 (7.8e−3)	5782.8 (6.6e+0)	231.9 (2.0e−0)	313.9 (2.0e+1)*
		1.159e−1 (1.3e−2)	5272.4 (1.4e+1)	350.5 (3.7e+0)	
6	15	2.443e−2 (9.0e−5)	6148.4 (1.8e+0)	260.1 (6.9e−1)	554.9 (1.0e+1)
6	16	6.037e−3 (2.8e−5)	6555.7 (2.9e+0)	271.4 (1.3e+0)	576.3 (1.4e+1)
6	17	4.290e−4 (3.2e−6)	6979.3 (1.2e+1)	276.7 (1.5e+1)	574.5 (1.5e+1)
7	14	3.266e−1 (3.8e−3)	5715.0 (1.1e+1)	261.1 (5.1e+0)	569.1 (3.4e+1)
7	15	1.088e+0 (8.2e−3)	6113.9 (3.5e+0)	248.8 (1.2e+0)	535.1 (4.9e+0)
7	16	1.505e−1 (2.1e−3)	6530.0 (4.3e+0)	258.5 (1.2e+0)	544.5 (5.8e+0)
7	17	6.315e−2 (3.5e−4)	6957.6 (2.2e+0)	265.6 (7.4e−1)	591.0 (6.7e+0)
7	18	9.690e−3 (3.9e−5)	7353.7 (2.4e+0)	276.3 (9.7e−1)	629.3 (2.0e+1)
7	19	2.155e−3 (1.1e−5)	7741.6 (4.0e+0)	299.7 (2.0e+0)	552.5 (1.0e+1)
7	20	1.450e−4 (1.7e−6)	8208.4 (2.0e+1)	266.4 (2.6e+1)	628.9 (2.2e+1)
8	16	9.611e−1 (5.5e−3)	6429.7 (8.3e+0)	289.4 (4.7e+0)	508.9 (2.0e+1)
8	17	6.411e−1 (6.0e−3)	6860.5 (7.2e+0)	277.2 (2.8e+0)	504.8 (7.2e+0)
8	18	4.544e−1 (4.8e−3)	7296.3 (3.7e+0)	273.1 (1.0e+0)	520.3 (3.9e+0)
8	19	9.630e−2 (8.7e−4)	7726.3 (3.1e+0)	277.6 (9.6e−1)	539.6 (5.4e+0)
8	20	2.575e−2 (1.1e−4)	8142.5 (2.4e+0)	284.7 (9.1e−1)	618.1 (1.3e+1)
8	21	2.726e−3 (1.6e−5)	8563.5 (4.0e+0)	286.0 (1.7e+0)	634.2 (2.1e+1)
8	22	3.597e−4 (3.9e−6)	8936.9 (8.0e+0)	308.2 (3.7e+0)	536.9 (1.5e+1)
8	23	1.099e−5 (5.4e−7)	9183.4 (9.3e+1)	468.3 (7.3e+1)	575.6 (1.6e+2)
8	24	8.571e−7 (1.3e−7)	9608.5 (2.1e+2)	325.1 (4.1e+2)	271.6 (2.1e+2)

Z_f	A_f	A [$\frac{mb}{(sr \cdot MeV/c)}$]	P_0 [MeV/c]	σ_H [MeV/c]	σ_L [MeV/c]
9	18	2.744e−1 (2.6e−3)	7187.8 (1.3e+1)	333.5 (8.3e+0)	443.0 (2.6e+1)
9	19	8.007e−1 (6.3e−3)	7647.5 (6.1e+0)	289.6 (2.6e+0)	508.2 (5.9e+0)
9	20	6.334e−1 (5.8e−3)	8103.8 (3.5e+0)	276.1 (1.2e+0)	537.6 (3.3e+0)
9	21	2.560e−1 (2.1e−3)	8537.7 (3.1e+0)	278.3 (9.4e−1)	562.8 (3.7e+0)
9	22	4.582e−2 (3.1e−4)	8932.7 (2.8e+0)	290.2 (9.7e−1)	602.0 (9.4e+0)
9	23	9.059e−3 (4.0e−5)	9347.6 (2.7e+0)	295.4 (1.2e+0)	624.9 (1.9e+1)
9	24	6.708e−4 (6.8e−6)	9772.8 (6.6e+0)	293.2 (3.0e+0)	606.7 (2.1e+1)
9	25	5.493e−5 (1.7e−6)	10143.0 (2.4e+1)	320.6 (1.0e+1)	500.4 (6.0e+1)
9	26	3.087e−6 (2.3e−7)	10521.0 (7.1e+1)	368.6 (5.8e+1)	387.8 (7.8e+1)
10	20	7.571e−1 (4.2e−3)	7993.6 (7.8e+0)	319.8 (4.9e+0)	483.8 (1.5e+1)
10	21	1.457e+0 (8.1e−3)	8429.7 (4.6e+0)	303.2 (2.3e+0)	501.0 (4.2e+0)
10	22	1.567e+0 (9.2e−3)	8908.5 (3.3e+0)	275.3 (1.3e+0)	522.2 (2.2e+0)
10	23	3.596e−1 (3.5e−3)	9303.9 (3.9e+0)	287.4 (1.1e+0)	524.5 (3.5e+0)
10	24	1.053e−1 (7.9e−4)	9746.6 (2.9e+0)	284.9 (9.6e−1)	571.6 (6.3e+0)
10	25	1.042e−2 (8.2e−5)	10162.0 (4.4e+0)	292.5 (1.7e+0)	608.7 (2.4e+1)
10	26	1.615e−3 (1.4e−5)	10592.0 (6.0e+0)	290.9 (2.6e+0)	604.4 (2.4e+1)
10	27	4.662e−5 (1.5e−6)	11062.0 (2.2e+1)	277.8 (1.1e+1)	528.2 (3.7e+1)
10	28	1.379e−5 (6.1e−7)	11408.0 (3.8e+1)	308.2 (1.8e+1)	518.1 (5.4e+1)
11	22	6.099e−1 (3.5e−3)	8777.2 (8.3e+0)	331.9 (5.3e+0)	480.6 (1.5e+1)
11	23	2.496e+0 (1.0e−2)	9217.2 (3.6e+0)	312.1 (2.2e+0)	489.9 (3.0e+0)
11	24	1.709e+0 (9.5e−3)	9700.5 (4.1e+0)	282.5 (1.7e+0)	515.1 (2.4e+0)
11	25	9.675e−1 (6.9e−3)	10103.0 (2.8e+0)	286.3 (8.9e−1)	501.2 (2.3e+0)
11	26	1.767e−1 (1.2e−3)	10572.0 (2.8e+0)	276.6 (9.2e−1)	558.1 (4.9e+0)
11	27	3.880e−2 (2.6e−4)	11008.0 (2.8e+0)	274.7 (1.0e+0)	579.1 (1.2e+1)
11	28	3.628e−3 (2.4e−5)	11421.0 (4.3e+0)	280.1 (2.0e+0)	573.4 (1.8e+1)
11	29	5.761e−4 (6.0e−6)	11869.0 (7.9e+0)	266.9 (3.8e+0)	592.0 (1.9e+1)
11	30	4.383e−5 (1.6e−6)	12208.0 (2.7e+1)	298.0 (1.3e+1)	498.3 (5.5e+1)
11	31	5.069e−6 (3.5e−7)	12565.0 (5.4e+1)	334.8 (2.6e+1)	538.8 (9.2e+1)

Z_f	A_f	A $[\frac{mb}{(sr \cdot MeV/c)}]$	P_0 [MeV/c]	σ_H [MeV/c]	σ_L [MeV/c]
12	24	1.902e+0 (5.9e−3)	9571.6 (4.3e+0)	330.8 (2.8e+0)	450.6 (6.6e+0)
12	25	3.441e+0 (1.2e−2)	10008.0 (3.3e+0)	321.1 (2.2e+0)	469.6 (2.4e+0)
12	26	4.091e+0 (1.5e−2)	10519.0 (2.7e+0)	277.3 (1.2e+0)	499.5 (1.5e+0)
12	27	1.413e+0 (8.8e−3)	10941.0 (2.7e+0)	274.3 (1.1e+0)	498.4 (1.9e+0)
12	28	4.197e−1 (2.7e−3)	11408.0 (3.0e+0)	266.1 (9.6e−1)	539.9 (3.6e+0)
12	29	4.716e−2 (3.8e−4)	11874.0 (3.4e+0)	251.1 (1.3e+0)	618.1 (1.3e+1)
12	30	1.115e−2 (8.1e−5)	12285.0 (4.1e+0)	254.1 (1.6e+0)	539.4 (1.3e+1)
12	31	9.529e−4 (1.0e−5)	12703.0 (6.5e+0)	249.2 (3.3e+0)	568.0 (2.3e+1)
12	32	1.675e−4 (3.1e−6)	13153.0 (1.3e+1)	233.2 (6.7e+0)	537.1 (2.3e+1)
12	33	6.513e−6 (5.0e−7)	13486.0 (6.5e+1)	276.9 (4.2e+1)	361.8 (6.5e+1)
13	26	1.113e+0 (4.4e−3)	10375.0 (5.6e+0)	330.1 (3.7e+0)	466.2 (8.2e+0)
13	27	5.841e+0 (1.6e−2)	10832.0 (2.4e+0)	315.3 (1.6e+0)	451.0 (1.6e+0)
13	28	4.523e+0 (1.5e−2)	11407.0 (2.5e+0)	255.7 (1.3e+0)	522.2 (1.4e+0)
13	29	3.192e+0 (1.4e−2)	11806.0 (2.2e+0)	254.1 (9.7e−1)	495.2 (1.3e+0)
13	30	7.597e−1 (4.9e−3)	12226.0 (2.6e+0)	254.7 (8.6e−1)	489.3 (3.0e+0)
13	31	2.176e−1 (1.3e−3)	12699.0 (2.1e+0)	238.1 (7.1e−1)	508.5 (5.8e+0)
13	32	2.375e−2 (1.4e−4)	13162.0 (2.4e+0)	221.4 (1.1e+0)	521.3 (9.1e+0)
13	33	5.282e−3 (2.7e−5)	13553.0 (3.3e+0)	234.0 (1.6e+0)	482.2 (8.2e+0)
13	34	3.618e−4 (5.7e−6)	13980.0 (1.3e+1)	213.9 (6.3e+0)	492.5 (2.0e+1)
13	35	5.847e−5 (1.7e−6)	14338.0 (1.8e+1)	229.7 (1.0e+1)	451.1 (2.0e+1)
14	28	3.521e+0 (8.3e−3)	11221.0 (2.6e+0)	313.1 (1.9e+0)	407.3 (2.6e+0)
14	29	8.238e+0 (2.1e−2)	11694.0 (2.3e+0)	287.6 (1.4e+0)	432.9 (1.8e+0)
14	30	1.306e+1 (2.7e−2)	12059.0 (1.6e+0)	322.1 (1.0e+0)	400.1 (8.4e−1)
14	31	5.657e+0 (2.2e−2)	12657.0 (1.9e+0)	235.1 (8.8e−1)	431.6 (1.6e+0)
14	32	2.260e+0 (9.4e−3)	13142.0 (1.5e+0)	211.2 (7.5e−1)	440.7 (1.9e+0)
14	33	3.794e−1 (1.7e−3)	13589.0 (1.6e+0)	199.4 (7.0e−1)	465.3 (4.0e+0)
14	34	9.857e−2 (4.7e−4)	14030.0 (1.6e+0)	187.3 (5.9e−1)	406.0 (3.6e+0)
14	35	7.864e−3 (6.0e−5)	14450.0 (4.3e+0)	177.0 (1.9e+0)	405.7 (7.9e+0)
14	36	1.509e−3 (1.4e−5)	14873.0 (4.5e+0)	166.0 (2.9e+0)	391.0 (6.2e+0)
15	33	1.387e+1 (4.1e−2)	13559.0 (2.1e+0)	195.3 (9.8e−1)	406.6 (1.5e+0)
15	34	5.043e+0 (1.7e−2)	13996.0 (1.9e+0)	183.2 (8.3e−1)	388.8 (1.5e+0)
15	35	2.029e+0 (4.9e−3)	14479.0 (3.6e+0)	159.5 (1.4e+0)	383.4 (2.5e+0)
15	36	2.278e−1 (7.5e−4)	14915.0 (2.3e+0)	150.4 (1.0e+0)	416.5 (3.2e+0)

A.2 Results of Ta Target Data

The momentum distributions of fragments produced in Ar+Ta are shown with the fitting results with the Type-II function.

A.2.1   Momentum Distributions of Ta Target Data
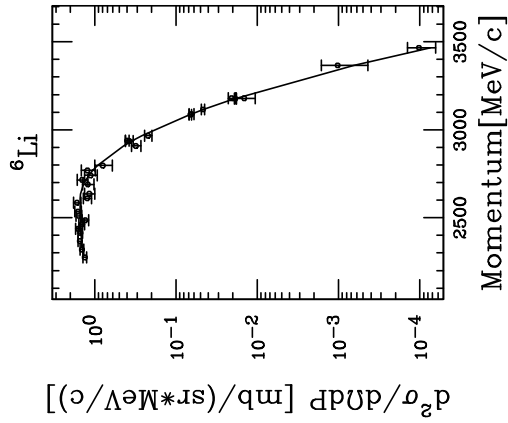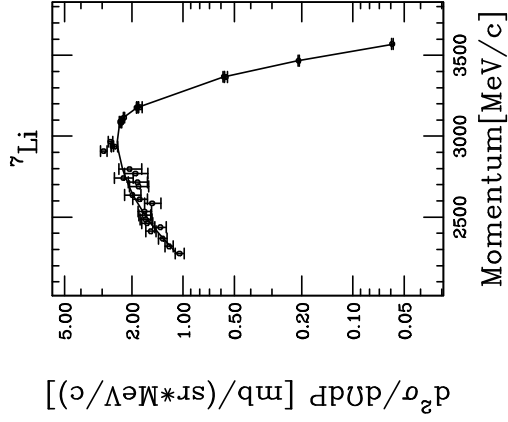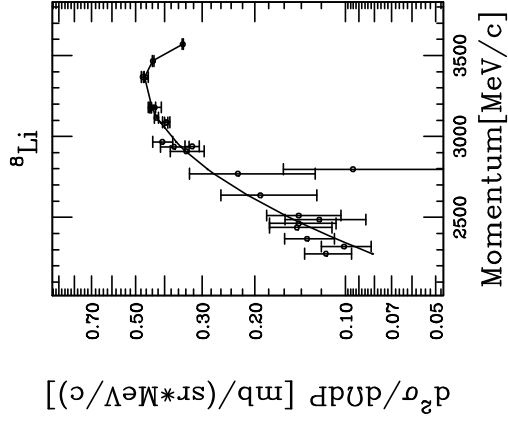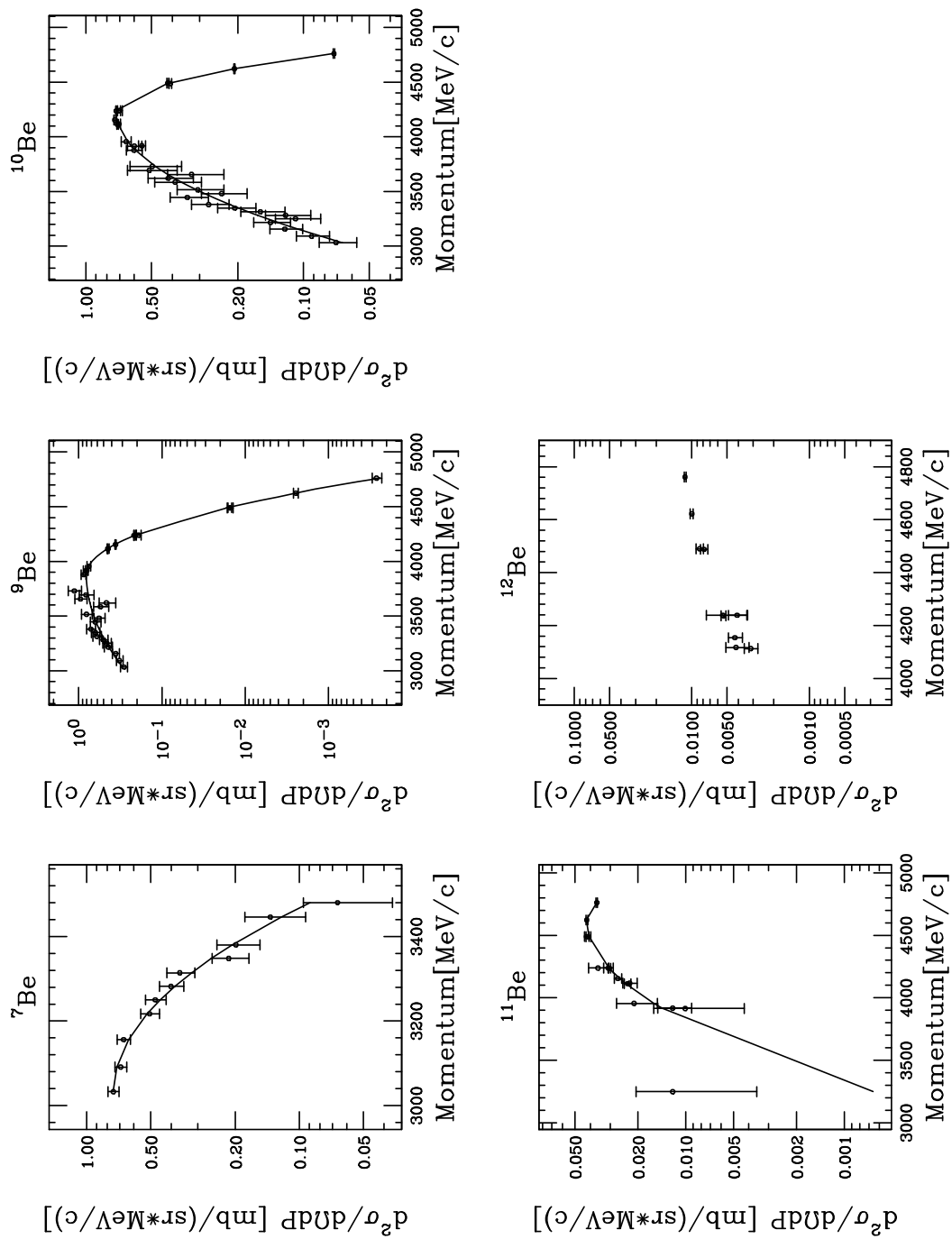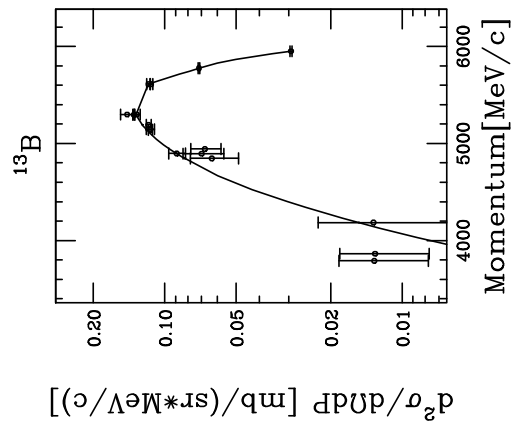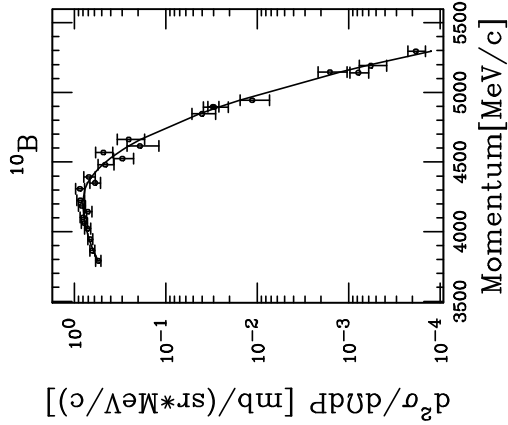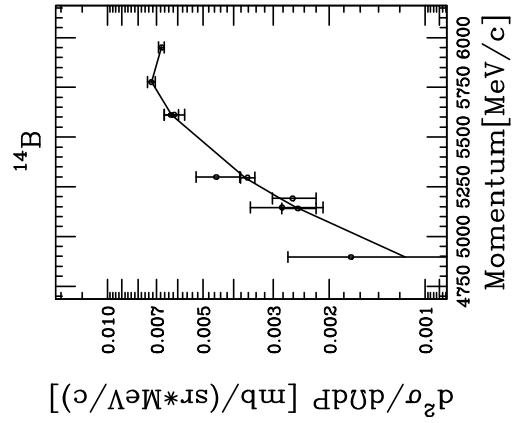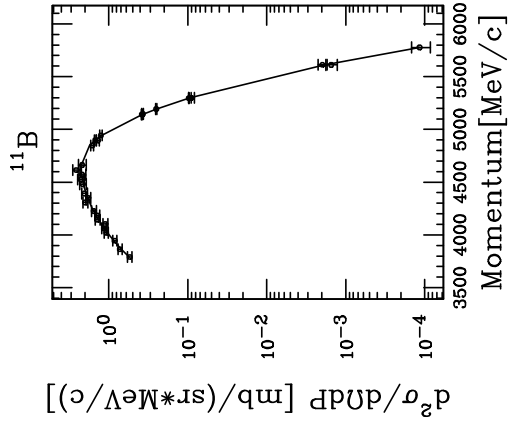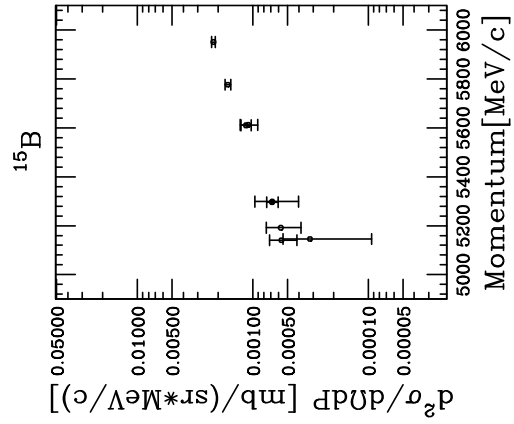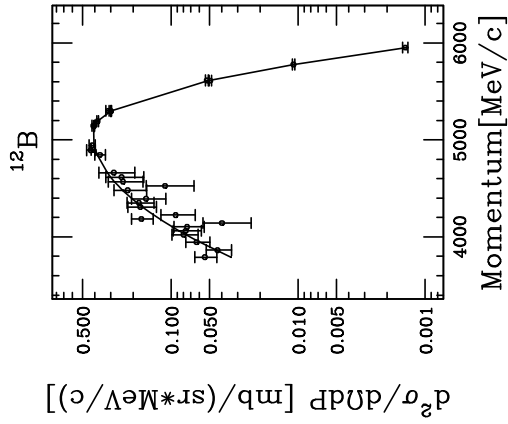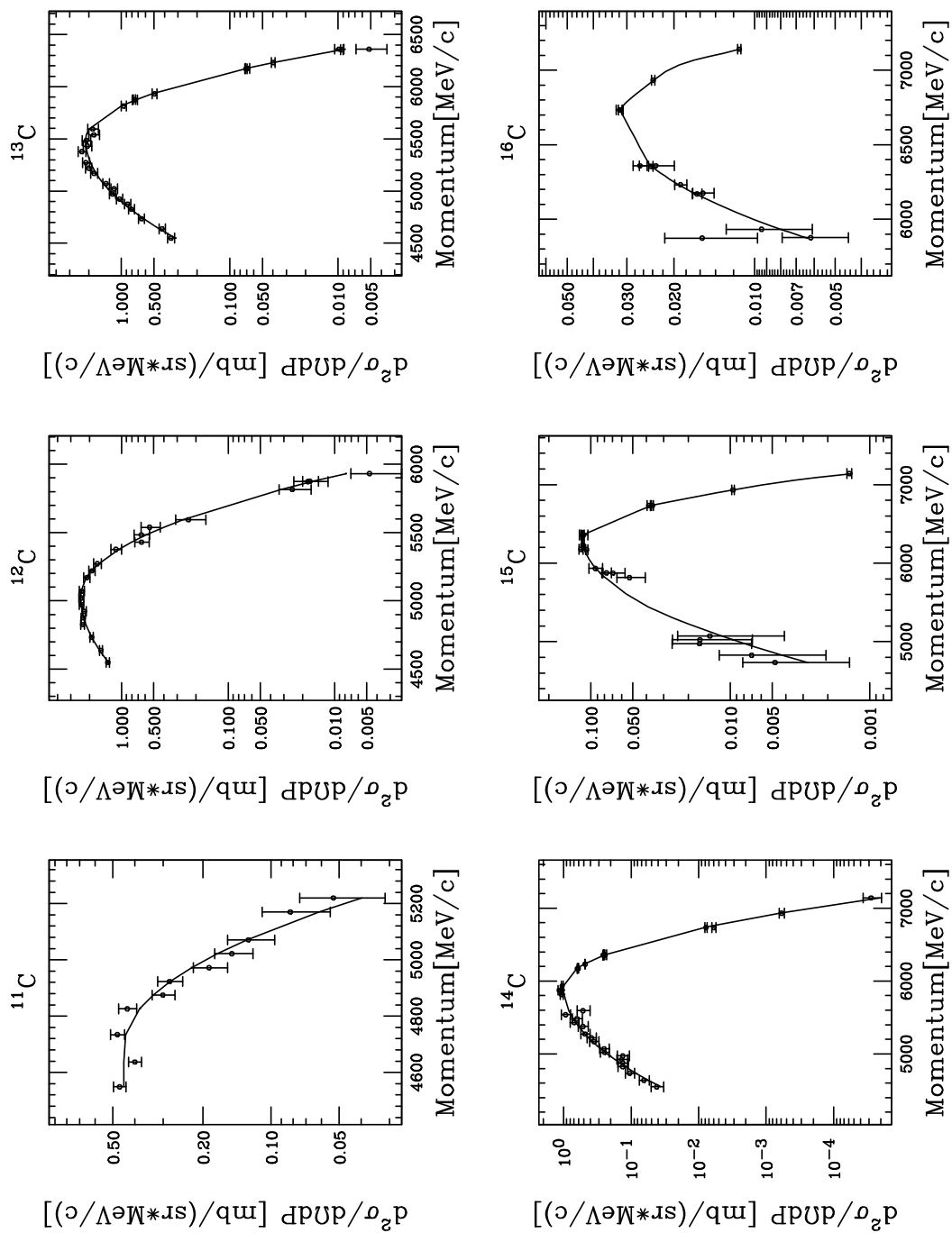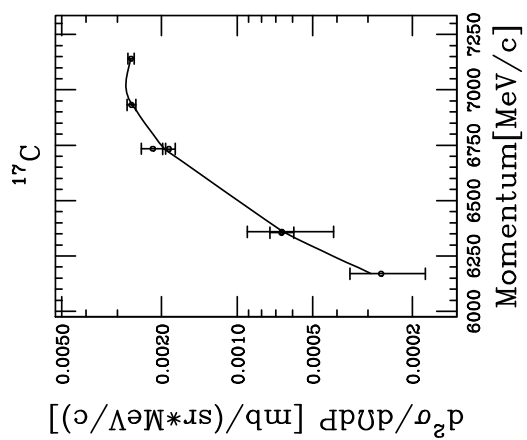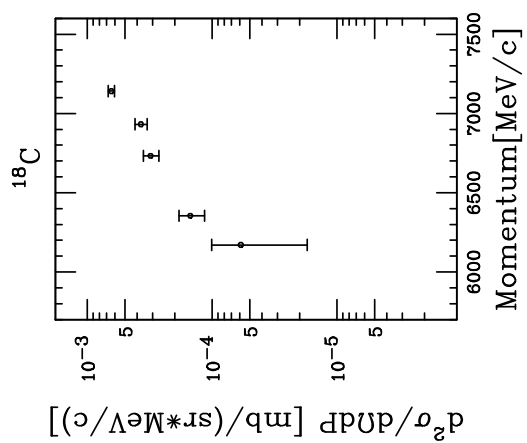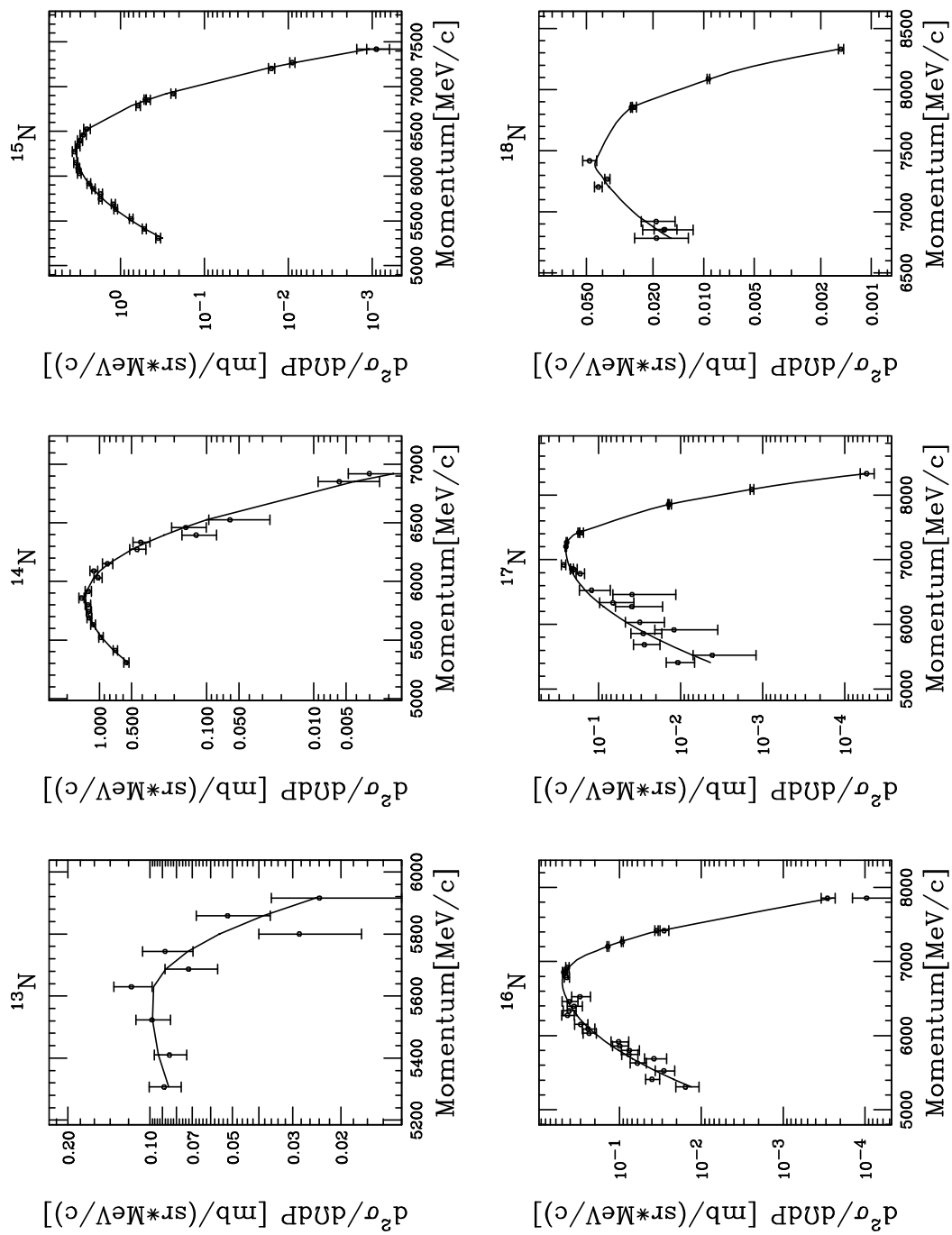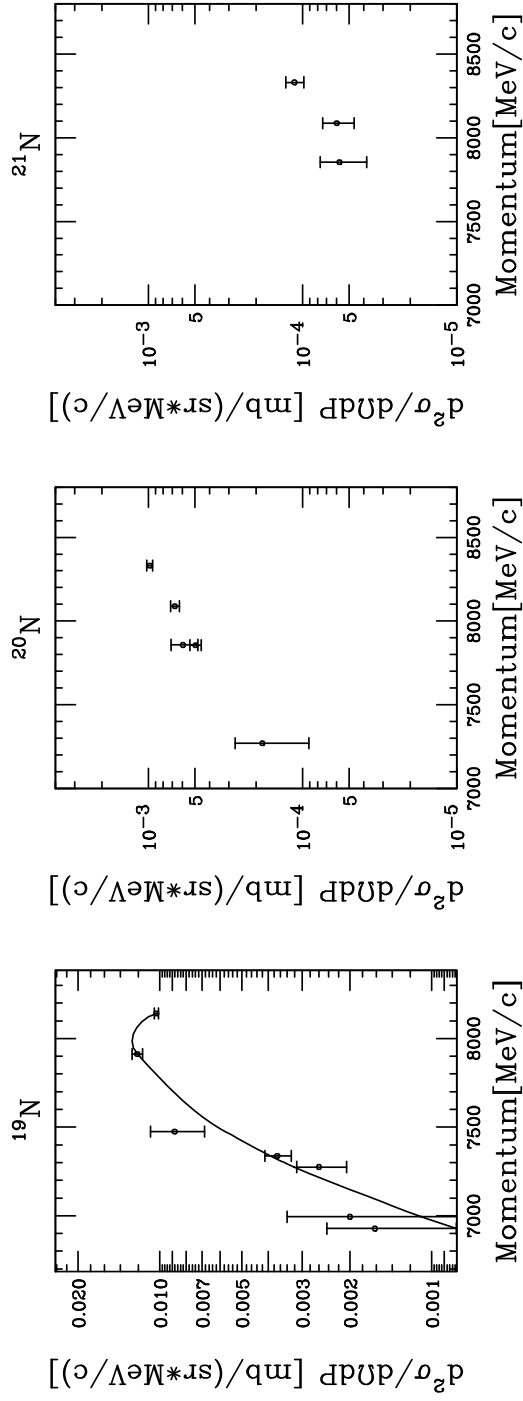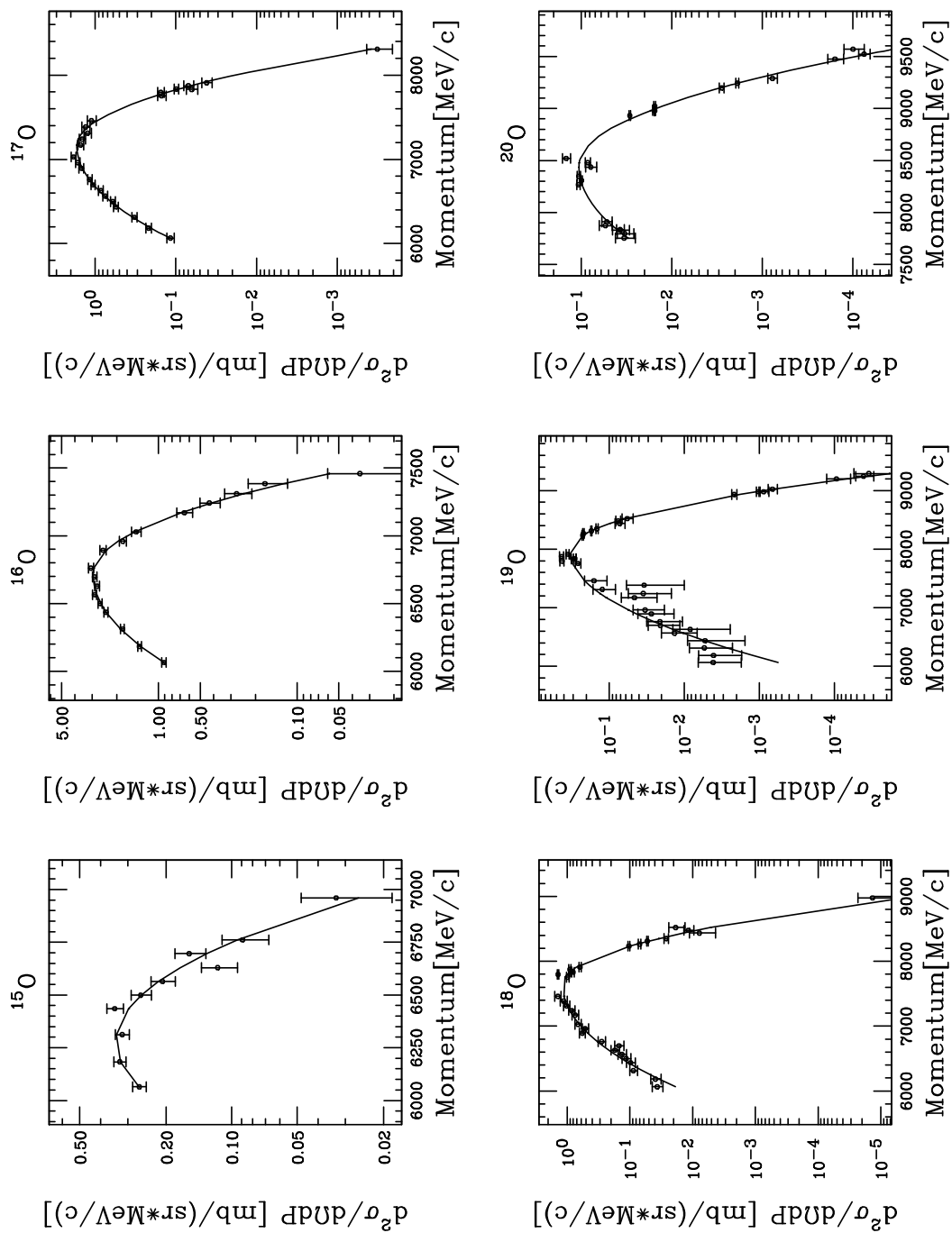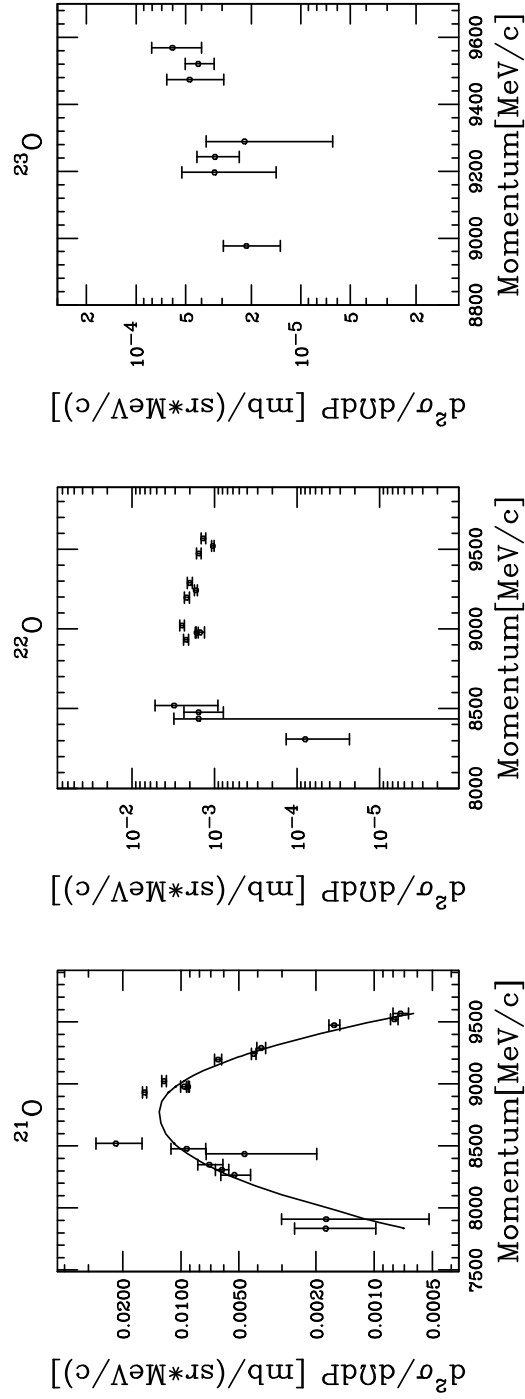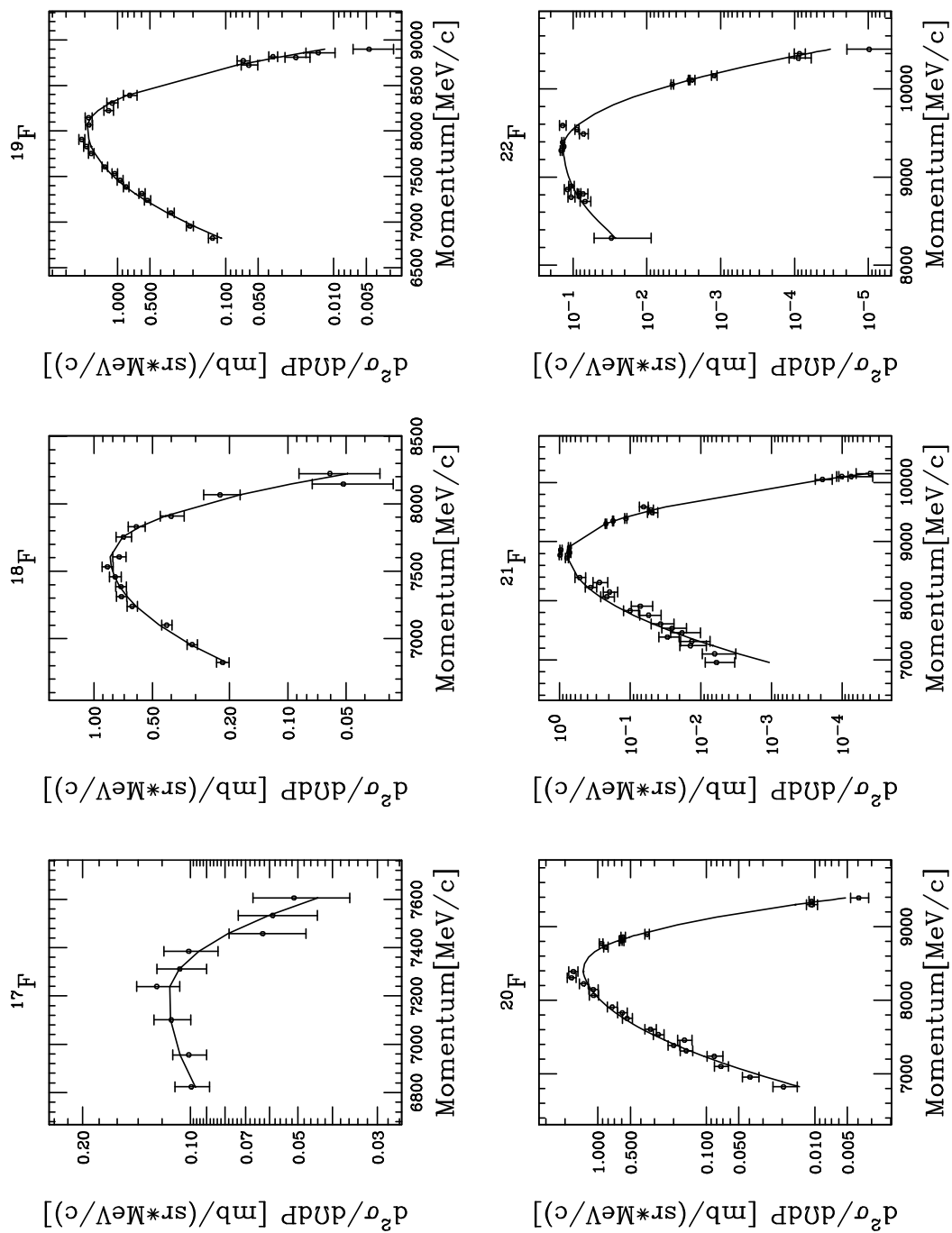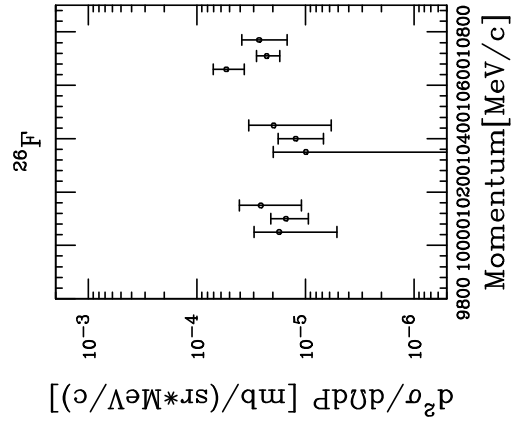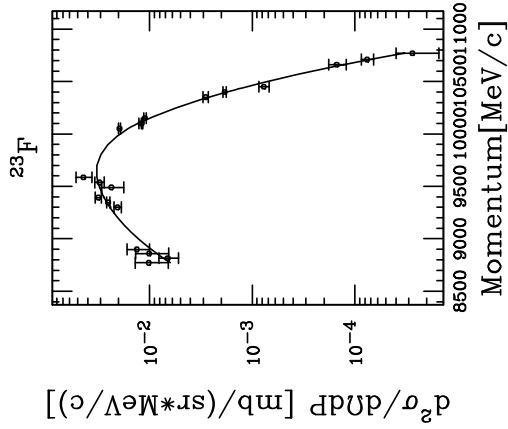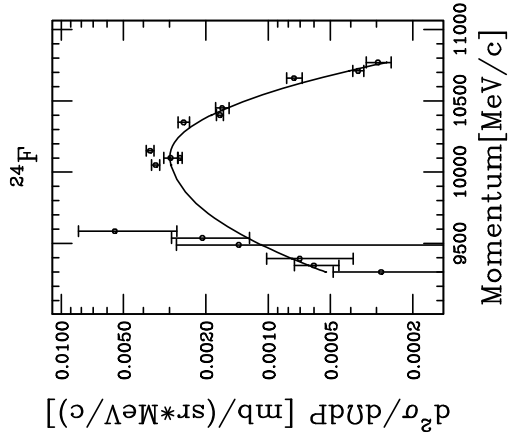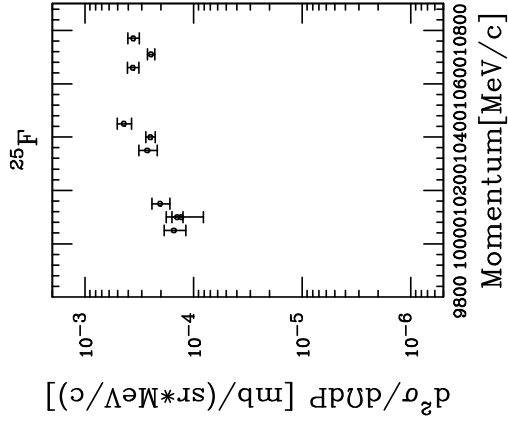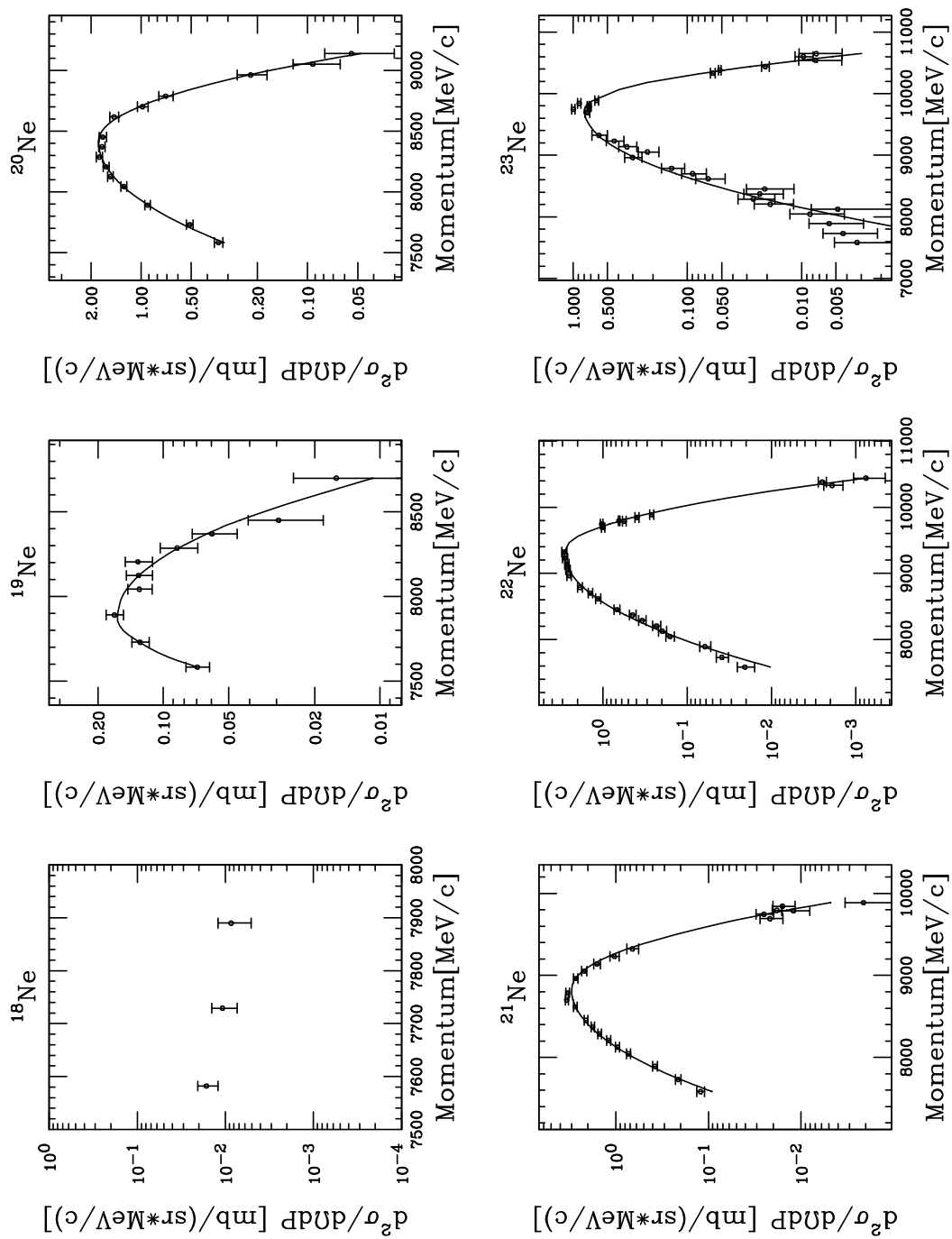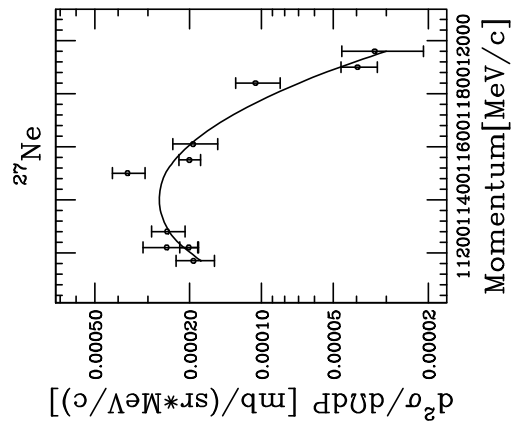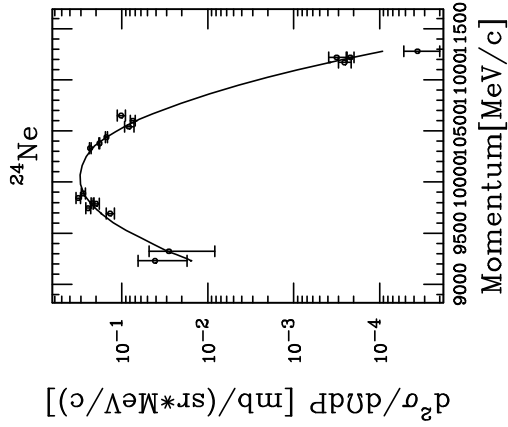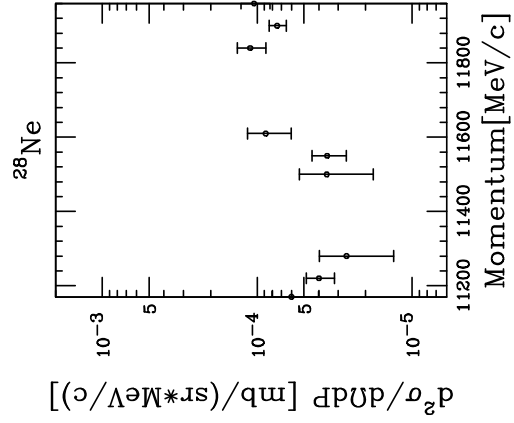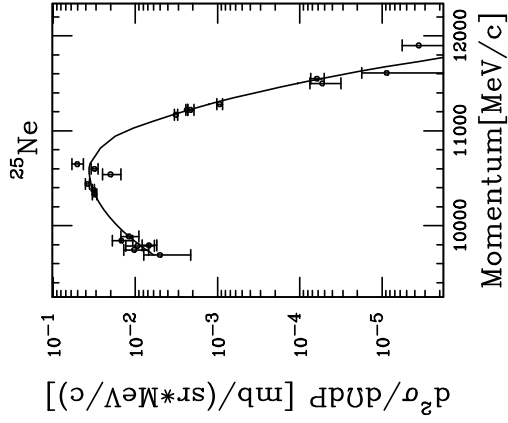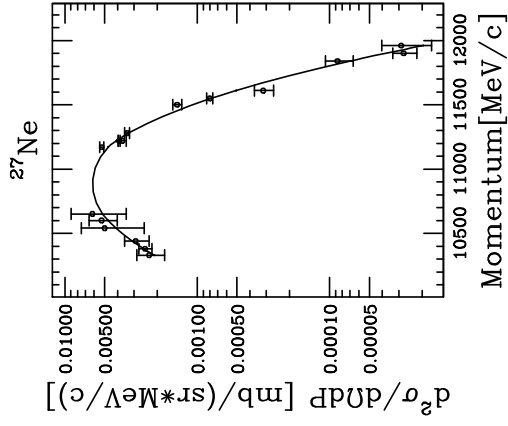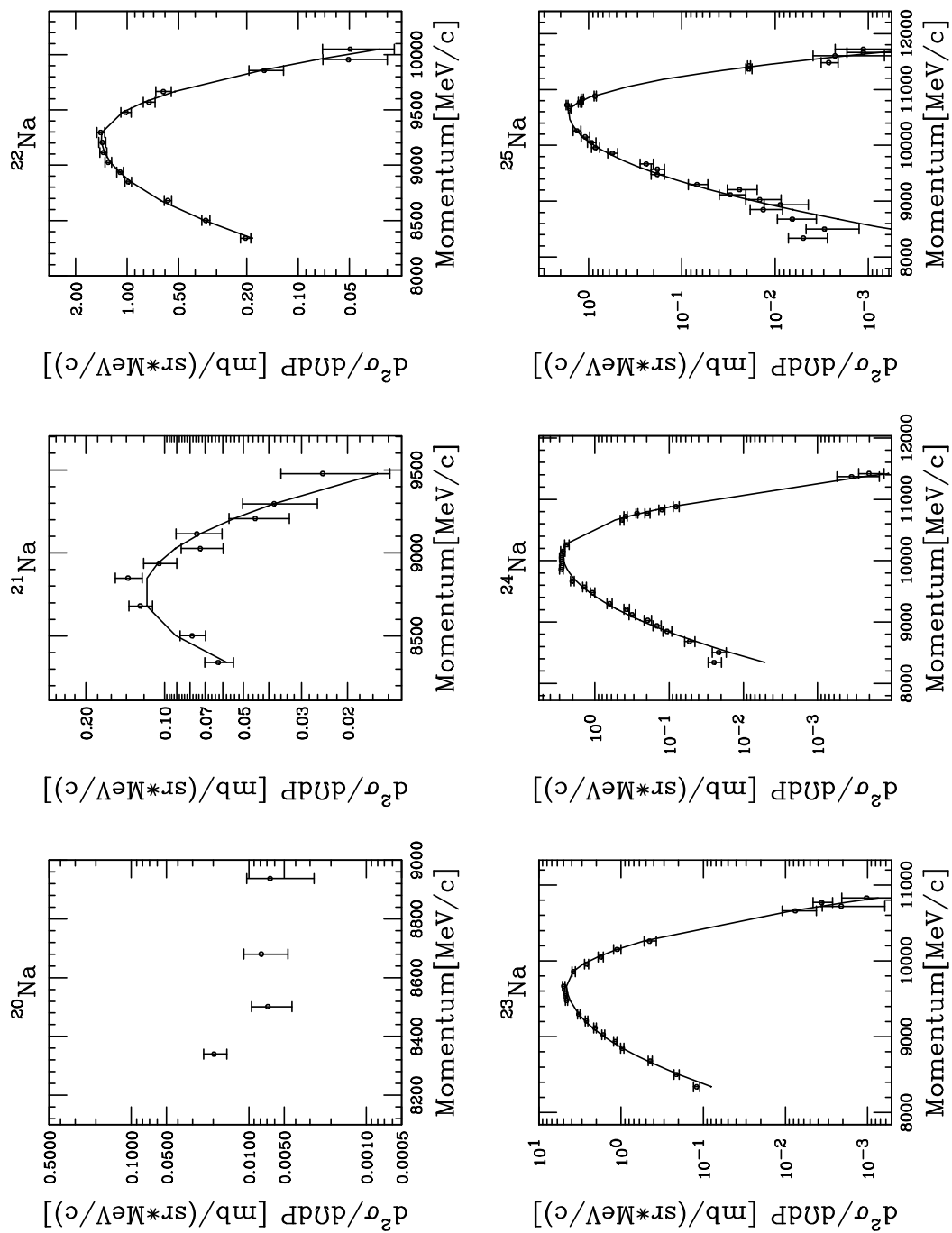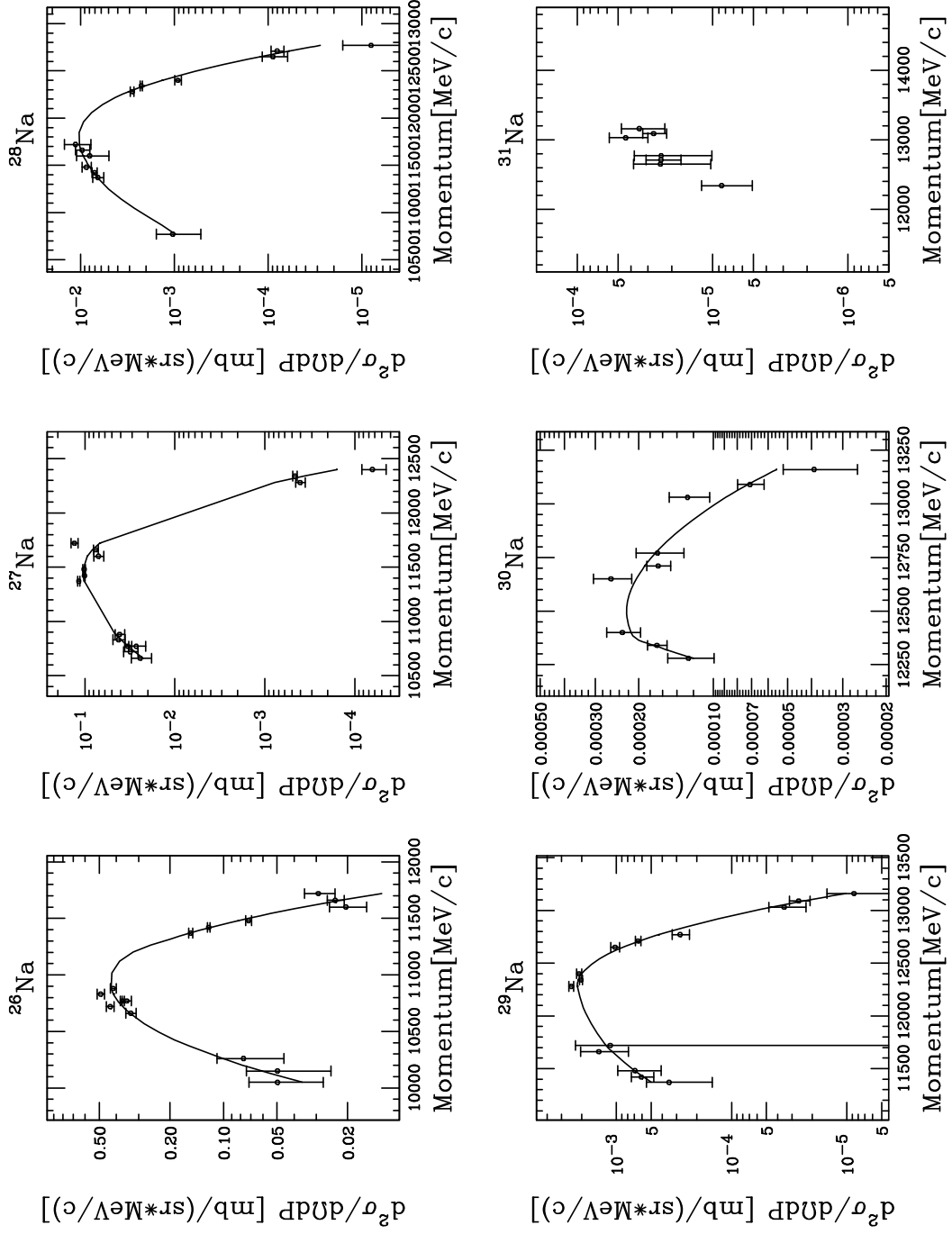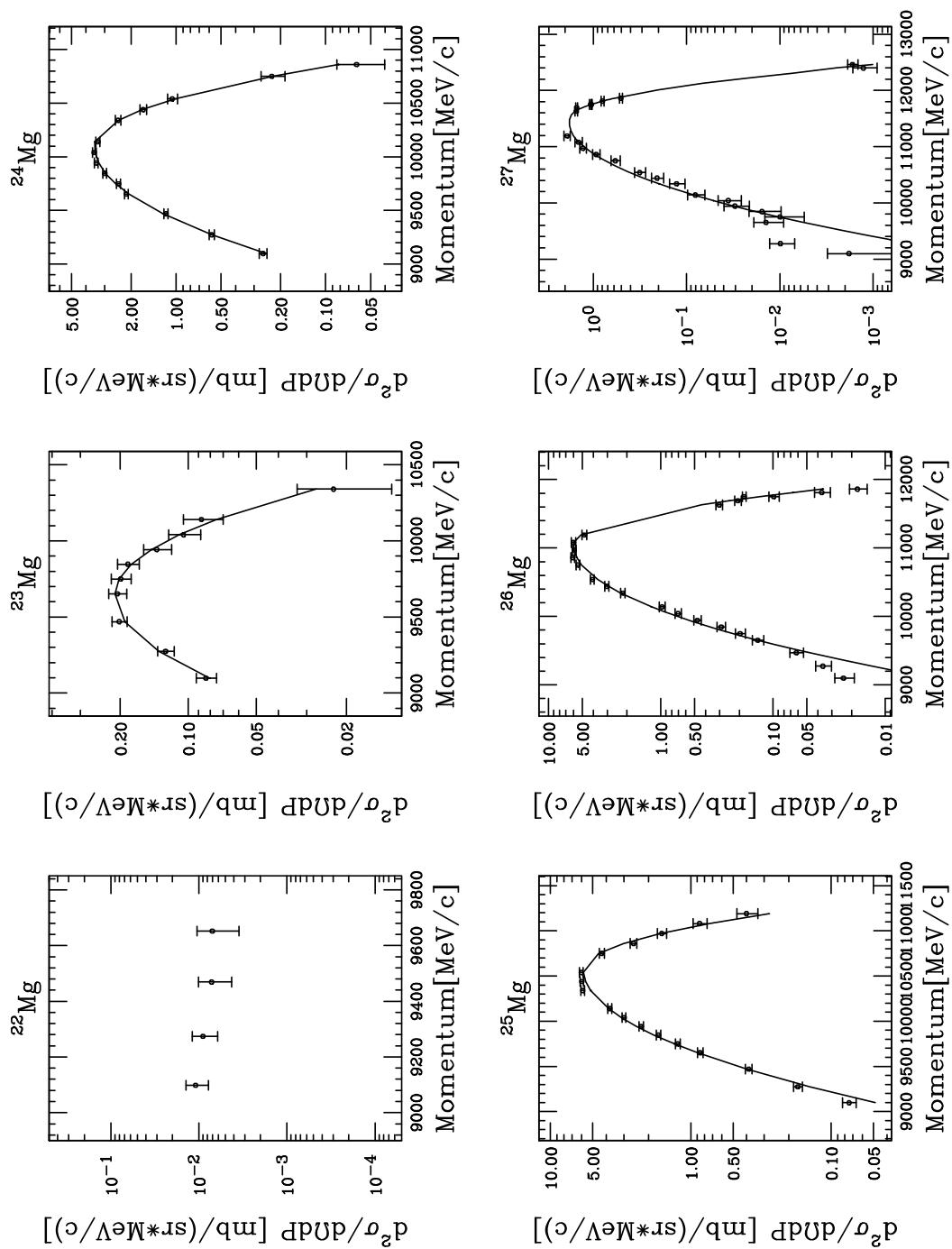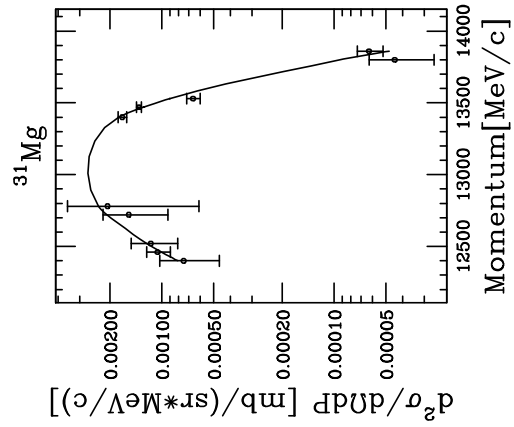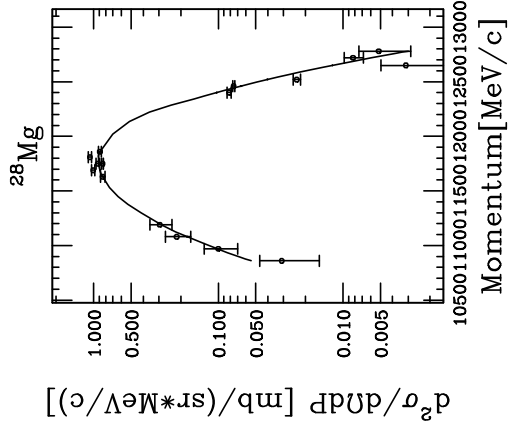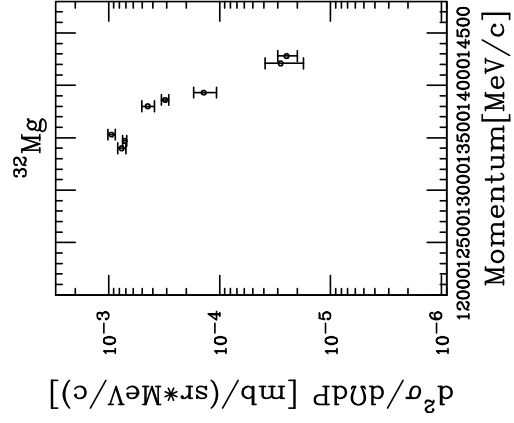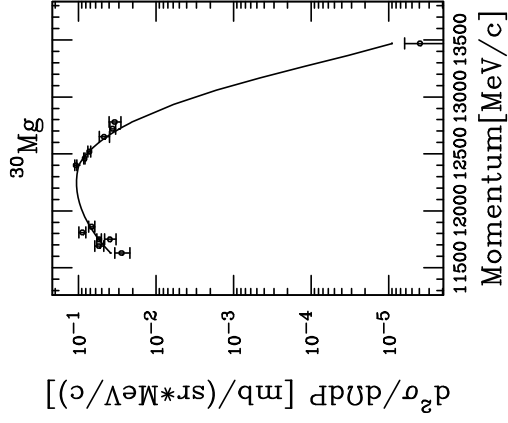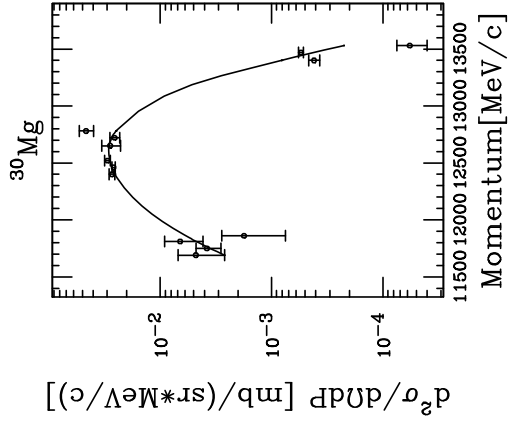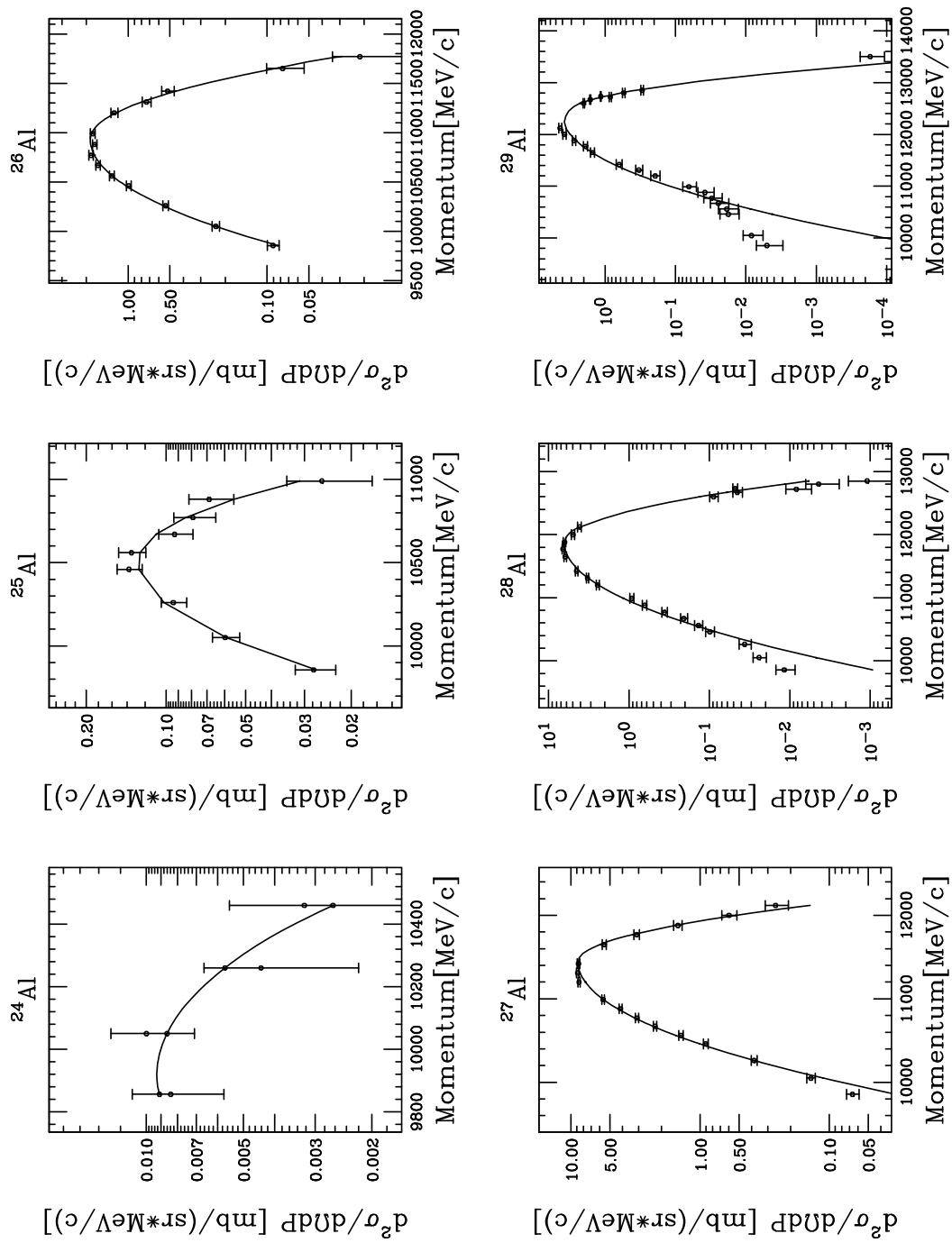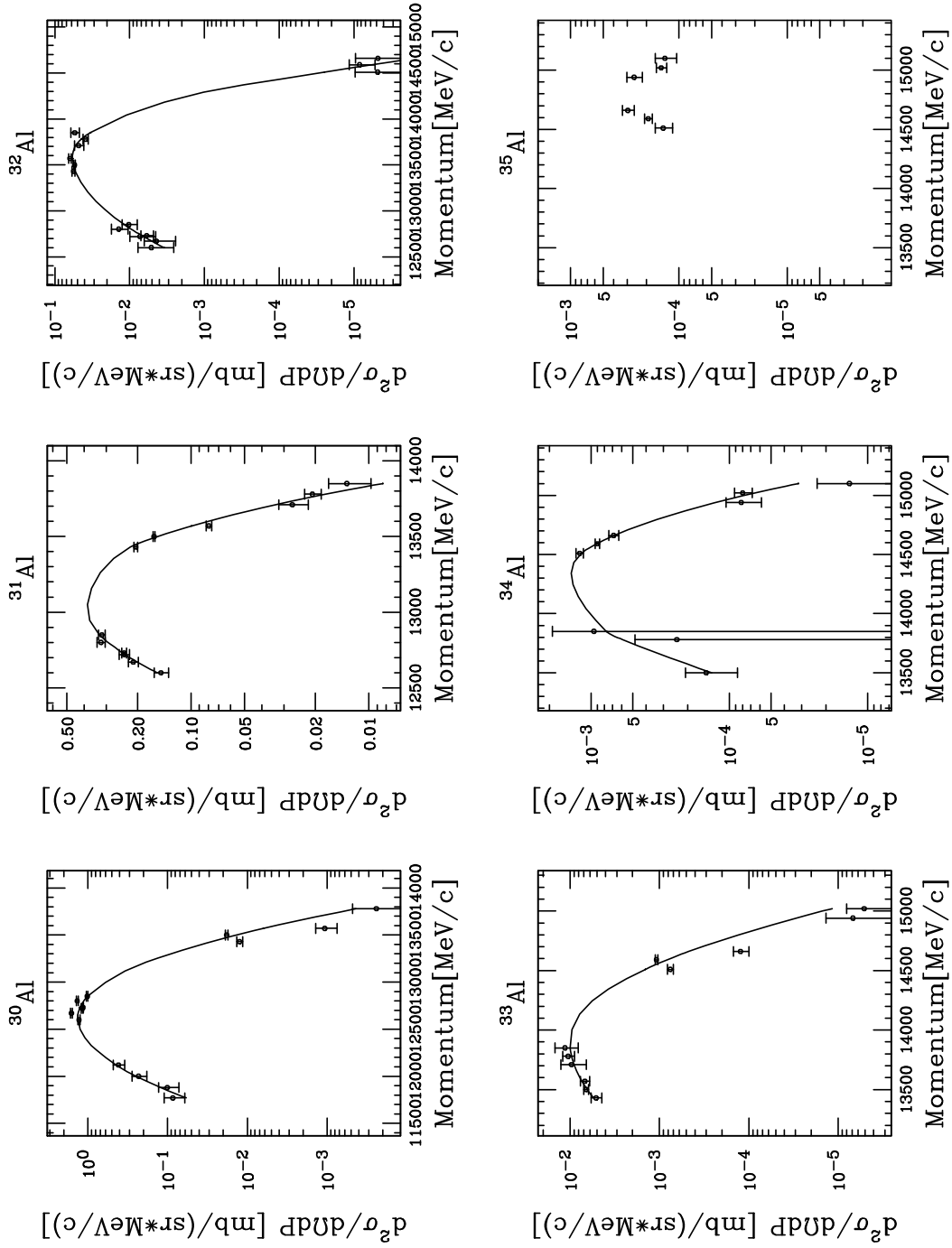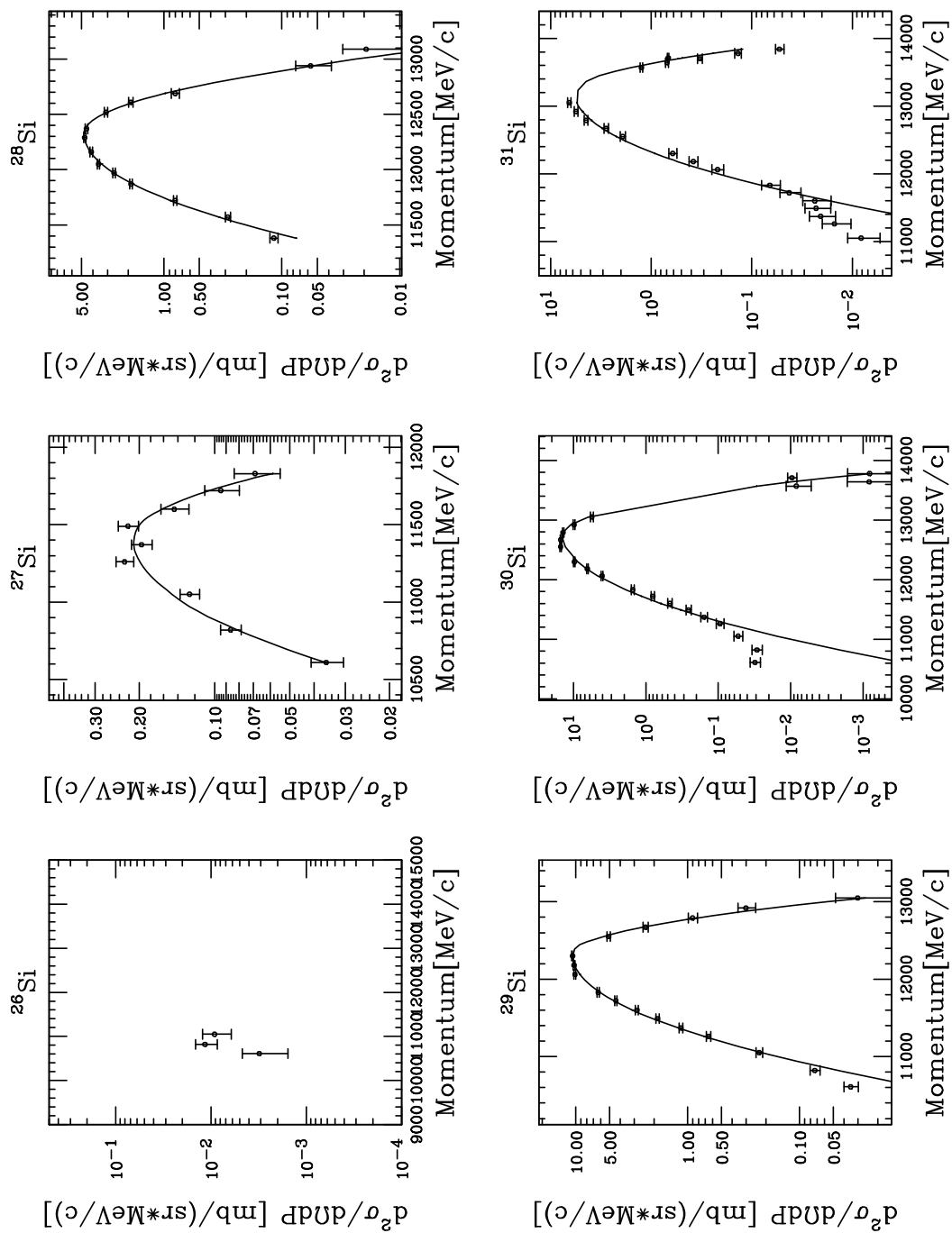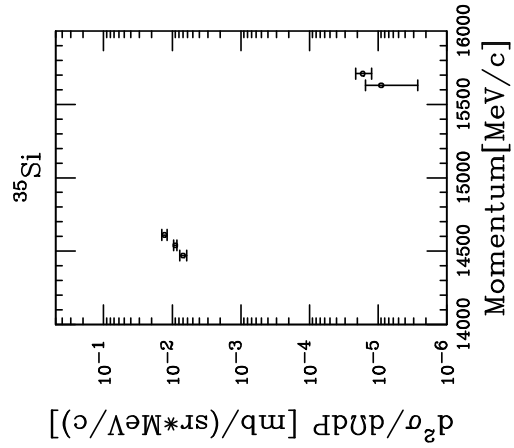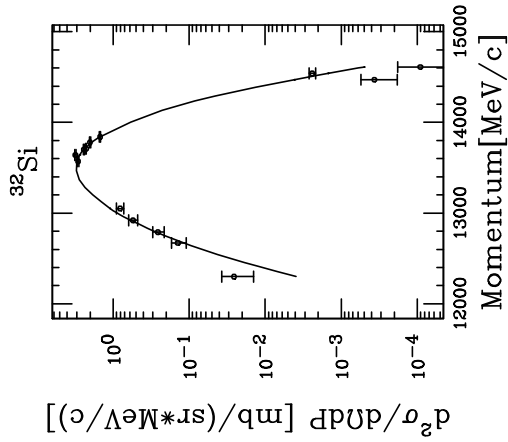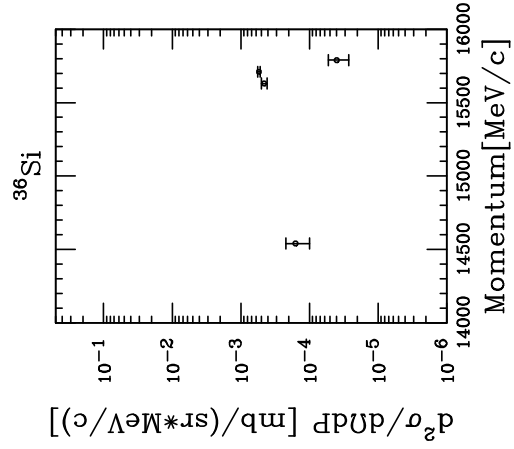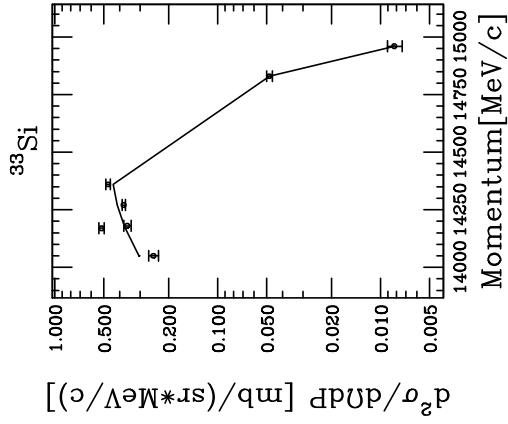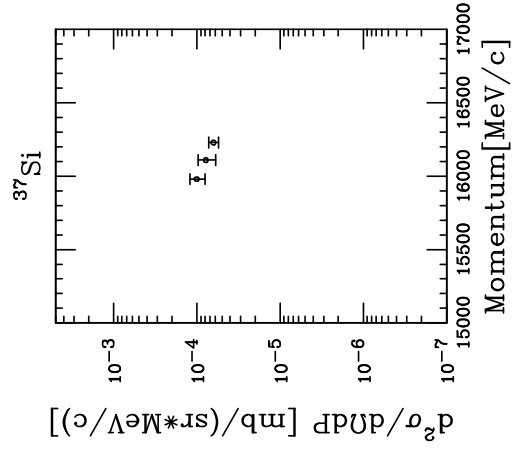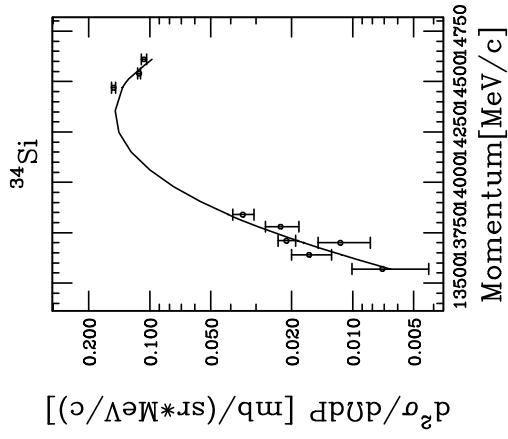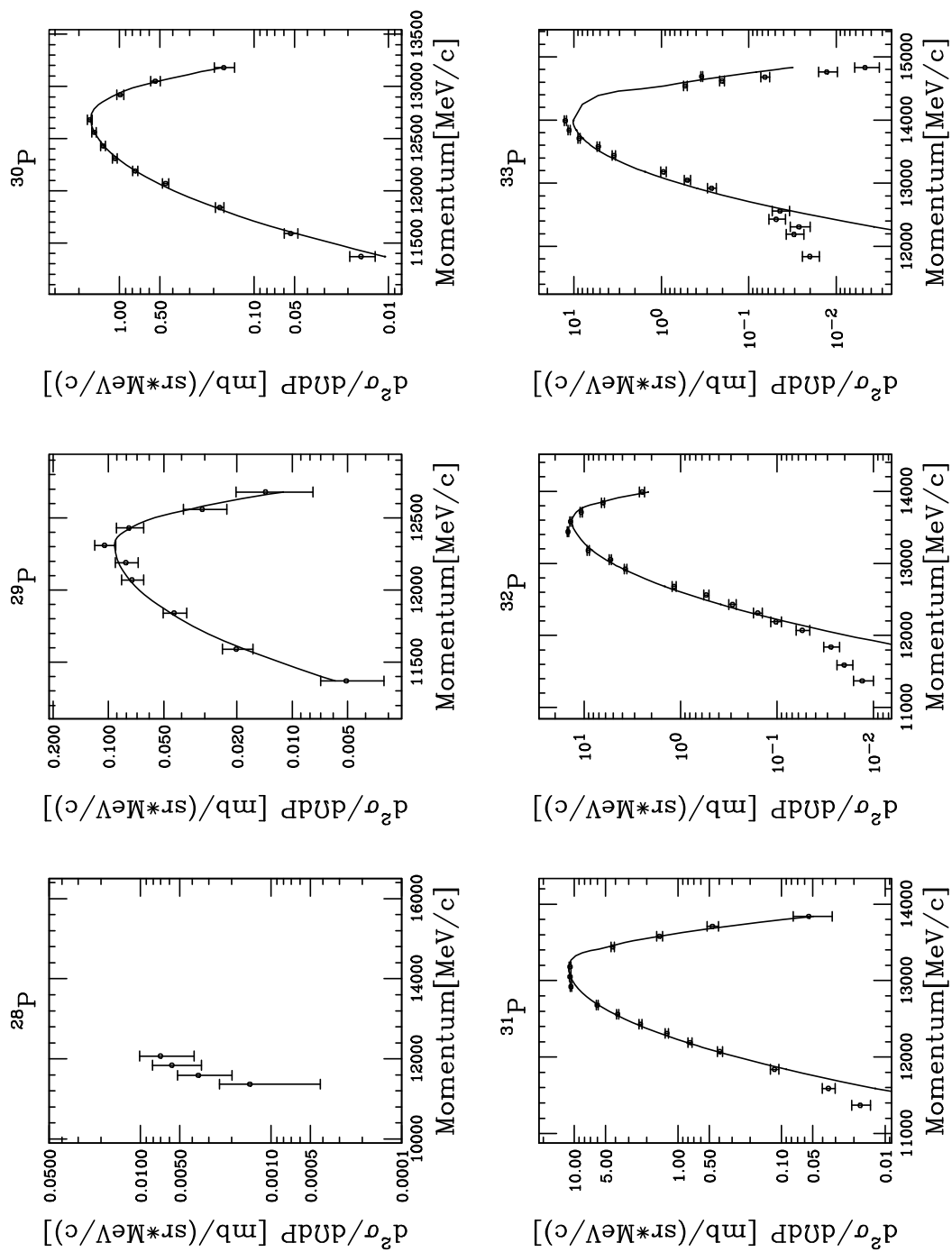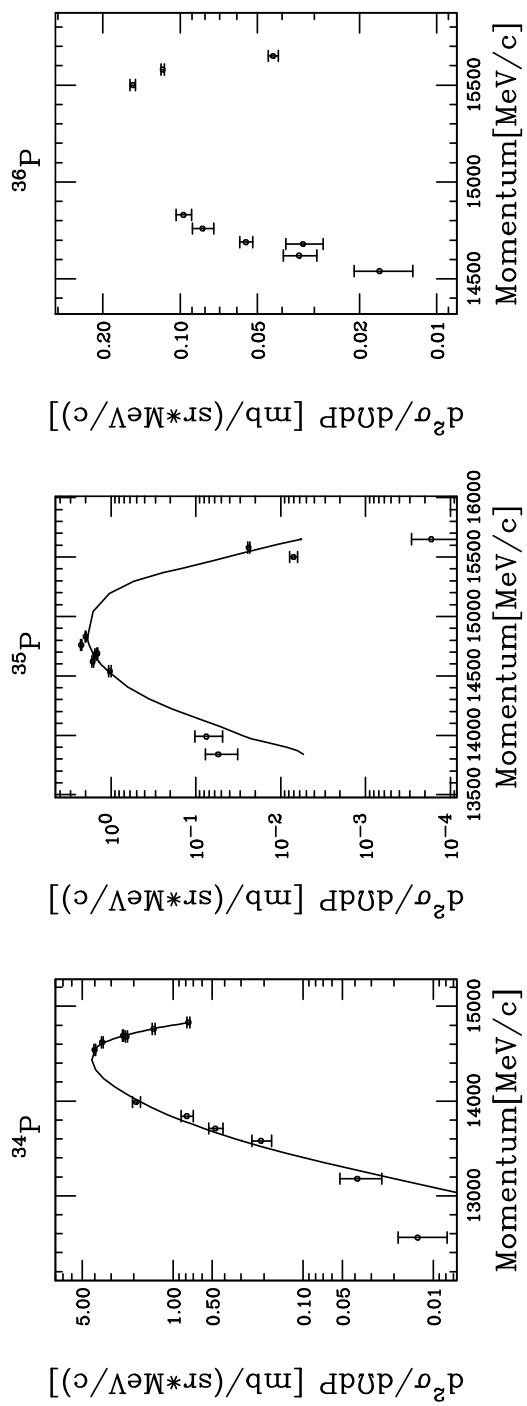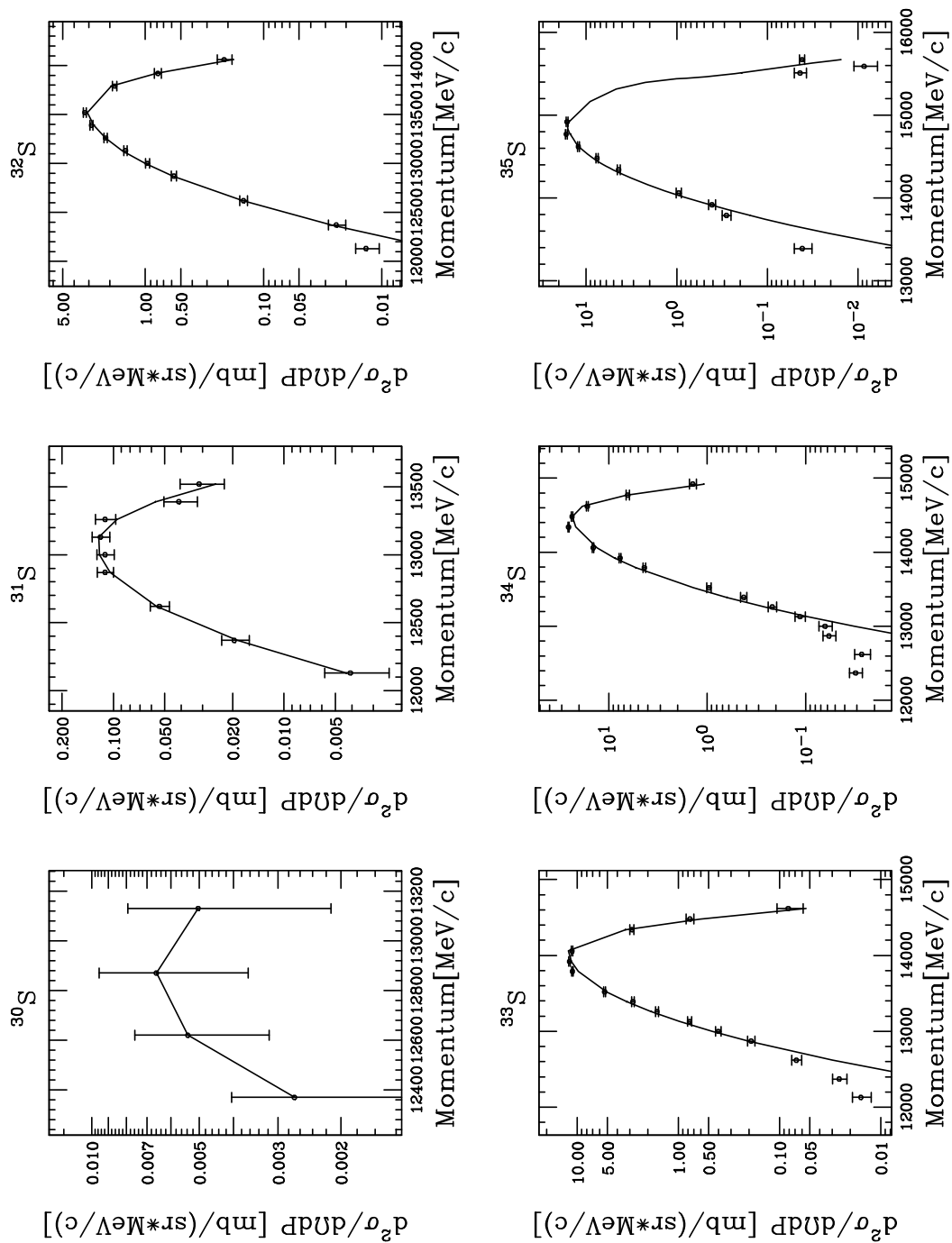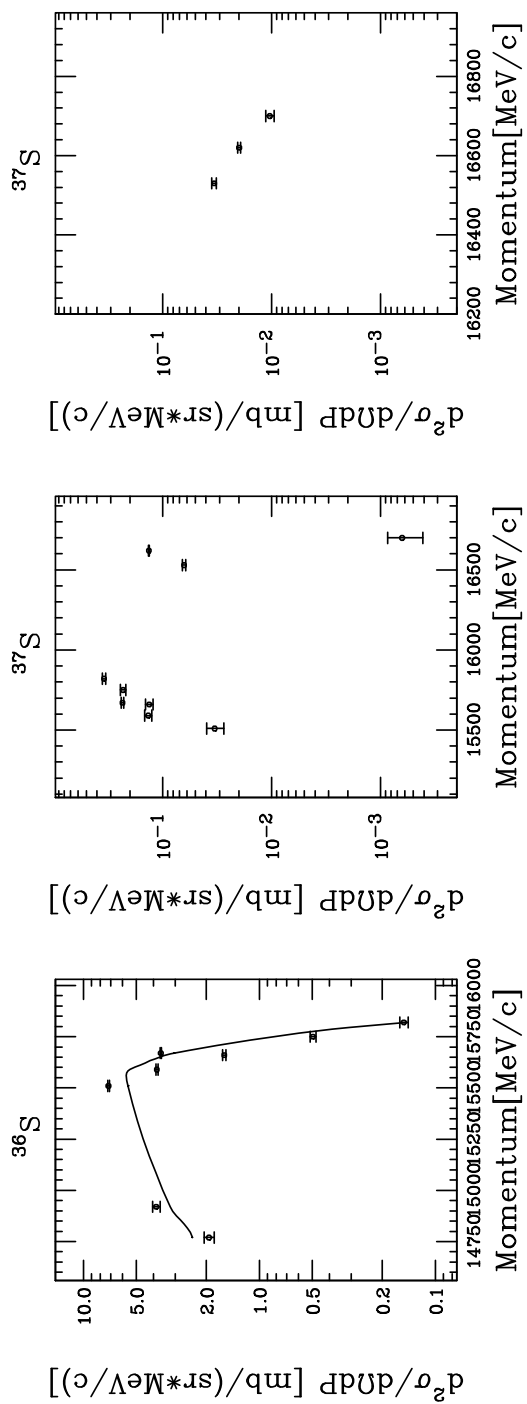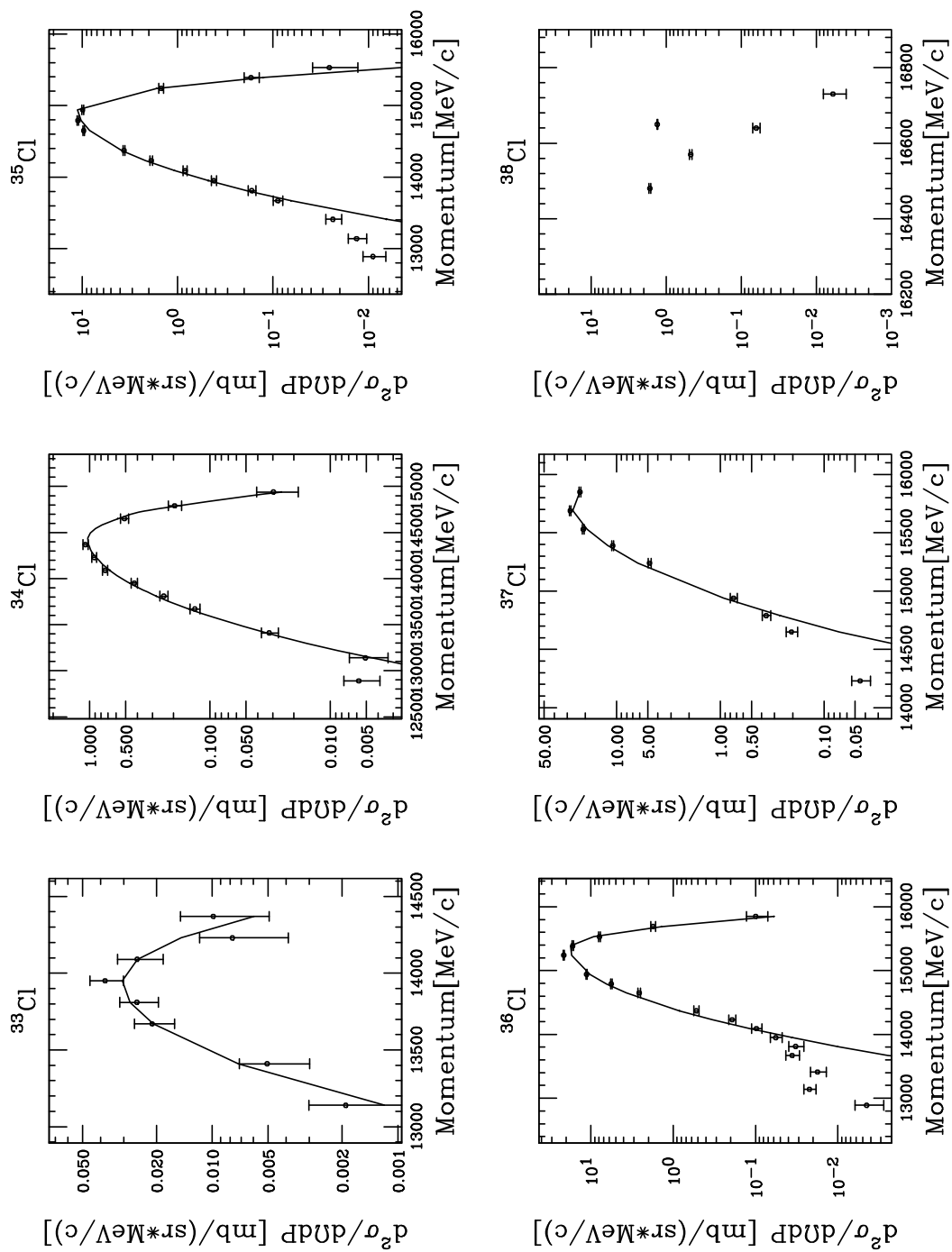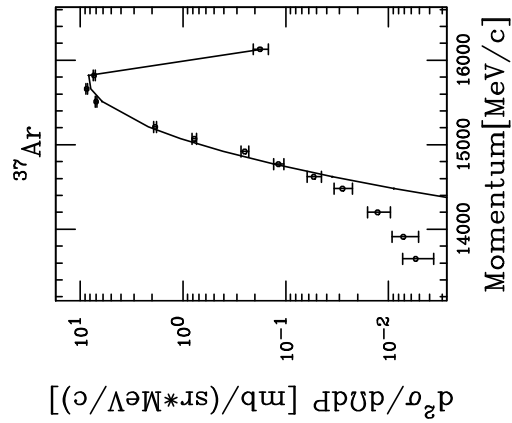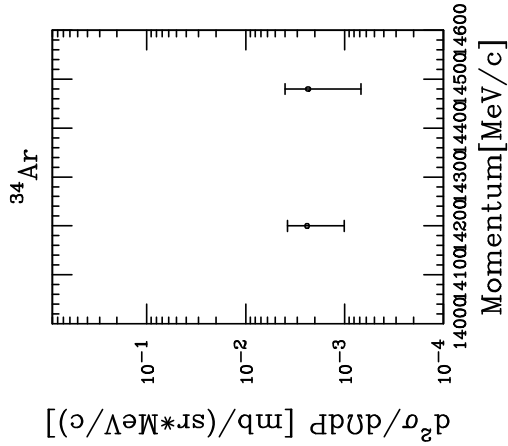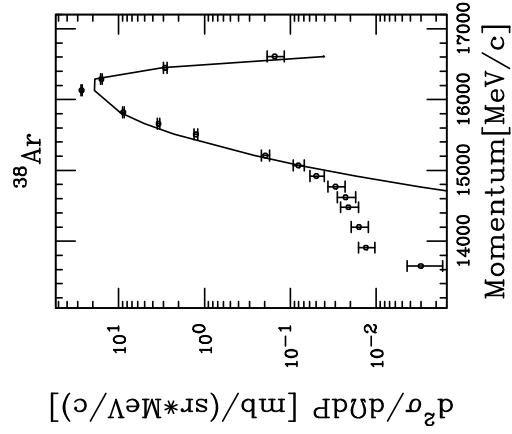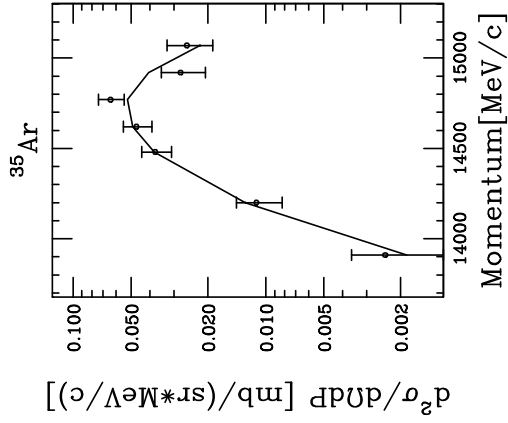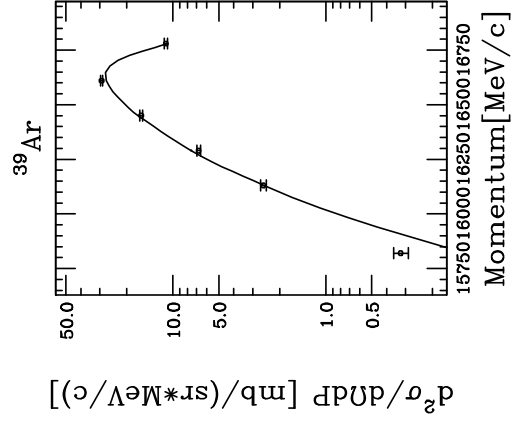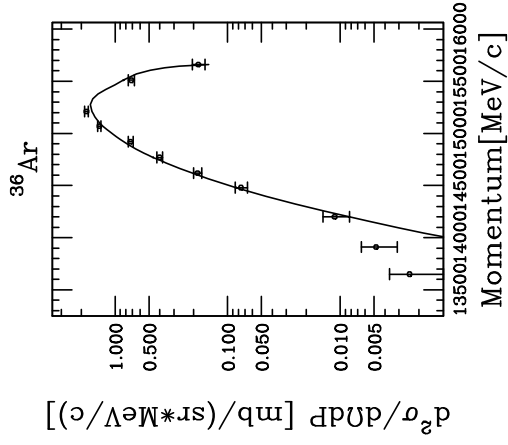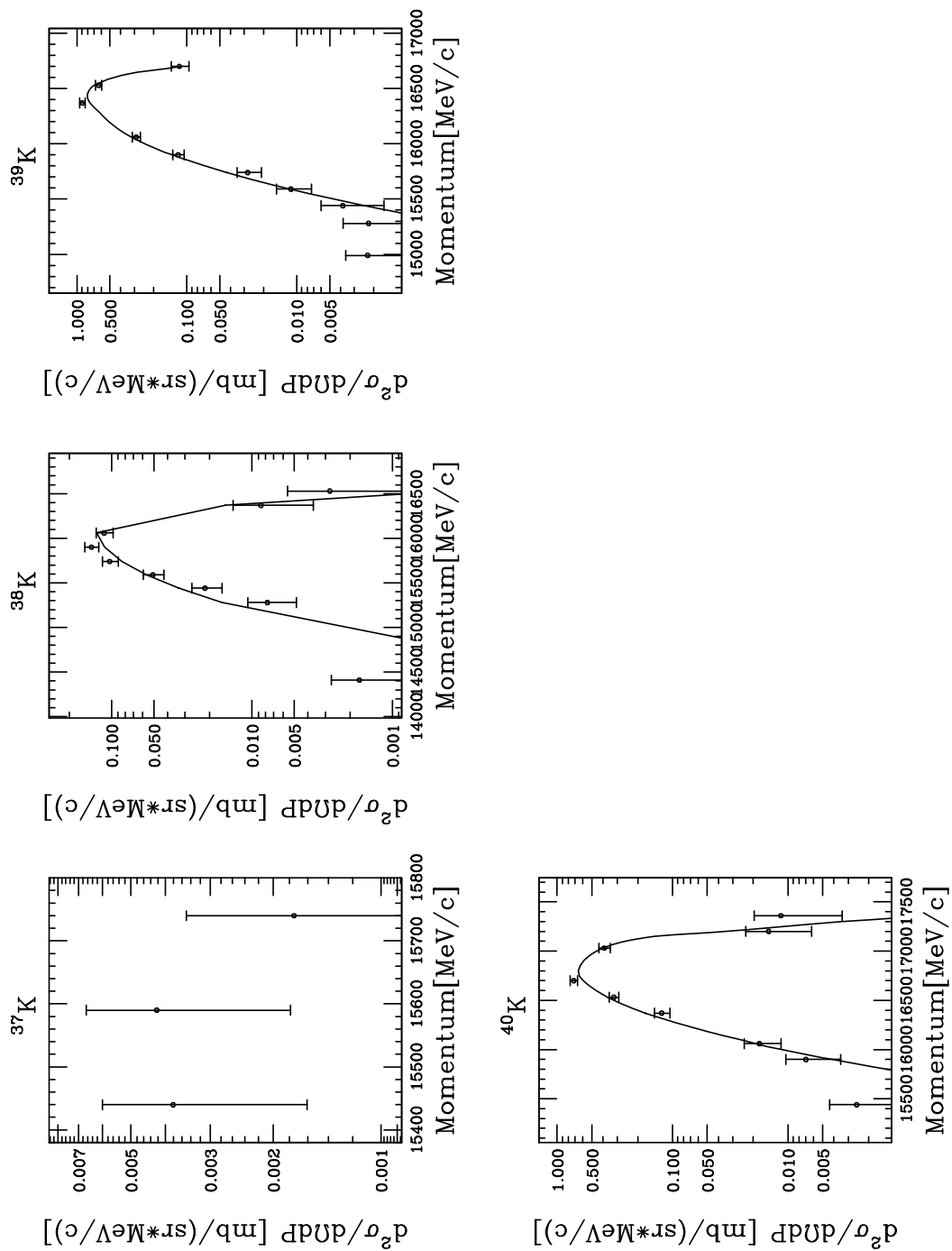
A.2.2 Fitting Results of Ta Target Data

We show the results of fitting parameters, A, P_0, σ_H and σ_L for Ta target data. We found a single component for all fragments in momentum region where the experimental data were measured.
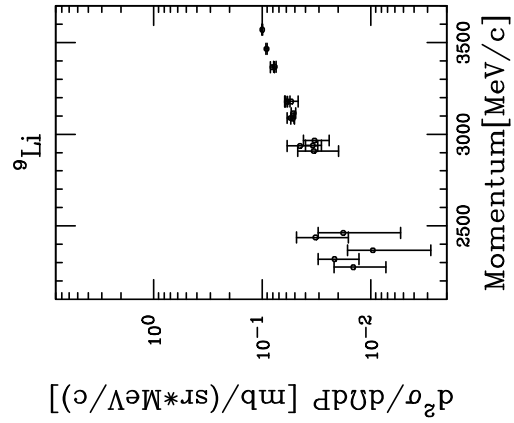
Z_f	A_f	A [$\frac{mb}{(sr \cdot MeV/c)}$]	P_0 [MeV/c]	σ_H [MeV/c]	σ_L [MeV/c]
3	6	1.523e+00(5.2e−02)	2602.7(1.1e+01)	193.7(3.7e+00)	758.3(2.6e+02)
3	7	2.456e+00(1.6e−02)	3031.3(2.6e+00)	196.7(9.2e−01)	592.5(1.3e+01)
3	8	4.665e−01(2.1e−03)	3376.6(6.5e+00)	252.4(8.8e+00)	588.9(1.8e+01)
4	9	8.060e−01(1.8e−02)	3880.2(6.1e+00)	218.8(2.0e+00)	598.9(2.1e+01)
4	10	7.267e−01(2.4e−03)	4228.5(3.2e+00)	248.2(1.7e+00)	546.8(1.0e+01)
4	11	4.234e−02(5.9e−04)	4622.4(4.6e+01)	251.9(9.0e+01)	475.6(4.7e+01)
5	10	8.027e−01(2.7e−02)	4226.6(2.3e+01)	255.5(6.9e+00)	502.1(5.8e+01)
5	11	2.238e+00(5.1e−02)	4672.4(6.9e+00)	248.9(2.2e+00)	527.7(1.3e+01)
5	12	4.173e−01(4.3e−03)	5087.0(5.1e+00)	255.9(1.8e+00)	578.2(1.3e+01)
5	13	1.363e−01(1.0e−03)	5453.5(5.8e+00)	284.2(3.5e+00)	605.6(2.9e+01)
5	14	7.636e−03(2.0e−04)	5950.5(2.4e−01)	1.0(4.8e−01)	542.0(1.8e+01)
6	12	2.422e+00(4.3e−02)	5039.6(1.6e+01)	263.4(6.8e+00)	446.9(2.3e+01)
6	13	2.143e+00(5.0e−02)	5491.2(7.6e+00)	261.2(2.3e+00)	481.2(1.0e+01)
6	14	1.008e+00(1.4e−02)	5917.6(4.7e+00)	263.4(1.7e+00)	530.9(8.1e+00)
6	15	1.149e−01(8.3e−04)	6317.3(6.3e+00)	276.3(2.8e+00)	580.9(3.2e+01)
6	16	3.207e−02(4.4e−04)	6692.4(1.4e+01)	311.9(9.2e+00)	455.7(2.2e+01)
6	17	2.919e−03(1.1e−04)	7139.3(2.3e+00)	3.9(5.3e+00)	451.9(1.6e+01)

Z_f	A_f	A [$\frac{mb}{(sr \cdot MeV/c)}$]	P_0 [MeV/c]	σ_H [MeV/c]	σ_L [MeV/c]
7	13	9.890e−02(9.7e−03)	5591.1(6.3e+01)	195.2(5.1e+01)	524.9(3.6e+02)
7	14	1.344e+00(3.0e−02)	5860.8(2.1e+01)	291.6(1.3e+01)	411.8(2.1e+01)
7	15	3.408e+00(6.1e−02)	6299.2(8.4e+00)	279.0(3.3e+00)	455.3(7.2e+00)
7	16	4.943e−01(1.5e−02)	6755.6(1.4e+01)	282.1(5.4e+00)	538.5(1.4e+01)
7	17	2.513e−01(3.5e−03)	7179.7(9.4e+00)	280.8(3.3e+00)	620.6(2.2e+01)
7	18	4.550e−02(1.4e−03)	7547.5(1.3e+01)	301.7(4.7e+00)	523.1(4.6e+01)
7	19	1.335e−02(6.4e−04)	8140.9(3.0e−01)	1.5(4.2e−01)	513.0(2.1e+01)
8	15	3.405e−01(1.7e−02)	6278.3(5.0e+01)	300.7(3.7e+01)	304.9(1.1e+02)
8	16	2.968e+00(4.5e−02)	6716.8(1.5e+01)	264.9(1.1e+01)	424.7(1.2e+01)
8	17	1.682e+00(4.4e−02)	7159.8(1.9e+01)	280.1(7.9e+00)	474.9(1.2e+01)
8	18	1.193e+00(3.3e−02)	7636.6(1.3e+01)	267.7(4.4e+00)	545.7(1.2e+01)
8	19	3.335e−01(6.3e−03)	7968.5(7.8e+00)	298.1(2.4e+00)	532.4(1.5e+01)
8	20	1.058e−01(1.6e−03)	8440.0(6.7e+00)	282.2(2.9e+00)	434.2(1.7e+01)
8	21	1.324e−02(5.3e−04)	8762.7(2.4e+01)	326.4(8.9e+00)	382.9(3.1e+01)
9	17	1.149e−01(9.0e−03)	7204.1(8.7e+01)	290.2(8.1e+01)	648.0(3.4e+02)
9	18	8.260e−01(2.4e−02)	7613.1(3.0e+01)	257.2(2.3e+01)	474.7(2.3e+01)
9	19	1.906e+00(4.5e−02)	8041.3(1.8e+01)	269.4(7.0e+00)	509.1(1.1e+01)
9	20	1.373e+00(4.1e−02)	8470.0(1.0e+01)	276.4(3.3e+00)	542.9(1.0e+01)
9	21	7.820e−01(1.0e−02)	8824.5(7.9e+00)	300.0(3.8e+00)	514.5(9.8e+00)
9	22	1.362e−01(2.2e−03)	9327.3(2.1e+01)	274.9(7.2e+00)	565.2(4.1e+01)
9	23	3.344e−02(1.1e−03)	9705.7(1.1e+01)	286.2(3.7e+00)	511.2(3.2e+01)
9	24	2.982e−03(5.7e−05)	10113.0(1.9e+01)	299.3(1.1e+01)	436.7(3.0e+01)
10	19	1.625e−01(9.8e−03)	7889.9(4.9e+01)	348.1(4.3e+01)	236.3(4.7e+01)
10	20	1.801e+00(3.5e−02)	8414.2(1.9e+01)	268.5(1.4e+01)	446.9(1.3e+01)
10	21	3.021e+00(5.5e−02)	8830.4(1.2e+01)	294.6(5.0e+00)	472.6(7.2e+00)
10	22	2.853e+00(6.1e−02)	9306.8(7.8e+00)	278.9(3.6e+00)	514.3(6.5e+00)
10	23	7.989e−01(1.5e−02)	9721.3(1.6e+01)	277.7(6.1e+00)	531.8(1.2e+01)
10	24	3.198e−01(1.1e−02)	10071.0(1.3e+01)	299.5(3.4e+00)	342.3(3.1e+01)
10	25	3.635e−02(9.7e−04)	10591.0(1.9e+01)	266.1(8.4e+00)	471.7(2.5e+01)
10	26	6.584e−03(7.6e−04)	10920.0(5.0e+01)	304.8(1.5e+01)	391.6(6.4e+01)
10	27	2.723e−04(3.0e−05)	11396.0(6.5e+01)	268.5(3.2e+01)	248.1(1.3e+02)

Z_f	A_f	A $[\frac{mb}{(sr \cdot MeV/c)}]$	P_0 [MeV/c]	σ_H [MeV/c]	σ_L [MeV/c]
11	21	1.203e−01(8.0e−03)	8763.1(5.4e+01)	352.6(4.8e+01)	349.8(6.2e+01)
11	22	1.424e+00(3.0e−02)	9259.1(2.0e+01)	288.5(1.5e+01)	455.1(1.3e+01)
11	23	4.628e+00(6.9e−02)	9691.6(9.6e+00)	272.3(5.6e+00)	474.9(5.5e+00)
11	24	2.773e+00(6.5e−02)	10146.0(1.4e+01)	283.1(6.8e+00)	509.1(7.6e+00)
11	25	1.619e+00(3.9e−02)	10579.0(1.2e+01)	276.3(3.5e+00)	521.1(9.9e+00)
11	26	4.353e−01(9.0e−03)	10954.0(1.6e+01)	288.6(1.0e+01)	405.0(2.8e+01)
11	27	1.049e−01(1.4e−03)	11484.0(2.1e+01)	254.1(6.6e+00)	469.7(1.9e+01)
11	28	1.073e−02(8.2e−04)	11865.0(2.2e+01)	262.1(8.5e+00)	499.9(6.1e+01)
11	29	2.179e−03(7.1e−05)	12292.0(3.2e+01)	265.1(1.5e+01)	537.0(4.5e+01)
12	23	2.110e−01(1.0e−02)	9649.3(5.2e+01)	341.2(4.4e+01)	396.9(5.1e+01)
12	24	3.524e+00(4.9e−02)	10103.0(1.3e+01)	275.8(9.9e+00)	436.6(7.3e+00)
12	25	5.837e+00(8.6e−02)	10572.0(1.0e+01)	250.6(7.9e+00)	476.1(5.2e+00)
12	26	6.016e+00(9.9e−02)	11047.0(1.2e+01)	254.1(4.6e+00)	507.1(5.6e+00)
12	27	1.876e+00(5.3e−02)	11478.0(9.4e+00)	253.3(3.5e+00)	536.0(9.6e+00)
12	28	9.186e−01(9.9e−03)	11786.0(1.6e+01)	293.7(7.3e+00)	389.5(1.7e+01)
12	29	1.085e−01(7.0e−03)	12275.0(3.2e+01)	275.6(1.0e+01)	449.1(5.1e+01)
12	30	2.911e−02(9.6e−04)	12617.0(3.8e+01)	292.7(1.4e+01)	423.1(2.7e+01)
12	31	3.200e−03(7.3e−04)	13128.0(6.7e+01)	252.7(1.9e+01)	438.9(9.2e+01)
13	24	9.097e−03(1.7e−03)	9941.1(1.0e+00)	−329.9(1.0e+00)	1593.3(1.0e+00)
13	25	1.275e−01(7.9e−03)	10510.0(5.2e+01)	286.6(4.7e+01)	371.4(4.0e+01)
13	26	1.872e+00(3.5e−02)	10929.0(1.7e+01)	291.3(1.3e+01)	430.6(9.3e+00)
13	27	8.828e+00(1.1e−01)	11438.0(8.5e+00)	237.0(6.0e+00)	470.0(4.2e+00)
13	28	6.397e+00(9.8e−02)	11872.0(1.1e+01)	261.2(3.8e+00)	479.6(5.5e+00)
13	29	4.002e+00(9.5e−02)	12362.0(8.4e+00)	223.9(4.4e+00)	514.2(7.2e+00)
13	30	1.332e+00(2.3e−02)	12634.0(1.4e+01)	286.1(4.3e+00)	345.4(1.3e+01)
13	31	4.380e−01(1.9e−02)	13129.0(1.5e+01)	256.2(7.6e+00)	367.6(2.6e+01)
13	32	5.846e−02(1.0e−03)	13611.0(2.0e+01)	228.1(6.9e+00)	425.3(1.6e+01)
13	33	1.010e−02(1.2e−03)	13919.0(4.2e+01)	299.3(1.6e+01)	439.2(9.0e+01)
13	34	1.631e−03(3.9e−04)	14270.0(9.8e+01)	295.5(3.0e+01)	344.5(6.9e+01)

Z_f	A_f	A $[\frac{mb}{(sr \cdot MeV/c)}]$	P_0 [MeV/c]	σ_H [MeV/c]	σ_L [MeV/c]
14	26	1.409e−02(1.6e−02)	10938.0(4.6e+02)	121.8(6.6e+02)	188.7(2.0e+02)
14	27	2.112e−01(1.0e−02)	11408.0(4.1e+01)	263.7(3.8e+01)	424.1(3.0e+01)
14	28	4.764e+00(5.7e−02)	12323.0(7.5e+00)	206.1(6.1e+00)	327.5(4.1e+00)
14	29	1.069e+01(1.2e−01)	12306.0(7.9e+00)	214.2(5.1e+00)	449.5(3.8e+00)
14	30	1.431e+01(1.5e−01)	12752.0(6.0e+00)	232.6(2.9e+00)	459.9(3.3e+00)
14	31	5.711e+00(1.2e−01)	13192.0(8.8e+00)	233.9(4.2e+00)	466.6(5.9e+00)
14	32	3.008e+00(5.5e−02)	13531.0(8.4e+00)	258.4(2.9e+00)	337.9(8.4e+00)
14	33	4.470e−01(1.1e−02)	14445.0(2.3e+01)	182.2(1.0e+01)	449.9(4.6e+01)
14	34	1.526e−01(8.1e−03)	14330.0(3.6e+01)	296.4(3.1e+01)	302.8(2.2e+01)
15	29	9.262e−02(6.8e−03)	12319.0(4.8e+01)	175.9(3.5e+01)	403.4(3.2e+01)
15	30	1.636e+00(3.9e−02)	12717.0(1.7e+01)	218.1(1.3e+01)	424.4(8.6e+00)
15	31	1.136e+01(1.3e−01)	13174.0(8.3e+00)	201.8(5.1e+00)	428.9(3.9e+00)
15	32	1.341e+01(1.5e−01)	13620.0(7.0e+00)	194.0(5.5e+00)	446.7(3.7e+00)
15	33	1.014e+01(1.8e−01)	14011.0(8.7e+00)	241.3(3.5e+00)	427.7(4.7e+00)
15	34	4.024e+00(7.4e−02)	14518.0(6.5e+00)	169.4(3.5e+00)	410.5(8.1e+00)
15	35	1.892e+00(2.6e−02)	14852.0(9.8e+00)	234.7(3.6e+00)	295.5(1.0e+01)
15	36	1.559e−01(3.6e−03)	15517.0(5.1e+00)	83.5(3.6e+00)	566.4(1.4e+01)
16	30	6.599e−03(2.7e−03)	12849.0(5.5e+02)	381.2(9.9e+02)	358.1(4.1e+02)
16	31	1.237e−01(7.8e−03)	13085.0(5.1e+01)	243.9(4.3e+01)	368.7(3.0e+01)
16	32	3.151e+00(5.8e−02)	13601.0(1.1e+01)	192.0(7.6e+00)	398.1(5.5e+00)
16	33	1.216e+01(1.5e−01)	14072.0(8.4e+00)	166.7(4.7e+00)	419.1(3.8e+00)
16	34	2.343e+01(2.1e−01)	14505.0(4.6e+00)	167.5(3.1e+00)	414.4(2.6e+00)
16	35	1.570e+01(2.3e−01)	14883.0(8.6e+00)	211.3(2.9e+00)	359.8(4.4e+00)
16	36	5.598e+00(1.1e−01)	15566.0(5.1e+00)	94.0(2.6e+00)	612.4(2.2e+01)
16	37	2.707e+00(2.1e−02)	15802.0(1.2e+01)	180.7(3.9e+00)	394.7(1.6e+01)

Z_f	A_f	A [$\frac{mb}{(sr \cdot MeV/c)}$]	P_0 [MeV/c]	σ_H [MeV/c]	σ_L [MeV/c]
17	33	3.048e−02(4.0e−03)	13948.0(6.4e+01)	233.7(5.9e+01)	317.0(4.2e+01)
17	34	1.042e+00(3.3e−02)	14459.0(1.7e+01)	176.4(1.2e+01)	400.0(9.4e+00)
17	35	1.124e+01(1.6e−01)	14957.0(1.0e+01)	144.5(5.2e+00)	400.8(4.4e+00)
17	36	1.794e+01(1.9e−01)	15365.0(4.9e+00)	143.7(3.1e+00)	401.9(3.0e+00)
17	37	2.959e+01(3.9e−01)	15850.0(4.5e−02)	0.2(5.4e−02)	345.6(2.2e+00)
18	35	5.255e−02(5.4e−03)	14740.0(5.9e+01)	249.9(6.7e+01)	321.1(3.5e+01)
18	36	1.714e+00(4.9e−02)	15335.0(1.2e+01)	146.6(8.2e+00)	347.9(6.6e+00)
18	37	8.470e+00(1.2e−01)	15795.0(1.4e+01)	119.8(5.3e+00)	355.3(6.3e+00)
18	38	2.031e+01(2.3e−01)	16251.0(4.6e+00)	101.8(2.3e+00)	353.6(3.0e+00)
18	39	3.248e+01(1.6e+00)	16779.0(8.7e+00)	0.5(5.9e+00)	287.3(4.3e+00)
19	37	4.231e−03(2.6e−03)	15597.0(1.0e+03)	107.2(7.7e+02)	343.9(1.4e+03)
19	38	1.294e−01(1.3e−02)	16125.0(5.7e+01)	118.8(2.8e+01)	415.6(3.4e+01)
19	39	7.999e−01(3.6e−02)	16467.0(1.6e+01)	117.3(9.9e+00)	301.5(1.0e+01)
19	40	7.268e−01(4.9e−02)	16895.0(1.8e+01)	123.5(1.2e+01)	309.6(1.3e+01)

Appendix B

Differential Cross Sections

The peak shift of momentum distributions and the differential cross sections are shown in the next table.

B.1 Results of Be Target Data

The differential cross sections were obtained from the fitting results as shown in Appendix A.

Z_f	A_f	Peak Energy [A MeV]	Peak Momentum [A MeV/c]	Peak Rapidity	Differential Cross-section[mb/sr]
3	6	92.64 (0.93)	425.7 (1.2e+0)	0.4424 (1.4e−3)	1.10e+2 (1.0e+1)
3	7	93.38 (0.93)	427.4 (2.4e−1)	0.4441 (2.8e−4)	6.88e+1 (2.1e+0)
4	9	89.09 (0.89)	417.0 (2.3e−1)	0.4340 (2.7e−4)	2.17e+2 (4.5e+0)
4	10	91.17 (0.91)	422.1 (5.1e−2)	0.4389 (6.1e−5)	1.32e+2 (1.1e+0)
4	11	90.36 (0.90)	420.1 (2.8e−1)	0.4370 (3.3e−4)	5.94e+0 (7.7e−2)
5	10	91.68 (0.92)	423.3 (1.3e+0)	0.4401 (1.6e−3)	1.22e+2 (8.4e+0)
5	11	88.38 (0.88)	415.3 (2.2e−1)	0.4322 (2.6e−4)	5.47e+2 (1.2e+1)
5	12	88.82 (0.89)	416.4 (1.2e−1)	0.4333 (1.4e−4)	8.43e+1 (1.1e+0)
5	13	88.11 (0.88)	414.6 (9.1e−2)	0.4316 (1.1e−4)	2.29e+1 (3.1e−1)
5	14	86.88 (0.87)	411.6 (6.7e−1)	0.4286 (7.9e−4)	1.04e+0 (3.0e−2)
6	12	86.39 (0.86)	410.4 (6.7e−1)	0.4274 (7.8e−4)	5.54e+2 (2.6e+1)
6	13	86.33 (0.86)	410.2 (2.5e−1)	0.4273 (2.9e−4)	5.66e+2 (1.1e+1)
6	14	85.99 (0.86)	409.4 (1.3e−1)	0.4264 (1.5e−4)	2.66e+2 (3.0e+0)
6	15	86.20 (0.86)	409.9 (1.2e−1)	0.4269 (1.4e−4)	2.50e+1 (4.1e−1)
6	16	86.13 (0.86)	409.7 (1.8e−1)	0.4268 (2.1e−4)	6.41e+0 (1.3e−1)
6	17	86.46 (0.86)	410.5 (6.9e−1)	0.4276 (8.1e−4)	4.58e−1 (1.5e−2)

Z_f	A_f	Peak Energy [A MeV]	Peak Momentum [A MeV/c]	Peak Rapidity	Differential Cross-section[mb/sr]
7	14	85.52 (0.86)	408.2 (7.7e−1)	0.4253 (9.1e−4)	3.40e+2 (1.8e+1)
7	15	85.27 (0.85)	407.6 (2.3e−1)	0.4247 (2.7e−4)	1.07e+3 (1.5e+1)
7	16	85.48 (0.85)	408.1 (2.7e−1)	0.4252 (3.2e−4)	1.52e+2 (3.2e+0)
7	17	85.95 (0.86)	409.3 (1.3e−1)	0.4263 (1.5e−4)	6.78e+1 (9.1e−1)
7	18	85.65 (0.86)	408.5 (1.3e−1)	0.4256 (1.5e−4)	1.10e+1 (2.8e−1)
7	19	85.22 (0.85)	407.5 (2.1e−1)	0.4245 (2.5e−4)	2.30e+0 (4.0e−2)
7	20	86.41 (0.86)	410.4 (1.0e+0)	0.4275 (1.2e−3)	1.63e−1 (8.1e−3)
8	16	82.99 (0.83)	401.9 (5.2e−1)	0.4190 (6.0e−4)	9.62e+2 (3.0e+1)
8	17	83.66 (0.84)	403.6 (4.2e−1)	0.4207 (4.9e−4)	6.28e+2 (1.2e+1)
8	18	84.37 (0.84)	405.4 (2.1e−1)	0.4225 (2.4e−4)	4.52e+2 (7.1e+0)
8	19	84.89 (0.85)	406.6 (1.6e−1)	0.4238 (1.9e−4)	9.86e+1 (1.6e+0)
8	20	85.08 (0.85)	407.1 (1.2e−1)	0.4242 (1.4e−4)	2.91e+1 (5.6e−1)
8	21	85.35 (0.85)	407.8 (1.9e−1)	0.4249 (2.2e−4)	3.14e+0 (9.1e−2)
8	22	84.72 (0.85)	406.2 (3.6e−1)	0.4233 (4.2e−4)	3.81e−1 (1.1e−2)
8	23	81.97 (0.82)	399.3 (4.1e+0)	0.4165 (4.7e−3)	1.44e−2 (3.1e−3)
8	24	82.39 (0.82)	400.4 (8.6e+0)	0.4176 (1.0e−2)	6.41e−4 (5.9e−4)
9	18	81.98 (0.82)	399.3 (7.4e−1)	0.4165 (8.7e−4)	2.67e+2 (1.2e+1)
9	19	83.24 (0.83)	402.5 (3.2e−1)	0.4197 (3.8e−4)	8.01e+2 (1.3e+1)
9	20	84.31 (0.84)	405.2 (1.8e−1)	0.4223 (2.1e−4)	6.46e+2 (8.7e+0)
9	21	84.86 (0.85)	406.6 (1.5e−1)	0.4237 (1.7e−4)	2.70e+2 (3.4e+0)
9	22	84.65 (0.85)	406.0 (1.3e−1)	0.4231 (1.5e−4)	5.12e+1 (8.9e−1)
9	23	84.80 (0.85)	406.4 (1.2e−1)	0.4235 (1.4e−4)	1.04e+1 (2.6e−1)
9	24	85.11 (0.85)	407.2 (2.8e−1)	0.4243 (3.2e−4)	7.56e−1 (2.6e−2)
9	25	84.52 (0.85)	405.7 (9.4e−1)	0.4228 (1.1e−3)	5.65e−2 (5.9e−3)
9	26	84.10 (0.84)	404.7 (2.7e+0)	0.4218 (3.2e−3)	2.93e−3 (5.9e−4)

Z_f	A_f	Peak Energy [A MeV]	Peak Momentum [A MeV/c]	Peak Rapidity	Differential Cross-section[mb/sr]
10	20	82.13 (0.82)	399.7 (3.9e−1)	0.4169 (4.6e−4)	7.62e+2 (1.9e+1)
10	21	82.81 (0.83)	401.4 (2.2e−1)	0.4186 (2.6e−4)	1.47e+3 (1.7e+1)
10	22	84.21 (0.84)	404.9 (1.5e−1)	0.4221 (1.7e−4)	1.57e+3 (1.4e+1)
10	23	84.04 (0.84)	404.5 (1.7e−1)	0.4217 (2.0e−4)	3.66e+2 (5.3e+0)
10	24	84.68 (0.85)	406.1 (1.2e−1)	0.4232 (1.4e−4)	1.13e+2 (1.7e+0)
10	25	84.83 (0.85)	406.5 (1.8e−1)	0.4236 (2.1e−4)	1.18e+1 (4.0e−1)
10	26	85.19 (0.85)	407.4 (2.3e−1)	0.4245 (2.7e−4)	1.81e+0 (6.4e−2)
10	27	86.12 (0.86)	409.7 (8.1e−1)	0.4268 (9.5e−4)	4.71e−2 (3.8e−3)
10	28	85.21 (0.85)	407.4 (1.4e+0)	0.4245 (1.6e−3)	1.43e−2 (1.6e−3)
11	22	81.84 (0.82)	399.0 (3.8e−1)	0.4162 (4.4e−4)	6.21e+2 (1.6e+1)
11	23	82.55 (0.83)	400.7 (1.6e−1)	0.4179 (1.9e−4)	2.51e+3 (2.2e+1)
11	24	83.91 (0.84)	404.2 (1.7e−1)	0.4213 (2.0e−4)	1.71e+3 (1.6e+1)
11	25	83.88 (0.84)	404.1 (1.1e−1)	0.4213 (1.3e−4)	9.55e+2 (9.7e+0)
11	26	84.88 (0.85)	406.6 (1.1e−1)	0.4237 (1.2e−4)	1.85e+2 (2.4e+0)
11	27	85.32 (0.85)	407.7 (1.0e−1)	0.4248 (1.2e−4)	4.15e+1 (8.7e−1)
11	28	85.39 (0.85)	407.9 (1.5e−1)	0.4250 (1.8e−4)	3.88e+0 (1.1e−1)
11	29	85.95 (0.86)	409.3 (2.7e−1)	0.4263 (3.2e−4)	6.20e−1 (2.0e−2)
11	30	85.01 (0.85)	406.9 (9.0e−1)	0.4240 (1.1e−3)	4.37e−2 (4.7e−3)
11	31	84.36 (0.84)	405.3 (1.7e+0)	0.4225 (2.0e−3)	5.55e−3 (9.9e−4)
12	24	81.79 (0.82)	398.8 (1.8e−1)	0.4160 (2.1e−4)	1.86e+3 (2.3e+1)
12	25	82.38 (0.82)	400.3 (1.3e−1)	0.4175 (1.6e−4)	3.41e+3 (2.6e+1)
12	26	84.07 (0.84)	404.6 (1.0e−1)	0.4217 (1.2e−4)	3.98e+3 (2.4e+1)
12	27	84.32 (0.84)	405.2 (1.0e−1)	0.4224 (1.2e−4)	1.37e+3 (1.2e+1)
12	28	85.21 (0.85)	407.4 (1.1e−1)	0.4245 (1.3e−4)	4.24e+2 (4.7e+0)
12	29	86.02 (0.86)	409.4 (1.2e−1)	0.4265 (1.4e−4)	5.14e+1 (1.2e+0)
12	30	86.04 (0.86)	409.5 (1.4e−1)	0.4266 (1.6e−4)	1.11e+1 (2.7e−1)
12	31	86.15 (0.86)	409.8 (2.1e−1)	0.4268 (2.5e−4)	9.76e−1 (3.8e−2)
12	32	86.65 (0.87)	411.0 (4.2e−1)	0.4281 (4.9e−4)	1.62e−1 (8.0e−3)
12	33	85.70 (0.86)	408.7 (2.0e+0)	0.4257 (2.3e−3)	5.21e−3 (1.0e−3)

Z_f	A_f	Peak Energy [A MeV]	Peak Momentum [A MeV/c]	Peak Rapidity	Differential Cross-section[mb/sr]
13	26	81.87 (0.82)	399.0 (2.2e−1)	0.4163 (2.5e−4)	1.11e+3 (1.7e+1)
13	27	82.72 (0.83)	401.2 (8.9e−2)	0.4184 (1.0e−4)	5.61e+3 (3.2e+1)
13	28	85.19 (0.85)	407.4 (9.0e−2)	0.4245 (1.1e−4)	4.41e+3 (2.5e+1)
13	29	85.08 (0.85)	407.1 (7.7e−2)	0.4242 (9.0e−5)	3.00e+3 (2.0e+1)
13	30	85.25 (0.85)	407.5 (8.6e−2)	0.4246 (1.0e−4)	7.08e+2 (7.6e+0)
13	31	86.10 (0.86)	409.6 (6.9e−2)	0.4267 (8.1e−5)	2.04e+2 (2.8e+0)
13	32	86.77 (0.87)	411.3 (7.4e−2)	0.4283 (8.7e−5)	2.21e+1 (4.0e−1)
13	33	86.52 (0.87)	410.7 (9.9e−2)	0.4277 (1.2e−4)	4.74e+0 (7.9e−2)
13	34	86.71 (0.87)	411.2 (3.9e−1)	0.4282 (4.6e−4)	3.20e−1 (1.5e−2)
13	35	86.10 (0.86)	409.7 (5.0e−1)	0.4267 (5.9e−4)	4.99e−2 (3.1e−3)
14	28	82.55 (0.83)	400.8 (9.3e−2)	0.4179 (1.1e−4)	3.18e+3 (2.2e+1)
14	29	83.53 (0.84)	403.2 (8.0e−2)	0.4204 (9.4e−5)	7.44e+3 (4.2e+1)
14	30	83.03 (0.83)	402.0 (5.4e−2)	0.4191 (6.3e−5)	1.18e+4 (4.6e+1)
14	31	85.55 (0.86)	408.3 (6.2e−2)	0.4254 (7.2e−5)	4.73e+3 (3.1e+1)
14	32	86.52 (0.87)	410.7 (4.7e−2)	0.4277 (5.5e−5)	1.85e+3 (1.4e+1)
14	33	86.96 (0.87)	411.8 (4.9e−2)	0.4288 (5.8e−5)	3.16e+2 (3.4e+0)
14	34	87.31 (0.87)	412.6 (4.7e−2)	0.4297 (5.6e−5)	7.33e+1 (7.9e−1)
14	35	87.39 (0.87)	412.9 (1.2e−1)	0.4299 (1.5e−4)	5.74e+0 (1.2e−1)
14	36	87.51 (0.88)	413.1 (1.2e−1)	0.4301 (1.5e−4)	1.05e+0 (2.3e−2)
15	33	86.59 (0.87)	410.9 (6.2e−2)	0.4279 (7.3e−5)	1.05e+4 (6.3e+1)
15	34	86.90 (0.87)	411.6 (5.7e−2)	0.4287 (6.7e−5)	3.61e+3 (2.4e+1)
15	35	87.73 (0.88)	413.7 (1.0e−1)	0.4307 (1.2e−4)	1.38e+3 (1.0e+1)
15	36	87.98 (0.88)	414.3 (6.4e−2)	0.4313 (7.5e−5)	1.62e+2 (1.5e+0)

B.2   Results of Ta Target Data

Z_f	A_f	Peak Energy [A MeV]	Peak Momentum [A MeV/c]	Peak Rapidity	Differential Cross-section[mb/sr]
3	6	96.05(0.96)	433.8(1.9e+00)	0.4503(2.2e−03)	1.82e+03(5.6e+02)
3	7	95.74(0.96)	433.0(3.7e−01)	0.4496(4.4e−04)	2.43e+03(5.5e+01)
3	8	91.16(0.91)	422.1(8.1e−01)	0.4389(9.6e−04)	4.92e+02(1.4e+01)
4	9	94.93(0.95)	431.1(6.7e−01)	0.4477(8.0e−04)	8.26e+02(4.0e+01)
4	10	91.48(0.91)	422.9(3.2e−01)	0.4396(3.8e−04)	7.24e+02(1.2e+01)
4	11	90.40(0.90)	420.2(4.2e+00)	0.4371(4.9e−03)	3.86e+01(5.9e+00)
5	10	91.40(0.91)	422.7(2.3e+00)	0.4395(2.7e−03)	7.62e+02(8.4e+01)
5	11	92.28(0.92)	424.8(6.3e−01)	0.4415(7.4e−04)	2.18e+03(8.6e+01)
5	12	91.92(0.92)	423.9(4.3e−01)	0.4407(5.0e−04)	4.36e+02(1.2e+01)
5	13	90.10(0.90)	419.5(4.4e−01)	0.4364(5.2e−04)	1.52e+02(6.1e+00)
5	14	92.39(0.92)	425.0(1.7e−02)	0.4418(2.0e−05)	5.20e+00(3.1e−01)
6	11	92.85(0.93)	426.1(3.1e+00)	0.4429(3.7e−03)	4.16e+04(5.3e+06)
6	12	90.29(0.90)	420.0(1.3e+00)	0.4368(1.6e−03)	2.16e+03(1.1e+02)
6	13	91.30(0.91)	422.4(5.8e−01)	0.4392(6.9e−04)	1.99e+03(7.4e+01)
6	14	91.42(0.91)	422.7(3.4e−01)	0.4395(4.0e−04)	1.00e+03(2.4e+01)
6	15	90.78(0.91)	421.2(4.2e−01)	0.4380(5.0e−04)	1.23e+02(5.5e+00)
6	16	89.60(0.90)	418.3(8.7e−01)	0.4352(1.0e−03)	3.09e+01(1.4e+00)
6	17	90.29(0.90)	420.0(1.3e−01)	0.4368(1.6e−04)	1.67e+00(1.3e−01)

Z_f	A_f	Peak Energy [A MeV]	Peak Momentum [A MeV/c]	Peak Rapidity	Differential Cross-section[mb/sr]
7	13	94.49(0.94)	430.1(4.8e+00)	0.4467(5.7e−03)	8.93e+01(5.4e+01)
7	14	89.75(0.90)	418.6(1.5e+00)	0.4355(1.8e−03)	1.18e+03(6.9e+01)
7	15	90.29(0.90)	419.9(5.6e−01)	0.4368(6.6e−04)	3.14e+03(9.0e+01)
7	16	91.22(0.91)	422.2(8.6e−01)	0.4390(1.0e−03)	5.08e+02(2.4e+01)
7	17	91.27(0.91)	422.3(5.5e−01)	0.4391(6.5e−04)	2.84e+02(1.1e+01)
7	18	90.02(0.90)	419.3(7.4e−01)	0.4362(8.7e−04)	4.70e+01(4.1e+00)
7	19	93.82(0.94)	428.5(1.6e−02)	0.4451(1.9e−05)	8.61e+00(7.6e−01)
8	15	89.71(0.90)	418.6(3.3e+00)	0.4354(3.9e−03)	2.58e+02(6.1e+01)
8	16	90.23(0.90)	419.8(9.1e−01)	0.4367(1.1e−03)	2.57e+03(1.0e+02)
8	17	90.79(0.91)	421.2(1.1e+00)	0.4380(1.3e−03)	1.59e+03(7.1e+01)
8	18	92.06(0.92)	424.3(7.2e−01)	0.4410(8.5e−04)	1.22e+03(5.2e+01)
8	19	90.06(0.90)	419.4(4.1e−01)	0.4363(4.8e−04)	3.47e+02(1.3e+01)
8	20	91.13(0.91)	422.0(3.4e−01)	0.4388(4.0e−04)	9.50e+01(3.7e+00)
8	21	89.19(0.89)	417.3(1.1e+00)	0.4342(1.3e−03)	1.18e+01(1.0e+00)
9	17	91.86(0.92)	423.8(5.1e+00)	0.4405(6.0e−03)	1.35e+02(6.1e+01)
9	19	91.64(0.92)	423.2(9.3e−01)	0.4400(1.1e−03)	1.86e+03(7.5e+01)
9	20	91.75(0.92)	423.5(5.1e−01)	0.4403(6.0e−04)	1.41e+03(6.0e+01)
9	21	90.40(0.90)	420.2(3.7e−01)	0.4371(4.4e−04)	7.98e+02(2.1e+01)
9	22	91.95(0.92)	424.0(9.6e−01)	0.4407(1.1e−03)	1.43e+02(9.4e+00)
9	23	91.13(0.91)	422.0(4.6e−01)	0.4388(5.4e−04)	3.34e+01(2.4e+00)
9	24	90.87(0.91)	421.4(7.9e−01)	0.4382(9.3e−04)	2.75e+00(1.7e−01)
10	19	88.37(0.88)	415.3(2.6e+00)	0.4322(3.0e−03)	1.19e+02(2.0e+01)
10	20	90.60(0.91)	420.7(9.5e−01)	0.4376(1.1e−03)	1.61e+03(7.5e+01)
10	21	90.51(0.91)	420.5(5.8e−01)	0.4373(6.8e−04)	2.90e+03(8.6e+01)
10	22	91.56(0.92)	423.0(3.6e−01)	0.4398(4.2e−04)	2.84e+03(8.7e+01)
10	23	91.41(0.91)	422.7(6.8e−01)	0.4395(8.0e−04)	8.10e+02(2.8e+01)
10	24	90.15(0.90)	419.6(5.3e−01)	0.4365(6.3e−04)	2.57e+02(2.1e+01)
10	25	91.81(0.92)	423.6(7.8e−01)	0.4404(9.2e−04)	3.36e+01(2.1e+00)
10	26	90.31(0.90)	420.0(1.9e+00)	0.4369(2.2e−03)	5.75e+00(1.2e+00)
10	27	91.16(0.91)	422.1(2.4e+00)	0.4389(2.8e−03)	1.76e−01(6.4e−02)

Z_f	A_f	Peak Energy [A MeV]	Peak Momentum [A MeV/c]	Peak Rapidity	Differential Cross-section[mb/sr]
11	21	89.20(0.89)	417.3(2.6e+00)	0.4342(3.0e−03)	1.06e+02(1.9e+01)
11	22	90.67(0.91)	420.9(8.9e−01)	0.4377(1.1e−03)	1.33e+03(6.3e+01)
11	23	90.87(0.91)	421.4(4.2e−01)	0.4382(4.9e−04)	4.33e+03(1.1e+02)
11	24	91.44(0.91)	422.8(5.9e−01)	0.4395(7.0e−04)	2.75e+03(1.0e+02)
11	25	91.61(0.92)	423.2(4.7e−01)	0.4399(5.5e−04)	1.62e+03(6.0e+01)
11	26	90.85(0.91)	421.3(6.1e−01)	0.4381(7.1e−04)	3.78e+02(2.4e+01)
11	27	92.51(0.93)	425.3(7.9e−01)	0.4421(9.3e−04)	9.52e+01(3.9e+00)
11	28	91.86(0.92)	423.8(7.8e−01)	0.4405(9.2e−04)	1.02e+01(1.6e+00)
11	29	91.90(0.92)	423.9(1.1e+00)	0.4406(1.3e−03)	2.19e+00(2.0e−01)
12	23	90.12(0.90)	419.5(2.3e+00)	0.4364(2.7e−03)	1.95e+02(2.7e+01)
12	24	90.70(0.91)	421.0(5.3e−01)	0.4378(6.2e−04)	3.15e+03(9.8e+01)
12	25	91.50(0.91)	422.9(4.1e−01)	0.4397(4.9e−04)	5.32e+03(1.5e+02)
12	26	92.33(0.92)	424.9(4.5e−01)	0.4416(5.3e−04)	5.74e+03(1.5e+02)
12	27	92.42(0.92)	425.1(3.5e−01)	0.4419(4.1e−04)	1.86e+03(7.6e+01)
12	28	90.69(0.91)	420.9(5.9e−01)	0.4378(6.9e−04)	7.87e+02(3.0e+01)
12	29	91.66(0.92)	423.3(1.1e+00)	0.4401(1.3e−03)	9.85e+01(1.3e+01)
12	30	90.54(0.91)	420.6(1.3e+00)	0.4374(1.5e−03)	2.61e+01(2.0e+00)
12	31	91.75(0.92)	423.5(2.2e+00)	0.4403(2.5e−03)	2.77e+00(1.0e+00)
13	24	87.94(0.88)	414.2(4.2e−02)	0.4312(4.9e−05)	1.44e+01(2.7e+00)
13	25	90.47(0.90)	420.4(2.1e+00)	0.4372(2.4e−03)	1.05e+02(1.6e+01)
13	26	90.45(0.90)	420.3(6.4e−01)	0.4372(7.6e−04)	1.69e+03(7.0e+01)
13	27	91.81(0.92)	423.6(3.2e−01)	0.4404(3.7e−04)	7.82e+03(1.8e+02)
13	28	91.96(0.92)	424.0(3.9e−01)	0.4408(4.6e−04)	5.94e+03(1.4e+02)
13	29	92.90(0.93)	426.3(2.9e−01)	0.4430(3.4e−04)	3.70e+03(1.3e+02)
13	30	90.77(0.91)	421.1(4.6e−01)	0.4380(5.4e−04)	1.05e+03(4.1e+01)
13	31	91.76(0.92)	423.5(5.0e−01)	0.4403(5.8e−04)	3.42e+02(2.9e+01)
13	32	92.52(0.93)	425.3(6.3e−01)	0.4421(7.4e−04)	4.79e+01(2.1e+00)
13	33	91.04(0.91)	421.8(1.3e+00)	0.4386(1.5e−03)	9.35e+00(2.2e+00)
13	34	90.19(0.90)	419.7(2.9e+00)	0.4366(3.4e−03)	1.31e+00(4.7e−01)

Z_f	A_f	Peak Energy [A MeV]	Peak Momentum [A MeV/c]	Peak Rapidity	Differential Cross-section[mb/sr]
14	26	90.59(0.91)	420.7(1.8e+01)	0.4375(2.1e−02)	5.48e+00(1.9e+01)
14	28	98.74(0.99)	440.1(2.7e−01)	0.4565(3.2e−04)	3.19e+03(8.2e+01)
14	29	92.10(0.92)	424.3(2.7e−01)	0.4411(3.2e−04)	8.89e+03(1.9e+02)
14	30	92.40(0.92)	425.1(2.0e−01)	0.4418(2.4e−04)	1.24e+04(2.1e+02)
14	31	92.60(0.93)	425.5(2.9e−01)	0.4423(3.4e−04)	5.01e+03(1.6e+02)
14	32	91.48(0.91)	422.8(2.6e−01)	0.4396(3.1e−04)	2.25e+03(7.5e+01)
14	33	97.72(0.98)	437.7(7.0e−01)	0.4541(8.3e−04)	3.54e+02(3.5e+01)
14	34	90.91(0.91)	421.5(1.1e+00)	0.4383(1.3e−03)	1.15e+02(1.3e+01)
15	29	92.29(0.92)	424.8(1.6e+00)	0.4415(1.9e−03)	6.73e+01(1.0e+01)
15	30	91.92(0.92)	423.9(5.7e−01)	0.4407(6.7e−04)	1.32e+03(6.4e+01)
15	31	92.36(0.92)	425.0(2.7e−01)	0.4417(3.2e−04)	8.98e+03(2.0e+02)
15	32	92.63(0.93)	425.6(2.2e−01)	0.4424(2.6e−04)	1.08e+04(2.3e+02)
15	33	92.20(0.92)	424.6(2.6e−01)	0.4413(3.1e−04)	8.50e+03(2.2e+02)
15	34	93.21(0.93)	427.0(1.9e−01)	0.4437(2.3e−04)	2.93e+03(9.9e+01)
15	35	92.10(0.92)	424.3(2.8e−01)	0.4411(3.3e−04)	1.26e+03(4.2e+01)
15	36	94.89(0.95)	431.0(1.4e−01)	0.4476(1.7e−04)	1.27e+02(5.8e+00)
16	30	93.75(0.94)	428.3(1.8e+01)	0.4450(2.2e−02)	6.11e+00(1.1e+01)
16	31	91.17(0.91)	422.1(1.6e+00)	0.4389(1.9e−03)	9.50e+01(1.4e+01)
16	32	92.39(0.92)	425.0(3.3e−01)	0.4418(3.9e−04)	2.33e+03(8.0e+01)
16	33	92.97(0.93)	426.4(2.6e−01)	0.4431(3.0e−04)	8.93e+03(2.0e+02)
16	34	93.05(0.93)	426.6(1.4e−01)	0.4433(1.6e−04)	1.71e+04(2.7e+02)
16	35	92.47(0.92)	425.2(2.5e−01)	0.4420(2.9e−04)	1.12e+04(2.7e+02)
16	36	95.46(0.95)	432.4(1.4e−01)	0.4490(1.7e−04)	4.96e+03(2.6e+02)
16	37	93.24(0.93)	427.1(3.2e−01)	0.4438(3.8e−04)	1.95e+03(7.2e+01)

Z_f	A_f	Peak Energy [A MeV]	Peak Momentum [A MeV/c]	Peak Rapidity	Differential Cross-section[mb/sr]
17	33	91.41(0.91)	422.7(1.9e+00)	0.4395(2.3e−03)	2.10e+01(5.5e+00)
17	34	92.48(0.92)	425.3(5.1e−01)	0.4420(6.0e−04)	7.53e+02(4.4e+01)
17	35	93.35(0.93)	427.3(2.9e−01)	0.4440(3.5e−04)	7.68e+03(2.0e+02)
17	36	93.12(0.93)	426.8(1.4e−01)	0.4435(1.6e−04)	1.23e+04(2.2e+02)
17	37	93.78(0.94)	428.4(1.2e−03)	0.4450(1.4e−06)	1.28e+04(2.5e+02)
18	35	90.78(0.91)	421.1(1.7e+00)	0.4380(2.0e−03)	3.76e+01(8.8e+00)
18	36	92.78(0.93)	426.0(3.4e−01)	0.4427(4.0e−04)	1.06e+03(5.3e+01)
18	37	93.16(0.93)	426.9(3.8e−01)	0.4436(4.5e−04)	5.04e+03(1.6e+02)
18	38	93.48(0.93)	427.7(1.2e−01)	0.4443(1.4e−04)	1.16e+04(2.3e+02)
18	39	94.56(0.95)	430.2(2.2e−01)	0.4468(2.6e−04)	1.17e+04(8.8e+02)
19	37	90.94(0.91)	421.5(2.7e+01)	0.4384(3.2e−02)	2.39e+00(1.0e+01)
19	38	92.10(0.92)	424.3(1.5e+00)	0.4411(1.8e−03)	8.67e+01(1.6e+01)
19	40	91.29(0.91)	422.4(4.6e−01)	0.4392(5.4e−04)	3.95e+02(4.3e+01)

Appendix C

Cross Sections

The production cross sections of fragments are shown in the following table.The integration of doubly-differential cross sections has been done with the region of two peaks (σ^{HE}, σ^{LE} [mb]), using a deflection-effect parameter, $\sigma_D = 195A$ MeV for the estimation of the transverse momentum.

Further more, the high-energy side of the peak (HE) was separated to the symmetric and asymmetric parts (σ_{sym}^{HE}, σ_{asym}^{HE}). The symmetric part is the integration of a Gauss function (width=σ_HMeV/c) and the asymmetric part is defined with σ_{asym}^{HE} = σ^{HE} - σ_{sym}^{HE}.

C.1   Results of Be Target Data

Z_f	A_f	$\sigma^{HE}(Err)[mb]$	$\sigma^{HE}_{sym}(Err)[mb]$	$\sigma^{HE}_{asym}(Err)[mb]$	$\sigma^{LE}[mb]$
3	6	1.85e+00 (4.2e−01)	7.12e−01 (1.0e−01)	1.14e+00 (4.0e−01)	
3	7	7.91e−01 (6.2e−02)	7.42e−01 (2.6e−02)	4.86e−02 (5.6e−02)	
4	9	5.20e+00 (8.3e−02)	2.35e+00 (2.7e−02)	2.84e+00 (7.9e−02)	
4	10	2.45e+00 (1.6e−02)	9.30e−01 (2.1e−03)	1.52e+00 (1.6e−02)	
4	11	9.86e−02 (1.2e−03)	4.70e−02 (7.9e−04)	5.16e−02 (9.0e−04)	
5	10	2.17e+00 (1.3e−01)	1.16e+00 (5.3e−02)	1.01e+00 (1.2e−01)	
5	11	1.02e+01 (1.5e−01)	4.27e+00 (4.5e−02)	5.94e+00 (1.4e−01)	
5	12	1.35e+00 (1.1e−02)	6.04e−01 (2.9e−03)	7.45e−01 (1.1e−02)	
5	13	3.46e−01 (2.7e−03)	1.75e−01 (5.2e−04)	1.70e−01 (2.7e−03)	
5	14	1.94e−02 (3.1e−04)	1.20e−02 (2.6e−04)	7.44e−03 (1.8e−04)	
6	12	9.89e+00 (3.0e−01)	5.25e+00 (8.6e−02)	4.64e+00 (2.9e−01)	
6	13	8.55e+00 (1.1e−01)	4.54e+00 (4.5e−02)	4.01e+00 (9.6e−02)	
6	14	3.65e+00 (2.4e−02)	2.08e+00 (1.1e−02)	1.57e+00 (2.1e−02)	
6	15	3.30e−01 (2.8e−03)	1.93e−01 (7.0e−04)	1.37e−01 (2.7e−03)	
6	16	8.14e−02 (8.2e−04)	4.80e−02 (2.4e−04)	3.34e−02 (7.9e−04)	
6	17	5.31e−03 (1.0e−04)	3.20e−03 (9.5e−05)	2.11e−03 (3.9e−05)	

Z_f	A_f	$\sigma^{HE}(Err)[mb]$	$\sigma^{HE}_{sym}(Err)[mb]$	$\sigma^{HE}_{asym}(Err)[mb]$	$\sigma^{LE}[mb]$
7	14	5.26e+00 (1.6e−01)	3.00e+00 (5.5e−02)	2.26e+00 (1.5e−01)	
7	15	1.31e+01 (1.1e−01)	7.67e+00 (5.8e−02)	5.46e+00 (9.6e−02)	
7	16	1.76e+00 (2.0e−02)	1.05e+00 (1.1e−02)	7.11e−01 (1.7e−02)	
7	17	7.40e−01 (5.0e−03)	4.23e−01 (1.9e−03)	3.18e−01 (4.6e−03)	
7	18	1.17e−01 (1.3e−03)	6.56e−02 (2.4e−04)	5.14e−02 (1.3e−03)	
7	19	2.51e−02 (1.9e−04)	1.67e−02 (8.3e−05)	8.43e−03 (1.7e−04)	
7	20	1.32e−03 (4.1e−05)	7.26e−04 (3.9e−05)	5.91e−04 (1.1e−05)	
8	16	1.40e+01 (2.2e−01)	9.54e+00 (9.9e−02)	4.43e+00 (2.0e−01)	
8	17	7.45e+00 (7.7e−02)	4.98e+00 (4.8e−02)	2.46e+00 (6.0e−02)	
8	18	4.65e+00 (3.6e−02)	3.02e+00 (2.2e−02)	1.63e+00 (2.9e−02)	
8	19	9.43e−01 (7.0e−03)	6.04e−01 (3.6e−03)	3.38e−01 (6.0e−03)	
8	20	2.68e−01 (2.2e−03)	1.58e−01 (5.4e−04)	1.11e−01 (2.1e−03)	
8	21	2.67e−02 (3.3e−04)	1.54e−02 (8.2e−05)	1.12e−02 (3.1e−04)	
8	22	3.33e−03 (4.0e−05)	2.33e−03 (2.0e−05)	1.00e−03 (3.4e−05)	
8	23	2.55e−04 (1.2e−05)	2.24e−04 (8.2e−06)	3.05e−05 (8.7e−06)	
8	24	5.15e−06 (2.0e−06)	5.64e−06 (2.6e−06)		
9	18	3.97e+00 (7.0e−02)	3.33e+00 (4.1e−02)	6.45e−01 (5.8e−02)	
9	19	8.35e+00 (6.6e−02)	5.78e+00 (4.4e−02)	2.58e+00 (4.9e−02)	
9	20	5.59e+00 (3.7e−02)	3.59e+00 (2.3e−02)	2.00e+00 (2.9e−02)	
9	21	2.16e+00 (1.3e−02)	1.35e+00 (7.1e−03)	8.11e−01 (1.1e−02)	
9	22	4.10e−01 (2.9e−03)	2.51e−01 (1.1e−03)	1.59e−01 (2.7e−03)	
9	23	7.96e−02 (7.6e−04)	4.81e−02 (1.6e−04)	3.15e−02 (7.5e−04)	
9	24	5.23e−03 (7.2e−05)	3.23e−03 (2.7e−05)	2.00e−03 (6.7e−05)	
9	25	4.18e−04 (1.6e−05)	3.17e−04 (7.0e−06)	1.01e−04 (1.4e−05)	
9	26	2.53e−05 (1.7e−06)	2.46e−05 (1.5e−06)	7.00e−07 (7.7e−07)	

Z_f	A_f	$\sigma^{HE}(Err)[mb]$	$\sigma^{HE}_{sym}(Err)[mb]$	$\sigma^{HE}_{asym}(Err)[mb]$	$\sigma^{LE}[mb]$
10	19	8.53e−01 (9.1e−03)	6.11e−01 (6.6e−03)	2.42e−01 (6.3e−03)	
10	20	8.69e+00 (9.3e−02)	6.68e+00 (5.2e−02)	2.00e+00 (7.7e−02)	
10	21	1.38e+01 (7.3e−02)	1.00e+01 (5.3e−02)	3.80e+00 (5.0e−02)	
10	22	1.13e+01 (5.2e−02)	7.46e+00 (3.7e−02)	3.86e+00 (3.6e−02)	
10	23	2.63e+00 (1.7e−02)	1.79e+00 (1.0e−02)	8.47e−01 (1.3e−02)	
10	24	7.44e−01 (4.7e−03)	4.71e−01 (2.2e−03)	2.73e−01 (4.2e−03)	
10	25	7.57e−02 (1.0e−03)	4.66e−02 (2.6e−04)	2.91e−02 (9.7e−04)	
10	26	1.07e−02 (1.5e−04)	6.64e−03 (4.7e−05)	4.09e−03 (1.4e−04)	
10	27	2.37e−04 (8.8e−06)	1.57e−04 (4.7e−06)	7.95e−05 (7.4e−06)	
10	28	8.07e−05 (3.6e−06)	5.84e−05 (2.2e−06)	2.23e−05 (2.9e−06)	
10	29	2.92e−06 (3.3e−07)	1.81e−06 (2.0e−07)	1.11e−06 (2.7e−07)	
11	22	6.34e+00 (6.3e−02)	5.04e+00 (3.7e−02)	1.30e+00 (5.1e−02)	
11	23	2.11e+01 (8.0e−02)	1.59e+01 (6.5e−02)	5.18e+00 (4.6e−02)	
11	24	1.11e+01 (5.0e−02)	7.55e+00 (3.8e−02)	3.54e+00 (3.3e−02)	
11	25	5.89e+00 (2.6e−02)	4.14e+00 (1.8e−02)	1.75e+00 (1.9e−02)	
11	26	1.00e+00 (5.7e−03)	6.36e−01 (2.8e−03)	3.67e−01 (5.0e−03)	
11	27	2.09e−01 (1.8e−03)	1.28e−01 (5.7e−04)	8.04e−02 (1.8e−03)	
11	28	1.89e−02 (2.2e−04)	1.19e−02 (6.7e−05)	7.01e−03 (2.1e−04)	
11	29	2.64e−03 (4.0e−05)	1.57e−03 (1.7e−05)	1.07e−03 (3.6e−05)	
11	30	2.08e−04 (8.9e−06)	1.52e−04 (4.4e−06)	5.64e−05 (7.7e−06)	
11	31	3.06e−05 (1.8e−06)	2.28e−05 (1.0e−06)	7.74e−06 (1.5e−06)	
12	24	1.61e+01 (7.8e−02)	1.33e+01 (5.1e−02)	2.73e+00 (5.8e−02)	
12	25	2.58e+01 (8.2e−02)	2.05e+01 (7.3e−02)	5.35e+00 (3.6e−02)	
12	26	2.17e+01 (6.4e−02)	1.50e+01 (5.1e−02)	6.74e+00 (3.9e−02)	
12	27	6.86e+00 (2.9e−02)	4.71e+00 (2.1e−02)	2.15e+00 (2.0e−02)	
12	28	1.90e+00 (9.8e−03)	1.21e+00 (5.4e−03)	6.94e−01 (8.1e−03)	
12	29	2.00e−01 (2.2e−03)	1.10e−01 (6.9e−04)	9.01e−02 (2.1e−03)	
12	30	4.11e−02 (4.7e−04)	2.54e−02 (1.6e−04)	1.58e−02 (4.4e−04)	
12	31	3.36e−03 (6.4e−05)	1.97e−03 (2.2e−05)	1.39e−03 (6.0e−05)	
12	32	4.79e−04 (1.3e−05)	2.79e−04 (6.7e−06)	2.00e−04 (1.1e−05)	
12	33	1.86e−05 (1.7e−06)	1.60e−05 (1.4e−06)	2.62e−06 (1.0e−06)	

Z_f	A_f	$\sigma^{HE}(Err)[mb]$	$\sigma^{HE}_{sym}(Err)[mb]$	$\sigma^{HE}_{asym}(Err)[mb]$	$\sigma^{LE}[mb]$
13	26	8.28e+00 (4.9e−02)	6.73e+00 (3.3e−02)	1.56e+00 (3.6e−02)	
13	27	3.58e+01 (8.4e−02)	2.89e+01 (7.9e−02)	6.90e+00 (3.0e−02)	
13	28	1.85e+01 (5.8e−02)	1.17e+01 (4.7e−02)	6.81e+00 (3.5e−02)	
13	29	1.18e+01 (4.0e−02)	7.73e+00 (3.0e−02)	4.05e+00 (2.7e−02)	
13	30	2.64e+00 (1.4e−02)	1.76e+00 (8.0e−03)	8.88e−01 (1.1e−02)	
13	31	6.51e−01 (4.5e−03)	4.01e−01 (1.8e−03)	2.50e−01 (4.1e−03)	
13	32	6.09e−02 (6.1e−04)	3.50e−02 (2.0e−04)	2.59e−02 (5.7e−04)	
13	33	1.34e−02 (1.2e−04)	8.53e−03 (5.0e−05)	4.91e−03 (1.1e−04)	
13	34	7.77e−04 (2.2e−05)	4.56e−04 (1.1e−05)	3.21e−04 (1.9e−05)	
13	35	1.28e−04 (4.4e−06)	8.41e−05 (2.9e−06)	4.36e−05 (3.3e−06)	
14	27	8.13e−01 (3.8e−03)	7.05e−01 (4.2e−03)	1.08e−01	
14	28	1.87e+01 (5.5e−02)	1.61e+01 (4.6e−02)	2.65e+00 (3.0e−02)	
14	29	3.57e+01 (9.5e−02)	2.80e+01 (8.1e−02)	7.75e+00 (5.0e−02)	
14	30	6.45e+01 (9.6e−02)	5.70e+01 (9.6e−02)	7.50e+00	
14	31	1.48e+01 (5.5e−02)	1.02e+01 (3.9e−02)	4.62e+00 (3.8e−02)	
14	32	4.75e+00 (2.2e−02)	2.99e+00 (1.3e−02)	1.75e+00 (1.7e−02)	
14	33	7.26e−01 (4.9e−03)	4.22e−01 (2.0e−03)	3.04e−01 (4.4e−03)	
14	34	1.50e−01 (1.1e−03)	9.22e−02 (4.6e−04)	5.74e−02 (9.6e−04)	
14	35	1.07e−02 (1.6e−04)	6.33e−03 (7.5e−05)	4.35e−03 (1.5e−04)	
14	36	1.78e−03 (3.0e−05)	1.04e−03 (1.8e−05)	7.45e−04 (2.3e−05)	
15	29	4.30e−01 (2.2e−02)	3.92e−01 (3.2e−03)	3.84e−02 (2.1e−02)	
15	33	2.34e+01 (1.0e−01)	1.48e+01 (7.3e−02)	8.58e+00 (7.0e−02)	
15	34	7.22e+00 (3.5e−02)	4.52e+00 (2.3e−02)	2.70e+00 (2.6e−02)	
15	35	2.30e+00 (1.6e−02)	1.32e+00 (1.1e−02)	9.83e−01 (1.1e−02)	
15	36	2.50e−01 (1.9e−03)	1.29e−01 (9.7e−04)	1.21e−01 (1.7e−03)	
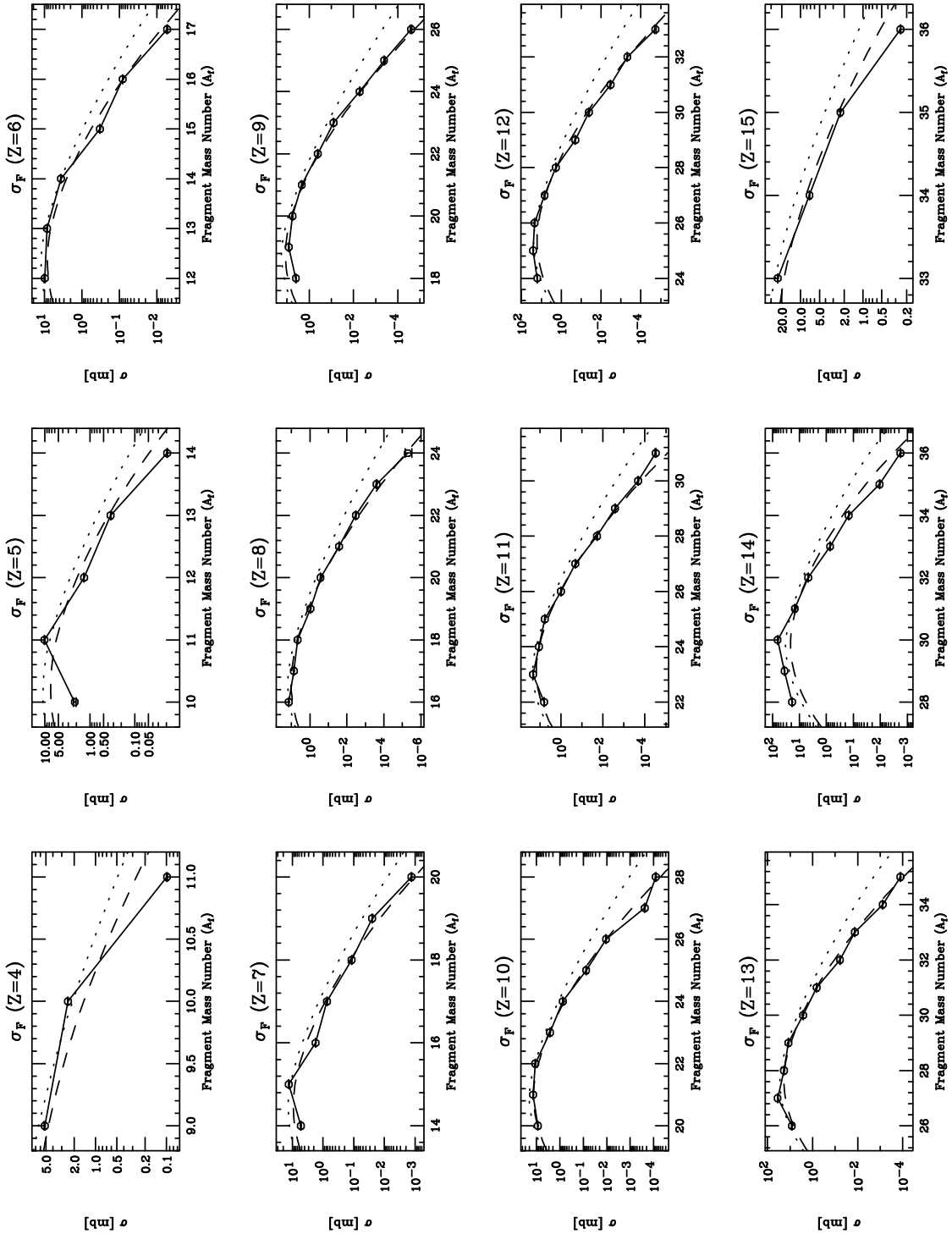
Figure C.1: Production cross sections measured with RIPS. The experimental data are compared with predictions obtained with the semi-empirical formula EPAX. The dotted lines are the EPAX predictions using an U_n-parameter of 1.5. The U_n-parameter was corrected to 1.7 (dashed lines) for the very neutron-rich isotopes produced in the Ar+Be reaction.

C.2   Results of Ta Target Data

Z_f	A_f	$\sigma^{HE}(Err)[mb]$	$\sigma^{HE}_{sym}(Err)[mb]$	$\sigma^{HE}_{asym}(Err)[mb]$
3	6	1.27e+02 (2.0e+01)	2.67e+01 (1.6e+00)	1.01e+02 (2.0e+01)
3	7	8.91e+01 (1.6e+00)	3.33e+01 (4.1e−01)	5.59e+01 (1.6e+00)
3	8	2.22e+01 (4.1e−01)	1.08e+01 (2.7e−01)	1.14e+01 (3.2e−01)
4	9	2.10e+01 (7.1e−01)	9.23e+00 (2.4e−01)	1.18e+01 (6.7e−01)
4	10	1.88e+01 (1.9e−01)	1.02e+01 (7.0e−02)	8.56e+00 (1.7e−01)
4	11	8.28e−01 (9.6e−02)	5.24e−01 (1.2e−01)	3.03e−01
5	10	2.04e+01 (1.3e+00)	1.23e+01 (4.9e−01)	8.10e+00 (1.2e+00)
5	11	4.56e+01 (1.1e+00)	2.62e+01 (5.3e−01)	1.95e+01 (9.4e−01)
5	12	8.25e+00 (1.2e−01)	4.49e+00 (4.8e−02)	3.75e+00 (1.1e−01)
5	13	3.05e+00 (5.6e−02)	1.75e+00 (1.7e−02)	1.31e+00 (5.3e−02)
5	14	4.79e−03 (2.1e−03)	1.46e−05 (6.6e−05)	4.78e−03 (2.1e−03)
6	11	9.59e+04 (5.7e+04)	4.79e+00 (4.6e−01)	9.59e+04 (5.7e+04)
6	12	4.17e+01 (1.3e+00)	2.89e+01 (7.5e−01)	1.27e+01 (1.1e+00)
6	13	3.23e+01 (6.8e−01)	2.12e+01 (3.9e−01)	1.12e+01 (5.5e−01)
6	14	1.45e+01 (1.9e−01)	8.86e+00 (9.8e−02)	5.62e+00 (1.6e−01)
6	15	1.74e+00 (3.7e−02)	1.03e+00 (9.3e−03)	7.09e−01 (3.6e−02)
6	16	4.66e−01 (9.6e−03)	3.65e−01 (6.4e−03)	1.01e−01 (7.2e−03)
6	17	1.52e−03 (6.7e−04)	2.36e−05 (1.9e−04)	1.49e−03 (6.5e−04)
7	13	8.38e−01 (4.7e−01)	4.08e−01 (1.4e−01)	4.29e−01 (4.5e−01)
7	14	2.02e+01 (6.5e−01)	1.62e+01 (5.2e−01)	4.03e+00 (4.0e−01)
7	15	4.35e+01 (6.5e−01)	3.15e+01 (4.6e−01)	1.20e+01 (4.7e−01)
7	16	6.42e+00 (1.5e−01)	4.13e+00 (9.7e−02)	2.29e+00 (1.2e−01)
7	17	3.23e+00 (5.9e−02)	1.85e+00 (2.3e−02)	1.38e+00 (5.4e−02)
7	18	5.39e−01 (1.9e−02)	3.75e−01 (7.2e−03)	1.64e−01 (1.7e−02)
7	19	7.55e−03 (2.8e−03)	4.05e−05 (5.9e−05)	7.51e−03 (2.8e−03)

Z_f	A_f	$\sigma^{HE}(Err)[mb]$	$\sigma^{HE}_{sym}(Err)[mb]$	$\sigma^{HE}_{asym}(Err)[mb]$
8	15	3.96e+00 (4.8e−01)	3.93e+00 (2.9e−01)	3.13e−02 (3.8e−01)
8	16	2.84e+01 (7.2e−01)	2.09e+01 (6.2e−01)	7.43e+00 (3.6e−01)
8	17	1.74e+01 (4.3e−01)	1.24e+01 (3.3e−01)	5.09e+00 (2.7e−01)
8	18	1.11e+01 (2.5e−01)	6.84e+00 (1.6e−01)	4.23e+00 (2.0e−01)
8	19	3.52e+00 (5.5e−02)	2.40e+00 (2.7e−02)	1.12e+00 (4.8e−02)
8	20	7.68e−01 (1.4e−02)	5.88e−01 (6.8e−03)	1.81e−01 (1.2e−02)
8	21	1.14e−01 (3.7e−03)	1.04e−01 (2.4e−03)	1.01e−02 (2.8e−03)
9	17	1.63e+00 (3.4e−01)	9.23e−01 (1.5e−01)	7.08e−01 (3.1e−01)
9	19	1.54e+01 (3.5e−01)	1.01e+01 (2.6e−01)	5.27e+00 (2.4e−01)
9	20	1.12e+01 (2.3e−01)	7.15e+00 (1.4e−01)	4.03e+00 (1.8e−01)
9	21	6.74e+00 (7.8e−02)	4.77e+00 (5.0e−02)	1.97e+00 (6.0e−02)
9	22	9.50e−01 (3.1e−02)	5.90e−01 (1.2e−02)	3.60e−01 (2.8e−02)
9	23	2.19e−01 (6.7e−03)	1.51e−01 (2.8e−03)	6.76e−02 (6.0e−03)
9	24	1.78e−02 (5.0e−04)	1.42e−02 (3.1e−04)	3.63e−03 (3.9e−04)
10	19	1.52e+00 (1.0e−01)	1.81e+00 (1.1e−01)	
10	20	1.21e+01 (3.4e−01)	8.77e+00 (3.1e−01)	3.33e+00 (1.2e−01)
10	21	2.35e+01 (3.3e−01)	1.75e+01 (2.6e−01)	6.05e+00 (2.0e−01)
10	22	1.91e+01 (2.8e−01)	1.29e+01 (2.0e−01)	6.23e+00 (2.0e−01)
10	23	5.04e+00 (9.0e−02)	3.31e+00 (6.1e−02)	1.73e+00 (6.6e−02)
10	24	1.66e+00 (5.4e−02)	1.54e+00 (2.7e−02)	1.19e−01 (4.7e−02)
10	25	1.66e−01 (5.4e−03)	1.16e−01 (3.2e−03)	5.00e−02 (4.4e−03)
10	26	3.34e−02 (2.7e−03)	2.89e−02 (1.8e−03)	4.50e−03 (2.1e−03)
10	27	7.58e−04 (1.4e−04)	7.89e−04 (8.1e−05)	
11	21	1.17e+00 (7.7e−02)	1.17e+00 (7.7e−02)	
11	22	9.48e+00 (2.3e−01)	7.14e+00 (2.2e−01)	2.34e+00 (6.6e−02)
11	23	2.60e+01 (3.5e−01)	1.83e+01 (3.0e−01)	7.68e+00 (1.8e−01)
11	24	1.63e+01 (2.8e−01)	1.13e+01 (2.3e−01)	5.08e+00 (1.7e−01)
11	25	8.59e+00 (1.5e−01)	5.73e+00 (9.3e−02)	2.86e+00 (1.2e−01)
11	26	2.00e+00 (5.9e−02)	1.64e+00 (3.7e−02)	3.62e−01 (4.6e−02)
11	27	3.82e−01 (9.1e−03)	2.60e−01 (5.2e−03)	1.22e−01 (7.4e−03)
11	28	4.12e−02 (3.0e−03)	2.74e−02 (1.3e−03)	1.37e−02 (2.6e−03)
11	29	8.51e−03 (3.9e−04)	5.43e−03 (2.1e−04)	3.08e−03 (3.3e−04)

Z_f	A_f	$\sigma^{HE}(Err)[mb]$	$\sigma^{HE}_{sym}(Err)[mb]$	$\sigma^{HE}_{asym}(Err)[mb]$
12	23	1.71e+00 (9.4e−02)	1.57e+00 (8.7e−02)	1.43e−01 (3.4e−02)
12	24	1.78e+01 (3.0e−01)	1.34e+01 (3.0e−01)	4.36e+00 (1.9e−02)
12	25	2.40e+01 (4.0e−01)	1.60e+01 (3.8e−01)	8.00e+00 (1.1e−01)
12	26	2.47e+01 (3.6e−01)	1.59e+01 (2.8e−01)	8.80e+00 (2.3e−01)
12	27	7.49e+00 (1.6e−01)	4.62e+00 (9.4e−02)	2.87e+00 (1.2e−01)
12	28	3.77e+00 (6.7e−02)	3.20e+00 (4.5e−02)	5.68e−01 (5.0e−02)
12	29	4.02e−01 (2.4e−02)	2.99e−01 (1.3e−02)	1.03e−01 (2.0e−02)
12	30	1.12e−01 (3.8e−03)	9.01e−02 (2.8e−03)	2.18e−02 (2.5e−03)
12	31	8.94e−03 (1.5e−03)	6.39e−03 (8.8e−04)	2.55e−03 (1.3e−03)
13	24	1.20e−01 (6.6e−03)	1.00e−04	1.20e−01 (5.7e−03)
13	25	5.87e−01 (4.6e−02)	5.05e−01 (4.7e−02)	8.17e−02
13	26	9.17e+00 (1.8e−01)	7.25e+00 (1.8e−01)	1.91e+00
13	27	2.84e+01 (4.0e−01)	1.85e+01 (3.7e−01)	9.99e+00 (1.5e−01)
13	28	2.36e+01 (3.0e−01)	1.62e+01 (2.3e−01)	7.45e+00 (2.0e−01)
13	29	1.10e+01 (2.4e−01)	6.45e+00 (1.6e−01)	4.60e+00 (1.8e−01)
13	30	4.31e+00 (7.4e−02)	3.88e+00 (4.9e−02)	4.29e−01 (5.5e−02)
13	31	1.12e+00 (4.7e−02)	9.05e−01 (2.9e−02)	2.11e−01 (3.6e−02)
13	32	1.27e−01 (3.4e−03)	8.64e−02 (2.2e−03)	4.01e−02 (2.6e−03)
13	33	3.55e−02 (3.0e−03)	2.84e−02 (1.6e−03)	7.16e−03 (2.6e−03)
13	34	4.65e−03 (6.3e−04)	4.27e−03 (5.0e−04)	3.75e−04 (3.8e−04)
14	26	8.91e−03 (4.4e−02)	6.93e−03 (5.7e−02)	1.98e−03
14	28	8.14e+00 (1.6e−01)	6.20e+00 (1.7e−01)	1.95e+00
14	29	2.50e+01 (3.7e−01)	1.56e+01 (3.3e−01)	9.34e+00 (1.6e−01)
14	30	3.72e+01 (3.7e−01)	2.43e+01 (2.9e−01)	1.29e+01 (2.3e−01)
14	31	1.44e+01 (2.6e−01)	9.35e+00 (1.9e−01)	5.05e+00 (1.7e−01)
14	32	7.07e+00 (1.1e−01)	6.08e+00 (7.8e−02)	9.94e−01 (8.2e−02)
14	33	6.46e−01 (4.8e−02)	3.62e−01 (2.0e−02)	2.85e−01 (4.3e−02)
14	34	4.04e−01 (2.0e−02)	3.99e−01 (2.1e−02)	4.51e−03
15	29	1.45e−01 (2.1e−02)	8.58e−02 (1.8e−02)	5.96e−02 (1.0e−02)
15	30	3.61e+00 (1.2e−01)	2.39e+00 (1.1e−01)	1.22e+00 (2.7e−02)
15	31	2.12e+01 (3.4e−01)	1.32e+01 (3.0e−01)	7.98e+00 (1.5e−01)
15	32	2.32e+01 (3.7e−01)	1.36e+01 (3.4e−01)	9.55e+00 (1.4e−01)
15	33	2.33e+01 (3.2e−01)	1.65e+01 (2.5e−01)	6.84e+00 (2.0e−01)
15	34	5.01e+00 (1.3e−01)	2.85e+00 (7.8e−02)	2.16e+00 (1.0e−01)
15	35	3.03e+00 (5.5e−02)	2.66e+00 (3.6e−02)	3.61e−01 (4.2e−02)
15	36	1.31e−01 (6.4e−03)	3.21e−02 (2.2e−03)	9.91e−02 (6.1e−03)

Z_f	A_f	$\sigma^{HE}(Err)[mb]$	$\sigma^{HE}_{sym}(Err)[mb]$	$\sigma^{HE}_{asym}(Err)[mb]$
16	30	3.86e−02 (2.1e−02)	3.99e−02 (2.8e−02)	
16	31	2.90e−01 (2.5e−02)	2.28e−01 (2.6e−02)	6.25e−02
16	32	4.94e+00 (1.3e−01)	3.14e+00 (1.2e−01)	1.80e+00 (5.0e−02)
16	33	1.56e+01 (3.0e−01)	8.62e+00 (2.6e−01)	6.96e+00 (1.6e−01)
16	34	2.90e+01 (3.8e−01)	1.63e+01 (3.2e−01)	1.27e+01 (2.1e−01)
16	35	2.38e+01 (3.5e−01)	1.74e+01 (2.6e−01)	6.45e+00 (2.2e−01)
16	36	5.36e+00 (2.7e−01)	1.35e+00 (6.2e−02)	4.01e+00 (2.7e−01)
16	37	3.26e+00 (8.3e−02)	2.01e+00 (3.6e−02)	1.26e+00 (7.5e−02)
17	33	5.50e−02 (8.4e−03)	4.63e−02 (8.6e−03)	8.71e−03
17	34	1.35e+00 (6.1e−02)	8.09e−01 (5.3e−02)	5.45e−01 (3.0e−02)
17	35	1.10e+01 (2.7e−01)	5.70e+00 (2.2e−01)	5.34e+00 (1.5e−01)
17	36	1.72e+01 (2.8e−01)	8.82e+00 (2.1e−01)	8.37e+00 (1.8e−01)
17	37	1.08e+01 (2.4e−01)	1.10e−02 (4.0e−03)	1.07e+01 (2.4e−01)
18	35	1.00e−01 (1.2e−02)	8.70e−02 (1.4e−02)	1.31e−02
18	36	1.51e+00 (6.5e−02)	8.78e−01 (5.5e−02)	6.33e−01 (3.4e−02)
18	37	6.08e+00 (1.9e−01)	3.00e+00 (1.5e−01)	3.08e+00 (1.3e−01)
18	38	1.26e+01 (2.5e−01)	5.50e+00 (1.6e−01)	7.10e+00 (1.9e−01)
18	39	9.68e+00 (8.6e−01)	2.98e−02 (4.1e−01)	9.65e+00 (7.6e−01)
19	37	2.78e−03 (1.3e−02)	1.29e−03 (8.9e−03)	1.49e−03 (9.6e−03)
19	38	1.04e−01 (1.8e−02)	4.50e−02 (1.2e−02)	5.92e−02 (1.3e−02)
19	40	4.70e−01 (4.2e−02)	2.64e−01 (3.2e−02)	2.06e−01 (2.8e−02)
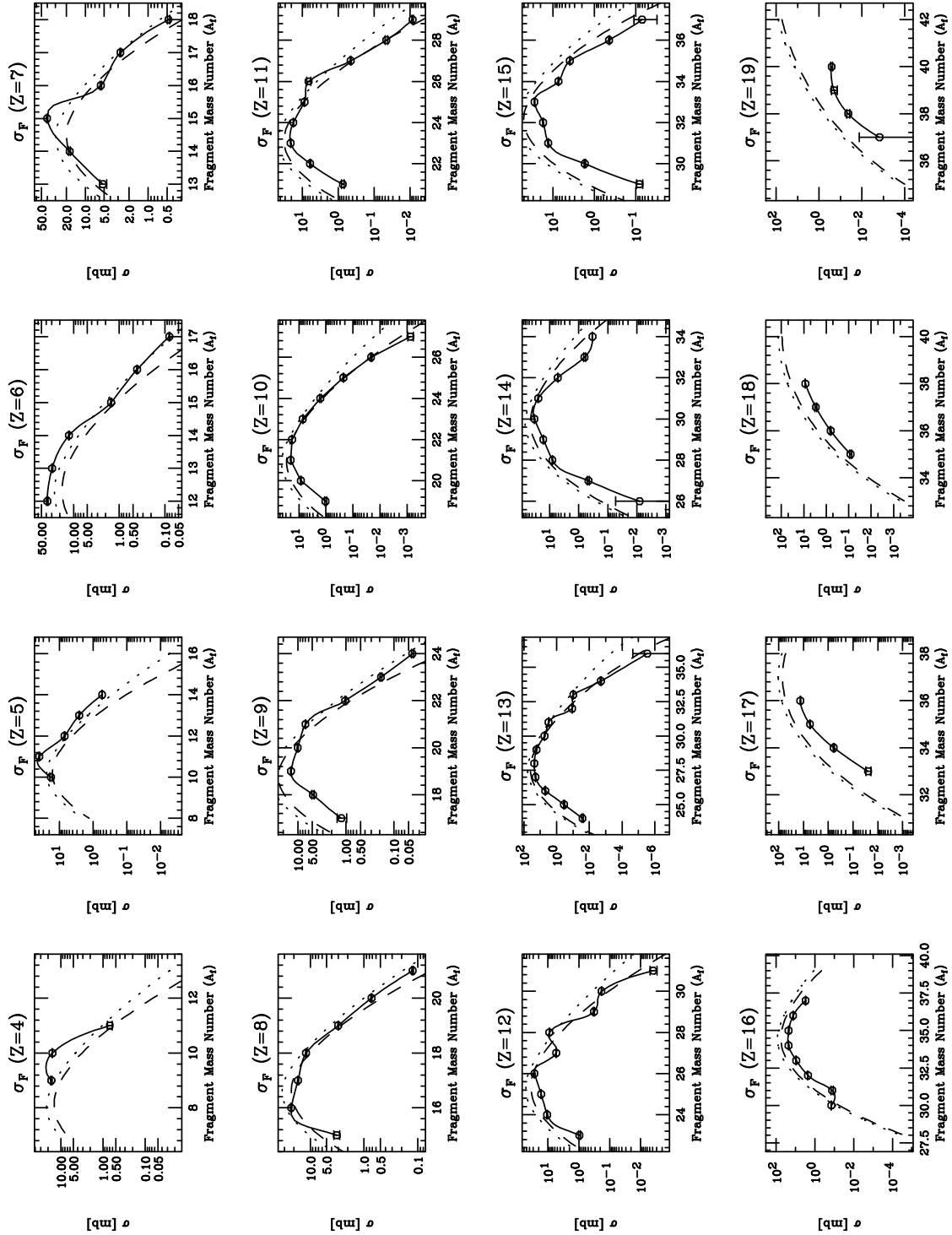
Figure C.2: Production cross sections of fragments by using the Ta target. The experimental data are compared with predictions obtained with the EPAX formula. The dotted curves are the EPAX predictions using an U-parameter of 1.5. The U_n-parameter was corrected to 1.63 for the very neutron-rich isotopes produced by the Ar+Ta reaction. The mass yield of EPAX was used for the predictions (not normalized by the experimental mass yield).

Appendix D

LE-component and Low Momentum Tail

The typical momentum distributions have one component described as a Gaussian-like function which includes an asymmetric part in the low momentum side. However, two components were found in the Be data for very light fragments. The clear evidence that the so-called "low momentum tail" is different from the LE-component is shown here.

Fig. D.1 shows the momentum distributions of a given fragment ^{10}Be produced in Ar+Be and Ar+Ta reactions. The figures of (a) and (b) are shown with the fitting results (solid line) of the Ar+Be and the Ar+Ta reactions, respectively. The both distributions are scaled as a function of velocity. The momentum peaks were described as the "LE" and "HE" marks.

Fig. D.2 shows the momentum distributions on the same coordinate. The both distributions are also scaled as a function of velocity. No significant difference of the high momentum side widths between both of the targets is observed. On the other hand, the momentum distributions at low momentum side are very different between the Be and Ta data. The low momentum side width of Ta data is wider than the high momentum side width, although no significant target dependence of σ_L was found in our data for the fragments $A_f > 20$. Thus, the difference of the momentum distributions at low momentum side between the Be and Ta data is an evidence that the LE-component should be distinguished with the low momentum tail.
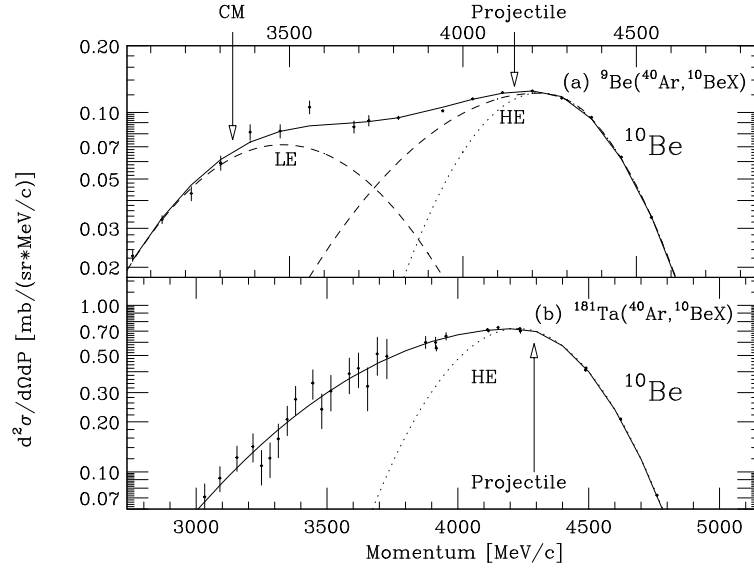
Figure D.1: Comparison of the momentum distributions of ^{10}Be isotope between the targets of Be and Ta.
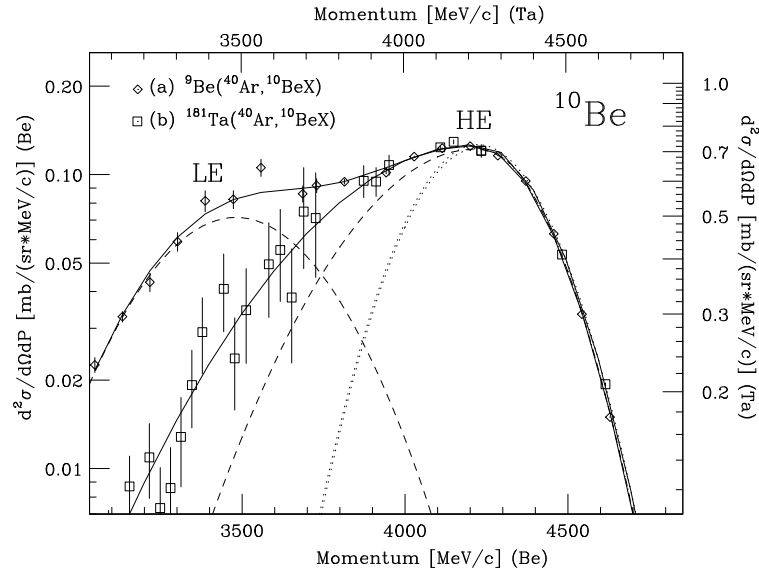

Figure D.2: The momentum distributions of ^{10}Be isotope from the targets of Be and Ta are drawn in the same coordinates.

Bibliography

[1] I. Tanihata, Nucl. Phys. A **552**, 275c (1991).

[2] I. Tanihata et al., Phys. Lett. B **289**, 261 (1992).

[3] N. Fukunishi, T. Otsuka and I. Tanihata, Phys. Rev. C **48**, 1468 (1993).

[4] T. Motobayashi et al., Phys. Lett. B **346**, 9 (1995).

[5] I. Tanihata et al.: Phys. Rev. Lett. **55** (1985) 2676.

[6] J.P. Dufour et al.: Nucl. Instrum. Methods Phys. Res. A **248** (1986) 267.

[7] B.M. Sherrill et al.: Nucl. Instrum. Methods Phys. Res. B **56/57** (1991) 1106.

[8] H. Geissel et al.: Nucl. Instrum. Methods Phys. Res. B **70** (1992) 286.

[9] T. Kubo et al.: Nucl. Instrum. Methods Phys. Res. B **70** (1992) 309.

[10] H.A. Grunder, W.D. Hartsough, and E.J. Lofgren: Science 174, 1128 (1971).

[11] H.H. Heckman et.al.: Science 174, 1130 (1971).

[12] G.D. Westfall et al. : Phys. Rev. Lett. **37**, 1202 (1976).

[13] J.D. Bowman et al.: LBL Report **LBL**-2908 (unpublished) (1973).

[14] J.B. Cumming et al.: Phys. Rev. C **17**, 1632 (1978).

[15] J.R. Cummings et al.: Phys. Rev. C **42**, 2530 (1990).

[16] R.P. Feynman et al.: Phys. Rev. Lett. **23**, 1415 (1969).

[17] J. Benecke et al.: Phys. Rev. **188**, 2159 (1969).

[18] D. J. Olson et al.: Phys. Rev. C **28**, 1602 (1983).

[19] H.H. Heckman et al.: Phys. Rev. Lett. **28**, 926 (1972).

[20] D.E. Greiner et al.: preprint LBL-3650 (March 1975).

[21] D.E. Greiner et al.: Phys. Rev. Lett. **152**, 35 (1975).

[22] A. Abul-Magd et al.: Phys. Lett. **60B**, 327 (1976).

[23] F. Uchiyama: Phys. Rev. C **23**, 935 (1981).

[24] A.S. Goldhaber: Phys. Lett. **53B**, 244 (1974).

[25] J.V.Lepore and R.J. Rinddell, Jr.: LBL report No. LBL-3086, 1974 (unpublished).

[26] N. Masuda and F. Uchiyama: Phys. Rev. C **15**, 972 (1977).

[27] H. Feshbach and K. Huang: Phys. Lett. B **47**, 300 (1973).

[28] E.J. Monitz et al.: Phys. Rev. Lett. **26**, 445 (1971).

[29] F. Rami et al., Nucl. Phys. A **444**, 325 (1985).

[30] F. Rami et al., Z.Phys. A **327**, 207 (1987).

[31] Y.P. Viyogi et al.: Phys. Lett. **42**, 33 (1979).

[32] Ch. Egelhaaf et al., Nucl. Phys. A **405**, 397 (1983).

[33] W.A. Friedman: Phys. Rev. C **27**, 569 (1983).

[34] G.F. Bertsch et al.: Phys. Rev. Lett. **46** 472 (1981).

[35] M.J. Murphy et al.: Phys. Lett. **135B**, 25 (1984).

[36] H.H. Gan et al.: Phys. Lett. **234B**, 4 (1990).

[37] L. Tassan-Got et al.: Nucl. Phys. A **524**, 121 (1991).

[38] A.Ono: private communications.

[39] J. Gosset et al. : Phys. Rev. C **16**, 629 (1977).

[40] W.D. Myers : Nucl. Phys. A **296**, 177 (1978).

[41] X. Campi and J. Hüfner: Phys. Rev. C **24**, 2199 (1981).

[42] J. Hüfner et al.: Phys. Rev. C **12**, 1888 (1975).

[43] J.D. Bowman, W.J. Swiatecki and C.F. Tsang (unpublished).

[44] D.J. Morrissey et al.: Phys. Rev. C **18**, 1267 (1978).

[45] J.W. Wilson et al.: Nucl. Instrum. Methods Phys. Res. B **18** 225 (1987).

[46] L.F. Oliveira et al. : Phys. Rev. C **19**, 826 (1979).

[47] J.J. Gaimard and K.H.Schmidt: Nucl. Phys. A **531**, 709 (1991).

[48] A.G. Artukh et al.: Phys. Lett. **33B**, 407 (1970).

[49] A.Y. Abul-Magd et al.: Phys. Lett. **39B**, 166 (1972).

[50] T. Mikumo et al.: Phys. Rev. C **14**, 1458 (1976).

[51] V.V. Volkov et al.: Phys. Rep. **44**, 93 (1978).

[52] R. Stock and A.M. Poskanzer: Comments on Nuclear and Particle Physics, 41 (1977).

[53] W. Scheid et al.: Phys. Rev. Lett. **32**, 741 (1974).

[54] A.A. Amsden et al.: Phys. Rev. Lett. **35**, 905 (1975).

[55] C.K. Gelbke et al.: Phys. Rep. **42**, 311 (1978).

[56] V. Borrel et al.: Z.Phys. A **314**, 191 (1983).

[57] M.C. Mermaz et al.: Z.Phys. A **324**, 217 (1986).

[58] C. Grégoire and B. Tamain: Ann. Phys. Fr. **11**, 323 (1986).

[59] D.Guerreau et al.: Phys. Lett. **131B**, 293 (1983).

[60] J. Barrette et al.: Proceedings of the XXXIInd International Meeting on Nuclear Physics, Bormio(Italy), 561(1984).

[61] G.D. Westfall et al. : Phys. Rev. Lett. **43**, 1859 (1979).

[62] J.A. Winger et al.: Nucl. Instr. Meth. B70, 380 (1992).

[63] N. Iwasa et al., Nucl. Instr. Meth. B126, 284 (1997); Th.Schwab, GSI Report No. 91-10 (1991).

[64] G. Rudstam: Ph.D. thesis, University of Uppsala (1957).

[65] G. Rudstam: Z. Naturforsch. A **21**, 1027 (1966).

[66] G. Rudstam: Nucl. Phys. A **126**, 401 (1969).

[67] R. Silberberg and C.H. Tsao: Astrophys. J. Suppl. **25**, 315 (1973).

[68] R. Silberberg et al. : Astrophys. J. Suppl. **58**, 873 (1985).

[69] K. Sümmerer et al.: Phys. Rev. C **51**, 1348 (1990).

[70] J. Hüfner et al. : Phys. Rep. **125**, 129 (1985).

[71] M. Noguchi et al. : Phys. Rev. C **38**, 1811 (1988).

[72] Y.Y. Chu et al. : Phys. Rev. C **4**, 2202 (1971).

[73] Y.Y. Chu et al. : Phys. Rev. C **10**, 156 (1974).

[74] P. Marmier and E. Sheldon : *Physics of Nuclei and Particles* (Academic, New York and London), Vol.I, 15 (1971).

[75] D. Guillemaud-Müeller et al.: Phys. Rev. C **41**, 937 (1990).

[76] M. Notani: RIKEN Acc.Prog. **29**, 31 (1995).

[77] H. Sakurai et al., Phys. Lett. B **448**, 180 (1999).

[78] O. Tarasov et al.: Phys. Lett. B **409**, 64 (1997).

[79] L. Sihver et al. : Phys. Rev. C **47**, 1225 (1993).

[80] H. Sakurai et al., Nucl. Phys. A **616**, 311c (1997).

[81] Y. Doki: JAERI-M 94-028, p. 70; Master thesis, Tokyo University (1994).

[82] K. Van Bibber et al.: Phys. Rev. Lett. **43**, 840(1979).

[83] B. Robinet et al., Nucl. Instr. Meth. 190, 197 (1981).

[84] T. Ichihara, T. Inamura, T. Wada and M. Ishihara, IEEE Trans. on Nucl. Sci. **NS36** (1989) 1628.

[85] R. Pfaff et al.: Phys. Rev. C **51**, 1348 (1995).

[86] D. Bazin et al.: Nucl. Phys. A **515**, 349 (1990).

[87] Ch. O. Bacri et al.: Nucl. Phys. A **555**, 477 (1993).

[88] F. Auger et al.: Phys. Rev. C **35**, 190 (1987).

[89] D. Guerreau et al.: Nucl. Phys. A **447**, 37 (1985).

[90] R. Dayras et al.: Nucl. Phys. A **460**, 299 (1986).

[91] S. Momota et al.: Proceeding of RNB5 to be published(2000).

[92] R. Serber, Phys. Rev. **72**, 1114 (1947).

[93] W. Swiatecki: LBL report, 1976 (unpublished).

[94] M. Weber et al.: Nucl. Phys. A **578**, 659 (1994).

[95] V. Borrel et al.: Z.Phys. A **324**, 205 (1986).

[96] J.B. Cumming et al.: Phys. Rev. Lett. **44**, 17 (1980).

[97] J.B. Cumming et al.: Phys. Rev. C **24**, 2162 (1981).

[98] S.B. Kaufman et al.: Phys. Rev. C **26**, 2694 (1982).

[99] D.J. Morrissey et al.: Phys. Rev. C **39**, 460 (1989).

[100] B. Mottelson : "Nuclear Structure" in Cours de l'Ecole d'Eté de Physique Théorique des Houches (1958).

[101] A.G. Artukh et al. : Nucl. Instrum. Methods Phys. Res. A **426** (1999) 605.

[102] K. Sümmerer and B. Blank: Phys. Rev. C **61**, 034607 (2000).

[103] S. Kox et al.: Phys. Rev. C **35**, 1678 (1987).

[104] M. Buenerd et al.: Nucl. Phys. A **424**, 313 (1984).

[105] M. Lefort and Ch. Ngô: Ann. Phys. **3**, 5 (1978).

[106] J. Galin : J. Phys. C **5, 37**, 83 (1976).

[107] T.H. Chiang et al.: Phys. Rev. C **20**, 1408 (1979).

[108] Y. Yanagisawa et al.: to be published.

[109] H. Otsu: Doctor thesis, Tokyo University (1997).

[110] W.A. Friedman: Phys. Rev. C **62**, 064609 (2000).